DOSIMETRIC VERIFICATION OF STEREOTACTIC BODY RADIOTHERAPY TREATMENT PLANS FOR EARLY STAGE NON-SMALL CELL LUNG CANCER USING MONTE CARLO SIMULATION

Sri Herwiningsih

B.Sc (Physics), M.AppSc (Medical Physics)

Submitted in fulfilment of the requirements for the degree of
Doctor of Philosophy

School of Chemistry, Physics and Mechanical Engineering
Science and Engineering Faculty
Queensland University of Technology

2017

Keywords

Collapsed Cone Convolution Algorithm, Dose Calculation Accuracy, Elekta Axesse Linear Accelerator, Lung Cancer, Monte Carlo Simulation, Non-small Cell Lung Cancer, Normal Tissue Complication Probability, Stereotactic Body Radiotherapy, Tumour Control Probability

Abstract

Calculation of the absorbed dose delivered to a patient during radiotherapy treatment is extremely important and has a direct impact on the treatment outcome. The calculation of the dose to tumour and normal tissues is particularly challenging for lung cancer treatments where large density variations can exist. Previous studies have compared different algorithms used for dose calculation in the treatment planning system (TPS). However, the impact of dose calculation accuracy on treatment outcomes prediction has not been widely studied, especially in regards to lung stereotactic body radiotherapy treatment (SBRT). This research aims to investigate the accuracy of the collapsed cone convolution algorithm employed in the Pinnacle^3 TPS for dose calculation of lung SBRT plans and the potential impact of any dose uncertainties on treatment outcomes prediction. For this purpose, a EGSnrc/BEAMnrc Monte Carlo model of an Elekta Axesse linear accelerator equipped with the Beam Modulator collimation system was developed and commissioned. The commissioned model was used to perform Monte Carlo simulations of the dose distribution of twenty early stage non-small cell lung cancer patient plans. The dosimetric parameters of the planning treatment volume (PTV) and organs at risk (OARs) were evaluated and compared with the TPS calculation. The effects of dose calculation uncertainties to the tumour control probability (TCP) and normal tissue complication probability (NTCP) were modelled using the Linear Quadratic Poisson TCP model and the Lyman-Kutcher-Burman NTCP model. The study found that no significant difference was observed in the PTV dose parameters between the TPS and Monte Carlo calculations. An agreement of ±6% was observed for the PTV coverage of the prescribed isodose, and even greater agreement of ±2% for the coverage of the 90% prescribed isodose. The TPS algorithm tended to overestimate the dose to OARs, with the exception of normal lung tissue, brachial plexus, and pericardium. A significant difference was mostly observed for the maximum point dose parameter. However, most dose parameters to OARs were still below the dose constraints outlined in the RTOG 1021 protocol for both the TPS and Monte Carlo plans. The only significant dose constraint violation was observed for the maximum point dose to the ribs, occurring in plans with a tumour located closest to the chest wall. The radiobiological analysis showed that the TCP parameters were more sensitive to dose calculation uncertainties than NTCP parameters. The sensitivity varied among different patients and was influenced by the selection of the radiobiological model parameters. There were significant differences in the TCP calculated from the TPS and MC dose distributions. A lower value of alpha and higher clonogenic density caused a greater reduction in the TCP, especially for the large PTV volume. No significant difference was observed for the NTCP of the radiation pneumonitis and rib fractures between the TPS and MC dose distributions. Although a significant difference was observed for the NTCP of acute oesophagitis, the value was <1%, which indicates no dose which could cause toxicity to the oesophagus. No toxicity to the pericardium was observed. Possible toxicity might occur to the ribs, especially in plans with the PTV overlapping the chest wall. Overall, the collapsed cone convolution algorithm used in the Pinnacle^3 TPS is sufficiently accurate for treatment planning of lung SBRT plans. However, the prescribed dose of 54 Gy in three fractions may need to be reduced for tumours located at the chest wall due to the high probability of rib fracture complication. The findings from this research serve to increase confidence in the algorithms used in the TPS for planning of complex SBRT treatments that involve a larger number of small treatment fields in the presence of tissue heterogeneities.

Table of Contents

List of Figures

List of Tables

List of Abbreviations

3DCRT : Three-dimensional Conformal Radiation Therapy
4DCT : Four-dimensional Computed Tomography
AAA : Anisotropic Analytical Algorithm
AAPM : American Association of Physicist in Medicine
AIHW : Australian Institution of Health and Welfare
AJCC : American Joint Committee on Cancer
BCSE : Bremsstrahlung Cross Section Enhancement
BED : Biologically Effective Dose
BIOPLAN : Biological evaluation of Plans
CCC : Collapsed Cone Convolution
CERR : Computational Environment for Radiotherapy Research
CI : Conformity Index
CM : Component Modules
CT : Computed Tomography
CTCAE : Common Terminology Criteria for Adverse Events
CW : Chest wall
D_{2cm} : The maximum dose received at 2 cm away from the PTV in any direction
DBS : Directional Bremsstrahlung Splitting
DICOM : Digital Imaging and Communication in Medicine
D_{max} : maximum dose
D_{mean} : mean dose
D_{min} : minimum dose
DNA : Deoxyribonucleic Acid
DSB : Double-strand Breaks
DTA : Distance-to-Agreement
DVH : Dose-Volume Histogram
ECUT : Electron Energy Cut-off
EORTC : European Organization for Research and Treatment of Cancer
EPL : Equivalent Path Length
ETAR : Equivalent-Tissue-to-Air-Ratio
EUD : Equivalent Uniform Dose
FSU : Functional Sub Units
FWHM : Full Width at Half Maximum
GTV : Gross Tumour Volume
IARC : International Agency for Research in Cancer
ICRU : International Commission on Radiation Units and Measurements
IMRT : Intensity Modulated Radiotherapy
ITV : Internal Treatment Volume
IVC : Inferior Vena Cava
LENT : Late Effects Normal Tissue
LKB : Lyman-Kutcher-Burman
LPL : Lethal-potentially Lethal
LQ : Linear Quadratic
LQC : Linear-quadratic-cubic
MC : Monte Carlo

MLC : Multi Leaf Collimator
MLD : Mean Lung Dose
MPD : Maximum Point Dose
MU : Monitor Unit
NSCLC : Non-small Cell Lung Cancer
NTCP : Normal Tissue Complication Probability
OAR : Organ-at-Risk
PB : Pencil Beam
PBC : Pencil Beam Convolution
PCUT : Photon Energy Cut-off
PET : Positron Emission Tomography
PIV : Prescribed Isodoses Volumes (Total volume of the covering isodose in the patient)
PTV : Planning Treatment Volume
PTV$_{48.6Gy}$: PTV coverage of the 90% prescribed dose (i.e. 48.6 Gy)
PTV$_{54Gy}$: PTV coverage of the prescribed dose (i.e. 54 Gy)
R$_{50\%}$: Ratio of the volume of 50% of the prescription dose (i.e. 27 Gy) isodose to the PTV volume
RD$_{50}$: Radiation dose required for 50% complication
RP : Radiation Pneumonitis
RTOG : Radiation Therapy Oncology Group
RTPS : Radiotherapy Treatment Planning System
SABR : Stereo Ablative Body Radiotherapy
SBRT : Stereotactic Body Radiotherapy
SBS : Selective Bremsstrahlung Splitting
SCLC : Small Cell Lung Cancer
SOMA : Subjective Objective Management Analytic
SRS : Stereotactic Radio Surgery
SSB : Single-strand Breaks
SVC : Superior Vena Cava
TCD$_{50}$: Radiation dose required for 50% tumour control
TCP : Tumour Control Probability
TERMA : Total Energy Released per Mass
TLD : Thermo Luminescent Detector
TNM : Tumour-Node-Metastases
TPS : Treatment Planning System
TROG : The Trans-Tasman Radiation Oncology Group
UBS : Uniform Bremsstrahlung Splitting
V$_{20}$: Volume of the entire structure organ irradiated by more than 20 Gy
VMAT : Volumetric Modulated Arc Therapy
WHO : World Health Organization
XVMC : X-ray Voxel Monte Carlo

Statement of Original Authorship

The work contained in this thesis has not been previously submitted to meet requirements for an award at this or any other higher education institution. To the best of my knowledge and belief, the thesis contains no material previously published or written by another person except where due reference is made.

QUT Verified Signature

Signature:

Date: 23/06/2017

Acknowledgements

I would like to thank Dr. Andrew Fielding, who has been very helpful in supervising and supporting me during my PhD candidature.

My thanks also to Dr. Jamie Trapp, Rhys Fitzgerald, Scott Crowe, Cathy Hardgrave, Paul Charles, and all of the QUT staff and medical physicists at Princess Alexandra Hospital, Brisbane, who assisted me during the completion of this research.

I would also like to thank professional editor, Kylie Morris, who provided copyediting and proofreading services, according to university-endorsed guidelines and the Australian Standards for editing research theses.

I wish to thank all of my friends, who always supported me with their du’a and sharing beautiful moments.

My greatest thanks go to my beloved parents, husband, and son for their patience, du’a, and support during the long separation period.

The simulation performed in this work was supported by High Performance Computing and Research Support, Queensland University of Technology, Brisbane, Australia.

Chapter 1: Introduction

Calculation of the dose of tumour and normal tissues for lung cancer patients where large density variations exist is difficult and must be accurate to avoid tumour recurrence and significant radiation toxicity to the patients. The investigation of the accuracy of dose calculation algorithms and the impact of any uncertainties in the dose calculation on tumour control and normal tissue complication probabilities is critical for lung stereotactic treatments. This is because a small change in dose could cause a large change in tissue responses, especially for tissue that has a steep slope in the dose-response curve. This chapter outlines the background of the research (Section 1.1), the context of the research (Section 1.2), and its purposes (Section 1.3), the significance and scope of the research (Section 1.4), and concludes with a description of the remaining chapters of the thesis (Section 1.5).

1.1 BACKGROUND

Lung cancer is a significant health issue, as it has a high incidence rate and the highest mortality rate of all cancer worldwide [1]. Based on World Health Organization (WHO) data, in 2012, the global incidence of death caused by lung cancer was around 1.59 million deaths from about 8.2 million cancer cases (19.4%). In Australia, the Australian Institute of Health Welfare (AIHW) [2] reported that lung cancer has the fifth highest incidence, and this is predicted to increase by 2020. The most common lung cancer type is non-small cell lung cancer (NSCLC), making up 80% of all lung cancer cases. Although surgical resection is the best treatment option, with the highest cure rate for NSCLC patients, a limited number of lung cancer patients are eligible for surgery due to comorbidities [3]. Radiotherapy is the best alternative for those who are ineligible or refuse surgery.

Radiotherapy, which uses a radiation source to kill cancer cells, has been shown to be an effective non-surgical method for treating various types of cancer [4]. There is growing interest in using radiotherapy, as it offers good cosmetic results [4], for example in breast cancer treatment [5] and cutaneous squamous and basal cell carcinomas treatment [6]. A study in breast cancer treatment using intensity modulated radiotherapy reported an excellent cosmetic result of 99% with no skin telengiectasias and fibrosis [5]. Although radiotherapy has played a significant role in lung cancer treatment, both as primary modality or adjuvant modality, it has been reported that the survival rate from this treatment is quite low, at between 10-30% [3, 7]. The main reason for this poor outcome is a failure in local tumour control due to progression of the disease [8]. Several factors, such as respiratory motion, inaccurate tumour definition, and inadequate dose to the tumour, also influence the success of radiotherapy treatment [9]. It is therefore necessary to formulate strategies to improve local tumour control in the treatment of NSCLC to obtain a higher survival rate.

One approach to achieving the above objective is by increasing the lethal dose delivered to the tumour target. The radiation dose can be delivered in a large dose per fraction, known as hypo-fractionated treatment, often referred to as stereotactic body radiotherapy (SBRT). SBRT has been rapidly adopted for the treatment of medically inoperable early stage NSCLC over the past five years, as it shows excellent local tumour control, up to 90% [3]. Although SBRT has shown promising results, there is growing concern regarding the negative aspects of implementing such a large dose per fraction. The presence of critical structures close to lung tumours, such as the spinal cord, oesophagus, heart, and normal lung tissue, could be at high risk from unnecessary high dose exposure, particularly if there are inaccuracies in radiation delivery and target definition. Therefore, it is necessary to protect those critical structures to minimise possible toxicity after SBRT treatment. The use of high conformal dose delivery techniques for SBRT treatments is one solution to ensure the safe delivery of high lethal doses that tightly conform to the target volume. Advanced radiotherapy technologies, such as improved imaging systems and precise radiation delivery techniques, have also supported the implementation of SBRT for NSCLC treatment. However, the benefit from these technologies could be limited if the algorithms used for dose calculation in the treatment planning systems are inaccurate.

1.2 CONTEXT

One important aspect of SBRT treatments for NSCLC is an accurate dose calculation in the treatment planning system (TPS). As one potential source of error in the radiotherapy process, dose calculation uncertainties could limit the achievement of a higher therapeutic ratio [10]. This is because the selection of the best radiotherapy plan to be delivered in the actual treatment relies on the evaluation of the dose distributions calculated by the TPS algorithms. Overestimation of the dose to the target could cause the tumour to receive an inadequate dose, which could have a consequence for tumour recurrence. Alternatively, underestimation of the dose to the normal organs could cause excessive exposure, leading to severe complications. It is therefore important to ensure that the dose calculation algorithms used in the TPS meet the accuracy requirement of 2-3% recommended by the International Commission on Radiation Units and Measurements Report 24 [11].

Previous studies have shown that conventional dose calculation algorithms, such as pencil beam algorithms, have difficulties in calculating the dose accurately in the lungs due to the low density value of lung tissue [12-20]. These correction-based algorithms fail to predict the increased photon attenuation in the lung region and penumbral broadening at the tumour edge adjacent to normal lung tissue [20-22]. More advanced model-based algorithms, such as convolution/superposition algorithms, that take into account tissue heterogeneity corrections, have shown an improved agreement with measurement [23] and are recommended for dose calculation of hypo-fractionated lung treatment plans [24, 25]. However, the accuracy of the convolution/superposition model is highly dependent on the accurate modelling of the primary radiation fluence [10]. Inaccurate modelling of these parameters will lead to significant uncertainties in the dose calculation.

The most accurate dose calculation engine for tissue heterogeneity and low density regions able to meet the required accuracy of <3% is the Monte Carlo technique [11]. However, Monte Carlo-based TPS algorithms are not as widely available as pencil beam algorithms and convolution/superposition algorithms. Longer computation time and huge computer resources are other limiting factors of the implementation of the Monte Carlo-based TPS in busy clinical practices. Therefore, the Monte Carlo technique has often been used as a reference algorithm for dose calculation in heterogeneous tissue due to its increased accuracy in modelling photon and electron transport [14]. The Monte Carlo technique serves as a computer-based verification tool for existing TPS dose calculation algorithms used for planning of complex treatment plans, such as lung SBRT. One of the most popular Monte Carlo codes used for this purpose is the BEAMnrc/DOSXYZnrc user codes which are based on the EGSnrc Monte Carlo system code [26, 27].

Collapsed cone convolution (CCC) algorithm is a model-based algorithm recommended for SBRT planning, as it models lateral electron scattering [24].

Although CCC algorithms are less accurate compared to Monte Carlo codes, CCC algorithms are widely adopted in many radiotherapy centres due to faster computation speeds and random-error free characteristics. The CCC algorithms are incorporated in commercial TPS, such as Helax-TMS, Oncentra Masterplan, and Pinnacle^3.

CCC algorithms have been shown to have a better performance than pencil beam algorithms [23, 28, 29] and anisotropic analytical algorithm (AAA) [14, 30-32] when compared to the measurement and Monte Carlo simulation in studies using simple slab phantoms [21, 31, 33-35], anthropomorphic phantoms [20, 23, 30, 36], and clinical patient plans [18, 28, 32, 37, 38]. It also has been showed in a retrospective study that the NSCLC patient plans calculated using CCC algorithms results in a lower local recurrence compare to the plans calculated using pencil beam algorithm [29]. However, some discrepancies have been observed. A dose difference between the CCC and Monte Carlo calculations of up to 10.4% of the median target dose was reported in a study using a virtual phantom with a 2 cm tumour model enclosed with a low density lung tissue ($\rho = 0.1$ g/cm^3) [14]. Although CCC algorithms generally show an agreement of 2-5% of the dose to the PTV parameters [18, 19, 28, 37, 39], a difference of higher than 5% has been observed for the dose to organs at risk in clinical cases [28]. In some cases, a difference of >5% was observed in individual patients [28, 38], indicating that the dose difference varies among different patients. However, these studies were investigated in conventionally fractionated treatments.

This raises a question regarding the accuracy of CCC algorithms in SBRT treatments for early stage NSCLC that involves a large ablative dose (>10 Gy/fraction), a larger number of treatment fields (7-14 fields), and complex shapes and small fields (<5 cm) in the presence of large density variations (tissue heterogeneities). To the best of the researcher's knowledge, only a few studies have investigated the performance of the CCC algorithms in clinical lung SBRT cases [19, 38, 39]. Most of these studies used a small number of patient plans (<20 plans) and a smaller number of beams (≤7 beams). Moreover, there is a variation in the fractionation size and the type of TPS algorithms used in these studies. The second question raised regards the potential impact of the dose uncertainties of CCC algorithms on the treatment outcomes, as a small change (5%) in dose could cause a change of 10-20% of local tumour control and possibly a larger change to the normal tissue complication [11, 40]. In the AAPM TG-105, Chetty et al. [41] recommended further investigation of the effect of dose calculation uncertainties on the treatment outcome prediction, as only a few studies are available. This research therefore focusses on addressing this issue.

The Monte Carlo technique was used to verify the dose calculation accuracy of the CCC algorithms used in the Pinnacle^3 Radiotherapy TPS for the planning of SBRT treatment for medically inoperable early stage NSCLC. BEAMnrc/DOSXYZnrc Monte Carlo user codes were employed to model photon beams generated from an Elekta Axesse linear accelerator, which was specifically designed for stereotactic treatments and to compute the dose deposition in phantom/patient geometry. The Elekta Axesse accelerator is equipped with the Beam Modulator micro multi leaf collimator (MLC) system, which has a leaf spacing of 4 mm at the isocenter. The research further evaluated the impact of the dose calculation uncertainties of the treatment plans on the treatment outcomes prediction, represented as tumour control probability (TCP) and normal tissue complication probability (NTCP) through radiobiological modelling.

The research was divided into three stages: 1) developing and commissioning a Monte Carlo model for the Elekta Axesse linear accelerator, including the Beam Modulator microMLC, 2) calculating Monte Carlo dose distributions of lung SBRT treatment plans and comparing them to dose distributions from TPS calculation, and 3) using radiobiological models to determine the effect of dose calculation uncertainties on TCP and NTCP.

1.3 PURPOSES

This research addresses the following research questions:

1. What is the accuracy of the dose calculation of lung SBRT treatment plans using a collapsed cone convolution (CCC) algorithm compared to a Monte Carlo algorithm?
2. How might dose calculation uncertainties in lung SBRT treatment plans affect treatment outcomes?

The main aim of this research was to evaluate the dose calculation accuracy of the CCC algorithm used for planning of SBRT treatment for early stage NSCLC using the EGSnrc/BEAMnrc Monte Carlo codes and to evaluate its impact on treatment outcomes. This aim was achieved through several objectives as follows:

1. Development and validation of a Monte Carlo model of the Elekta Axesse linear accelerator equipped with Beam Modulator microMLC used for delivery of the lung SBRT treatment plans as the first step in Monte Carlo simulation of lung SBRT plans.
2. Re-calculation of the dose distribution of lung SBRT treatment plans using the EGSnrc/BEAMnrc Monte Carlo codes and comparison to the TPS dose calculation using dosimetric criteria from the RTOG clinical trial protocol.
3. Estimation of the effect of dose calculation uncertainties on the tumour control probability (TCP) and normal tissue complication probability (NTCP) through the use of radiobiological models.

1.4 SIGNIFICANCE AND SCOPE

1.4.1 Significance

The increasing trend of SBRT adoption for the treatment of early stage NSCLC offers many benefits for individual patients, radiotherapy centres, and the community. Individual patients benefit in terms of saving time and in the cost associated with hospital stays and transport from a shorter overall treatment course of SBRT treatment (typically two weeks compared to six-seven weeks) and an increased chance of cure due to the use of a high dose/fraction. This benefits patients living in rural areas or remote regions who have limited access to well-equipped radiotherapy centres. The benefits for the radiotherapy centres relate to the possibility of treating more patients using existing resources. This also reduces the waiting period for patients to undergo treatment, reducing the chance of disease progression during this period. In addition to the optimisation of the treatment program to increase the survival rate of lung cancer patients, prevention programs such as a quit smoking campaign and regulation of tobacco or cigarette industries are important for reducing lung cancer incidences. Therefore, optimisation in both prevention and intervention are complementary in reducing the global burden of lung cancer.

In Australia, a randomised phase III TROG trial 09.02 (CHISEL) was completed comparing hypo-fractionated SBRT treatment (54 Gy in three fractions) with the conventionally fractionated radiotherapy treatment (60-66 Gy given in 2 Gy/fraction daily) for medically inoperable early stage NSCLC. In the protocol, convolution/superposition algorithms that take into account tissue heterogeneities are specified as a requirement in the treatment plan design. Unless the dose calculation accuracy of the TPS algorithms used for the SBRT planning has been verified and the impact of any uncertainties on the estimation of tumour control and normal tissue complication probabilities have been quantified, the effectiveness of lung SBRT treatment may not be guaranteed.

This research contributes by providing knowledge about the dose calculation accuracy of the TPS algorithms used for lung SBRT planning. This will serve to increase confidence in the algorithms used in TPS for planning of complex SBRT treatments that involve a larger number of small treatment fields in the presence of tissue heterogeneities. The use of radiobiological models assists in estimating the clinical impact of any dose uncertainties in the TPS dose calculation algorithms in terms of the TCP and NTCP. The inclusion of TCP and NTCP parameters (also known as biological indices) in the treatment plan evaluation, together with isodose evaluation and DVH evaluation, aids in optimising the treatment plan to achieve as high as possible therapeutic ratio. The findings of this research provide valuable information for use prior to implementing lung SBRT treatment in local radiotherapy centres and support the results of the CHISEL randomised trial. As fast Monte Carlo based TPS algorithms are now becoming commercially available, knowledge regarding the accuracy of the convolution/superposition algorithms will be useful in making decisions about whether or not existing algorithms should be replaced with the fast Monte Carlo based algorithms.

The novelty of this research is a fine tuning of a BEAMnrc model for a specific linac/micro-MLC combination; an Elekta Axesse equipped with the Beam Modulator micro-collimator system. The results of this research will be important to other researchers interested in SBRT verification for lung or other cancer sites. This research also offers a comprehensive evaluation of the dosimetric accuracy of CCC algorithms employed in the Pinnacle^3 treatment planning system for lung SBRT treatments delivered using a 3DCRT technique consisting of 10 coplanar and non-coplanar beams. The findings of this research complement the study by Calvo et al. [39] that focussed on lung SBRT plans delivered using the IMRT technique. In addition, this research also provides an evaluation of the impact of the dose calculation uncertainty on the clinical outcome assessed using radiobiological models.

1.4.2 Scope

This research uses a retrospective study focusing on the dosimetric verification of twenty SBRT plans for early stage NSCLC patients (stage I-IIa N0 M0) with a PTV size of < 100 cm^3 using Monte Carlo simulation. The plans were previously designed using the $Pinnacle^3$ RTPS to deliver a total dose of 54 Gy in three fractions using a 3DCRT technique consisting of 10 coplanar and non-coplanar beams with a 6 MV photon energy. The plans were then recomputed using a Monte Carlo technique involving the BEAMnrc/DOSXYZnrc Monte Carlo user codes. The simulated dose distributions were compared with the TPS dose distributions.

The evaluation of the CCC algorithms was only performed for the one used in the $Pinnacle^3$ Radiotherapy TPS. The evaluation of dosimetric criteria of the plans was based on the planning objectives and normal tissue constraints outlined in RTOG 1021 clinical trial protocol due to the similarity of the fractionation schedules.

Further evaluation of dose calculation uncertainties using the radiobiological models was performed using the Marsden Poisson TCP model and Lyman-Kutcher-Burman NTCP model implemented in the Biosuite Software. The parameters of the TCP and NTCP models used for the calculation were based on the existing published values. The NTCP calculation was performed for radiation pneumonitis, pericarditis, oesophagus complications, and rib fracture endpoints. This research consisted only of a planning study, and did not include the evaluation of complications occurring in patients after the actual treatment.

1.5 THESIS OUTLINE

This thesis is structured into seven chapters. Chapter 2 reviews the literature on stereotactic body radiotherapy treatment for lung cancer to identify the problem and relevant previous studies, followed by a description of the use of Monte Carlo technique for dosimetry verification of TPS algorithms in Chapter 3.

Chapter 4 discusses the development and commissioning of the BEAMnrc Monte Carlo model of the Elekta Axesse linear accelerator and Beam Modulator collimation system.

The use of the model in the verification of the dose distribution of twenty NSCLC patient plans and its comparison to the CCC algorithm calculation is presented in Chapter 5.

Chapter 6 discusses the impact of the dose calculation uncertainties using the TCP and NTCP.

Finally, Chapter 7 provides the general conclusions and recommendations from the study.

Chapter 2: Stereotactic Body Radiotherapy for treatment of early stage non-small cell lung cancer

Non-small cell lung cancer (NSCLC) is the most common type of lung cancer. Stereotactic body radiation therapy (SBRT) has played an increasingly important role in the treatment of medically inoperable early stage NSCLC with excellent local tumour control. The use of a very high dose per fraction has raised questions regarding its effect on normal tissue and critical organs. Precise and accurate planning and delivery are very important for this technique. One of the important planning steps is accurate calculation of the dose distribution, which is complicated by the presence of tissue heterogeneities. This chapter provides a brief overview of lung cancer (Section 2.1), and reviews the literature on the following topics: radiotherapy for lung cancer treatment (Section 2.2), SBRT (Section 2.3), and radiobiology (Section 2.4). Section 2.5 provides a summary of the gaps in the literature and develops the conceptual frameworks for the study.

2.1 A HIGH BURDEN FROM LUNG CANCER

2.1.1 Terms and definition

Cancer is a global disease problem related to a rapid and uncontrolled growth of abnormal cells [42]. The terms 'malignant tumours' and 'neoplasm' are also often used to describe the disease. Cancer types are usually classified based on the tissues in which the cancer cells start to grow, for example, carcinoma (in epithelial tissues) or sarcoma (in connective or supportive tissues, e.g., bone, cartilage, muscle, blood vessels). Cancer is also named based on its location in the body. Cancer cells that originate in the lung are known as lung cancer.

The lungs are part of the respiratory system, which has an important function, as this is where the exchange between oxygen and carbon dioxide occurs. Anatomically, the lung consists of the left and right lungs. The right lung comprises of three lobes and is larger in size than the left lung, which only has two lobes. Right and left bronchi pass the air from the trachea to the lungs. The branches of the bronchus are known as bronchioles, with alveoli on their end (tiny air sacs). There are two lining membranes known as visceral pleura (covers the lung) and parietal pleura (lines inside the chest) [43, 44].

2.1.2 Lung cancer statistics

Lung cancer is reported to be the most common cause of death from cancer worldwide [45-47]. The GLOBOCAN data series published by the International Agency for Research in Cancer (IARC), part of the WHO, reported that there were 1.8 million new lung cancer cases in 2012 and the estimated deaths from lung cancer were 19.4% of the total deaths from cancer [47]. This places lung cancer as the highest in term of incidence and mortality rates as shown in Figure 2.1. The global burden from lung cancer is very high in both developed and developing countries, as reported in GLOBOCAN 2012. In Australia, although prostate and breast cancers are more prevalent, the mortality rate of lung cancer remains the highest [48].

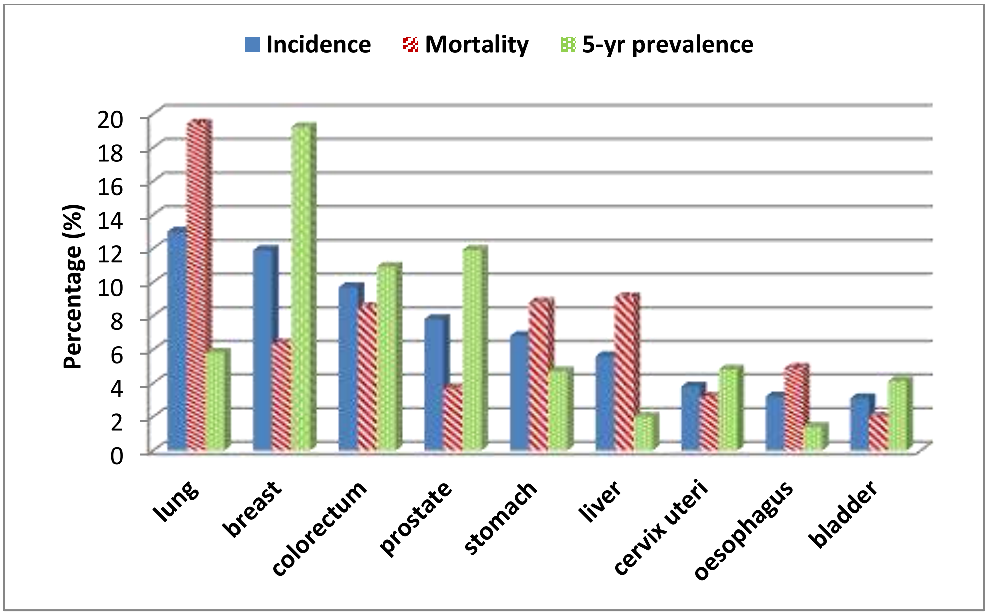

Figure 2.1. The incidence, mortality and five-year prevalence for nine top cancer types based on GLOBOCAN 2012 data [47].

The five-year prevalence data, representing the number of patients having lung cancer who survive for five year periods, is relatively low, approximately 5.7% of the total lung cancer cases. The low survival rate of lung cancer has been reported to be mainly due to the advanced progression of the disease at diagnosis and distant metastases [49]. This has led to a growing need to diagnose the disease earlier and to treat lung cancer patients more effectively to improve the survival rate.

Early detection and accurate staging of the disease are important factors for success in lung cancer treatment. The chance of curing the disease is higher for those in the early stage compared to the advanced stage. As different lung cancer types show different growth characteristics, the selection of the best treatment option for patients should be based on the type and stage of the disease [7, 49-51].

2.1.3 Lung cancer types

There are two types of lung cancer, non-small cell lung cancer (NSCLC) and small cell lung cancer (SCLC), as shown in Figure 2.2. In addition to size, the difference between these two types is the speed of cell growth and spread. NSCLC are more common and generally grow and spread more slowly than SCLC.

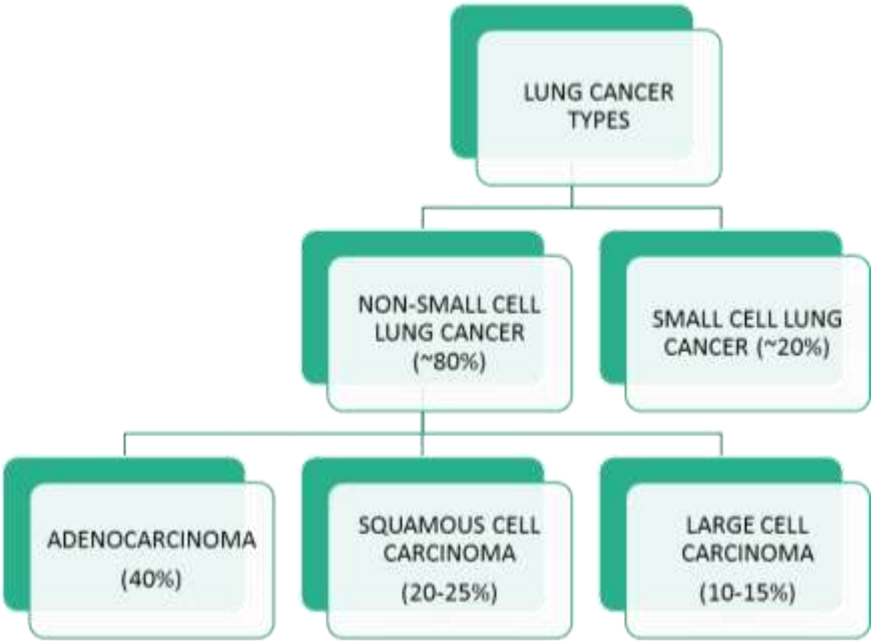

Figure 2.2. Lung cancer types and their proportion. NSCLC has a higher proportion compared to the SCLC, accounting for approximately 80% of lung cancer cases [7].

The characteristic of the two types of lung cancer are presented below:

1. NSCLC represents nearly 80-85% of all lung cancer cases, with several forms existing:

    a. Adenocarcinoma: mostly found on the outer edges of the lung (lung periphery), these arise from the tiny glands that produce mucus in alveoli and are the most common type of NSCLC [51], accounting for 40% of all NSCLC cases [7].
    b. Squamous cell carcinoma: mostly found on the bronchial tubes in the centre of the chest (central location), grows in the squamous cell of bronchial lining, and shows late development of distant metastasis), these account for 20-25% of all NSCLC cases [7, 51].
    c. Large cell carcinoma: large peripheral mass, accounting for 10-15% of all NSCLC cases [7].
2. SCLC represents 10-20% of lung cancer cases. These occur in the lining of the major breathing tubes in the centre of chest, show rapid growth, and are quickly spread to lymph nodes and the circulation system [7, 51].

2.1.4 Staging of lung cancer

Staging of lung cancer is based on the Tumour-Node-Metastases (TNM) classification system, which was updated into the "7th lung cancer TNM classification and staging system" in January 2010. 'T' represents the primary tumour or direct extent of the tumour into adjacent structures, 'N' represents the degree of spread to regional lymph nodes (nodal involvement), and 'M' describes the presence of metastases beyond regional lymph nodes. A detailed description of the TNM staging is presented in Table 2.1. Important revisions in this new system have been summarised by Mirsadraee et al. [50]. This staging system is primarily useful for NSCLC, in which the disease is categorised into four different stages from stage I to stage IV. Stage I is classified as early stage, while stage IV is classified as advanced (late) stage. In the early stage, the size of the tumour is less than or equal to 5 cm in diameter and the tumour has not spread to adjacent lymph node, while in the advanced stage the cancer has spread to the other parts of the body. In contrast, SCLC is classified into only two stages: the limited disease stage (33%) and extensive disease stage (67%). The limited stage represents a situation where the cancer only exists on one side of the chest, while in extensive stage the cancer is found in both sides and other organs. The cancer spread is frequently occurring through the lymphatic system, causing the metastatic spread into distant organs such as the brain and bone [52].

Table 2.1: *The American Joint Committee on Cancer (AJCC) TNM Staging of NSCLC*

Categories	Tumour Size	Description
Tx	-	The main tumour cannot be assessed.
T0	-	No evidence of primary tumour.
Tis	-	*Carcinoma in situ.*
T1: T1a T1b	≤3 cm ≤2 cm >2, ≤3 cm	Has not reached the visceral and pleura membranes, does not affect the bronchi.
T2: T2a T2b	>3 cm, ≤7 cm ≤5 cm >5, ≤7 cm	Involves main bronchus, but is not closer than 2 cm to the carina. Has grown to visceral pleura. The tumour partially clogs airways.
T3	>7 cm	Has grown to the chest wall, the breathing muscle, mediastinal pleura, or parietal pericardium. Has invaded a main bronchus and is closer than 2cm to the carina, but not involved the carina. Has clogged the airways, can cause pneumonia. Two or more separate tumour nodules are present in the same lobe of the lung.
T4	Any size	Has grown into mediastinum (the space between the lung), the heart, the large blood vessels near the heart, the oesophagus, the backbone or the carina. Two or more separate tumour nodules are present in the different loves of the same lung.
Nx		Nearby lymph nodes cannot be assessed.
N0		No spread to nearby lymph nodes.
N1		Has spread to lymph nodes within the lung (the same side as the primary tumour).
N2		Has spread to lymph nodes around the carina or in the mediastinum (the same side as the primary tumour).
N3		Has spread to lymph nodes near the collarbone on either side, and/or spread to hilar or mediastinal lymph nodes on the side opposite the primary tumour.
M0		No spread to distant organs or areas, including the other lung.
M1a		Has spread to the other lung, cancer cells are found in the fluid around the lung and fluid around the heart.
M1b		Has spread to distant lymph nodes or to other organs such as the liver, bones, or brain.

Reference: [49, 50]

This research focusses on medically inoperable early stage NSCLC (T1a/b or T2), with no nodal involvement (N0), and no distant metastases (M0) as defined in the TROG 0902 CHISEL trial protocol [24]. The tumour size is ≤5 cm and located in a peripheral location.

2.1.5 Lung cancer management for non-small cell lung cancer (NSCLC)

Three modalities are currently available for the treatment of lung cancer: surgical resection, radiotherapy, and chemotherapy. Table 2.2 summarises the treatment options for NSCLC. Surgical resection is the first primary treatment option for early stage NSCLC, with a survival rate between 40-67% [3, 7]. Surgical resection offers a higher chance to cure the disease by removing all malignant tissues. However, there are certain conditions where patients are not eligible for surgery due to several factors, such as age and heart failure, or those who refuse surgery [3]. Radiotherapy, being less invasive, is the best alternative modality to treat these patients. There is an increasing number of patients refuse surgery and choose radiotherapy. Chemotherapy is mostly used for advanced NSCLC, usually in combination with radiotherapy, especially when the disease has spread into many sites of the body, such as the brain or adrenal glands [3, 51]. Further detail regarding radiotherapy treatment for lung cancer is presented in the next section.

Table 2.2: *The Treatment Options for NSCLC [3]*

Stage of disease	TNM categories	Treatment options
Stage 0	Tis, N0, M0	
Stage I A	T1a/T1b, N0, M0	Surgery if medically fit, followed by postoperative radiotherapy. Radiotherapy if not medically fit or refuses surgery.
Stage IB	T2a, N0, M0	
Stage IIA	T1a/T1b, N1, M0 T2a, N1, M0 T2b, N0, M0	
Stage II B	T2b, N1, M0 T3, N0, M0	
Stage III A	T1-T3, N2, M0 T3, N1, M0 T4, N0 or N1, M0	Lobectomy if possible, may be followed by chemo-radiation. Concurrent chemo-radiation if lobectomy is not possible.
Stage IIIB	Any T, N3, M0 T4, N2, M0	Concurrent chemo-radiation
Stage IV	Any T, Any N, M1a Any T, Any N, M1b	Chemotherapy Palliative Radiotherapy

2.2 RADIOTHERAPY FOR TREATMENT OF LUNG CANCER

2.2.1 Limitations of conventional radiotherapy

Radiotherapy, also known as radiation therapy, is defined as the use of an ionising radiation source to treat or kill cancerous cells (curative) or to reduce the pain of an advanced disease (palliative) [52]. Radiotherapy plays a significant role in treating cancer in many sites of the body, including the lungs. It is estimated that more than a half of NSCLC patients currently benefit from radiotherapy treatment External beam radiotherapy, in which radiation is delivered from outside of the body to kill the tumour, is commonly used in the treatment of lung cancer. As the tumour is usually located within healthy normal tissues, the irradiation of normal tissues or critical structures during radiotherapy treatment is difficult to avoid [51]. This condition creates limitations in achieving the main goal of radiotherapy, which is to eradicate the tumour by delivering a lethal dose precisely to the tumour volume, while keeping normal tissues and critical organs free from unnecessary radiation exposure [53]. This goal, usually termed the therapeutic ratio, is maximised by a high tumour control probability (TCP) and minimum normal tissue complication probability (NTCP). However, achieving high TCP in the treatment of lung cancer is often limited by the presence of several critical organs close to the tumour target, such as normal lung tissue, the spinal cord, oesophagus, blood vessels, and heart [51].

Moreover, treating tumours in the lung is very challenging, as the tumour is subject to motion, for instance respiratory motion and heart motion. It has been reported that the long term survival rate of lung patients from conventional radiotherapy treatment is very low, between 10% and 30% [3, 7, 54]. In conventional radiotherapy, radiation is typically delivered with the total dose of 60-66 Gy over a six to seven week fractionated treatment course, with a fraction size of 1.8 to 2 Gy per fraction using simple beam arrangements [9]. Kong et al. [3] reviewed the treatment outcomes from 11 lung cancer studies using conventional radiotherapy. They found that five-year overall survival rate was only about 20%, with local recurrence and distant metastases the most common causes of failure [3].

Several factors cause the failure of local tumour control, as highlighted by Martel [9]. The first factor is inaccurate tumour definition during the image based treatment planning that does not cover the extent of the disease in the target volume. The next factor is the geographic miss of the target due to respiratory motion. Uncertainties in the dose calculation algorithm due to the presence of lung tissue inhomogeneities also contribute to poor local tumour control. Inaccurate dose calculation could cause an under-dosage to the tumour, failing to kill all tumour clonogens. The prescribed dose is another factor that can cause poor local tumour control due to an insufficient dose to kill the tumour cells. In addition, accelerated repopulation of tumour clonogens due to prolongation of treatment time may also limit the achievement of high tumour local control [55].

These limitations of conventional radiotherapy have driven the significant development in radiotherapy technology with the aim of improving the therapeutic gain, and hence, the survival rate. This technological development includes imaging systems, treatment planning algorithms, and radiation delivery techniques [56, 57]. In addition to the technological aspect, the dose escalation strategy has been proposed by modifying the fractionation dose and schedule in order to have a higher local tumour control [8]. One of the modified fractionation schedules is hypo-fractionation, in which the dose is delivered in a higher dose per fraction over fewer fractions. The hypo-fractionated treatment offers advantages, such as reducing the overall treatment time, reducing the chance of tumour cell repopulation, and convenience for patients [58-60].

2.2.2 Advances in radiotherapy technology

The motive behind the development of radiotherapy technology is primarily to improve the treatment outcome by improving local tumour control and maintaining low normal tissue complications [61]. Improvements in advanced technologies are now available for the complete radiotherapy process, from treatment simulation to treatment planning, treatment delivery, and verification.

New imaging devices have provided significant improvement in target definition. The use of four-dimensional computer tomography (4DCT) in treatment simulation has allowed for a reduction in the safety margins applied to the target volume(s) [61]. This consequently reduces the amount of normal tissues receiving a high radiation dose and creates the potential for the implementation of a high-dose-per fraction treatment, such as stereotactic body radiotherapy (SBRT). In addition, the ability of 4DCT to image the tumour position at different points in the respiratory cycle allows for the effect of tumour motion to be taken into account in the treatment planning process. The use of 4DCT was highly recommended in the TROG 0902 CHISEL trial, rather than fluoroscopy [24]. Moreover, more accurate target positioning is now possible with on board imaging capability, such as the cone beam CT scanner [61].

Significant improvement has also been seen in the treatment planning system (TPS) through the introduction of more accurate dose calculation algorithms. Dose calculation uncertainty is a critical problem in lung radiotherapy treatment due to the inhomogeneity of the lungs, in which conventional algorithms have struggled to accurately calculate the dose. The use of model-based algorithms is now more common in the TPS, for example, convolution/superposition algorithms. Monte Carlo-based algorithms are now also commercially available, namely Peregrine in Corvus TPS [62], Monaco (CMS), and Brainlab AG (iPlan) [53]. The issue of dose calculation uncertainty for lung radiotherapy is discussed further in Section 2.3.5.

In terms of radiation delivery, conformal radiation techniques have been widely adopted in many radiotherapy centres. Three-dimensional conformal radiation therapy (3DCRT) has increased normal tissue sparing through a conformal treatment field shape. However, there is a potential for the organs at risk (OARs) close to the target volume to receive a higher dose, particularly for complex treatment volume shapes. The introduction of intensity modulated radiotherapy (IMRT) offers the potential for improved conformity of dose distribution, along with improved normal tissue sparing through the use of non-uniform beam intensity across the field [63]. Beam shaping is governed by a complex movement of the multi-leaf collimator (MLC) enabling the treatment of an irregular tumour shape. However, radiation delivery using IMRT usually takes longer than 3DCRT. Karl Otto recently developed a more efficient radiation delivery method, known as volumetric modulated arc radiotherapy (VMAT) [64]. In VMAT, the radiation is delivered using gantry rotation with three variable parameters: rotation of the gantry angle, MLC movement and dose rate [65].

Coplanar and non-coplanar 3DCRT treatment beams are usually used for radiation dose delivery of SBRT treatment [3]. In the TROG 0902 CHISEL trial protocol, 8-12 non-opposing conformal photon beams were required to meet the dosimetric criteria delivered using the linear accelerator with an MLC leaf width of 1 cm or smaller at the isocenter. There are several mini MLCs commercially available from different manufacturers that are specifically designed for small-field radiotherapy application such as SBRT (Table 2.3). Elekta has released the Beam Modulator^{TM}, which has a 4 mm leaf spacing at the isocenter that offers a maximum treatment field of 21 cm x 16 cm, enabling stereotactic treatment of extra cranial tumours [66, 67].

Invention of the Cyberknife system in 1994 by Dr. John Adler allows for delivery of high radiation doses through a robotic-mounted linac and allows for accurate target tracking through an integrated continuous image guidance. The ability of the robotic arm to compensate any patient or tumour movements detected by the tracking system offers a great advantage to minimise the patient immobilization. This integrated system is suitable for SBRT delivery not only for intracranial site, but also extracranial sites [68]. Therefore, advanced radiotherapy technologies allow for implementation of dose escalation schemes, such as SBRT treatment for early stage NSCLC [69].

Table 2.3: *Several Commercial Mini MLCs Designed for SBRT Application*

Collimation systems/MLC	Number of leaves	MLC design
Varian High-definition MLC (HD120^{TM}) [66]	60 leaf pairs	▪ Leaf width at isocenter: 3 mm (64 inner leaves), 5 mm (56 outer leaves, 2 x 28) ▪ Straight leaf-end ▪ Tongue and groove design
Varian Millennium 120 MLC [66]	60 leaf pairs	▪ Leaf width as isocenter: 5 mm (80 inner leaves, 10 mm (40 outer leaves)
Elekta Beam Modulator [70]	40 leaf pairs	▪ Leaf width at isocenter: 4 mm ▪ Rounded leaf-end ▪ No tongue and groove design ▪ No movable backup jaws
Elekta Agility [71]	80 leaf pairs	▪ Leaf width at isocenter: 5 mm

2.3 STEREOTACTIC BODY RADIATION THERAPY (SBRT)

2.3.1 Overview

Dose escalation can improve the low survival rate of conventional radiotherapy for treatment of lung cancer. The main focus is improving local tumour control by delivering a higher biologically effective dose (BED) to the tumour volume [8, 9]. An increase of dose by 1 Gy might translate to an improvement of five-year tumour control by 1% [3]. Although dose escalation can be performed using the conventional fractionation scheme, the consequences of a lengthened treatment course can include a rapid repopulation of tumour clonogens, reducing control of the tumour. The accelerated repopulation of tumour cells usually occurs five to seven weeks after the first treatment fraction [8]. As an alternative, shortening the treatment course would avoid this effect. The combination of a large dose per fraction and a short overall treatment time is one approach for increasing the BED to the tumour, as BED is a function of the fraction size [60]. Therefore, the adoption of the SBRT treatment that delivers a higher radiation dose in fewer fractions within a two-week course can be used to achieve a higher therapeutic ratio.

However, based on basic radiobiology theory, increasing the dose would also increase the complication of normal tissues surrounding the target, especially late-responding normal tissues [4, 60]. This issue has become the main concern in implementing SBRT for lung treatment, in which the respiratory motion could cause the geographical miss of the radiation dose, resulting in radiation toxicities to the adjacent normal tissues and OARs. This section briefly discusses SBRT treatment, its complexities and the importance of dose calculation accuracy in SBRT treatment of NSCLC.

2.3.2 Definition of stereotactic body radiotherapy (SBRT)

SBRT is also known as stereotactic ablative body radiotherapy [72, 73]. It can be defined as a radiotherapy treatment that delivers a very high dose per fraction (>3 Gy/fraction) in fewer treatment fractions [54, 74]. Hypo-fractionation is also used to describe SBRT [54] [4].

SBRT was adapted from stereotactic radiosurgery (SRS) for intracranial lesion in the mid 1990's. Further detail on the history of SBRT has been presented by Martin and Gaya [72]. The term 'stereotactic' refers to the precise targeting of the tumour through the use of an immobilisation system and a reference coordinate system. The success of the SBRT treatment for intracranial sites has been extended to other extra-cranial sites, such as the liver, pancreas, kidney, prostate, and spine, [72, 75]. Currently, there is an increasing trend in the adoption of SBRT for the treatment of lung cancer, and SBRT is increasingly accepted as a standard treatment for medically inoperable early stage NSCLC.

SBRT lies between SRS, which delivers a large dose in a single fraction, and conventional fractionation, which delivers 1.8-2 Gy/fractions in five day/weeks over six to seven weeks [72]. In many SBRT schedules, the dose is delivered with a fraction size of 10-20 Gy per fraction in three to five fractions over a two-week course. The use of a higher fraction size for SBRT enables the delivery of a higher BED to the tumour target, of two to five times greater than the conventional 2 Gy/fraction treatment [76]. For instance, delivering a total dose of 60 Gy in 30 fractions will result in the BED value of 72, while giving the same dose in three fractions will result in a BED value of 180.

2.3.3 SBRT for treatment of medically inoperable early stage NSCLC

SBRT treatment for medically inoperable early stage lung cancer has shown an excellent local tumour control and survival rate, with low rates of radiation toxicities. Retrospective studies in Japan show that a prescribed dose of 30-84 Gy in one to 14 fractions resulted in a five-year local control of 84% [77]. Delivering the total dose of 60-66 Gy in three fractions resulted in two-year local tumour control of 95% for a phase II study in the USA [74]. This study revealed that a centrally located tumour has a higher risk of lung toxicity compared to the peripheral tumour after SBRT treatment. Therefore, it is necessary to reduce the fraction size for the central tumour, such as delivering the total dose of 60 Gy in four fractions instead of three fractions. Other outcomes of SBRT studies were reviewed by Martin and Gaya [72] and Solberg et al. [78]. Low to mild toxicities were reported such as grade 1-3 pneumonitis, dermatitis, oesophagitis, and chest wall pain.

2.3.4 Complexities of SBRT for treatment of NSCLC

The complexities of SBRT rely on the involvement of many technologies during treatment to ensure the safe and accurate delivery of the radiation dose. The presence of lung inhomogeneities adds to the complexity, causing difficulty in achieving accurate dose calculations. The use of small radiation fields (usually less than 5 cm x 5 cm) to treat the small lesion volume in early stage NSCLC also causes difficulty in accurately measuring the dose, due to the limitations of available dosimeter devices [79]. The dose distribution of the SBRT treatment is characterised by its rapid fall-off at the tumour edge and adjacent tissue, as shown in Figure 2.3.

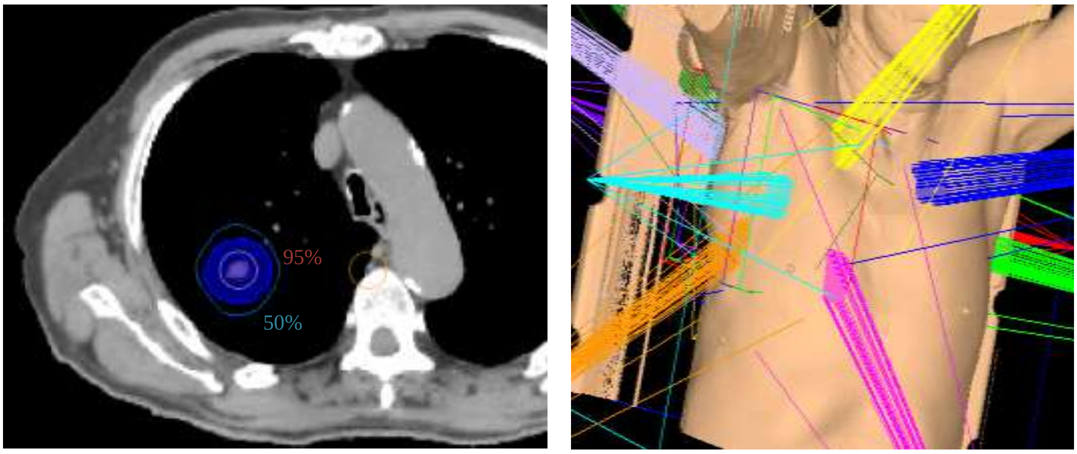

Figure 2.3. Example of the SBRT treatment plan for stage I NSCLC. The left figure shows the rapid fall-off of the dose (red line is 95% of isodose, blue line is 50% isodose) and the right figure shows the typical beam arrangement of the plan consisting of coplanar and non-coplanar beams.

SBRT differs from other radiation delivery techniques in three aspects: precise targeting, precise radiation beam delivery, and dose fractionation [3]. The use of a large dose per fraction requires the precise delivery of a highly conformal dose to the patient, with precise positioning of the tumour target to minimise normal tissue toxicities. To minimise complication in surrounding normal tissues, the SBRT usually uses small margins of the order of mm, while conventional radiotherapy may use a larger margin of the order of cm [79].

Patient immobilisation, tumour motion assessment, and image acquisition for treatment planning are three important aspects for the precise targeting of the radiation dose [75]. Immobilisation devices, such as custom foam cradles, are commonly used in SBRT treatment for precise positioning of the patient for each treatment fraction. The concept of ‘frame’ is introduced for the precise positioning of the tumour target during simulation and the actual treatment. Precise targeting can be achieved by tracking the tumour during the treatment using on board imaging devices [75].

Different approaches to respiratory motion management are used to manage tumour motions, which are categorised into imaging and intervention [78]. Four-dimensional computed tomography imaging is commonly used to consider the change in tumour positions at different phases of the respiratory cycle for precise definition of the tumour volume [9]. In addition, magnetic resonance imaging and positron emission tomography may be used for better imaging. Several techniques, such as abdominal compression, breath-holding techniques, free-breathing gating techniques, and tumour tracking to compensate radiation delivery for respiratory motion are categorised as intervention.

2.3.5 Importance of accurate dose calculation in lung SBRT treatment

Equally important to the precise targeting and motion management described above is the dose calculation accuracy of the SBRT treatment plan, which forms the main focus of this research. Once the target volume has been defined and the radiation beam has been designed, dose calculation is performed based on the prescribed dose and the patient geometry to evaluate whether or not the treatment plan will meet the objectives. The evaluation of the treatment plan is usually performed using dose volume histograms (DVHs) derived from the calculated dose distributions to estimate the target coverage and dose to normal and critical structures [9]. Inaccurate dose calculations can compromise the treatment efficacy [41].

The dose calculation of photon beam irradiation is based on the energy deposition of the secondary charged particles (electron and positron) resulting from interactions between the indirectly ionizing photon beam with tissues (phantoms/patients geometry). These charged particles are set in a predominantly forward motion by Compton scattering, the dominant interaction type for megavoltage radiotherapy. The range of secondary charged particles can be several cm. As these charged particles are slowed down and come to rest, their energy is deposited into the tissue. The energy absorbed per unit mass is known as the absorbed dose [9]. The unit of absorbed dose is J/kg, which is known as gray (Gy), in which 1 Gy = 1 J/kg.

Obtaining an accurate dose calculation for a lung treatment plan is a very challenging task due to the presence of tissue heterogeneities [3, 9]. It has been reported that conventional algorithms that employ path-length scaling, such as the pencil beam algorithm, have difficulty accurately calculating the dose at interfaces of different density materials, such as tumours and normal lung tissue [9, 22]. This is because the tumour, which has a density similar to water, is usually enclosed by surrounding normal lung tissue that has a lower density than water, which is about 0.2-

0.4 g/cm^3 [9, 13]. The low density of lung tissue results in lower photon attenuation than in water. Therefore, density correction is required in order to obtain a more accurate result. Xiao et al. [25] recalculated the lung treatment plans used in the RTOG 0236 trial and demonstrated that a dose calculation with a heterogeneity correction is essential. Based on this result, the prescribed dose in the TROG 0902 CHISEL trial was adjusted to 54 Gy in three fractions after recalculating the prescription dose of the RTOG 0236 protocol (i.e., 60 Gy in three fractions) using an inhomogeneity correction.

Two types of algorithms are generally used for dose calculation in the treatment planning system, as shown in Figure 2.4: correction-based algorithms (also known as type A algorithms) and model-based algorithms (also known as type B algorithms) [80].

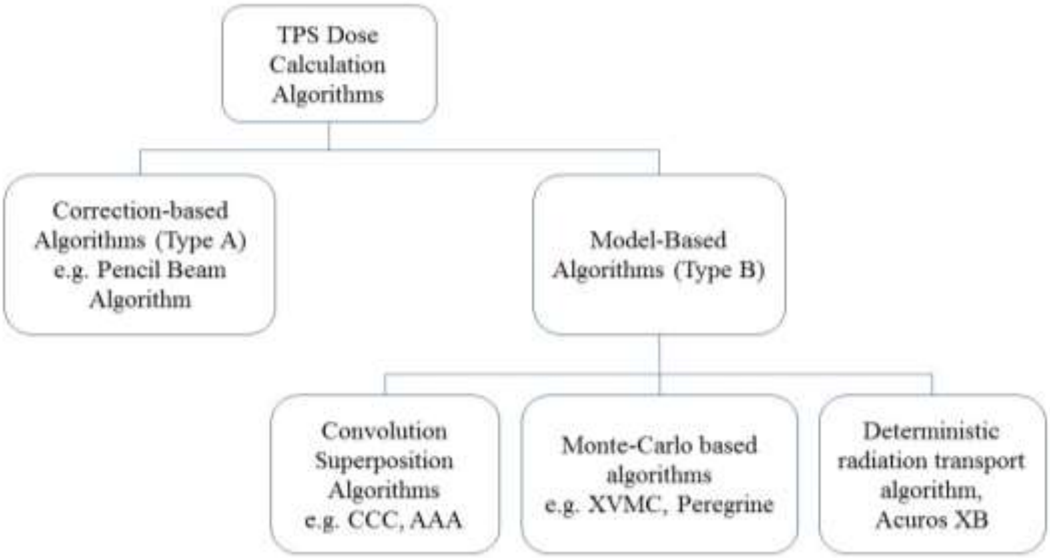

Figure 2.4. Types of dose calculation algorithms for the photon beam employed in the Treatment Planning System (TPS).

There are several correction-based algorithms, such as the equivalent path length (EPL) method, generalised Batho power law, and equivalent-tissue-to-air ratio (ETAR) methods, which employ simple correction for beam attenuation and scattering. However, these algorithms do not accurately calculate the dose in the lung and tumour-lung tissue interfaces, as they do not accurately model lateral electron scatter [9, 81]. Model-based algorithms, such as convolution/superposition methods, are more accurate than correction-based methods, as they directly predict the dose distribution using primary particle fluence and a dose kernel incorporating the lateral electron transport in the calculation [81, 82]. The kernel might be derived from a measurement or Monte Carlo simulation [10]. Monte Carlo method is also considered a model-based algorithm. However, the Monte Carlo method provides more accurate results than convolution/superposition algorithms, as it explicitly models the transport of photons and electrons [11].

Several studies have compared pencil beam algorithms from commercial TPS with more advanced model-based algorithms, such as collapsed cone convolution (CCC) algorithm [12, 14, 21, 23], anisotropic analytical algorithm (AAA) [14, 16, 83, 84], and Acuros XB [16]. Acuros XB is a dose calculation algorithm that based on a deterministic grid-based Boltzmann equation solver. This algorithm models the behaviour of radiation particle in material explicitly. Similar with Monte Carlo algorithm, the dose calculation using Acuros XB requires cross-section data of the materials where the radiation transport is investigated and the dose reporting is dose to medium [35, 85, 86]. The studies found that a pencil beam algorithm that employs simple correction-based methods, such as Batho, modified Batho, and ETAR, overestimates the dose in low density media. This algorithm also fails to predict the penumbral widening at tissue interfaces where large densities variation exists. One extensive study on the performance of the difference in dose calculation algorithms was the study undertaken by Carrasco et al. [21], which compared the Cadplan v.6.7 pencil beam model and Helax-TMS pencil beam algorithm with Helax-TMS CCC algorithm and Monte Carlo method (Penelope MC code). The study was performed in a heterogeneous phantom containing water-lung-water slab layers using a single beam. The results showed that overestimation of the dose in the lung substitute by the pencil beam algorithms increased as the field size decreases and the photon energy increases. Dobler et al. found that the pencil beam algorithm over-estimated the measured dose by 15% compared to film measurement in an anthropomorphic phantom study [23]. Aarup et al. evaluated the influence of variable lung density from 0.01 g/cm^3 to 1 g/cm^3 and found that the overestimation of the planning target volume (PTV) coverage by the pencil beam algorithms was more significant for lower density [14]. In a clinical situation, Ding et al. evaluated the dose calculation for ten NSCLC patient treatment plans using the pencil beam algorithm with a modified Batho correction method [13].

The study showed that the pencil beam algorithm overestimated the PTV coverage by 10% compared to the AAA calculation.

Other investigators compared pencil beam algorithms with Monte Carlo-based algorithms, such as Peregrine [87], Xray Voxel Monte Carlo (XVMC) [23] and the fast commercial Monte Carlo algorithms in BrainLab's iPlan [15, 88]. These studies demonstrate that the accuracy of Monte Carlo-based algorithms is better than other algorithms compared to the measurement. Considering the inaccuracy of the pencil beam algorithms, the use of such algorithms in lung SBRT treatment planning is not recommended, convolution/superposition algorithms or Monte Carlo algorithms that take into account the inhomogeneity should be used instead as they have better agreement with the measurement [23, 83, 89]. Although the Monte Carlo method has been shown to be the most accurate dose calculation algorithm in heterogeneous media, long computation times and high computational demands are well-known limiting factors of its implementation in clinical workflow. Convolution/superposition algorithms therefore remain preferred over the Monte Carlo method, as they are faster in terms of computation speed and are not subject to statistical uncertainty.

As the measured data are usually used to define the primary radiation fluence and the dose kernel of the convolution/superposition algorithms, inaccuracy in dose measurement influences the accuracy of dose calculation of the algorithms. Taylor et al. [79] highlighted the uncertainties of dose measurement for small field treatments due to the limitation of detector dimensions that are close to the radiation field size. The use of detectors with a finite size, as commonly used for large radiation fields, is not appropriate, as it causes a volume averaging effect and broadening effect on the penumbra. In addition, for dose measurement, it is usually assumed that electronic equilibrium conditions are reached, which is not always true for small field treatments in patients. Therefore, in the TROG 0902 CHISEL trial the size of treatment field was recommended to be >4 cm. Two factors cause electronic disequilibrium in the small field lung treatments: lateral secondary electron scattering and the low density of lung [79]. The range of secondary electrons in the lung tissue is two to five times higher than that in the water.

The CCC algorithm is one of the dose calculation algorithms listed in the TROG 0902 CHISEL trial protocol for the planning of early stage NSCLC SBRT planning. In this algorithm, the kernel is convolved by total energy released per mass (TERMA) distribution, collapsed onto their axis [81, 90]. The CCC algorithms are incorporated in several commercial radiotherapy treatment planning systems (RTPS), such as Pinnacle^3 Phillip, Helax TMS, and Oncentra Masterplan. The CCC implemented in Pinnace^3 distinguish between primary photons (TERMA) and secondary electron scatter, although the kernel is not separated into these two components during the convolution [25].

CCC algorithms have been reported to have a better performance than AAA in heterogeneous phantom studies relative to the measurement and Monte Carlo calculation [14, 30, 80, 85] and in clinical lung treatment studies [18, 32]. The CCC is a potential alternative to the Monte Carlo simulation, as it offers a faster computation and is able to predict the penumbra broadening inside the lung substitute material. Although the CCC is considered accurate, some inaccuracy can remain. Dobler et al. [23] found that the CCC algorithms show discrepancies of 8% with the film measurement in calculating the dose in a 2 cm tumour model within the anthropomorphic phantom. A difference in the median target dose up to -10.4% between the CCC and MC was reported by Aarup et al. [14] in a 2 cm central tumour enclosed in the lung tissue with a density of 0.1 g/cm^3 using a virtual phantom. They found that the difference was higher for the lower density of the lung. As these studies were performed in a simplified phantom, the difference in actual clinical cases might vary between patients depending on the tumour size and location. In addition, the CCC algorithms from different commercial TPSs have been reported to show different performance in predicting the dose to the target and OARs [28, 91].

Evaluation of the CCC algorithm performance in clinical lung treatment plans has been reported in several studies, as presented in Table 2.4. CCC generally shows an agreement to within 2-5% of the target dose [18, 19, 28, 37, 39, 92]. However, a difference of >5% was observed between the CCC and Monte Carlo calculations for the dose to critical organs (D_{max} of the heart, D_{33} of the esophagus and V_{20} of the lungs) [28]. In addition, a dose difference of >5% for PTV-D_{min} was also observed in individual patients, indicating the variation of dose difference among different patients [28]. However, these studies were performed for a standard fractionation schedule (2 Gy/fraction). Only a few studies have reported the performance of CCC algorithms in lung SBRT cases. Fotina et al. [38] investigated the performance of the enhanced collapsed cone algorithm in the Oncentra RTPS for two lung SBRT cases with the

XVMC, a commercial MC-based TPS algorithm. They found discrepancies of up to 5% for the dose to the target, and even higher for the spinal cord, of up to 10%. The inclusion of more patient plans was performed in a study by Calvo et al. [39] for the SBRT schedule of 45 Gy in three fractions, comparing the CCC Pinnacle with EGSnrc Monte Carlo simulation. The findings show that a dose difference of up to 4% was observed for the minimum and maximum dose to the target, and up to 7% for the ipsilateral uninvolved lung. However, this study focused on lung SBRT plans delivered using the IMRT technique. The CCC Pinnacle was reported to have a reasonably accurate dose and a shorter computation time than XVMC, with the agreement of within 2.5% for the isocentre dose in a study by Takahashi *et al.* [92]. Another recent study by Troeller et al. [19] investigated 17 lung SBRT plans with small tumours (≤4 cm in diameter) using a 7.5 Gy x 8 fractions schedule. However, the comparison was performed for the pencil beam and enhanced CCC algorithms in Oncentra, for which it is well-known that the pencil beam model can overestimate the dose to the target even in a simple heterogeneous phantom geometry. Overestimation of the pencil beam algorithm is more significant for smaller PTV volumes and for a tumour volume that is fully surrounded by normal lung tissue. Another superposition algorithm, CMS/Xio has been also reported to have a good agreement with Monte Carlo algorithms (MCSIM) [93]. However, this study focuses on the evaluation of collapsed cone convolution algorithm. Ideally, uncertainties in dose calculation algorithms should be kept to below 3% to maintain the overall uncertainty of the radiotherapy treatment of below 5% [82]. In addition, most of these studies involved the use of a smaller number of treatment fields (<7 beams). Therefore, it is important to check the dose calculation accuracy of the TPS that employs the CCC algorithms with the more accurate Monte Carlo technique for planning small-field lung SBRT treatments that typically involve 10 coplanar and non-coplanar beams. The Monte Carlo technique has been widely used as a benchmarking tool for other dose-calculation algorithms and is presented in more detail in Chapter 3.

Table 2.4: *Studies on the performance of CCC algorithms in lung radiotherapy treatment plans*

Reference	Evaluated algorithms	Treatment plans
Vanderstraeten et al. [28]	CCC Pinnacle, PB Helax TMS, CCC Helax TMS, Full Monte Carlo BEAMnrc/EGSnrc	10 lung plans delivered using 9 fields IMRT technique, 6 and 18 MV photon beams, standard fractionation.
Hasenbalg et al. [32]	AAA Eclipse, CCC Masterplan, VMC++	3 lung plans, 3 fields technique, 15 MV photons or mixed 6 MV and 15 MV photon beams.
Pearson et al. [37]	PB and CCC Masterplan	10 lung plans, stage T1-T4, 3 fields technique, 6 MV photon beams, standard fractionation.
Zhao et al. [18]	PBC and CCC Oncentra, EGSnrc Monte Carlo	24 lung plans, delivered using 3DCRT and IMRT, 8 MV photon beam, standard fractionation (2 Gy/fraction).
Fotina et al. [38]	Enhanced CC Oncentra, XVMC Monaco	2 lung SBRT plans delivered using 7 coplanar fields 3DCRT technique, dose fractionation did not specified.
Calvo et al. [39]	CCC Pinnacle, EGSnrc Monte Carlo	11 lung SBRT plans delivered using 5 coplanar fields IMRT technique, 6 MV photon beam, 45 Gy total dose in 3 fractions.
Troeller et al. [19]	Enhanced PB and Enhanced CC Oncentra	17 lung SBRT plans, tumour size < 4 cm, 7 beams mixed (6 and 15 MV) 3DCRT technique, 7.5 Gy x 8 fractions.
Takahashi *et al.* [92]	Scatter Homogenous Phantom Pinnacle, CCC Pinnacle, Superposition Xio, XVMC Monaco	20 lung SBRT plans, 6 MV photon beam, 48 Gy in 4 fractions.

2.3.6 Accuracy of dose calculation algorithms and treatment outcome prediction

The success of radiotherapy is determined by the success in optimising the tumour control probability (TCP) while maintaining minimal normal tissue complication probability (NTCP) as the predicting factors of the treatment outcome. As TCP and NTCP prediction are usually calculated using DVHs derived from the dose distribution computed using the TPS dose calculation algorithms, the impact of the dose calculation uncertainties on these parameters should be further investigated, as suggested by Chetty et al. [41]. Two recent publications attempted to address this issue by recalculating the treatment plans originally calculated using the effective path length (EPL) method with a convolution/superposition algorithm and Monte Carlo method [22, 94]. They found that the EPL calculation overestimated the dose, causing a significant reduction in TCP. However, they suggested that further studies were required to confirm their findings. As CCC algorithms are considered to have a smaller dose uncertainty than the EPL, it would be interesting to investigate the impact of any dose calculation uncertainties of CCC algorithms to the TCP and NTCP through the use of radiobiological modelling.

2.4 RADIOBIOLOGY

2.4.1 Role of radiobiology in radiotherapy

Radiation biology (or radiobiology) plays an important role in radiotherapy. In addition to explaining the underlying mechanism of the tumour and normal tissue response to the radiation exposure, it plays a role in evaluating the benefit of new treatment approaches or schedules in radiotherapy, such as hypo-fractionation. Therefore, radiobiological analysis assists in improving current therapy strategies to gain more benefit for cancer patients [4].

2.4.2 Radiation-induced damage

The use of radiation in cancer treatments is mainly due to its ability to cause damage to cells. This includes the cells of both tumours and healthy tissue. X-ray photons are categorised as non-directly ionising radiation because they interact and produce charged particles such as electrons and positrons. These secondary charged particles then interact through ionisation and excitation of the atoms or molecules [95].

The interaction between radiation and biological systems occurs at the atomic level and involves three sequential phases: the physical phase, chemical phase, and biological phase. The first phase is the physical phase, where the charged particles interact with the atoms/molecules within the tissues, causing ionisation and excitation of the molecules. These processes can cause the breakage of the chemical bonds of the molecules, altering the molecular composition through direct effect or indirect effect. Direct effect/damage occurs when the charged particles interact directly with deoxyribonucleic acid (DNA) molecules, causing single and/or double strand breaks. Indirect effect/damage occurs when charged particles interact with the non-nuclear part of the cell, predominantly water, producing free radicals of H* and OH* (i.e., hydroxyl radicals). These free radicals are highly reactive and able to diffuse within a short distance in the cells, causing damage to the DNA. This type of interaction is predominant in sparsely ionising radiation (low Linear Energy Transfer) such as X-rays and gamma rays [96]. The reaction of the damaged molecules or free radicals with other components of the cell involves a cascade of chemical reaction occurring in the chemical phase. This phase occurs within 1 ms following radiation exposure. The last phase is the biological phase, which involves complex enzymatic reactions occurring several hours to years after radiation. The effects can occur within days of radiation, known as the early effect, or occur several months after radiation, known as the late effect, or they can manifest as secondary tumours (radiation carcinogenesis), which occur many years after radiation [4, 97].

DNA is one of the important nucleic acids besides ribonucleic acid (RNA), which is located primarily in the cell nuclei. DNA plays a critical role in controlling cellular activities. Therefore, DNA is often considered the most critical and sensitive target of radiation. Damage to DNA presents in several forms: base damage, single-strand breaks (SSB), and double-strand breaks (DSB). Among these, DSB is considered the most important form of DNA damage, as it is the most difficult damage to repair and leads to the death of the cells [4, 96].

2.4.3 Survival curve

The main aim in radiation therapy is to kill tumour cells using a high dose of radiation. However, it should be noted that it is not only the tumour cells that are killed, but also a certain amount of normal cells/tissue. In the radiobiology context, cell death is usually defined as the loss of the reproductive or proliferative ability of the cells, which means the cell may still be alive but has been inactivated. The two most common of types of cell death after irradiation are apoptosis and mitotic catastrophe. Autophagy, necrosis, and senescence are other types of cell death. Apoptosis is a programmed cell death, which can occur in highly proliferating normal cells and radiation-induced tumour cells. Mitotic death is considered the most common cell death after irradiation, where cells die after attempting to enter a mitotic process due to damaged chromosomes [4].

It is important to understand the correlation between dose and biological response. The assay technique, i.e. clonogenic survival assay, can be used to detect the surviving tumour cells after irradiation, often referred to as 'clonogenic' due to their ability to proliferate and form a colony in a growth environment. The surviving fraction of clonogens is quantified as the linear-logarithmic plot between the dose and surviving fraction, known as a 'cell survival curve' [4]. To describe the sensitivity of the cell, the parameter ED_{50} is commonly used, representing the radiation dose that causes death of 50% of the cells [4].

The most popular model to describe the shape of cell-survival curve is the linear-quadratic model (LQ), although other models also exist, such as target theory, lethal-potentially lethal model (LPL), saturation repair model, and linear-quadratic-cubic model (LQC) [4]. The mathematical expression of the LQ model for cell survival (S) irradiated with a total dose of D is given in Equations 2.1 and 2.2:

$$-\ln(S) = \alpha D + \beta D^2 \tag{2.1}$$

$$S = \exp(-\alpha D - \beta D^2) \tag{2.2}$$

The plot of cell survival shows a continuous bending in which the curve shape is determined by the ratio of α/β (Figure 2.5).

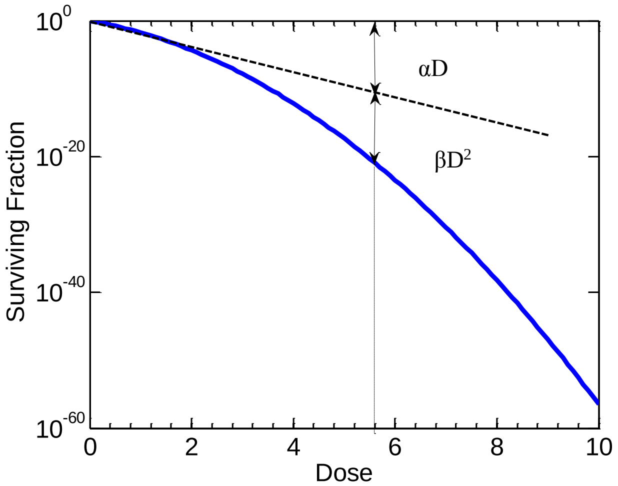

Figure 2.5. Linear quadratic model of cell survival.

The linear portion of cell killing (αD) is equal to the quadratic portion (βD^2) when the dose is equal to the alpha and beta ratio as expressed in Equations 2.3 and 2.4.

$$\alpha D = \beta D^2 \tag{2.3}$$

$$D = \alpha/\beta \tag{2.4}$$

Alpha (α) and beta (β) parameters represent the probability of damage from irradiation, in which α-damage represents irreparable damages, while β-damage represents repairable damages [98]. The shape of the survival curves is determined by the α/β value. The tumour tissue usually has a high value of α/β (from 5 to 20 Gy, mean ~10 Gy), while late responding normal tissue has a low value of α/β (from 1 to 4 Gy, mean ~ 2.5 Gy) [98].

It should be noted that the value of α/β varies between different tissues, namely early responding tissues and late responding tissues. Early responding tissues tend to have a higher α/β than late responding tissue due to their high proliferative capability. The LQ model has been proven to work well for low dose ranges between 1 and 5 Gy. Although the validity for large fraction size, such as SBRT, is still controversial, Joiner and Kogel [4] still recommend the use of the LQ model but using great care and appropriate selection of the alpha beta ratio value. For doses > 10 Gy, an addition of a third term with negative cubic exponent was suggested by Joiner and Kogel.

2.4.4 Tumour and normal tissues response to radiation

In radiotherapy, it is important to understand the biological effect on both the tumour and normal tissue following irradiation. The responses of the tumour and normal tissue to the radiation are influenced by dose, volume of irradiated tissues, and fractionation. Instead of using the cell survival curve, which is often used in the experimental studies with animals, it is more interesting to relate the dose and the response of the tissues that is expressed as a dose-response curve. For this purpose, an endpoint concept has been introduced to classify the radiation effect to the tissues or organs. In general, the severity of the radiation effect would be expected to be proportional to an increase of the given dose [4]. A sigmoidal dose-response curve (Figure 2.6) relates the dose with the tumour response, known as tumour control probability (TCP), and the normal tissue response, known as normal tissue complication probability (NTCP) [96].

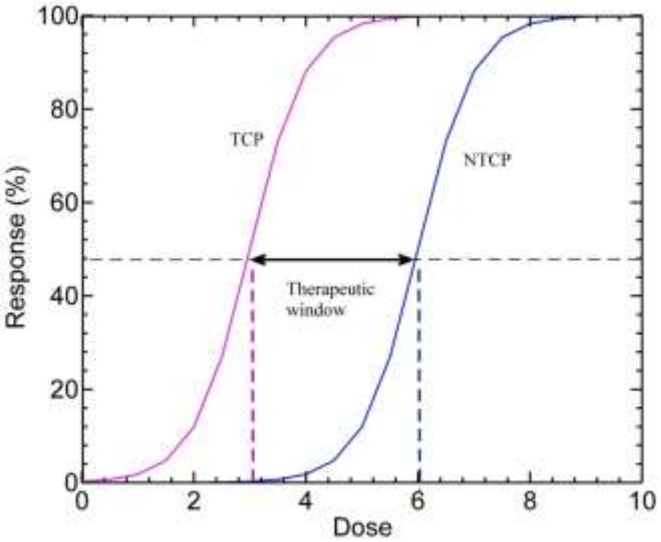

Figure 2.6. Dose-response curves for tumour (red line) and for normal tissues (blue line) with a wide therapeutic window.

It is common in radiotherapy practice to use the concept of a therapeutic ratio. One possible definition of therapeutic ratio is the ratio of the TCP to the NTCP for a particular dose. Another definition is the ratio of the doses where the value of NTCP and TCP are equal. The ideal goal in radiotherapy is to have 100% TCP and 0% NTCP, which is unlikely to be achieved in daily clinical practice. Practically, a high therapeutic ratio should correlate with good local control and minimal toxicity or normal tissue complications. This can be illustrated as a wide therapeutic window between the tumour dose-response curve and the normal tissue dose-response curve.

It should be noted that the values of TCP and NTCP are greatly influenced by the position and slope of the dose-response curve. There are three factors that affect the slope of the curve: radiosensitivity of the cells, the size of the tumour and normal organs, and clonogen density. The curve tends to shift in the left direction for a more sensitive cell population, a smaller tumour volume, and a smaller clonogen density [82].

The most popular mathematical model used to describe the dose-response of the tumour is the Poisson model. This model is based on an assumption that the number of surviving clonogenic tumour cells was a negative exponential function of the dose. This model is mathematically expressed in Equation 2.5:

$$TCP = \exp[-N_0 exp(-\alpha D - \beta d D)] \tag{2.5}$$

Where, N_0 is the number of clonogenic tumour cells per tumour volume, D is the total dose, and d is the dose per fraction [4].

Another mathematical model commonly used to describe the dose response is the logistic dose-response model, also known as logit analysis. Joiner and Kogel pointed out that this model is more pragmatic without a simple mechanistic background; therefore, it is more convenient to use to predict tumour control probability [4]. This model could be expressed mathematically as shown in Equations 2.6 to 2.7:

$$P = \frac{\exp(u)}{1+\exp(u)} \tag{2.6}$$

Where, for fractionated therapy, u has the form:

$$u = a_0 + a_1.D + a_2.D.d + \cdots \tag{2.7}$$

The coefficients a_0, a_1, and so on are estimated using logistic regression. Although parameter a_1/a_2 plays a similar role to α/β, a_1 is not an estimate of α and a_2 is not an estimate of β [4].

The parameters used in the dose-response curve are TCD_{50} for the tumour, which is the radiation dose required for 50% tumour control and RD_{50} for the normal tissues, which is the radiation dose required for 50% complication. The steepness of the curve is expressed as ‘gamma value’ (γ), which is often selected at a 37% response level (γ_{37}) if the Poisson model is used, representing the maximum steepness of the response level. For the logistic model, the gamma value is selected at a 50% response (γ_{50}) [4].

Four factors influence local tumour control, often known as the four *Rs*. The first is ‘recovery’ from sub-lethal damage, which increases tumour cell survival or reduces normal tissue damage when appropriate time is given for recovery to occur. This is the main reason for the fractionated treatment, which allows the damaged normal tissue cells to recover before the next fraction. The second is cell-cycle ‘redistribution’, where the clonogenic cells show the same distribution following radiation as prior to radiation if the interval between fractions is prolonged due to the varying radiosensitivity between cell-phases. The third is cellular ‘repopulation’ as the result of prolongation of overall treatment time. As a consequence, a higher dose is required to compensate for this repopulation of clonogenic cells. The last is ‘reoxygenation’, which is based on the fact that a lower oxygen level (hypoxia) in the tumour cells results in them being more radioresistant. In addition, tumour volume also contributes to local tumour control. It has been reported that a large tumour is more difficult to cure than a small tumour due to it tending to be more hypoxic, as it has a larger proportion of the clonogenic cells, and its large size may require a lower dose in order to protect a larger volume of the adjacent normal tissue [4].

The delivery of the lethal dose to the tumour is often limited by the presence of normal tissues and critical organs close to the target. The response of normal tissues to radiation can generally be classified into early complication (acute effect) and late complication (chronic effect). Early complication occurs within hours or days of radiation exposure, which primarily affects highly proliferating tissue, such as epithelial tissues of the skin, the mucosa, and intestinal tract. These tissues are known as early-responding tissue. Late complications occur months or years after radiation. Although repair of the chronic damage is possible, it is often irreversible. Tissues that exhibit late-response to radiation are known as late-responding tissues. The lungs, heart, and kidney are included in this category [4].

Several complication grade systems are available for clinical practice in order to classify the severity of the complication to the normal tissues. For example: the RTOG/EORTC classification, CTCAE v3 classification, WHO classification, and LENT/SOMA system. The reactions are often categorised into grade 1 for mild reactions, grade 2 for moderate reactions, grade 3 for severe reactions, and grade 4 for a life-threatening reaction.

In determining the dose response of normal tissue, it is important to include the volume-effect factor. In addition to the dose, the irradiated volume and tissue structural arrangement also contribute to the complications occurring in normal tissues after irradiation. Tissues can be assumed to be an arrangement of functional sub units (FSU). Tissues such as nephrons in kidney, acinus in lung, and lobule in livers are considered to have a parallel tissue arrangement, as each FSU can function independently from other FSUs. In this type of tissue arrangement, the radiation damage is characterised by a threshold volume. If the volume irradiated is below the threshold volume, no functional damage will be seen, and if the irradiated volume is above the threshold volume, the damage will increase as the dose increases. On the other hand, tissues such as the spinal cord and digestive track are considered to have a serial tissue arrangement, in which damage of one FSU could propagate to other FSUs, causing dysfunction of the tissues and organs. Therefore, in serial tissue architecture, the dose response is an all or nothing response characterised by a threshold dose. Below this value, the tissue will function normally, conversely, if the irradiated dose is above the threshold, the tissue will not function [96].

The lung is categorised among the most sensitive of the late responding organs that has a parallel tissue arrangement [99]. The amount of the irradiated lung volume and radiation dose determines the radiation response of the lung. Two possible radiation responses of the lung are radiation pneumonitis, which occurs between three and six months after irradiation, and lung fibrosis, which occurs months to years after irradiation [99]. The most common endpoint used in lung treatment plan evaluation is radiation pneumonitis.

The Lyman dose-volume model is often used in clinical practice in order to quantify normal tissue damage in which the NTCP is presented as the function of dose (D) and the irradiated volume (V). The model can be expressed mathematically as in Equation 2.8:

$$NTCP(D,V) = \frac{1}{\sqrt{2\pi}} \int_{-\infty}^{u(D,V)} \exp\left(-\frac{1}{2}.x^2\right) dx \tag{2.8}$$

The upper limit of the integral is a function of dose and volume,

$$u(D,V) = \frac{D - D_{50}(V)}{m.D_{50}(V)} \tag{2.9}$$

The relationship between D_{50} and the irradiated volume (V) is:

$$D_{50}(V) = \frac{D_{50}(1)}{V^n} \tag{2.10}$$

Three parameters are involved in this model; the steepness of the curve (m), the volume exponent (n), and the uniform total dose to produce a 50% complication ($D_{50}(1)$). The curve is steeper if m has a smaller value. The volume exponent (n) has a value from 0 to 1, the larger the value, the larger the volume effect. It should be noted that the parameters used for TCP and NTCP modelling are based on the best-fit of the parameter in a large patient cohort. Therefore, the parameters published in the literature commonly have a wide confidence interval.

2.4.5 Fractionation

In order to produce optimum local tumour control with minimal normal tissue damage, the radiation dose is often divided into a particular number of treatments. This is known as fractionation. Fractionation is an important factor that determines the response of tumour and normal tissues, apart from the prescribed dose. Radiobiological understanding of radiotherapy indicates that fractionation produces better tumour control and normal tissue sparing [96]. This is because it spares normal tissues due to sub-lethal damage repair and repopulation of cells and increases damage to tumours due to re-oxygenation and re-distribution into a radiosensitive phase. Modifying the fractionation has a greater effect on the late-responding tissue rather than the early-responding tissue. By including a fractionation factor in Equation 2.2, the LQ model can be expressed as:

$$\boldsymbol{S = e^{-N(\alpha d - \beta d^2)}} \tag{2.11}$$

Where *N* is the number of fractions and *d* is the dose/fraction. A biologically effective dose (BED) can be derived from Equation 2.11. Fowler [100] defined the BED as “the dose that gives the same level of cell kill if it could be given as an infinite number of infinitely small fractions, i.e., at very low dose rate”. This concept is useful to estimate the effectiveness of the physical dose when given in different fractionation schedules, for instance, SBRT versus conventionally fractionated treatment, as described in Section 2.3.2. In addition, the BED concept aids in determining the new treatment schedule after an interrupted radiotherapy treatment to obtain the same effect as if no interruption occurred. The BED formula is shown in Equation 2.12:

$$\boldsymbol{BED = Nd\left(1 + \frac{d}{\alpha/\beta}\right)} \tag{2.12}$$

As the length of treatment time also influences the effectiveness of radiotherapy treatment, the relationship between the BED and the radiation dose can be derived from Equation 2.11 by involving the treatment time factor, as shown in Equation 2.13.

$$\boldsymbol{BED = Nd\left(1 + \frac{d}{\alpha/\beta}\right) - k(T - T_k)} \tag{2.13}$$

The first bracketed term, i.e. $\left(\mathbf{1}+\frac{d}{\alpha/\beta}\right)$ is known as relative effectiveness (RE). Parameter k represents the repopulation rate, in which for a rapidly repopulating tumour, a k value of 0.6 is often used. T is overall treatment time, which is seven weeks in a conventional fractionation scheme and T_k is the time at which accelerated tumour cell repopulation occurs (four weeks following the first treatment). As late-responding normal tissue is rarely repopulated during the treatment, $k = 0$ is often used for this tissue type [98].

In a conventionally fractionated radiotherapy, a fraction size of 1.8-2 Gy is given daily five times a week for a six to seven weeks treatment course. This schedule has been used widely as the standard practice in radiotherapy. Modified fractionation is introduced to improve local tumour control, especially for lung treatment. The first altered fractionation is hyper-fractionation, in which the dose is delivered in multiple daily fractions with a small fraction size for the same or reduced overall treatment time as the conventional fractionation. The advantage of this approach is sparing the late-responding tissue from radiation-induced damage. However, this approach might not be preferable due to resources. Another approach is hypo-fractionation, in which the dose is given in a larger fraction size. The obvious advantage of this approach is a shortened treatment time, avoiding the repopulation of tumour clonogens. However, the use of a large dose per fraction has the consequence of increased damage to the late-responding normal tissues [4, 96, 101].

This is why the use of SBRT is more beneficial for early stage NSCLC with a small tumour size ≤5 cm, rather than large tumour. This is because the delivery of the ablative dose to the large tumour volume poses greater risk of normal tissue damage. Excellent local tumour control and minimum reported toxicity of the SBRT has made the hypo-fractionation regaining interest over the last three decades. The availability of new image guidance technology has made it possible to reduce the margins; therefore, reducing the risks of normal tissue exposure from a high ablative dose. Researchers are investigating on the radiobiological explanation of the SBRT treatment [76, 102-104], as it is suspected that the linear quadratic model may not be valid for large doses/fraction treatment [74].

2.4.6 Radiobiological modelling

Using radiobiological modelling, it is possible to model the outcome of the treatment for the patient in terms of tumour control probability (TCP) and normal tissue complication probability (NTCP) [105]. They can be used as additional evaluation parameters of the treatment plan, in addition to the isodose display and DVHs [106]. Two possible implementations of radiobiological parameters in the clinical treatment planning system are as a plan optimisation tool and a plan evaluation tool, as comprehensively discussed in the AAPM TG-166 report [107]. Therefore, the software in the TPS often provides a biological response calculation tool to assist in designing the most effective treatment plans for patients [108, 109].

TPS software such as Pinnacle^3 provides tools to perform TCP and NTCP calculation, assisting in treatment plan evaluation. Pinnacle^3 TPS software uses Poisson models to calculate the TCP and the Lyman-Kutcher-Burman (LKB) model to calculate the NTCP. These models are commonly used for treatment plan evaluation [4, 98, 107, 110]. The use of radiobiological parameters as a plan optimisation tool is implemented in Pinnacle^3 to enhance the existing dose-volume optimisation process in IMRT inverse planning. Three biological cost functions are employed: min EUD (equivalent uniform dose), target EUD, and max EUD, as additional dose-volume cost functions (i.e., min dose, max dose, uniform dose, min DVH, max DVH, and uniformity) [107]. In EUD concept, inhomogenous dose distributions within one organ are converted to homogenous dose distributions, which would result in the same cell survival.

Independent radiobiological software has been also developed, enabling treatment plan evaluation outside the TPS environment. For example, Sanchez-Nieto and Nahum [111] developed the BIOlogical evaluation of PLANs (BIOPLAN) software, which enables treatment plan optimisation based on biological considerations and allows for the comparison of treatment plans. Deasy et al. [112] have developed the Computational Environment for Radiotherapy Research (CERR) software, which incorporates radiobiological models for evaluating radiotherapy treatment plans. Uzan and Nahum [113] developed the BioSuite software to optimise the treatment plan by customising the fractionation and prescribed dose as the key variables to improve the treatment outcome.

Nahum and Uzan [57] proposed different levels of biological optimisation of treatment plan. The first level involves optimisation of the prescribed dose (i.e., total dose) by maintaining a constant value of NTCP (for instance 10% for radiation pneumonitis) and constant number of fractions. The next optimisation level not only customises the prescribed dose at a constant NTCP, but also customises the number of fractions to achieve the highest TCP for an individual patient. These two levels do not alter the treatment plan dose distribution, only modifying the prescribed dose and the number of fractions. The third level is more complex, as it incorporates the radiobiological functions (EUD and/or NTCP and TCP) in the inverse planning algorithm. Differing from the existing dose-volume based approach inverse planning, this biological inverse planning TCP function replaces the role of target volume dose parameters in determining the effect of hot and cold spots. The fourth level is even more complex, as it includes the use of patient-specific information from functional imaging, such as the clonogen density, in radiobiological inverse planning. The last level incorporates individual patient biology, for example, the radiosensitivity of the tumour clonogen, in any level described previously. The key of this proposed radiobiological optimisation is changing the paradigm ‘one size fit all’ concept to an individualised prescribed dose and fraction number. This is because the same prescribed dose might not result in the same TCP and NTCP for different patients due to different tumour size and location between patients.

This research used radiobiological models to calculate the TCP and NTCP of the lung treatment plans in order to relate the dose calculation uncertainty of the TPS algorithms to the treatment outcomes. The ‘Marsden’ LQ Poisson TCP model and LKB NTCP model was used in the radiobiological analysis using the Biosuite software.

2.5 SUMMARY

SBRT has been rapidly adopted for the treatment of medically inoperable early stage NSCLC, as it has a potential to improve local tumour control and survival rates compared to conventional treatment. Dose calculation accuracy is important in lung SBRT treatments, in which a large dose is delivered to a small target tumour surrounded by low density normal lung tissue. Inaccuracies in the dose calculation will cause problems for the evaluation of the treatment plan, as well as the prediction of the treatment outcome, potentially causing serious consequences for the patients.

Collapsed cone convolution (CCC) algorithms were one of the model-based algorithms recommended by TROG 0902 CHISEL trial protocol for the dose calculation in the lung SBRT plans. Previous studies [18, 28, 32, 37, 38] have investigated the performance of the CCC algorithms in conventionally fractionated lung treatments with a daily fraction of 2 Gy. Although the agreement of the CCC algorithms was within 5% compared to the Monte Carlo for the dose parameters to the target, a larger discrepancy (>5%) was observed for the target dose in individual patients and for the dose to critical organs. Therefore, it is important to investigate the accuracy of the CCC algorithms in the lung SBRT treatments that employ a larger fraction size of >10 Gy using the Monte Carlo technique as the gold standard dose calculation engine. This research focusses on investigating this issue and further examining the possible impact of dose calculation uncertainty on treatment outcome prediction through the use of radiobiological modelling. The following chapter discusses the use of the Monte Carlo simulation for treatment plan verification.

Chapter 3: Monte Carlo Simulation for Treatment Plan Verification

The Monte Carlo technique has been widely implemented in radiotherapy fields over the last three decades. In addition to its implementation as the TPS dose calculation engine, the Monte Carlo technique is often used as a benchmarking tool for other dose-calculation algorithms, such as the pencil beam algorithm and convolution/superposition algorithm, due to its excellent agreement with the measurement dosimetry (uncertainty of ≤3%). However, the accuracy of the Monte Carlo simulation for external photon beam modelling relies on the accuracy of the beam source models, and the geometry and composition of the accelerator head and the phantom/patient the radiation will interact with. This chapter describes how Monte Carlo simulations based on the EGSnrc/BEAMnrc system can be used for verification of the accuracy of radiotherapy treatment plan dosimetry. It provides a definition and brief history of the Monte Carlo technique (Section 3.1), the advantages and performance issues of the Monte Carlo technique (Section 3.2), the principle of radiation transport using a Monte Carlo simulation (Section 3.3), Monte Carlo codes (Section 3.4), and the modelling of an external photon beam using BEAMnrc and DOSXYZnrc user codes (Section 3.5), with a summary provided in Section 3.6.

3.1 DEFINITION AND BRIEF HISTORY OF MONTE CARLO TECHNIQUES

3.1.1 What is Monte Carlo?

The Monte Carlo technique is a numerical solution to a complex problem that employs random numbers to sample a probability distribution of an event. The Monte Carlo technique solves a macroscopic problem (e.g., dose deposition in radiotherapy) by simulating microscopic interactions (e.g., interaction between radiation and absorbing medium) [114]. The solution is obtained by randomly sampling the microscopic interactions that rely on an iterative process of calculation using a computer [115, 116]. Therefore, the Monte Carlo technique serves as a bridge between theory and the experiment [117].

3.1.2 History of the Monte Carlo Technique

Historically, the Monte Carlo technique was initially introduced for the design of nuclear weapons involving neutron particle transport in the World War II era by researchers at the Los Alamos laboratory. They employed the first computer, called the electronic numerical integrator and computer, to perform statistical sampling. The concept of the Monte Carlo method was actually demonstrated much earlier, where the phenomena of needle drop experiments was used for prediction of the pi value [118]. The Monte Carlo technique has been widely applied in different fields that manage complex problems [27, 118]. In radiotherapy and medical physics, there is an increasing trend of employing this technique, as indicated by an increase of published works in this field [114]. Two potential applications of the Monte Carlo technique in regards to dose calculation are as a dose calculation engine in the TPS, in which a fast computation time becomes the essential feature [11], and as an independent verification tool of the existing dose calculation algorithms used in the TPS [10]. The Monte Carlo application as the independent verification tool requires accurate modelling of the treatment head of the linear accelerator and commissioning the model against the measured dosimetry data before the model can be used for verification of the TPS algorithms.

3.2 ADVANTAGES AND PERFORMANCE ISSUES OF MONTE CARLO TECHNIQUES

3.2.1 Advantages

Aside from its directness, convenience, and accuracy in solving complex problems, such as radiation transport in a complex geometry of the accelerator components and patient anatomy, the Monte Carlo technique is favoured due to its increased computational effectiveness rather than deterministic methods [115]. This increase in interest has occurred in parallel to the improved capacity and capability of computer system in the last few decades.

In terms of dose calculation accuracy, the Monte Carlo technique is known to be the most accurate dose calculation engine compared to correction-based and model-based algorithms. In radiotherapy, achieving a high radiotherapuetic ratio is often limited due to uncertainties arising from each step of a multi-chain radiotherapy treatment process [11]. Some of the major sources of uncertainty are uncertainty in patient setup, machine calibration, and dose calculation. Overall dose uncertainties should be lower than 5%, which implies that the accuracy of dose calculation algorithms of 2-3% should be achieved [11, 82]. It has been shown that the Monte Carlo technique has the potential to fulfil this criterion [10, 114]. Its superiority over conventional dose calculation algorithms is more significant in cases where heterogeneities exist (i.e., different tissue composition and density), at the boundary of air cavities [11], in a low density medium such as the lung, and surfaces with an irregular shape [53].

3.2.2 Monte Carlo performance in lung

It has been shown that the Monte Carlo calculation predicts the dose more accurately in low density media compared to other algorithms. A study by Carrasco et al. [21] comparing the correction based-algorithms, model based algorithm, and Monte Carlo (Penelope) simulation with thermoluminescent detector (TLD) measurements in a heterogenous phantom found that the Monte Carlo calculation of the dose within the lung substitute material agreed to within 3% of the measurement. The phantom consisted of three layers of water-lung-water slabs with an electron density of the lung substitute material of 0.195. The Monte Carlo simulation accurately predicted the dose reduction within the lung media that the correction-based algorithms (Batho, modified Batho, ETAR, and Helax pencil beam algorithm) failed to predict. The accurate prediction of the Monte Carlo simulation was not only for a large field size (10 cm x 10 cm), but also for a small field (2 cm x 2 cm) at a high energy (18 MV), where other algorithms experienced difficulties in calculating the dose within the lung media correctly due to the existence of electronic disequilibrium condition. In addition, they reported that the Monte Carlo calculation also predicted the penumbral widening more accurately in the lung substitute material, which occurs at the edge of the beam, compared to other algorithms. The superiority of the Monte Carlo calculation is more significant at extreme lung density [14], high energy, and small field size [21, 119].

Similar agreement was also reported by Dobler et al. [23] who compared the X-ray Voxel Monte Carlo (XVMC) with film measurement in an anthropomorphic phantom mimicking lung tissue, bone tissue, and lung tumour. They found that the XVMC calculation in the lung tissue part of the phantom was the best (to within 3%) compared to the CCC Helax-TMS and the PB Helax-TMS algorithms, which showed dose discrepancies of 8% and 15% relative to the film measurement, respectively. In this study, nine coplanar beams with energy of 6 MV were employed. The comparison of the dose inside the CTV of a 2 cm inserted tumour model between the Monte Carlo calculation and the film measurement showed agreement of 2%, whereas the PB (Helax-TMS) overestimated the dose by up to 5.4% and the CCC (Helax-TMS) underestimated by up to 5.0%. Similar superiority of the Monte Carlo simulation in a lung QUASAR phantom study with a 2 cm tumour model was reported by Zhao et al. [18]. They found that the Monte Carlo calculation of the dose to the center of the tumour model agreed with the ion chamber measurement to within 1%, while the PB convolution (Oncentra) showed a difference of 3.0% with the measurement.

As the Monte Carlo shows a closer agreement with the measurement to within 3%, it is often used to benchmark the performance of existing TPS algorithms. Vanderstraeten et al. [28] used Monte Carlo dose engine (MCDE) as the gold standard algorithm when comparing the dose calculation of 10 lung IMRT plans between the PB and CCC Helax TMS, and CCC Pinnacle algorithms. They found that the PB algorithm overestimated the dose to the PTV by up to 3.7% for D_{min}, and by up to 7.95% for the D_{max} when an 18 MV photon beam was used. The difference decreased to 3.24% and 2.70% for the PTV D_{min} and D_{max}, respectively, when the photon energy decreased to 6 MV. Calvo et al. [39] benchmarked the CCC algorithm used in the Pinnacle RTPS using the EGSnrc/BEAMnrc Monte Carlo code. The difference in the PTV mean dose between the CCC and Monte Carlo calculations was within 5.6% for 88 lung IMRT plans with a lesion size of <3.0 cm. The superiority of the Monte Carlo calculation has also been reported in many other studies [88, 120-123].

3.2.3 Performance issues

It should be noted that the use of the Monte Carlo technique is subject to statistical fluctuations or noise as a consequence of the stochastic nature of the individual particles interaction. The presence of noise might cause a problem in the evaluation of the treatment plan. Keall et al. [124] reported that the effect of noise is more significant to isodose distribution than to the DVHs and biological parameters (i.e., TCP and NTCP). However, the effect is considered to be less significant for the statistical uncertainty of $\leq$2%. A low statistical uncertainty will result in a smooth dose profile (depth dose curves, lateral dose profiles, and isodose line) [82]. One method to reduce the noise is by increasing the number of particle histories to be simulated, as the uncertainty is proportional to $1/\sqrt{N}$ [118]. However, this has a consequence of increasing the computation time to simulate such large histories, which is not preferable for a busy clinical practice [10]. Another approach used to limit the computation time while still achieving acceptable statistical uncertainties is to introduce variance reduction techniques [125, 126], as discussed in Section 3.5.5.

3.3 PRINCIPLE OF RADIATION TRANSPORT USING MONTE CARLO SIMULATION

3.3.1 Principle

The Monte Carlo technique basically provides an estimate of the expected value of a random event and the variance of the estimation [118]. The estimation will approach the true value if a large number of experiments are performed; thus, reducing the variance of the estimation. The essence of this technique is the generation of a (pseudo) random number to sample the probability distribution function describing a particular physical process. The term pseudo-random is used, since it reflects that the output of computer program is predictable, thus, not truly random. Two important requirements of the pseudo-random number to be used in the Monte Carlo simulation are that it should have a large sequence period and a uniform distribution in multiple dimension [127]. This is to ensure that the value obtained from the simulation of one particle history is not biased by the result of other histories.

The sampling of a random variable from its probability distribution function can be performed using two basic sampling techniques: the direct method and indirect method. The direct method, which is often referred to as the transformation method, is based on the invertible characteristic of the cumulative distribution function [118, 127]. The implementation of this method can be seen in sampling the distance to the first interaction site. If the direct method is impossible, sampling can be performed using indirect methods, also known as the rejection method. The rejection method is based on the selection of a point coordinate with respect to the probability distribution function. For a variable x, and a probability distribution function $f(x)$, a point coordinate (x, $f(x)$) is randomly selected. If a point is under the curve, the x value is accepted, otherwise x is rejected. An example of the rejection method is sampling the angle using the Klein-Nishina cross-section.

Another important feature of the Monte Carlo technique is the scoring of the quantity of interest, for instance the particle fluence and the amount of energy deposited in a certain volume of material. Assuming that each simulated particle history will give a score in a pre-defined scoring plane, the total score is an accumulation of the scores from total N particle histories. Prior to the simulation, each score accumulator is set to zero. As the random nature of the observed events, the score is subject to statistical uncertainties, which is proportional to $1/\sqrt{N}$. This implies that in order to reduce uncertainty by a factor of two, the number of particle histories must be increased four times [118].

3.3.2 Monte Carlo modelling of photon and electron transport

The Monte Carlo technique models the radiation transport straight away based on the physics of radiation-absorbing medium interactions. Unlike convolution/superposition algorithms that consider an averaged value of a large number of particles, the Monte Carlo technique models the transport of each incident particle, tracking its trajectories until the deposition of its energy to the region of interest in the medium. The term ‘particle history’ is used in the Monte Carlo simulation to describe the transport of the incident particles that contain information about the distance to the next interaction, type of collision process, trajectory and particle energy leaving collision, and production of the secondary particle. The particle history is randomly sampled from a probability distribution function that defines the likelihood of each interaction.

Photon interaction with absorbing medium

When radiation passes through the medium, there is an energy transfer process from the radiation to the medium. In X-ray or gamma-ray radiation, photons carry the radiation energy and transfer all or part of its energy to the medium/material. This process is known as photon attenuation, characterised by the attenuation coefficient (μ) expressed in units of cm^{-1}. The relationship between the attenuation coefficient and the intensity of the transmitted photon (I) as a function of the thickness of absorber material (x) is given by:

$$I(x) = I_0 e^{-\mu x} \tag{3.1}$$

The value of the attenuation coefficient is dependent on the energy of the incident photon, the density of the material (ρ), and the atomic composition of material. The attenuation coefficient can also be expressed as the mass attenuation coefficient by dividing μ with ρ with the unit of cm^2/g [128].

$$\frac{\mu}{\rho} = \frac{N_A}{A}.\sigma \tag{3.2}$$

N_A is Avogadro's number, A is an atomic mass number, and σ is cross section. The cross section is simply the area in the absorber material that the photon incident to it will interact with certain interaction types [82].

The photons interact with the medium via four main processes: coherent scattering, the photo electric interaction, the Compton interaction, and pair production. Coherent scattering or Rayleigh scattering is less important in the therapeutic energy range, as no energy transfer occurs, only the deflection of the photon travel direction [128]. Photoelectric absorption is predominant in low energy photons and high Z materials, in which the photon transfers all of its energy to the atomic electron, causing the release of the electron from its orbital. This mechanism is considered to be more important in diagnostic X-ray. The probability of the photoelectric interaction is proportional to Z^3 and inversely proportional to the photon energy (E^3). Compton scattering occurs when the incident photon interacts with a loosely bound electron. Only parts of the photon energy are transferred to this electron which results in an electron with a kinetic energy (E_k) of

$$E_k = E_P \left[\frac{\alpha(1-cos\theta)}{1+\alpha(1-cos\theta)}\right] \tag{3.3}$$

Where, $\alpha = E_p/m_0c^2$, E_p is the energy of the incident photon, m_0c^2 is the rest mass energy of the electron, and θ is the deflection angle of the photon after striking the electron. The probability of the Compton scattering is independent of the atomic number of the absorbing medium and decreases with an increase of the incident photon energy. Pair production is the most relevant interaction at a higher energy in which the photon energy is greater than 1.022 MeV. This interaction occurs when the photon travels very close to the nucleus of the absorbing medium resulting in a production of an electron and positron pair. The positron further interacts with an electron causing annihilation of both particles. As a result, two gamma-rays with an identical energy of 0.511 MeV are emitted at 180° to one another. The probability of the pair production interaction is proportional to Z^2 and the energy of the incident photon [82, 128].

Each interaction process has its own attenuation coefficient. Therefore, the total attenuation coefficient is given as the sum of each coefficient, which is expressed in Equation 3.4:

$$\frac{\mu}{\rho} = \frac{\sigma_{coh}}{\rho} + \frac{\tau}{\rho} + \frac{\sigma_c}{\rho} + \frac{\pi}{\rho} \tag{3.4}$$

where, $\frac{\sigma_{coh}}{\rho}$ is the probability of the coherent scattering, $\frac{\tau}{\rho}$ is the probability of the photoelectric effect, σ_c/ρ is the probability of Compton scattering and $\frac{\pi}{\rho}$ is the probability of interaction via pair production [128]. Among these processes, Compton scattering is predominant at the megavoltage energies used for radiotherapy.

Electron interaction with absorbing medium

Electrons interact with material via several processes: inelastic collisions with atomic electrons (ionisation or excitation), inelastic collisions with nuclei (Bremsstrahlung), elastic collisions with atomic electrons, and elastic collisions with nuclei [128]. Electron transport is more complicated than photon transport, as electrons undergo multiple interactions before eventually losing all of their energy and coming to rest. The interaction is categorised into 'catastrophic' and 'soft' interaction based on the amplitude of energy loss. Catastrophic interaction includes large energy-loss scattering, hard Bremsstrahlung emission, and positron annihilation. Soft interaction involves low-energy scattering, atomic excitation, and soft Bremsstrahlung emission [117].

The simulation of the electron transport requires a huge computation time, because electron might undergo thousand interactions before coming to the rest. Therefore, it is too costly to simulate event-by-event of individual electron. The introduction of a condensed history methods solves this problem by grouping a large number elastic and semielastic event of the electron interactions into one condensed history step. This is because the elastic and semielastic interactions transfer no or only a small amount energy to the surrounding matter and the particles only experience a small direction change [129].

3.4 MONTE CARLO CODES

Various Monte Carlo codes have been used for radiotherapy beam modelling, such as ETRAN/ITS, EGS4, EGSnrc, MCNP4, PENELOPE, GEANT3 and GEANT4. These codes are written in the Fortran programming language, with the exception of GEANT4 [130]. EGSnrc, the most popular Monte Carlo code for modelling linear accelerators [131], is an upgraded version of EGS4 developed by the National Research Council of Canada [27] as part of the OMEGA project. This Monte Carlo code can be used to simulate radiation transport for both photons and electrons in any element, component, or mixture. BEAMnrc and DOSXYZnrc used in the project are user codes built on the EGSnrc Code System to model the linear accelerator and to calculate the absorbed dose in a medium [132, 133].

3.4.1 BEAMnrc

BEAMnrc is a user code based on EGSnrc to model various radiotherapy machines from kilo-voltage units to megavoltage units. BEAM offers the flexibility to simulate individual elements of the linear accelerator machine without rewriting the routines by providing a set of predefined component modules (CMs).). In addition, a user can also generate a phase-space file that contains information about location, the energy of the particle, direction, the type of particle that crosses a specific plane, and all of the parameters required for transport simulation. This phase space file can be reused for many purposes, for example, to model the movable dynamic components of a linear accelerator below the phase space location, to characterise the radiation source, and to generate a virtual source model [130].

3.4.2 DOSXYZnrc

DOSXYZnrc is a user code based on EGSnrc to predict the dose deposited in a phantom composed of any medium. This code can model a complex patient geometry that has a different density and material composition. The dose distribution is determined over a rectilinear volume element (voxel) in three-dimensional Cartesian axes, as shown in Figure 3.1.

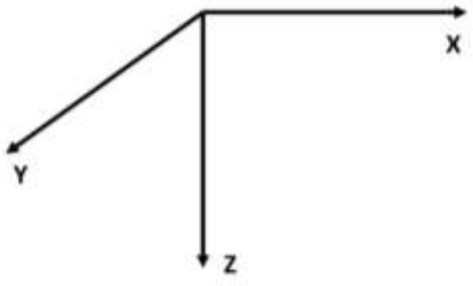

Figure 3.1. Coordinate system used in DOSXYZnrc.

The codes offer flexibility for users to define the geometry of the phantom that can be constructed with or without CT data. For a CT-based phantom, the CTCREATE program is available to convert the DICOM CT image to the format (i.e., EGSPHANT file) readable by the DOSXYZnrc. This conversion involves the use of a CT ramp to convert the CT number to the material and density of the voxel in the phantom. In addition, the size of the voxels can be defined uniformly or non-uniformly. The codes are able to handle different types of sources, including a phase-space source generated from the BEAMnrc simulation [133].

The user is also able to define the simulation parameters, such as the number of simulated particles, as well as the variance reduction techniques to be implemented. Directional Bremsstrahlung splitting, Russian Roulette (used when uniform Bremsstrahlung splitting and selective Bremsstrahlung splitting are selected), range rejection, and photon splitting can be enabled during the simulation to improve simulation efficiency [126, 134].

3.5 MODELLING OF AN EXTERNAL PHOTON BEAM USING BEAMNRC AND DOSXYZNRC USER CODES

The modern linear accelerator is capable of producing both photon and electron beams on the same machine. The photon beam is the most common radiation type used in the treatment of cancer, including the lung cancer investigated in this study. Modelling the linear accelerator is the first essential step in predicting the dose deposition in the patient using the Monte Carlo technique [27]. The model must be commissioned against the measured dosimetry data, which is usually obtained in a simple homogenous water phantom for various field sizes at various depths. Once the model has been validated, it can be used to compute the dose in heterogeneous patient anatomy. As the dose computed by the Monte Carlo technique is given in Gy/incident particles, an absolute dose calibration is required to convert the dose to Gy/MU. These steps are discussed briefly in the following subsections. A thorough discussion of the Monte Carlo method in dose calculation of external beam radiotherapy can be found in the AAPM TG Report No 105 [41] and reviews by Verhaegen and Seuntjens [27] and Reynaert et al. [11].

3.5.1 Modelling the linear accelerator

Modelling the linear accelerator for a photon beam begins with the electron beam striking the photon target, which is then collimated and flattened in the linear accelerator head. It is important to model the accelerator head based on the geometry, dimension, and composition details from the machine specification in order to obtain an accurate dose calculation. However, there is often only limited information about the details of the machine [135].

Verhaegen (2013) pointed out that target, flattening filter, and secondary collimators are the most important components to be modelled, as the first two components have a significant contribution to electron contamination of the fluence. Additionally, the flattening filter causes beam hardening of the lateral dose profiles. The monitor ion chamber and mirror are considered less important due to their small contribution to the beam [135].

The modelling of the MLC component is a challenging task due to its complex design [135]. There are several component modules available in BEAMnrc to model the MLC, such as MLC, MLCQ, MLCE, VARLMC, and DYNMLC. MLC CM was designed to model a flat face MLC, which would not be suitable for a curved leaf end design. In 1999, De Vlamynck et al. [136] introduced a new MLCQ CM to model the rounded leaf-end MLC of the Elekta SL 25 linear accelerator. An agreement of 1% was achieved for the depth dose distributions when compared with the measurement. As MLCQ CM does not take into account the tongue-and-groove design, VARMLC CM was introduced to overcome this issue. The VARMLC CM was initially designed for the Varian MLC, while the MLCE CM was introduced by Walle *et al.* [137] to model the Elekta rounded leaf MLC, including tongue-and-groove. The MLCE CM accounts for the air gap presence between the leaves. A modification of VARMLC CM was developed to deal with the simulation of dynamic treatment deliveries with the Varian MLC, referred to as DYNMLC [132].

There are two main approaches in simulating the photon beam: the phase-space file approach and virtual source approach. The first approach is to perform a full linear accelerator simulation from the target to the beam exit window. The phase space file is saved just below the exit window of the accelerator head, containing all information about particle histories, such as energy, location, and types of particles. The phase space can then be used as an input for patient dose calculations. Alternatively, the simulation can be split into two parts. The first part is by simulating the upper part of the linear accelerator, which consists of fixed components, such as the photon target, primary collimator, flattening filter, ionisation chamber, and mirror, and saving the phase space file above the collimator. The second phase space file is then generated for patient-specific components, such as MLCs and jaws. This second phase space file is then used as an input for patient dose calculation [130, 138]. The second approach is a virtual source model built from the phase-space file data or the measurement consisting of several sub-sources. This approach saves disk space and minimises noise [138].

3.5.2 Commissioning the accelerator model

As Monte Carlo simulation is a model-based approach, it is essential to benchmark the model with measured data through careful commissioning and validation [11]. The important part of the commissioning process is to optimise the incident electron energy and its spatial intensity distribution. These parameters must be carefully optimised, as they influence the dose distribution. The common assumption is that the electron beam is mono energetic, with an elliptical Gaussian intensity distribution in X and Y axes. An iterative process is required to obtain the best match with the measurement data.

Beam validation involves comparison of dose profiles and output factors of a set of dosimetry data for various field sizes between the simulation and the measurement [41, 53, 62, 139, 140]. These dose profiles are used for evaluation of the beam penumbra. The output factors are used to quantify the ratio of the absorbed dose on the central axis in a reference field (often 10 cm x 10 cm field) to the other field sizes. This is because the linear accelerator machine is usually calibrated for the reference field to produce 1.00 cGy per monitor unit (MU) under the specified normalisation condition. An increase or decrease of field size causes an increase or decrease in scatter, respectively, hence, the machine output. There are two sources of scatter: head or collimator scatter (S_c) (mainly due to photon scattering in the flattening filter component) and phantom scatter (S_p) (mainly due to a change in the amount of volume being irradiated) [128].

Fix [53] stated that determination of the tolerance and acceptance criteria can be a difficult task. The most commonly used quantities are dose difference, distance-to-agreement, and gamma index [141]. The dose difference is often used in the low dose gradient, while the distance-to-agreement is often used in the high dose gradient. A tolerance criteria of 3%, 3 mm is often used [141-143]. However, Keall *et al.* [144] recommended a tighter tolerance of 1% in beam modelling to obtain smaller uncertainties in dose calculation. Fix [53] suggested that it is more appropriate to use different tolerances for different locations and setup.

3.5.3 Absolute dose calculation

Absorbed dose is the total radiation energy absorbed (i.e., deposited) by the mass (*m)* of the material, given in SI units of gray (Gy). In daily radiotherapy practice, it is common to relate the dose and monitor unit (MU) for a set of reference conditions. The linear accelerator is calibrated to produce a dose rate of 1 cGy/MU at 10 cm depth in a water phantom for the reference field (i.e., 10 cm x 10 cm) [145].

The dose calculated using the Monte Carlo technique is expressed in Gy/initial particle incident to the target. To relate the simulated dose to the absolute dose, the simulation should be performed using the same calibration condition used in the measurement. The ratio of the Gy/MU and Gy/particle can be calculated and used to convert the Monte Carlo dose to an absolute dose [135].

3.5.4 Patient dose calculation

For patient simulation, two approaches can be used. In the first approach, CT numbers are converted to electron density in materials using a predefined CT conversion function. The original data, which is in DICOM format, is converted to a text file. The material number and density are stored for each voxel of the calculation grid using the conversion function. During Monte Carlo simulation, appropriate cross-section data for each material are sourced from the data base when the particles enter the specific voxel. The second approach is a conversion of CT data to tissue composition (i.e., atomic composition). This approach can be performed by dividing the CT numbers into several discrete intervals, which are associated with user-defined tissues. For example, four different tissue types: air, lung, water, and bone, might correspond with the CT number scale. Adipose and muscle tissues could be also added into the conversion of CT data [11]. Another approach is converting the CT numbers into interaction probabilities by correlating Hounsfield number with collision and radiation stopping power.

3.5.5 Variance reduction techniques

The efficiency of the Monte Carlo simulation ε is inversely proportional to the computation time $T(N)$ and the statistical uncertainty $s(N)^2$.

$$\varepsilon = \frac{1}{[s(N)]^2\, T(N)} \tag{3.5}$$

From Equation 3.5 [125], there are two ways to improve simulation efficiency: by reducing the statistical uncertainty for a certain computation time or by reducing the computation time for a certain statistical uncertainty. In practice, a combination of those two approaches is often used in order to enhance efficiency. Another solution to save computation time is through parallel computing, using a computer cluster. Variance reduction techniques are usually introduced to gain an acceptable level of uncertainty within a reasonable computation time.

The variance reduction techniques implemented in BEAMnrc are range rejection, Bremsstrahlung photon splitting, and photon interaction forcing [26, 132]. Range rejection is an approximation variance reduction technique implemented to save the computation time for the electron transport. In this method, the charged particle that cannot leave the current region with energy of larger than range rejection cut-off energy will be terminated. Therefore, all of its energy will be deposited in that region. This includes any Bremsstrahlung photons produced when the electrons are slowed down. To reduce the effect of losing Bremsstrahlung photons, a maximum energy for history termination, called ESAVE, should be defined by the user. If the Bremsstrahlung photon has an energy of >ESAVE, the photon can escape the region, although the electron cannot escape from the region. Setting the ESAVE value to 1 MeV reduces the statistical uncertainty to 2% in case of 10 MeV initial electron incident on tungsten [146]. The range rejection technique requires a computation of the charged particle range to the threshold energy, as a function of electron energy, which is performed in BEAM using the MXRNGE subroutine [132]. Particle splitting (i.e., Bremsstrahlung splitting in BEAMnrc and photon splitting in DOSXYZnrc) increases the number of photons generated, improving the efficiency in the calculation [134]. Different Bremsstrahlung splitting options are available in BEAMnrc: uniform Bremsstrahlung splitting (UBS), selective Bremsstrahlung splitting (SBS), and directional Bremsstrahlung splitting (DBS). Among these, the DBS has been shown to improve efficiency significantly [126]. In the DBS technique, the user is required to define the radius of the DBS splitting field, which should enclose the entire treatment field, the splitting number, and the SSD at which the field size is defined. Forcing photon interactions may be useful for dose calculation in the phantom, but less so in the linear accelerator simulation. Another variance reduction technique is the Bremsstrahlung Cross Section Enhancement (BCSE), which is important in low-energy ranges where the production of Bremsstrahlung photon is rare.

An approximation technique, known as transport cut-offs, is commonly used to reduce calculation time [138]. The transport cut-off energy is used to terminate the particle histories that have low probabilities in contributing to the dose deposition. This is achieved by setting a minimum electron energy and photon energy (ECUT and PCUT). The photon energy cut-off should be smaller than the electron cut-off energy due to its longer range [134]. The ECUT value of 0.70 MeV (kinetic + rest mass energy of electron) and PCUT value of 0.01 MeV are commonly used for therapy beam simulation [132]. The ECUT value is generally less than 1/3 of the smallest dimension of scoring region [132].

3.6 SUMMARY

Due to the potential of the Monte Carlo simulation as the benchmarking tool of TPS dose calculation algorithms, especially in low density media, this technique was employed in this research to verify the dose calculation of the CCC algorithm for lung SBRT treatment plans. The simulation was performed using the EGSnrc system with BEAMnrc user codes to model the Elekta Axesse linear accelerator head components and DOSXYZnrc user codes to calculate the dose in water phantom and patient anatomy. A detailed discussion of the linear accelerator modelling and the commissioning process as the first important step for the TPS algorithms verification using Monte Carlo simulation is presented in Chapter 4. The validated linear accelerator model was used in the verification of the CCC algorithm dose calculation (the Pinnacle^3 RTPS) in twenty lung SBRT plans as discussed in Chapter 5. The generated dose-volume histograms of the Monte Carlo and TPS dose distributions were then used to calculate the TCP and NTCP, as described in Chapter 6.

Chapter 4: Modelling and Commissioning of an Elekta Axesse Linear Accelerator and Beam Modulator micro-MLC

4.1 OVERVIEW

The first and important step in calculating the dose deposition in phantom or patient geometry using the Monte Carlo technique is modelling the linear accelerator. The accuracy of the model is crucial to obtain an accurate dose calculation. Therefore, the model should be developed based on the geometrical dimension and composition of the actual machine. The most common approach is to model the complete linear accelerator head from the electron beam, hitting the target to the exit window of the accelerator head. The model does not usually include the electron beam generation from the electron gun and travel through the waveguide tube. Once the model has been developed, it is crucial to determining the optimum beam source parameters and to commission the model against the measured dosimetry data.

This chapter presents the works on Monte Carlo modelling of the Elekta Axesse linear accelerator, including the integrated Beam Modulator collimation system, used for radiation delivery of lung SBRT plans in a local radiotherapy centre. This chapter also discusses the subsequent commissioning procedures to validate the model. This linear accelerator modelling and commissioning was required prior to the verification of the TPS algorithms using Monte Carlo simulation performed in the next stage of the research. Although many studies have been published on modelling various types of Elekta accelerator using BEAMnrc/EGSnrc Monte Carlo codes such as Elekta SLi [136, 137], Elekta Precise [147], Elekta Synergy [148, 149], and Elekta Synergy S [67, 150], no previous study has modelled a specific combination of the Elekta Axesse linear accelerator and Beam Modulator collimation system.

4.2 MATERIALS AND METHODS

4.2.1 Machine specification

The Elekta Axesse linear accelerator with a built-in Beam Modulator collimation system (Elekta AB) was modelled to produce a 6 MV photon beam. The machine is specifically designed for SBRT treatment delivery. The Beam Modulator is the commercial name of the design of a multi-leaf collimator system with a leaf spacing of 4 mm at the isocenter, which is designed to create the small radiation fields typically used for the SBRT treatment. The accelerator is also equipped with a cone-beam CT mounted on the gantry, as well as an amorphous silicon detector for portal imaging. The machine is compatible with the HexaPod RT treatment couch and iBEAM eco couchtop, as well as the Bodyfix immobilisation system [151].

The Beam Modulator consists of 40 leaf pairs within a housing located approximately 39 cm from the electron beam target. Each individual leaf can travel a distance of 21 cm allowing interdigitation of opposing leaves. Leaf movements are controlled by a drive mechanism. Leaves are made from tungsten alloy with a rounded end and straight leaf side. There is no tongue-and-groove design. To minimise the friction, a small gap separates between leaves. Leaves are slightly tilted to reduce the interleaf leakage [70]. An unused leaf is positioned behind the fixed outer diaphragm of the opposed leaf bank to minimise the beam transmission through a 5 mm gap of the closed leaf [150, 152]. The leaf side is focused towards the target in which the width of the bottom leaf (close to the patient) is 0.3 mm wider than the top leaf, thus the leaf side lines up with the beam divergence. The leaves are slightly defocused from the central axis and the target to avoid the interleaf leakage [150], because the Beam Modulator MLC has no tongue-and-groove design.

The difference between the Beam Modulator and the previous Elekta MLCs is a replacement of the movable back up jaws with two pairs of fixed diaphragms. Therefore, the field collimation is defined only by the MLCs. The maximum field size is 16 cm across the leaf bank and 21 cm along the travel direction of the leaves. Fixed diaphragms are made from the same material and density as the leaves.

One more important component in the Beam Modulator is the secondary collimator (millstone collimator), constructed from a large block of tungsten alloy with a 3 mm thick back scatter plate above it. The aperture of the secondary collimator is designed to restrict the radiation beam to the area shielded by the two pair of diaphragms. The leaf-end penumbra (80%-20% isodose levels) of the Elekta Beam Modulator is smaller than that of the previous MLCs, ranging from 3.1 to 5.3 mm. The maximum interleaf leakage was found to be 1.7% and the average of leaf transmission less than 1.0% [70]. The Beam Modulator can also be integrated to the Elekta Synergy S linear accelerator, which is another platform released by Elekta for stereotactic radiosurgery and SBRT [151]. The design of Elekta Axesse, Synergy, and Precise accelerator head above the Beam Modulator (from target to mirror) are the same. However, the optical system used in the Elekta Axesse is shorter than that used in the Elekta Precise.

4.2.2 Convention of axes

The axes convention used in this thesis is illustrated in Figure 4.1 to maintain consistency throughout the work. The crossplane direction or Y-axis is defined as parallel to the leaf direction of travel. Therefore, the rounded leaf end is in the Y direction and the maximum field size in this axis is 21 cm. The inplane direction or X-axis is defined as perpendicular to the leaf direction of travel (parallel to the gun-target direction). The maximum field size in this axis is 16 cm with an increment of 0.4 cm.

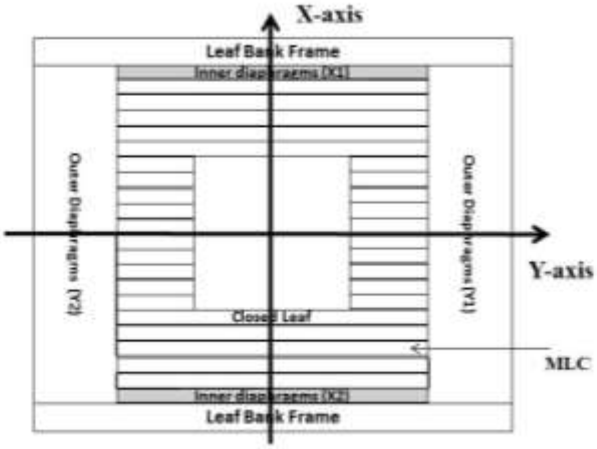

Figure 4.1. An illustration of the axes definition used in the thesis.

4.2.3 Measurement data

The measured dose to water data were used to validate the Monte Carlo accelerator head model, which were taken by the (clinical) medical physicist as part of quality assurance of the linear accelerator. The data consisted of the central-axis depth dose curves and lateral dose profiles of 4 cm x 4 cm, 10.4 cm x 10.4 cm, and 21 cm x

16 cm fields. The dose profiles of these fields were measured using a CC04 cylindrical ion chamber with a cavity radius of 2.0 mm and a cavity volume of 0.04 cm^3. The lateral dose profiles of 1.6 cm x 1.6 cm, 2.4 cm x 2.4 cm, and 3.2 cm x 3.2 cm fields were also used to validate the Monte Carlo model. The lateral dose profiles of these fields were measured using a PTW 31014 pin point chamber, with a cavity radius of 1 mm and a cavity volume of 0.015 cm^3. The central electrode of this chamber is made of aluminium with a diameter of 0.3 mm.

The dose profiles were measured at a source-to-surface distance (SSD) of 100 cm, in a servo water tank with a dimension of 48 cm x 48 cm x 48 cm. The lateral profiles were measured at four depths: 1.5 cm, 5 cm, 10 cm and 20 cm and were presented as a relative dose that was normalised to 100% at the central axis dose. The depth dose curves were normalised to the dose at the depth of maximum dose (d_{max}). The central axis depth-dose curves were only available for the field sizes of 4 cm x 4 cm, 10.4 cm x 10.4 cm, and 21 cm x 16 cm.

The output factors of various field sizes were measured at an SSD of 90 cm, at 10 cm depth. The output factor was defined here as the central axis (CAX) dose of a particular field size at a particular depth divided by the central axis dose of the reference field at the same depth. The depth used to define the output factor was 10 cm depth and the reference field used for all of this work was 10.4 cm x 10.4 cm. This is shown in Equation 4.1, with *i* as the field size of interest.

$$OF_i = \frac{CAX\ Dose_{i,10cm}}{CAX\ Dose_{10.4x10.4,10cm}} \tag{4.1}$$

Although the manufacturer suggested using 9.6 cm x 10.4 cm as the reference field, the local centre used 10.4 cm x 10.4 cm for the reference field. Therefore, the latter value was adopted in this study. The outputs for the small fields (1.6 cm to 3.2 cm) were measured using the pin point chamber, while the CC04 ion chamber was used to measure the output of the larger fields. The output of the reference field was measured using different chambers, the pin point chamber and the CC04 ion chamber, to be used as the reference for the small fields and the large fields output factor calculation, respectively.

4.2.4 Modelling linear accelerator head

The first step in modelling a 6 MV external photon beam was building a Monte Carlo model of the linear accelerator head. The model was started from the electron beam incident on the high Z target material (Tungsten) to produce Bremsstrahlung photons and then collimated and flattened using the components in the accelerator head.

The Monte Carlo linear accelerator was modelled using 11 component modules (CMs) available in the BEAMnrc package based on the geometry, dimensions, and compositions described in the machine specification. The upper part of the model from the target to the first back scatter plate had the same design as the Elekta Precise linac model, which was previously developed by Kairn et al. [147], with a shorter mirror dimension. The model of the secondary collimation system was completely different. A schematic diagram of the accelerator head model is presented in Figure 4.2.

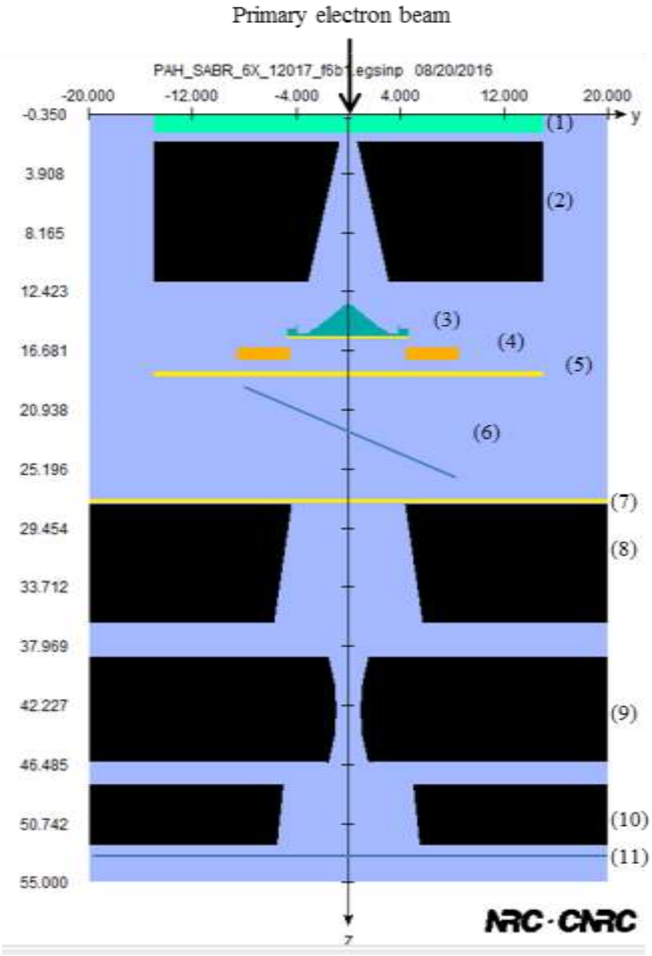

Figure 4.2. The Monte Carlo model of the Elekta Axesse linac head (YZ view). 1) target, 2) primary collimator, 3) flattening filter, 4) monitor ion chamber, 5) backscatter plate, 6) mirror, 7) backscatter plate, 8) millstone collimator, 9) MLC, 10) fixed outer jaw, and 11) X-wires.

It was assumed that the accelerator head had a modular structure built by an arrangement of CMs. The first modular structure was the target modelled using FLATFILT CM, which was composed of a high Z tungsten alloy. Below the target, the primary collimator was modelled using CONS3R CM. The FLATFILT CM was used to model a complex geometry of the flattening filter. The monitor ion chamber and mirror were also included in the model using CHAMBER CM and MIRROR CM, respectively. Between these components, a 3 mm thick backscatter plate was modelled using SLABS CM. In order to model the millstone collimator, a PYRAMIDS CM was used with SLABS CM above it to include the additional backscatter plate. The primary collimator and the millstone collimator were composed using the same materials. The MLCQ CM was used to model the straight leaf side design with the rounded-leaf end found in the Elekta Beam Modulator. A small offset was applied in the direction of the leaf travel to match the measured profile, as the MLCQ CM did not model the air gap. As the secondary collimator had the back scatter plate on top of its geometry, the photon beam passed through two back scatter plates in the linac head. The first back scatter plate was below the monitor ion chamber that aims to absorb the low energy back-scattered photon from the collimation system. The fixed inner diaphragm was modelled as an additional MLC leaf pair. The JAW CM was used to model the fixed outer diaphragm located below the MLC, which limited the field aperture in the direction of MLC travel to 21 cm.

4.2.5 Simulation parameters

The BEAMnrc code, a user code of EGSnrc, was used to simulate the particle transport of a 6 MV photon beam within the accelerator head geometry. The electron beam was modelled as an elliptical beam with a Gaussian distribution in X and Y (source 19), where the exact dimensions were obtained from the previously commissioned Elekta Precise accelerator model [147]. At the initial simulation, the electron beam was assumed to have a circular shape, with symmetrical FWHM in both axes.

In the simulation, a number of variance reduction techniques were used to save computation time by selecting the cut-off energy of the electron and photon to 0.7 MeV and 0.01 MeV, respectively. Therefore, the histories of electrons and photons lower than the pre-defined energy values were terminated. Variance reduction techniques were also used in the simulation in order to improve the simulation efficiency, such as range rejection and directional Bremsstrahlung splitting. Range rejection (ESAVE = 1.0 MeV) was enabled. Directional Bremsstrahlung splitting (DBS) was used in the simulation, with a splitting number of 1000 and the radius slightly larger than the minimum radius covered the defined square field. The number of initial particles simulated was ~ 1 x 10^8 initial electrons. In the BEAMnrc simulation, EXACT boundary crossing algorithms and PRESTA-II electron step algorithms were selected. The simulations were performed using parallel processing techniques to save computation time. All simulations were performed using the super computer SGI Altix XE Cluster provided by High Performance Computing and Research Support (HPC-RS) at Queensland University of Technology (QUT). This computer cluster has 128 computer nodes (15,264 GB of main memory) supporting for performing full Monte Carlo simulation. The simulations were performed using parallel jobs (10 jobs) running using the batch system.

The BEAMnrc phase space files were saved at the location of 55 cm from the source below the exit window of the accelerator head. The phase space files were then used as the input for the DOSXYZnrc simulation to calculate the dose to the phantom/patients. During the commissioning of the accelerator model, the DOSXYZnrc codes were used to simulate the dose deposition of the photon beam in a simple homogenous water phantom. The water phantom had a dimension of 50 cm x 50 cm x 50 cm positioned at 100 cm SSD. The air gap between the source (i.e., the phsp file position) and the surface of water phantom were also included in the phantom definition. For DOSXYZnrc simulation, ~ 3 x 10^8 particle histories were simulated for the small fields and up to 1 x 10^9 particle histories for the large fields. The output of the DOSXYZnrc simulation was in the form of the 3ddose file from which the dose profiles were extracted using in-house application software written in the Interactive Data Language (IDL) software (ITT Visual Information Solutions, Boulder CO).

4.2.6 Field size

Table 4.1 presents the field sizes used in the commissioning process and the detector used to measure the beam profiles and output factors. Three different field sizes were used during the commissioning of the accelerator model: 4 cm x 4 cm, 10.4 cm x 10.4 cm, and 21 cm x 16 cm. The use of the largest field in the commissioning process aimed to minimise the scattering contribution from the collimator. The inclusion of 4 cm x 4 cm field aimed to represent the typical beam used in SBRT treatment of early stage NSCLC. Additional small fields were simulated with the aim of commissioning the Monte Carlo model for small field calculations: 1.6 cm x 1.6 cm, 2.4 cm x 2.4 cm, and 3.2 cm x 3.2 cm. It should be noted that all of the field dimensions were defined at the isocenter plane. More field sizes were included in the output factor calculation: 4.8 cm x 4.8 cm, 5.6 cm x 5.6 cm, 7.2 cm, and 8 cm x 8 cm.

Table 4.1: *List of Studied Field Sizes and the Detector used for the Beam Profile Measurements*

	Detector used for measurement	
Field Sizes	Dose profiles	Output Factor
1.6 cm x 1.6 cm	Pin point chamber	Pin point chamber
2.4 cm x 2.4 cm	Pin point chamber	Pin point chamber
3.2 cm x 3.2 cm	Pin point chamber	Pin point chamber
4 cm x 4 cm	CC04 ion chamber	CC04 ion chamber
4.8 cm x 4.8 cm	-	CC04 ion chamber
5.6 cm x 5.6 cm	-	CC04 ion chamber
7.2 cm x 7.2 cm	-	CC04 ion chamber
8 cm x 8 cm	-	CC04 ion chamber
10.4 cm x 10.4 cm	CC04 ion chamber	Pin point chamber[a] CC04[b] ion chamber
21 cm x 16 cm	CC04 ion chamber	CC04 ion chamber

[a]For small field's (1.6 to 3.2 cm^2) output factor calculation

[b]For large field's output factor calculation

4.2.7 Incident electron beam energy

Comprehensive commissioning procedures of radiotherapy linear accelerator Monte Carlo models have been described in the literature [41, 139, 140, 149, 153-156]. There were two adjustable parameters in the accelerator photon beam modelling, the initial electron beam energy and its radial dimensions. The electron source was assumed to have a Gaussian spatial distribution and to be mono energetic. The Gaussian spatial distribution was defined by its full width half maximum (FWHM). As the precise values of these parameters were not provided by the manufacturer, the values were determined iteratively through an optimisation procedure. For the 6 MV photon beam, the nominal values of the primary electron beam energy and the full width half maximum (FWHM) of the electron-beam energy distribution were 6 MeV and 0.1 cm [139].

To determine the best value of those parameters, simulations were performed for various electron energy and FWHM values. The first step was performing the simulation with a fixed radial width for different electron energies. The electron energy was varied from 5.8 MeV to 6.5 MeV with an increment of 0.1 MeV. The FWHM was 0.1 cm and assumed to be symmetrical. Simulations were performed for three different field sizes: 4 cm x 4 cm, 10.4 cm x 10.4 cm and 21 cm x 16 cm. Phase space files for these linear accelerator models were produced and used as the input for DOSXYZnrc simulations of a water tank. The vertical voxel size (z-axis direction) of the DOSXYZnrc water phantom was 0.2 cm, with a lateral voxel (x and y axes directions) of 0.5 cm for the large fields and 0.2 cm for the small fields. The central axis depth dose profiles were extracted from the .3ddose data and then compared with the measured depth dose profiles. The measured depth dose profiles obtained from the commissioning of the linear accelerator machine were given in relative dose, normalised to the depth of maximum dose, d_{max}. The simulated depth dose curves were also normalised using a similar method.

The comparison between the simulated and measured data was performed through reduced chi-square fitting of the depth dose profiles. The mathematical expression of the reduced chi-square testing is given in Equation 4.2, where D_{MC} was the simulated dose, D_{Meas} was the measured dose, σ was the simulation uncertainty, and N was the number of dose points.

$$\chi^2_{red} = \frac{1}{N-1}\sum\frac{(D_{MC}-D_{Meas})^2}{\sigma^2} \tag{4.2}$$

The expression $N-1$ represented the number of degrees of freedom. The optimal value was indicated by the value of χ^2_{red} close to 1 [155, 157].

4.2.8 Radial dimensions of the electron beam

Once the optimum electron beam energy had been determined, the radial width of the electron beam was optimised using a similar method. The FWHM of the electron beam radial width was varied from 0.1 to 0.3 cm. The optimisation was performed for the field sizes of 2.4 cm x 2.4 cm, 4 cm x 4 cm, 10.4 cm x 10.4 cm and 21 cm x 16 cm with an initial assumption that $FWHM_x$ and $FWHM_y$ were symmetrical. The same

DOSXYZnrc model was used with a voxel size of 0.2 cm for the small fields (2.4 cm and 4 cm) and 0.5 cm for the larger fields. The vertical voxel size was maintained at 0.2 cm for all field sizes.

The simulated lateral dose profiles were obtained at 10 cm depth and normalised to 100% at the central axis dose. The 80%-20% penumbra widths were evaluated for both measured and simulated profiles. The penumbra matching was performed by plotting the electron beam FWHM against the penumbra widths (both measured and simulated penumbra widths) to determine the best FWHM value.

4.2.9 Leaf position optimisation

In a Monte Carlo simulation, the field size is usually determined by the setting of leaf opening and the number of opened leaves. The leaf opening determines the field size in the direction of MLC travel (Y-axis), which is usually defined using trigonometry rules, as illustrated in Figure 4.3. The number of opened leaves determines the field size in the direction perpendicular to the direction of MLC travel (X-axis). As the MLC width according to the manufacturer's specification is 4 mm, the increment of the field size in the X-axis direction is a multiplication factor of 4 mm.

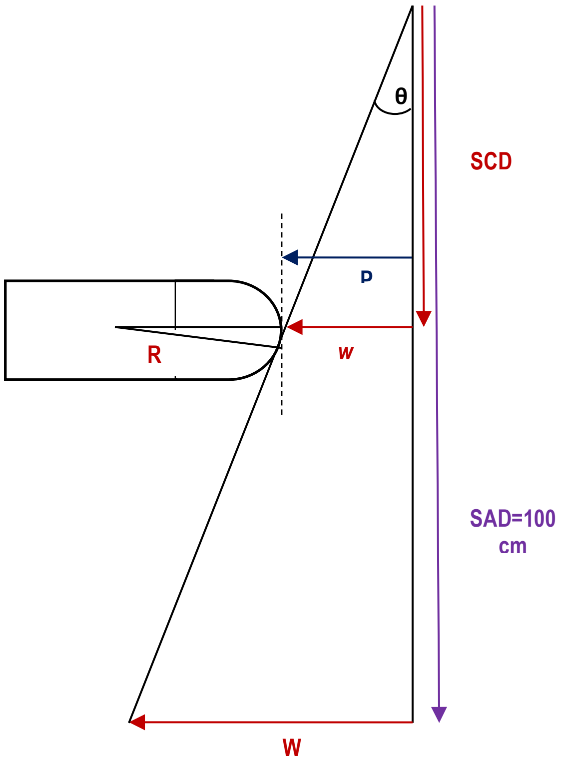

Figure 4.3. Schematic diagram of the actual position of the leaf tip and its projection at the isocenter plane [158].

P is the physical distance of the leaf tip to the beam axis, *w* is the distance from the beam axis to the line tangential to the curved face of leaf, *R* is the leaf radius, and *θ* (theta) is the angle between the beam axis and the tangential line. The distance of the isocenter from the source is referred to as *SAD,* which is usually 100 cm, and the distance of the collimator to the source is referred as *SCD*. Mathematically, the formula can be written as shown in Equation 4.3.

$$\boldsymbol{P = w + (\frac{R}{\cos\theta} - R)} \tag{4.3}$$

By employing similar triangle principle, *w*/SCD = W/SAD, Equation 4.3 can be rearranged as shown in Equation 4.4.

$$\boldsymbol{P = SCD\left(\frac{W}{SAD}\right) + R\left(\left(\frac{1}{cos\theta}\right) - 1\right)} \tag{4.4}$$

The variable input parameter for the formula is *W* (i.e. the radius of pre-defined field size at the isocenter), as the value of *SCD, SAD, R,* and *θ* remain constant. To determine *W*, the defined field size is divided by 2, for example for a 4 cm x 4 cm field, the value of *W* is 2 cm. This value is referred to as the prescribed MLC position or nominal field size.

The MLC position optimisation was performed to investigate whether there was a difference between the prescribed MLC position and the actual position. The investigation was performed for 2.4 cm x 2.4 cm and 10.4 cm x 10.4 cm fields by varying leaf offsets from 0.01 cm to 0.05 cm. The lateral width of the 50% isodoses of the dose at the central axis (i.e., referred to as field width) was compared with that of the measured data. As the distance of the 50% isodose levels from the central axis was potentially different between left and right leaf, the value was averaged for further analysis. The optimised leaf position was selected based on the minimum field width difference.

4.2.10 Validation in small field sizes (<4 cm)

In order to verify the optimised simulation parameters obtained from the previous sections in small-field treatment situations, the simulation was performed for three square field sizes of 1.6 cm, 2.4 cm, and 3.2 cm. The incident electron beam energy and radial dimensions of the electron beam used in the simulation were the optimum values obtained from Sections 4.2.7 and 4.2.8. An optimum leaf offset obtained from Section 4.2.9 was applied in defining the MLCQ aperture. The lateral dose profiles of the measurement and simulation were extracted for different depths of 1.5 cm, 5 cm, 10 cm, and 20 cm and normalised to the central axis dose.

The analysis was performed by calculating the local dose difference between the simulated and measured lateral dose profiles in the flat dose region. This involved the dose points with the relative dose value of larger than 90% of the central axis dose. The agreement in the penumbra region, where a high dose gradient exists, was analysed by calculating the lateral distance-to-agreement (DTA) of the simulated and measured profiles. The DTA was defined in this work as the distance between a point dose in the reference data and the nearest point of the evaluated dose distribution that had the same dose. As the profile comparison only involved one dimension, the DTA calculation was only performed in one dimension. The DTA criterion was used to overcome the limitations of the dose difference criterion in the high dose gradient in which the radiation dose changes very rapidly. In this analysis, the DTA calculation was performed for the dose points between 10% and 90% dose levels.

4.2.11 Output factor calculation

The output factors from the Monte Carlo simulation were determined by simulating the various field sizes listed in Table 4.1 using the optimum electron energy and the FWHM obtained from the previous optimisation procedures. The calculation was performed in a water phantom at an SSD of 90 cm with a vertical voxel size of 0.2 cm. The lateral voxel size was 0.2 cm for the small fields and 0.5 cm for larger fields. The mean dose of a 3 x 3 voxel central region-of-interest at 10 cm depth was used to calculate the output factor of a certain field by dividing it by the mean dose for the same region-of-interest and depth of the reference field (10.4 cm x 10.4 cm). The output factor calculation was performed for the square field sizes of 1.6 cm to 8 cm, with an increment of 0.8 cm, reference field size (i.e., 10.4 cm x 10.4 cm), and a rectangular field of 21 cm x 16 cm.

4.3 RESULTS

4.3.1 Incident electron beam energy

The reduced chi-square values of the depth dose curves fitting during energy optimisation are presented in Figure 4.4. The value of χ^2_{red} was presented as a function of the incident electron energy for three different field sizes. There was less variation in the χ^2_{red} values for the different energies of the incident electron observed in 10.4 cm x 10.4 cm and 21 cm x 16 cm. In contrast, a significant reduction of the χ^2_{red} values was observed in 4 cm x 4 cm, as the energy of the incident electron decreased from 5.8 MeV to 6.2 MeV. However, the χ^2_{red} values observed for the electron energy of >6.2 MeV were relatively close to each other. The minimum χ^2_{red} values were found for the electron energy of 6.2 MeV: 7.37 in 4 cm x 4 cm, 7.00 for 10.4 cm x 10.4 cm, and 4.36 for 21 cm x 16 cm. Therefore, this energy value was selected as the optimum value for the modelled 6 MV photon beam.

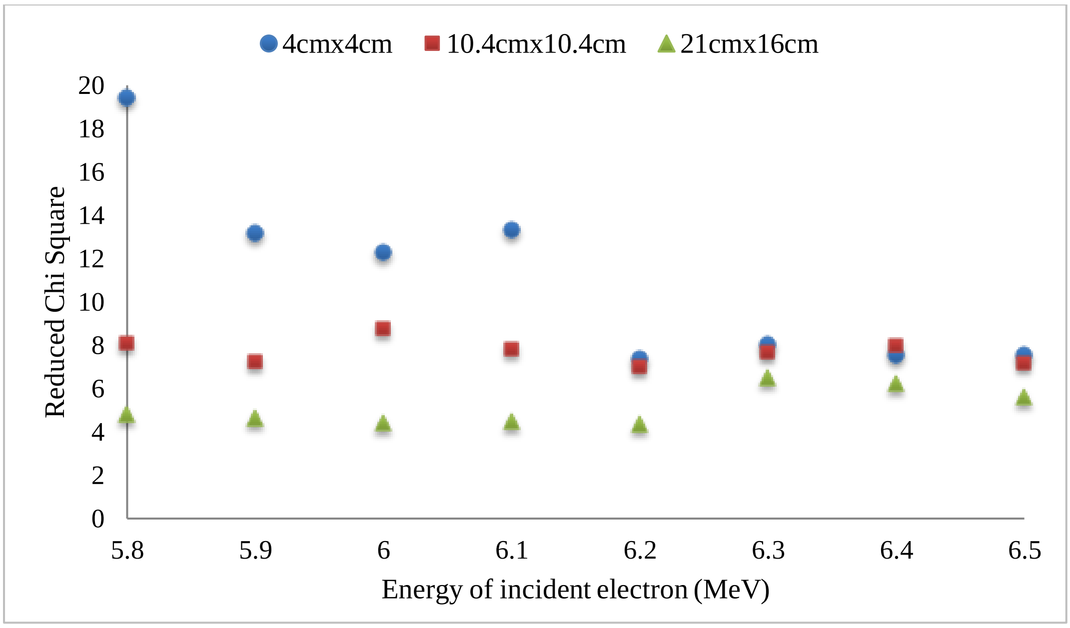

Figure 4.4. The reduced chi-square fitting of the depth dose profiles during energy optimisation.

Plotting the depth dose profiles for the optimum energy of 6.2 MeV shows good agreement between the measurement and the simulation, as shown in Figure 4.5.

The effect of the incident electron energy changes to the lateral dose profiles of the largest field size (21 cm x16 cm) is shown in Figure 4.6. It demonstrates that increasing the energy of the incident electron decreased the horn of the lateral profiles. However, the effect was only significant for the largest field size.

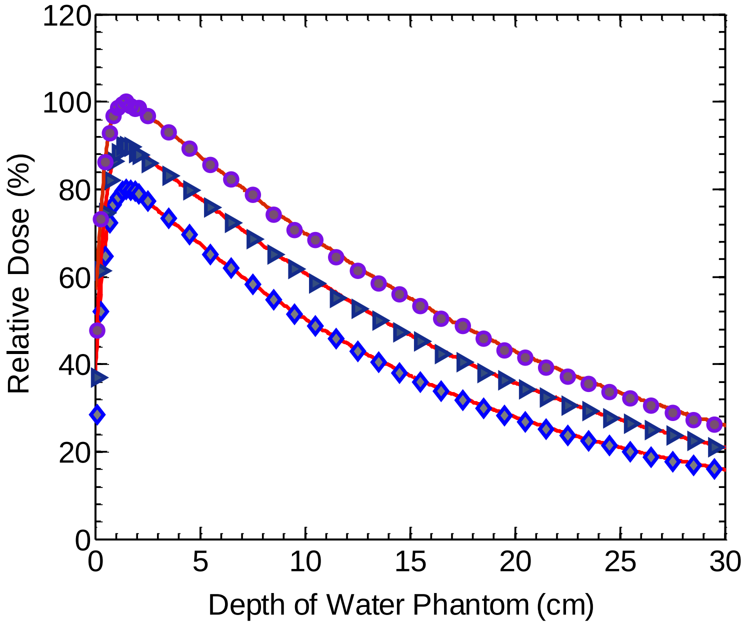

Figure 4.5. The central axis depth dose curves of the measured (solid line) and simulated profiles for 4 cm x 4 cm (diamond), 10.4 cm x 10.4 cm (triangle) and 21 x 16 cm fields (circle) with the optimum electron energy of 6.2 MeV.

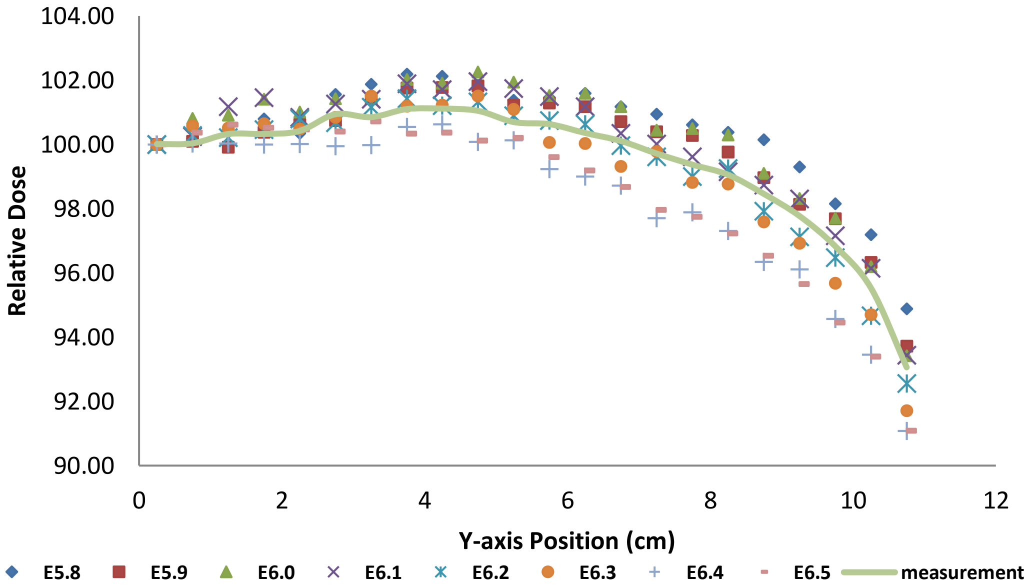

Figure 4.6. Sensitivity of the lateral dose profiles of the largest field to the change of the incident electron beam energy.

4.3.2 Radial dimensions of the electron beam

The FWHM optimisation shows the sensitivity of the lateral dose profiles to the change of the FWHM value. This effect is greater in the small field (i.e., 2.4 cm x 2.4

cm), where increasing the FWHM value resulted in a broader penumbra, as shown in Figure 4.7. The plots of half-lateral profiles presented in Figure 4.7 demonstrate that the optimum FWHM was obtained for values of 0.2 cm in the X-axis and 0.3 cm in the Y-axis directions.

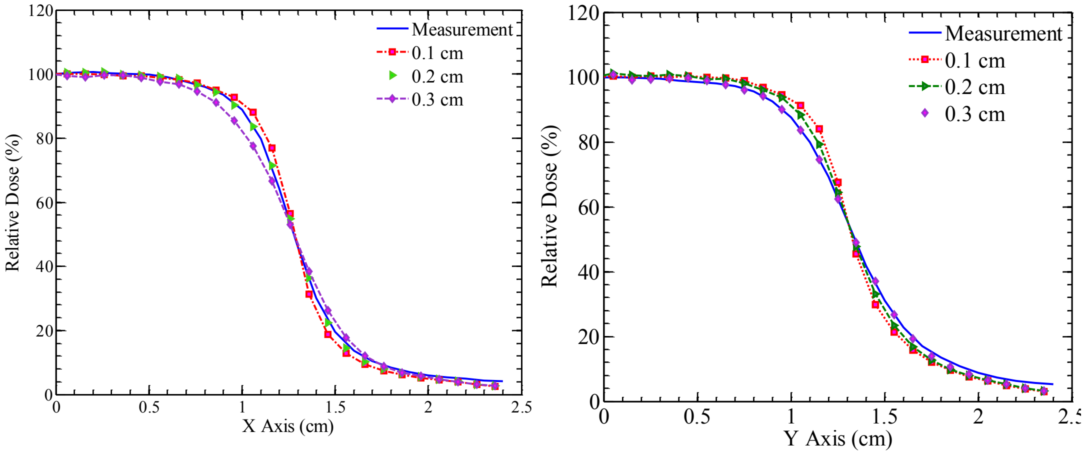

Figure 4.7. The plot of half-lateral profiles of 2.4 cm x 2.4 cm for different values of the FWHM radial intensity distribution. The best agreement was obtained for the FWHM value of 0.2 cm in the X-axis (left) and 0.3 cm in the Y-axis directions (right).

This result was confirmed by the penumbra matching shown in Figure 4.8, where the optimum radial intensity distribution has an elliptical shape rather than a circular shape.

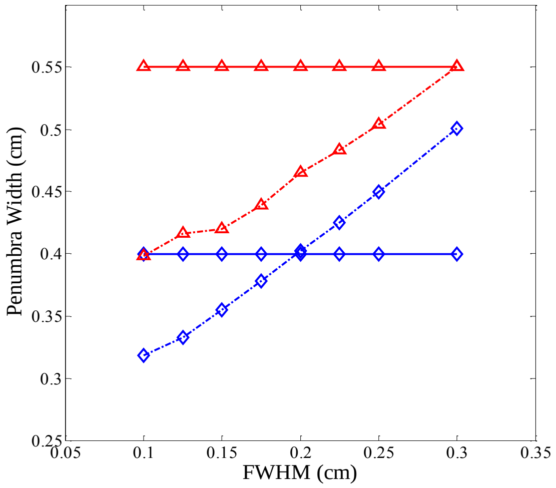

Figure 4.8. Penumbra width matching of the measured data (solid line) and the simulated data (dashed line) of 2.4 cm x 2.4 cm field. The measured X-axis penumbra (diamond) intersects with the simulated penumbra at the FWHM of 0.2 cm while the Y-axis penumbra (triangle) intersects at the FWHM of 0.3 cm.

The optimisation for the other field sizes showed similar results, where the best match was obtained with the elliptic-shaped radial intensity distribution. However, the effect of the FWHM change was less obvious for the largest field (Figure 4.9). The Monte Carlo simulation had an uncertainty better than 1% over the flat region of the lateral profiles for all tested field sizes.

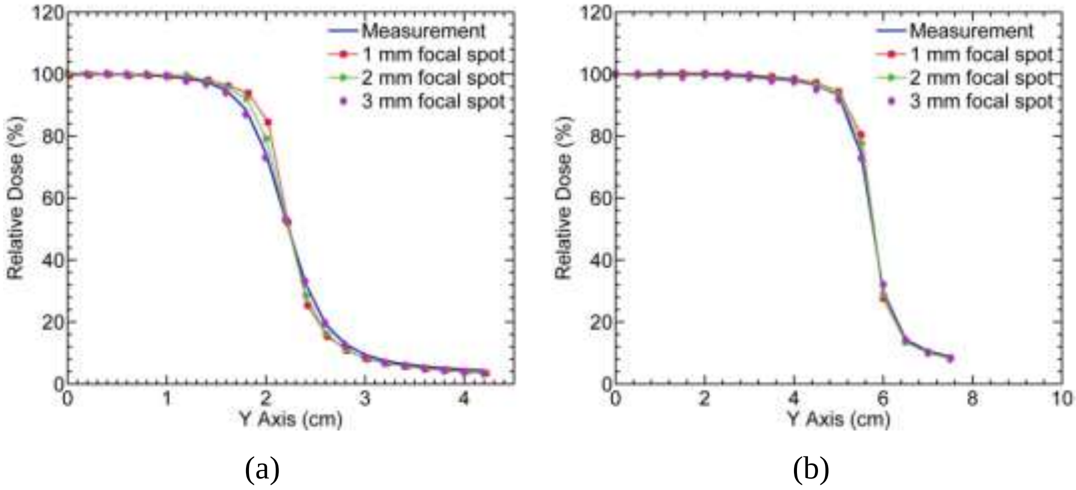

(a) (b)

Figure 4.9. The half-lateral profiles of 4 cm x 4 cm field (a) and 10.4 cm x 10.4 cm (b). The FHWM$_y$ of 0.3 cm shows better agreement with the measured data.

4.3.3 Leaf position optimisation

The size of the treatment field in the Elekta Axesse linear accelerator is defined only by the Beam Modulator MLC, with no involvement of the back-up jaws as normally used in previous Elekta accelerators. It is common to define the field size as the projection of the MLC aperture in the isocenter plane. Direct calculation of the MLC aperture using similar triangle rules would not take into account the offset produced from the rounded-leaf end effects.

The initial motivation of the leaf position optimisation study was the observed differences between the Monte Carlo and measurement cross-line profiles, when the nominal field size was used as the input for the calculation of the leaf opening in the MLCQ CMs. To minimise this effect during the FWHM optimisation, comparison between the simulated and measured profiles was performed after matching the distance of the 50% of the central dose to the central axis.

The plot of the field width difference as a function of the leaf offsets is presented in Figure 4.10. The result shows that an offset of 0.045 cm and 0.015 cm gave the minimum field width difference between the simulated and measured lateral dose profiles for 2.4 cm x 2.4 cm and 10.4 cm x 10.4 cm fields, respectively. Therefore, the offset of 0.045 cm was applied for the field sizes <5 cm, and the offset of 0.015 cm was used for the reference field.

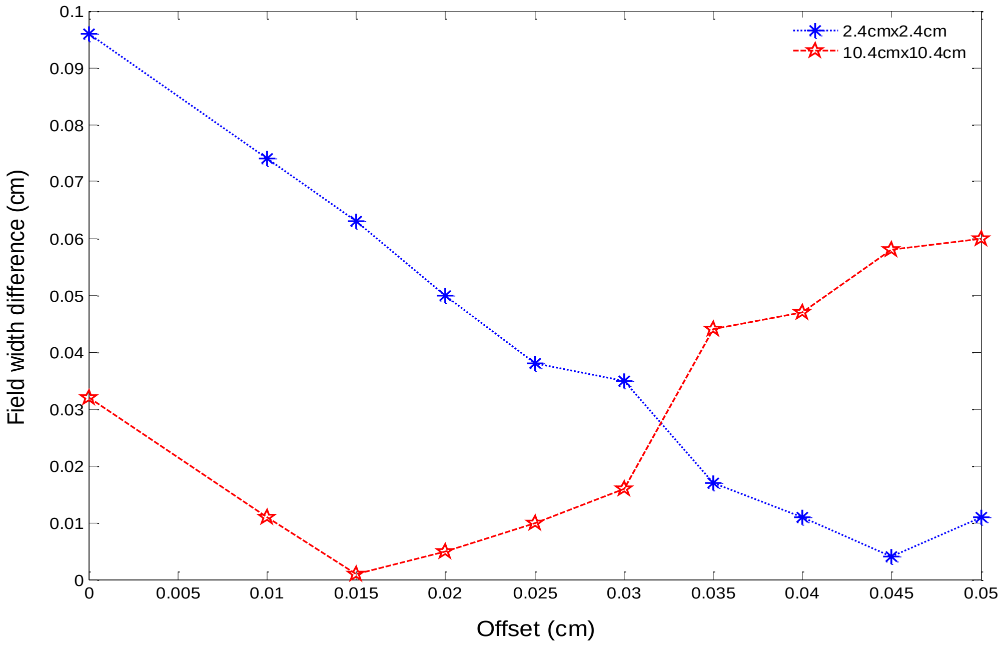

Figure 4.10. The relationship between the applied leaf offset and field width difference of the lateral dose profiles of 2.4 cm x 2.4 cm and 10.4 cm x 10.4 cm fields.

4.3.4 Validation in small field sizes (<4 cm)

The simulation of the optimised source parameters, that is, 6.2 MeV incident electron energy, elliptical radial intensity distribution of 0.2 cm x 0.3 cm, and leaf position offset of 0.045 cm to the small field sizes down to 1.6 cm^2, shows good agreement with the measured dosimetry data, as shown in Figure 4.11.

An agreement of 1% for the dose at the flat region was achieved, with an exception for the inline profile of the smallest simulated field (1.6 cm x 1.6 cm) at a depth of maximum dose (i.e., 1.5 cm), where the dose difference was 1.5%. The analysis of the penumbra region shows that the distance-to-agreement of the measured and simulated profiles was less than 1 mm.

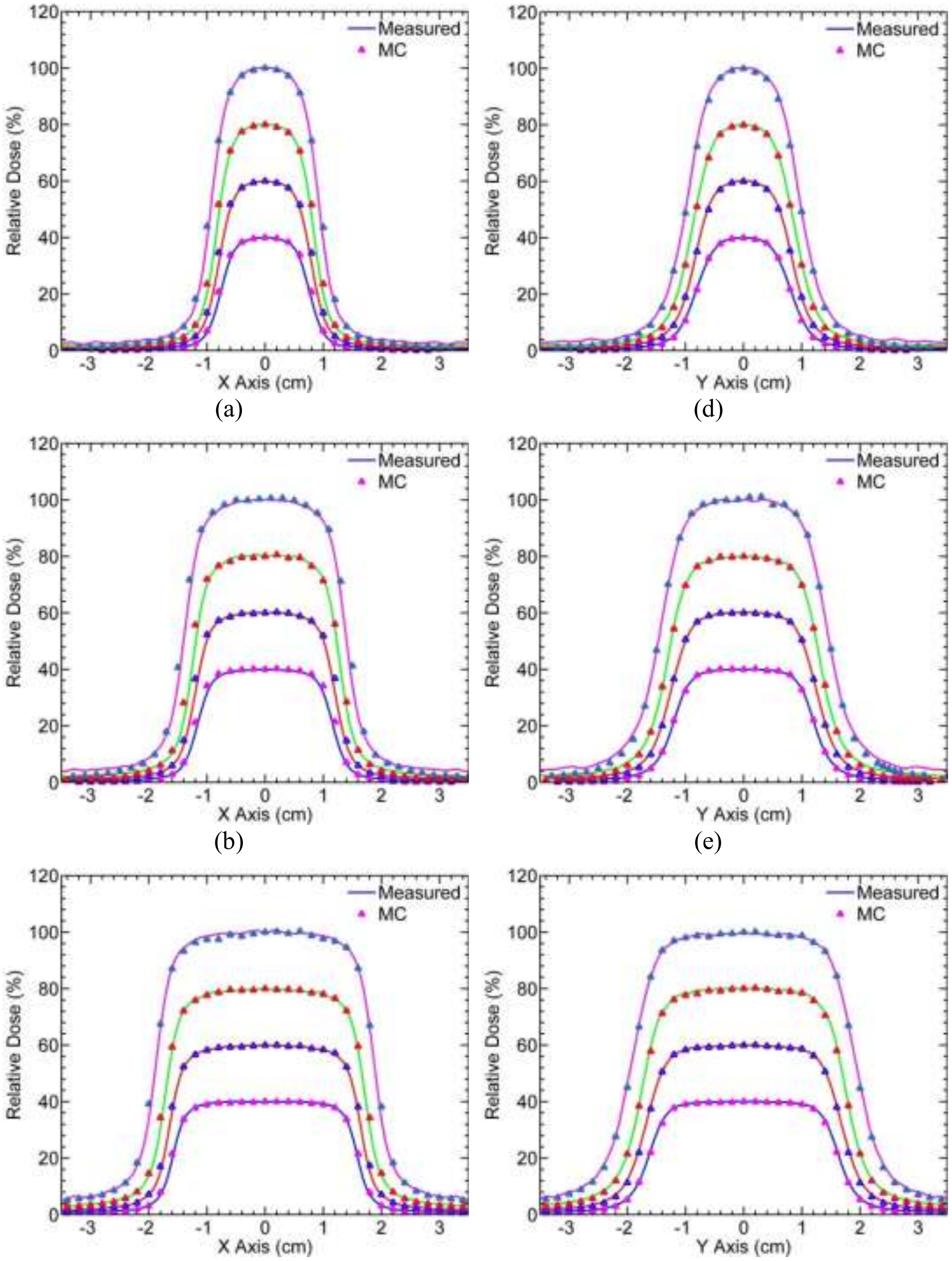

(a) (d)

(b) (e)

(c) (f)

Figure 4.11. The lateral dose profiles in X and Y axes of 1.6 x 1.6 cm^2 (a) and (d), 2.4 x 2.4 cm^2 (b) and (e), and 3.2 x 3.2 cm^2 (c) and (f) at the depths of 1.5 cm, 5 cm, 10 cm, and 20 cm from the bottom to the top lines, respectively. The solid line represents the measured profiles, and the markers represent the Monte Carlo (MC) profiles. The simulation was performed using the electron energy of 6.2 MeV, FWHMx of 0.2 cm and FWHMy of 0.3 cm. An MLC offset of 0.45 mm was applied.

4.3.5 Output factors

The calculated output factors using the optimised parameters were found to agree with the measured data within 1%, as shown in Figure 4.12. The simulated output factor had an average uncertainty of 0.41% (0.24-0.80%). The largest relative difference (0.85%) was observed for the smallest field size (1.6 x 1.6 cm^2).

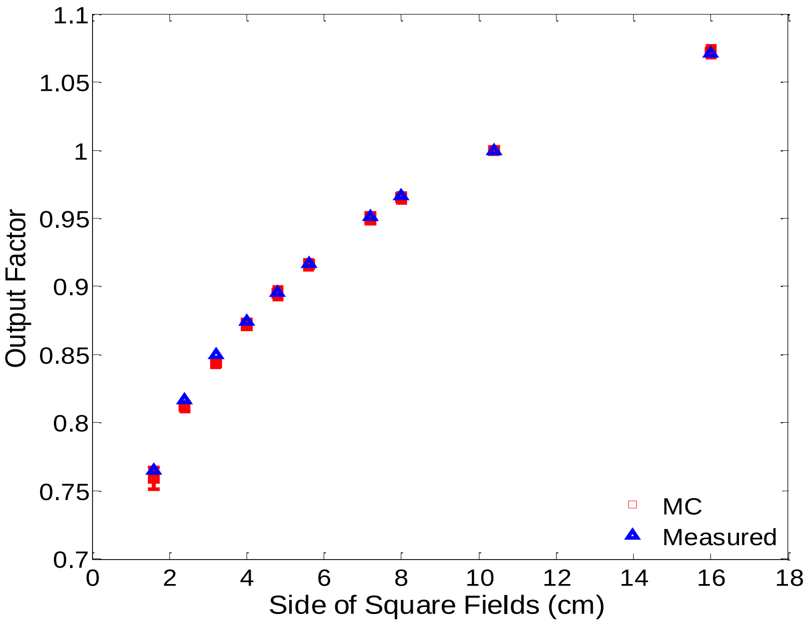

Figure 4.12. Output factors of a 6 MV photon beam Elekta Axesse linear accelerator using various field sizes.

4.4 DISCUSSION

Although it is accepted that the Monte Carlo technique is the most powerful dose calculation tool, its accuracy relies on the accuracy in modelling the beam produced by the linear accelerator. The commissioning of the model is crucial to ensuring the simulated dose is an accurate representation of the actual dose distribution. The commissioning process involves a comparison of the simulated dose profiles with the dose distribution from the experimental measurement, which is often performed in a homogenous water phantom at a given SSD value. During this process, the primary electron beam energy and the FWHM of its radial intensity distribution were two important parameters to be determined.

This work presents the modelling of a specific combination of Elekta Axesse linear accelerator and integrated Beam Modulator collimation system as the first step in the dosimetric verification of the lung SBRT plans using a Monte Carlo simulation. The commissioning of the Elekta Axesse linear accelerator head demonstrated the optimum incident electron energy value of 6.2 MeV. This value is the same as the value reported by Kairn et al. [147] for the 6 MV photon produced by Elekta Precise linear accelerator. This is not surprising, as the upper part of this model from the target down to the monitor chamber was the same as the Elekta Precise MC model. This value is lower than the value reported by Heydarian et al. [150], who modelled the Elekta Synergy S with the peak of the incident electron energy of 6.5 MeV. Almberg et al. [149], who modelled the Elekta Synergy linear accelerator, reported that electron energy of 6.45 MeV resulted in a better match with the measured data. Although there is a similarity in the machine design between the Elekta Synergy S and the Elekta Axesse linear accelerator, this work found that electron energy of 6.5 MeV resulted in a mismatch in the lateral profiles for the largest field size (21 cm x 16 cm). An increase in the electron energy for this field size resulted in a decrease in the horn of the lateral profiles. The sensitivity of the lateral profile horns to the beam energy was also reported by Keall et al. [144]. Commissioning of the linear accelerator model using only a small field would result in the selection of the higher electron energy. In this work, three different field sizes were used in the commissioning of the model to represent small and large field sizes. In contrast, the effect of the beam energy on the depth dose curves of the largest field was more subtle, indicating less sensitivity of the depth dose curves to this parameter. Similar findings were reported by Hartmann Siantar et al. [62] and Keall et al. [144].

This work found that the incident electron beam was best modelled as asymmetric in the X and Y directions. Heydarian et al. [150] and Asnaashari et al. [67] found the optimum FWHM of the source of the Elekta Synergy S is 0.11 cm with a circular shape. However, Podder et al. [159], who performed measurements using a collimator rotation, suggested an elliptical shape of the Elekta Synergy S radiation source due to the penumbra width being different between the leaf-end and the leaf-side. This was also reported by Francescon et al. [148], who found the best match of their Elekta Synergy Monte Carlo model using the elliptic radiation source shape. Similarly, an elliptical-shaped radiation source approach was also used by Almberg *et al.* [149] to model the 6 MV photon beam produced by the Elekta Synergy S. As the design of the Elekta Axesse is similar to the Elekta Synergy S, it was initially assumed that its radiation source parameters would be the same as reported by Heydarian et al. [150]. However, this work shows that the best match was obtained using the elliptic-shaped radiation source, although the optimum value found in this study was larger than that reported by Francescon *et al.* [148] which was FWHMx = 0.2 cm and FWHMy = 0.09 cm.

This work also confirmed that the lateral profile of the small fields was sensitive to the change of the FWHM. The penumbra width increased with an increase of the FWHM, indicated by a decrease in the horns of the lateral profiles shoulders. The work by Pena *et al.* [140] also demonstrated the sensitivity of small field sizes to the FWHM of the radial intensity distribution, however, they assumed that the electron beam radial intensity had a symmetrical shape.

The use of “in air off-axis factors” is also recommended for fine tuning the electron source parameters, as it is more sensitive to those parameters [41, 153, 160]. However, in this work, the commissioning of the linear accelerator model was performed using depth dose and lateral dose profiles data, which were the only available commissioning machine data.

In addition, this work demonstrates that leaf position optimisation is required during the matching of the simulated profiles with the measured profiles. As the leaf position determines the shape of the field, ensuring the accuracy of the leaf position would be beneficial for further implementation of the linear accelerator model for dose calculation of complex, irregularly shaped clinical treatment plans. This is especially true for the lung SABR, which employs a combination of 7-14 coplanar and non-coplanar beams. Inaccurate leaf position effects might accumulate in the overall dose distribution, leading to errors when comparing the simulated dose distribution with the TPS or measured dose distribution.

The validation of the optimised source parameters and leaf position in the small field sizes down to 1.6 x 1.6 cm^2 demonstrated excellent agreement of 1-1.5% with the measurement. This indicates the suitability of the model to be used in the study of the clinical radiotherapy plans. An agreement of the calculated output factor top within 1% of the measurement also supports the further use of the model for dose verification of lung patient SABR plans that involve a field dimension of >2.8 cm. Future studies could involve the investigation of very small fields (less than 1 x 1 cm^2).

Although a good agreement has been obtained between the Monte Carlo and measurement, there is some limitations in the Monte Carlo model arises from the limitations of the measured data used for commissioning of the model. This is because the measured data which includes lateral dose profiles, depth dose profiles, and output factor used to commission the Monte Carlo model were measured using a finite size ionisation chamber (i.e. CC04 with a cavity radius of 2.0 mm and a cavity volume of 0.04 cm3 for the field size ≥ 4 cm x 4 cm). It has been known that the use of finite size detector causes volume averaging effect which lead to penumbra broadening. It is recommended to use a detector with a very small sensitive volume for dose profiles measurement of small field, for example diamond and diode detector. However, the ionisation chamber was used for measuring dose profiles and output factor as it is regarded as the standard radiation dosimeter in the clinic.

4.5 CONCLUSION

A 6 MV photon beam of the Elekta Axesse linear accelerator equipped with the Beam Modulator collimation system was modelled and commissioned. Two source parameters were optimised during the commissioning, in which the best agreement was achieved with the incident electron energy of 6.2 MeV and an elliptical FWHM of 0.2 cm in the leaf-side direction and 0.3 cm in the leaf-end direction. The leaf position optimisation found that a leaf offset of 0.045 cm was required for the small field (2.4 x 2.4 cm^2) in order to obtain the best match with the measured profiles. The combination of optimised source parameters and the leaf offset of 0.045 cm for small field sizes <5 cm resulted in excellent agreement with the measured lateral dose profiles to within a 1.5% dose difference at the low dose gradient region and 1 mm distance-to-agreement at the high dose gradient region. The calculation of the output factor also showed an agreement of better than 1% with the measurement. Overall, the commissioning of the model down to 1.6 x 1.6 cm^2 demonstrates the suitability of the model to be used to evaluate lung patient SBRT plans for early stage NSCLC that involve treatment field dimensions of approximately 3-6 cm. The following chapter discusses the use of the BEAMnrc Monte-Carlo model validated in this chapter for the evaluation of the dosimetric performance of the collapsed cone convolution algorithm in the treatment planning of twenty clinical lung SBRT plans.

Chapter 5: Dosimetric Verification of Lung SBRT Plans

5.1 INTRODUCTION

The presence of tissue heterogeneities in the lungs is a challenge for TPS dose calculation algorithms. This is because TPS algorithms have a limitation when modelling lateral electron scattering in low density lung tissue and regions with large density variations. Many studies have investigated the performance of different algorithms in lung treatment plans [18, 19, 28, 32, 37-39, 161-166]. However, few studies have specifically investigated the performance of collapsed cone convolution (CCC) algorithms in lung SBRT treatment [19, 22, 38, 39]. Among these studies, only two focused on the performance of CCC algorithms implemented in the Pinnacle^3 RTPS. One study focused on recalculating the lung SBRT plans using different commercial TPS algorithms, including the CCC algorithm in Pinnacle and its relation to tumour control probability [22]. However, the plans were initially designed using the pencil beam algorithm, which is known to be inaccurate for lung SBRT planning, with no attempts to optimise the plans using CCC algorithms. Another study focused on lung SBRT plans originally planned using the CCC algorithm in Pinnacle^3; however, the plans were designed for the five-field IMRT delivery technique [39]. This work presents a comprehensive evaluation of the dosimetric performance of the CCC Pinnacle^3 in twenty lung SBRT plans for early stage NSCLC with a small PTV volume (<85 cm^3), where accuracy is more difficult to obtain. The verification was performed using the EGSnrc/BEAMnrc Monte Carlo (MC) simulation as the gold standard dose calculation. The plans were designed for the 3DCRT delivery technique consisting of a combination of 10 coplanar and non-coplanar beams. These beam arrangements have been found to be the optimum arrangement to meet high and intermediate dose constraints [167].

The previous chapter discussed the MC modelling and commissioning of a 6 MV photon beam produced by an Elekta Axesse linear accelerator used for radiation delivery in lung SBRT plans. It was shown that the model had excellent agreement with the measurement data for field sizes down to 1.6 x 1.6 cm^2 in a simple homogenous water phantom. The model is used in this chapter to simulate the dose deposition of the 6 MV photon beam in lung cancer patient treatments. The dose distribution obtained from the MC simulation is then compared with the dose distribution calculated from the CCC algorithm. The assessment of the dose distribution included the PTV coverage, conformity index (CI), intermediate dose spillage, as well as the dose received by organs at risk (OARs) based on the criteria defined in the RTOG 1021 protocol.

5.2 METHODS AND MATERIALS

5.2.1 Lung SBRT treatment plans

Institutional ethical approval (QUT Human Research Ethics Committee, Approval number 1400000993) was obtained for the analysis of twenty patient plans previously treated for early stage NSCLC with SBRT. The inclusion patient criteria for the research were stage IA/B or IIA of NSCLC with no nodal involvement of the disease (N0) and no distant metastases (M0). The tumours had a diameter of less than 5 cm and were located more than 2 cm away from the carina (i.e., the proximal bronchial tree).

The plans were created using the Pinnacle^3 Radiotherapy TPS version 9.6 (Phillips Medical system, Stockholm, Sweden). A four-dimensional computed tomography (4DCT) scan was used to account for tumour motion due to breathing. The breathing cycle image data was binned into 10 phases. The internal target volume (ITV) was created by combining the gross tumour volume (GTV) at each of the respiratory phases. A 5 mm margin was uniformly added to the ITV to create the PTV.

The dose distribution was calculated using the CCC algorithm available in the Pinnacle^3 RTPS using the dose grid of 2 mm in all directions, as recommended by the TROG Chisel trial protocol (i.e., <0.3 cm). The prescribed dose was 54 Gy in three fractions, resulting in a dose per fraction of 18 Gy given on days 1, 7, and 14. The dose was prescribed at the periphery of the PTV, instead of the isocenter [24]. The prescribed isodose line fell between 59-90% of the absolute maximum dose in the plan. The planning objective for the PTV was that more than 95% of the PTV volume should be covered by the prescription isodose (PTV_{54Gy}), with more than 99% of the PTV volume receiving 90% of the prescribed dose ($\mathrm{PTV}_{48.6Gy}$).

The treatment plans were designed using the 3DCRT dose delivery technique, in which the beam arrangement was optimised in the previous work by Fitzgerald *et* *al.* [167]. Each plan consisted of 10 beams, with a combination of two to four coplanar and six to eight non-coplanar beams, as this combination met the high and intermediate dose constraints [167]. This arrangement has advantages in closely shaping the treatment field to the target tumour and focusing the high dose in the centre of the tumour target. In addition, the use of non-coplanar beams allows for creation of a more isotropic dose distribution with a rapid dose fall-off at the edge of the PTV [3].

5.2.2 Extraction of Treatment Plan Information

The use of a MC simulation as a benchmarking tool of TPS algorithms requires treatment plan information for the generation of simulation input files. Unfortunately, the plan information from the Pinnacle^3 RTPS cannot be directly used in the EGSnrc/BEAMnrc system. Therefore, plan information must be transferred into the Digital Imaging and Communication in Medicine (DICOM) format, the standard format used in the radiotherapy field. This was performed by exporting the treatment plan information consisting of a set of patient CT images, the patient contour structure information (RT Struct), and plan data including dose prescription (RT Plan) and dose information (RT Dose) through the DICOM network.

The CT images contained detailed anatomical information about the patient. The CT images were obtained with the patient in a supine position, scanning from the head to the abdomen to fully cover the thorax region. The patient's forearms were positioned above the head to allow optimum beam configuration from different gantry rotations. The CT images had a slice thickness of 2 mm, as recommended for stereotactic treatment [24]. The conversion of the CT number to the density was based on the conversion table shown in Table 5.1. All patients had a 4DCT scan in which results in ten respiratory phases of 4DCT. This enable to show patient anatomy through a complete respiratory cycle. A free breathing scan technique was used with a slice thickness of 2 mm which was obtained covering the entire volume of the lungs. The image is then exported and registered to the 4DCT in the TPS.

The RTStruct.dcm file contained all outlined structures of the plans consisting of the tumour volume (i.e., ITV and PTV), OARs, and D_{2cm}. The evaluated OARs for lung SBRT treatment included total normal lung tissue (combined left and right lung minus ITV), oesophagus, pericardium, brachial plexus, spinal canal, trachea, chest wall, rib, aorta, superior vena cava, and inferior vena cava. For treatment plans where the PTV overlapped the chest wall, more than one rib bone was contoured and numbered based on the anatomical order. Anatomically, there are 12 rib bones, numbered from the superior to the inferior direction, where rib bones 1 to 7 are true ribs, ribs 8 to 10 are false ribs, and ribs 11 to 12 are floating ribs. The location of the tumour is an important factor affecting the dose received by the ribs. D_{2cm} was contoured by expanding the PTV by 2 cm, which was used to determine the dose spillage in the lung SBRT plans.

Table 5.1: *CT Number to Density Conversion Table of Toshiba Scanner*

CT Number	Density (g/cm^3)
0	0.000
297	0.290
481	0.480
906	0.942
1000	1.000
1021	1.053
1074	1.095
1216	1.140
1457	1.334
1823	1.562
2238	1.824
6403	4.590
11975	8.280
16596	11.340

The RTPlan.dcm file contained all beam information, such as beam energy, the number of beams, beam collimation, beam orientation, and beam meter set. Beam collimation contained information regarding the MLC and jaws positions. The beam orientation determined rotation of gantry, couch, and collimator angles. Beam meter set contained information regarding the weighting of the beams used in the treatment plan. Other information, such as SSD and the isocenter coordinate, was also recorded in the RTplan.dcm file. The isocenter was generally defined at the centre of the tumour mass, which is off-axis (not at (0,0,0) coordinate).

The dose calculated using the CCC algorithm was saved in the RTDose.dcm. The dose grid was defined as 0.2 cm in all directions. The dose distribution was used to generate cumulative and differential dose-volume histograms (DVHs) for further analysis of the dosimetric parameters of the plans. During the dose calculation, the treatment couch (patient table) were removed, thus, excluded from the calculation.

Extraction of above plan information was performed using scripts written in MATLAB version R2012a (MathWorks).

5.2.3 Input files of MC simulation

Prior to the MC simulation of lung SBRT plans, users must create the input files for simulation of the radiation transport within the head of the linear accelerator using the phantom and/or patient geometry. The EGSnrc/BEAMnrc MC codes were employed to simulate the transport of the radiation within the linear accelerator head. The DOSXYZnrc MC codes were employed to simulate the dose deposition in the patient geometry or water phantom. Two types of input files, that is, BEAMnrc and DOSXYZnrc input files were generated for each beam.

BEAMnrc input files

For BEAMnrc simulation, the geometry and composition of the accelerator components need to be defined. The detailed linear accelerator model (described in Chapter 4) was used for the patient simulations. The only parameters that were changed were the patient specific MLCQ aperture and directional Bremsstrahlung splitting (DBS) radius.

As the treatment field size was defined in the TPS and DICOM systems by the position of the MLC, conversion from the DICOM-defined MLC position to the MLCQ aperture was required. The DICOM-defined MLC position was extracted from the RT plan file and converted to the MLCQ aperture using Equation 4.4. It should be noted that DICOM defines the MLC position at the isocenter plane, while the BEAMnrc defines the MLCQ aperture at the source-to-collimator distance. The verification of the MLCQ aperture setting in a simple water phantom was performed to ensure the accuracy of the extraction and the conversion of the MLC position from DICOM to the BEAMnrc system and is further described in Section 5.2.6.

The DBS radius was determined using the maximum leaf apertures in the X and Y axes. The opening in X axis (FS_X) was determined from the number of opened leaves, which is perpendicular to the leaf travel direction. The opening in the Y axis (FS_Y) was determined from the maximum leaf opening in the travel direction. The DBS radius was then calculated using Equation 5.1:

$$r_{DBS} = \left(\sqrt{{FS_x}^2 + {FS_y}^2}\right) + 3\ cm \tag{5.1}$$

In Equation 5.1, an additional 3 cm was included to ensure that the DBS enclosed the entire field. The EGSnrc manual suggests that overestimation of the DBS radius by up to 5 cm is possible without any loss in efficiency [126, 132]. Another research group used an additional 2 cm to the minimum radius of the field [150].

DOSXYZnrc input files

DOSXYZnrc input files were created to model the radiation transport within the patient CT-based phantom and to predict the dose deposition in the patient's anatomy. The plan information required for DOSXYZnrc input creation is the CT images data set of the patient, beam arrangement setting, and the isocenter coordinate. The DBS radius used the same value as used in the BEAMnrc input files.

The CT image data sets were processed using the MCDTK software [168] to create EGSPHANT files that represented the patient's geometry in the DOSXYZnrc simulation. The EGSPHANT files were generated for each plan using a voxel size of 2 mm in all directions to match the dose grid used in the TPS calculation. The phantom was built using four different materials, that is, air, lung tissue, soft tissue, and bone (Table 5.2).

Table 5.2: *List of Materials used in EGSPHANT File*

Tissue	Pegs4dat material	Density (g/cm^3)
Air	AIR521ICRU	1.20E- 03
Lung	LUNG521ICRU	0.26
Soft Tissue	ICRUTISSUE521ICRU	1.00
Bone	ICRPBONE521ICRU	1.85

The orientations of the beams had to be defined relative to the patient coordinate system. It should be noted that the beam arrangement settings saved in DICOM data could not be directly used in the DOSXYZnrc system. This was because the DICOM and TPS systems define the beam orientation using the rotation angle of gantry, patient table (couch), and collimator, whereas the DOSXYZnrc system defines the beam orientation to the phantom plane using polar angle (θ), azimuthal angle (φ), and collimator angle (ϕ_{col}) [169-171]. Therefore, a further transformation of the gantry, couch, and collimator angles to the polar, azimuthal, and collimator angles was required. This involved a transformation of the DICOM coordinate system to the DOSXYZnrc coordinate system, which has been described in the literature [169-171].

The DICOM coordinate system was defined by the point within the patient and dependent on the patient orientation to the scanner. In this work, the coordinate system of the patient is defined using supine and head-first-to-scanner (HFS) patient orientation. Figure 5.1 illustrates the axes convention used in DICOM coordinate system based on the right-handed coordinate system.

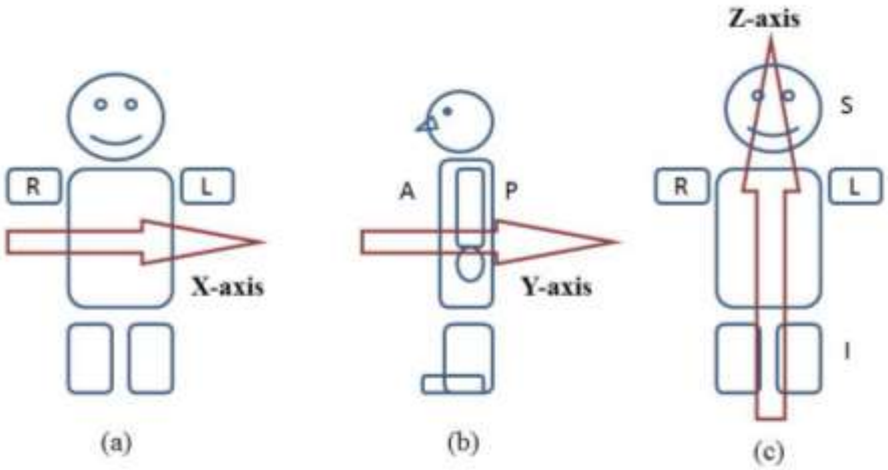

Figure 5.1. The axes convention in DICOM coordinates system. (a) X-axis points to the left-hand side (L) of the patient, (b) Y-axis points to the posterior (P) direction, (c) Z-axis points to the superior (S) direction.

The axes convention of the DICOM coordinates system was different to the axes convention of the Pinnacle^3 TPS for the Y and Z axes. The Y axis used in the Pinnacle^3 coordinate system was positive toward the anterior (A) direction, while in the DICOM coordinate system the Y axis was positive toward the posterior direction. The Z axis of the Pinnacle^3 coordinate system was positive toward the inferior (I) direction, opposite to the DICOM Z axis direction.

The DOSXYZnrc simulation used a full phase-space source file (isource option 2), which was generated from the BEAMnrc simulation. For this source type, the users define the source parameters: the isocenter coordinate in x, y, and z-axes, the beam orientation given as polar angle (θ), azimuthal angle (φ), and collimator angle (ϕ_{col}), the distance from the source to isocenter (d_{source}), DBS radius, and the associated phase space file. A screenshot of the DOSXYZnrc input window is presented in Figure 5.2.

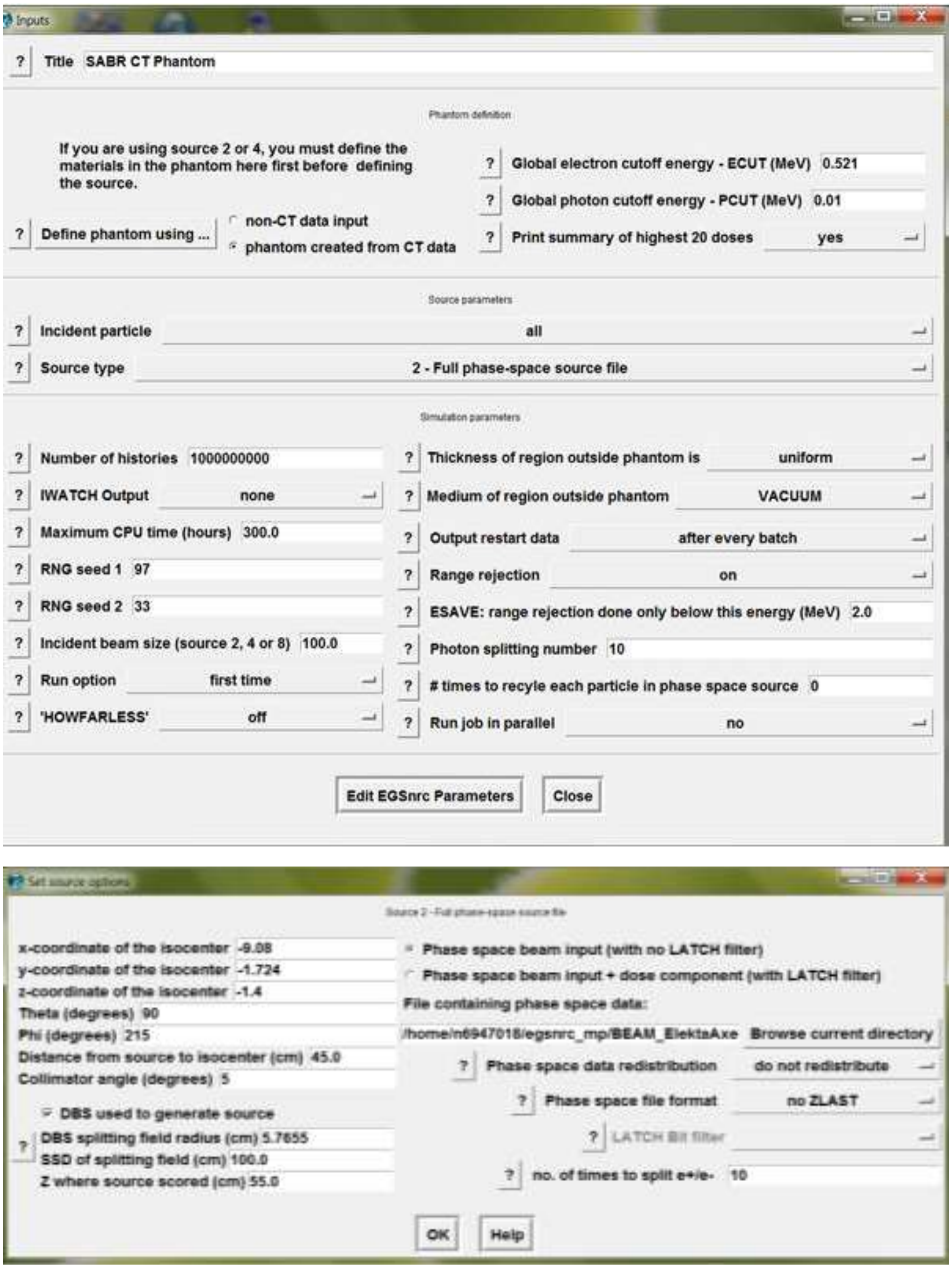

Title SABR CT Phantom

If you are using source 2 or 4, you must define the materials in the phantom here first before defining the source.

Define phantom using ... ○ non-CT data input ● phantom created from CT data

Global electron cutoff energy - ECUT (MeV) 0.521

Global photon cutoff energy - PCUT (MeV) 0.01

Print summary of highest 20 doses yes

Incident particle all

Source type 2 - Full phase-space source file

Number of histories 1000000000

IWATCH Output none

Maximum CPU time (hours) 300.0

RNG seed 1 97

RNG seed 2 33

Incident beam size (source 2, 4 or 8) 100.0

Run option first time

'HOWFARLESS' off

Thickness of region outside phantom is uniform

Medium of region outside phantom VACUUM

Output restart data after every batch

Range rejection on

ESAVE: range rejection done only below this energy (MeV) 2.0

Photon splitting number 10

times to recyle each particle in phase space source 0

Run job in parallel no

x-coordinate of the isocenter -9.08

y-coordinate of the isocenter -1.724

z-coordinate of the isocenter -1.4

Theta (degrees) 90

Phi (degrees) 215

Distance from source to isocenter (cm) 45.0

Collimator angle (degrees) 5

☑ DBS used to generate source

DBS splitting field radius (cm) 5.7655

SSD of splitting field (cm) 100.0

Z where source scored (cm) 55.0

● Phase space beam input (with no LATCH filter)

○ Phase space beam input + dose component (with LATCH filter)

File containing phase space data:

/home/n6947018/egsnrc_mp/BEAM_ElektaAxe

Phase space data redistribution do not redistribute

Phase space file format no ZLAST

LATCH Bit filter

no. of times to split e+/e- 10

Figure 5.2. The DOSXYZnrc input window showing the parameters that should be defined by the users, including the source parameters.

The isocenter coordinate used in the DOSXYZnrc input was based on the isocenter coordinate extracted from the DICOM RTPlan. However, there was a difference in the Z-axis direction between the DICOM and DOSXYZnrc system. The

Z-axis of DOSXYZnrc was the reverse of the DICOM Z-axis. The relationship between the DOSXYZnrc and DICOM isocenter coordinate is given in Equations 5.2 to 5.4.

$$X_{iso,DOSXYZ} = X_{iso,DICOM} \tag{5.2}$$

$$Y_{iso,DOSXYZ} = Y_{iso,DICOM} \tag{5.3}$$

$$Z_{iso,DOSXYZ} = -Z_{iso,DICOM} \tag{5.4}$$

Table 5.3 provides an example of the isocenter coordinate of one lung SBRT plan from the Pinnacle^3 RTPS, DICOM, and DOSXYZnrc systems.

Table 5.3: *An Example of the Isocenter Coordinate Conversion between the TPS, DICOM, and DOSXYZnrc Systems*

System	X-isocenter (cm)	Y-isocenter (cm)	Z-isocenter (cm)
Pinnacle^3 TPS	-9.15	1.83	-1.20
DICOM	-9.15	-1.83	1.20
DOSXYZnrc	-9.15	-1.83	-1.20

The distance from the source to the isocenter was defined as the distance from the scoring plane of the phase space file to the isocenter plane. The phase space file was saved at a 55 cm distance from the source (Z_{score}). Therefore, the distance from the source (d_{source}) was determined using Equation 5.5.

$$d_{source} = 100 - Z_{score} \tag{5.5}$$

The next DOSXYZnrc input parameter to be defined was beam orientation, described as a polar angle (θ), azimuth angle (φ), and collimator angle (ϕ_{col}). There was a difference in the way beam orientation was defined in the DICOM and DOSXYZnrc system. The beam orientation was defined as the combination of the gantry rotation angle (θ_G), the patient table (couch) rotation angle (θ_T), and the collimator rotation angle (θ_C). Conversion of the DICOM beam orientation to the DOSXYZnrc coordinate system was performed.

The polar and azimuth angles were calculated using Equations 5.6 and 5.7, respectively, as proposed by Thebaut and Zavgorodni [169].

$$\theta = cos^{-1}(\sin\theta_T \,.\, \sin\theta_G) \tag{5.6}$$

$$\varphi = tan^{-1}\left(\frac{-\cos\theta_G}{\sin\theta_G \cos\theta_T}\right) \tag{5.7}$$

The DOSXYZnrc collimator angle (ϕ_{col}) was initially determined using the formula proposed by Zhan et al. [171], as shown in Equation 5.8. However, a good match was not obtained with the TPS dose distribution. A change to the minus sign in Equation 5.8 was required in order to obtain a match with the TPS dose distribution employed in the MCDTK software (Equation 5.9).

$$\phi_{col,Zhan}^{(beam)} = \frac{3\pi}{2} - \theta_C - tan^{-1}\left(\frac{-sin\theta_T cos\theta_G}{cos\theta_T}\right) \tag{5.8}$$

$$\phi_{col,MCDTK}^{(beam)} = \frac{3\pi}{2} + \theta_C + tan^{-1}\left(\frac{-sin\theta_T cos\theta_G}{cos\theta_T}\right) \tag{5.9}$$

Further verification of the beam arrangement setting was performed to determine whether the conversion formula was correct, as discussed in Section 5.2.7.

5.2.4 Simulation parameters

Prior to the Monte Carlo simulation, other simulation parameters, such as the number of particle histories to be simulated, the selection of the variance reduction techniques, and the electron step algorithm, were also defined.

In the BEAMnrc simulation of the lung SBRT plans, ~10^8 particle histories were simulated using the electron energy cut-off and photon energy cut-off of 0.7 MeV and 0.01 MeV, respectively. The DBS radius was selected to improve simulation efficiency using a splitting number of 1000. The EXACT boundary crossing algorithms and PRESTA-II electron-step algorithms were enabled. All simulations were performed using the incident electron energy of 6.2 MeV and an elliptical FWHM (0.2 cm vs 0.3 cm) as described in the previous chapter. The phase space file was scored at a 55 cm distance from the source, located just below the exit window of the linear accelerator head. The same simulation parameters were used for verification of the MLCQ aperture setting and DOSXYZnrc beam arrangement setting.

In the DOSXYZnrc simulation of the lung SBRT plans, 5 x 10^8 particle histories were simulated using the electron energy cut-off and photon energy cut-off of 0.521 MeV and 0.01 MeV, respectively. The number of particle histories simulated in the BEAMnrc and DOSXYZnrc simulation was selected to obtain the statistical uncertainty of <1%. The combination of 10^8 histories in the BEAMnrc simulation and 5 x 10^8 histories in the DOSXYZnrc simulation resulted in an average uncertainty of less than 0.5% for the voxels having a dose larger than 50% maximum dose (D_{max}). The DBS variance reduction technique was also enabled with the splitting field defined at the isocenter plane (i.e., 100 cm from the source). In addition, photon splitting was also selected using the factor of 10 and range rejection was turned on using ESAVE of 2 MeV. The PRESTA-II electron-step algorithm and PRESTA-I boundary crossing algorithm were selected.

All simulations were performed using QUT high-performance computing and research support. Parallel computing was used to reduce the computation time. The simulation using 10 parallel jobs took about two hours for the BEAMnrc simulation and about six to eight hours for the DOSXYZnrc simulation for the number of particle histories specified above.

5.2.5 Monte Carlo absolute dose calibration

The dose predicted by the MC simulation is presented in the unit of Gy per the number of incident particles used in the simulation (Gy/particle). While the dose calculated by the TPS is presented in Gy per monitor unit (Gy/MU). To enable direct comparison between the MC dose and TPS dose, the MC dose must be converted to the Gy/MU. This can be obtained through absolute dose calibration of the MC dose, in which the simulation is performed using the same reference conditions as the dose calibration condition in the actual measurement.

The clinical absolute dose calibration was performed for the reference field (10.4 cm x 10.4 cm) at a homogenous water phantom using an SSD of 90 cm. The central axis dose at 10 cm depth was calibrated to 1 cGy/MU. The same reference conditions were used to determine the absolute dose calibration factor of the MC dose. The simulation of the reference field was performed in a water phantom using 10^9 particle histories with the voxel size of 0.2 cm^3. The central axis dose at 10 cm depth was extracted from the 3ddose file and used as the calibrated factor for the absolute dose calibration of the MC dose in the lung SBRT plan simulation. The mean dose and standard deviation of the central 5 x 5 voxels were used to determine the uncertainty of the absolute dose calibration factor. Increasing the particle histories from 10^9 to 2 x 10^9 reduces the uncertainty by only 0.1% (from 0.4% to 0.3%) with a significant increase of the computation time (from 11 hours to 36 hours). The result with a smaller uncertainty was used in the absolute dose calibration disregarding its long computation time.

5.2.6 Verification of MLCQ aperture setting

As described earlier, there is a difference in the MLC position definition between the TPS, DICOM, and BEAMnrc systems. The verification was performed to ensure that the conversion of the DICOM-defined MLC position to the BEAMnrc-defined MLCQ setting was correct. For this purpose, a simple method was employed by comparing the TPS and MC planar dose maps in a homogenous water phantom.

Firstly, it is important to know how TPS, DICOM, and BEAMnrc systems define the MLC position. In the accelerator head, the leaves are located in a paired leaf bank that can travel in its own leaf bank away from the beam axis and travel toward the opposed leaf bank crossing the beam axis (known as interdigitation). In the Pinnacle³ TPS, the leaf bank pairs were defined as X_1 for the right leaf bank and X_2 for the left leaf bank (Figure 5.3). The minimum leaf tip position was -11 cm and the maximum leaf tip position was 11 cm. The leaf has a positive position value if the leaf travels away from the beam axis in its own leaf banks (illustrated as leaf A1, A2, B2, and C1 in Figure 5.3) and a negative position value if the leaf travels toward the opposed leaf bank (illustrated as leaf B1 and C2 in Figure 5.3).

DICOM defines the X_1 leaf bank as the negative leaf bank and X_2 as the positive leaf bank. This means that if the leaf travels away from the beam axis in the negative leaf bank, it will have a negative sign (illustrated as leaf A1 and C1 in the Figure 5.3). If the leaf travels to the opposing leaf bank, then it will have a positive sign (illustrated as leaf B1 in Figure 5.3). Similarly, in the positive leaf bank, the leaf will have a positive sign if moves in its own leaf bank (illustrated as leaf A2 and B2 in Figure 5.3) and will have a negative sign if it travels across the mid-line towards the opposite leaf bank (illustrated as leaf C2 in Figure 5.3).

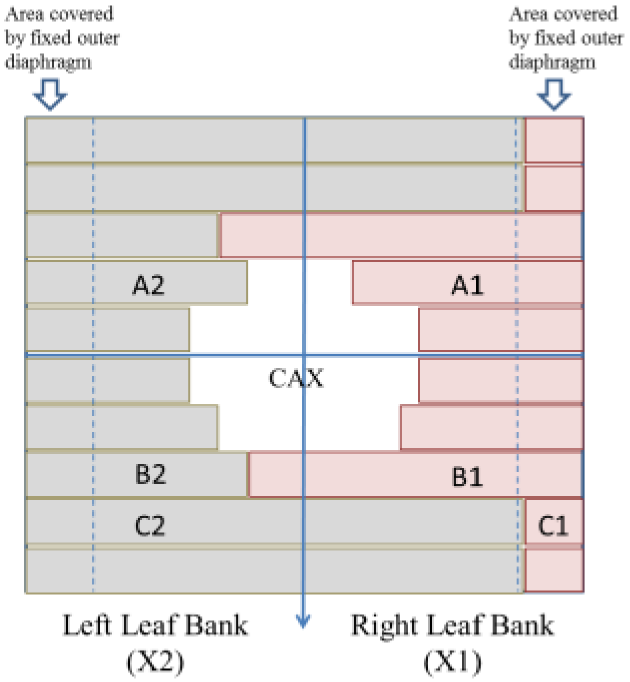

Figure 5.3. Illustration of the leaves configuration in the TPS. A1, A2, B2, and C1 illustrate the leaves that travel away from the beam axis in their own leaf bank, X1 and X2, respectively. B1 illustrates the leaf that crosses the beam axis, travelling toward the opposing leaf bank (from X1 to X2); similarly, C2 illustrates the leaf that travels from X2 toward the opposing leaf bank X1. CAX is the beam central axis.

The leaf position in the BEAMnrc system was defined in the MLCQ component module. The leaf opening was defined at the source-to-collimator distance (SCD) instead of at the isocenter, as used in the TPS and DICOM. Accurate modelling of leaf geometry was important in the small field simulation due to the importance of the effect of peripheral and penumbral features [172]. The mathematical approach to determine the physical leaf tip position at the SCD was described by Boyer and Li [173]. The conversion from the DICOM leaf position to the MLCQ aperture was determined using the step described previously in Section 4.2.9 by employing Equation 4.4. Similar to the DICOM convention, the BEAMnrc system defined the paired leaf bank as negative and positive leaf banks.

To validate the MLC position in the MC simulation, a simple water planar dose map comparison was performed for simple square fields and lung SBRT treatment fields. The BEAMnrc input files were generated using the calculated MLCQ opening setting described above. The simulation was performed using the incident energy of 6.2 MeV and the elliptical focal spot size of 0.2 cm and 0.3 cm in X and Y axes direction, respectively. The number of particle histories used in the BEAMnrc simulation was 10^8 particles, as described in Section 5.2.4. The BEAMnrc phase space files were then used as input in a simulation of a homogenous water phantom using the DOSXYZnrc code. The phantom had a dimension of 50 cm^3 with a voxel size of 0.2 cm in all directions. The simulation was performed with the beam incident on the surface of the phantom directly from the top and an SSD of 100 cm. The collimator angle was set to 270° in order to match the TPS dose map. The simulation was performed for various simple square fields (1.6 cm to 10.4 cm) and clinical lung SBRT plans.

The MC planar dose maps were extracted from the resulting DOSXYZnrc 3ddose files at a depth of 10 cm for each beam. Similarly, the TPS dose maps were generated at the same depth with a resolution of 0.2 cm and the area of 30 cm x 30 cm. The files were then exported in ASCII format to be compared with the MC planar dose maps. The comparison was performed using MATLAB R2012a (MathWorks) after normalising the dose distribution to the maximum dose for the TPS and to the mean dose of a central 2 x 2 voxels for the MC. The central axis profiles for both axes of square fields were extracted and the values of 50% of the central dose were then recorded for each beam and referred to as the field width. Field widths for the MC and TPS were compared.

5.2.7 Verification of DOSXYZnrc Beam Arrangement Setting

Once the MLC setting was validated, the next step was verifying the beam orientation in the DOSXYZnrc input files. For this purpose, a single beam was employed using various beam arrangements by varying the gantry rotation, couch rotation, and collimator rotation angles. The different settings were applied. The first setting was varying gantry angle at a fixed couch and collimator angles. The second setting was performed at a fixed gantry and couch angles with varied collimator angles. The final setting was a combination of the gantry, the couch, and the collimator rotations.

The DOSXYZnrc polar and azimuth angles were calculated using Equations 5.6 and 5.7, respectively. The DOSXYZnrc collimator angle was calculated using Equation 5.9. The angle conversion was performed using a script written in Matlab software R2012a (MatWorks). Table 5.4 presents the conversion of the DICOM beam arrangement parameters to the DOSXYZnrc theta, phi, and phicol angles.

Table 5.4: *Test of Beam Orientation Setting*

DICOM angle settings			DOSXYZnrc angle settings		
Gantry (°)	Couch (°)	Collimator (°)	Theta (°)	Phi (°)	Phicol (°)
0	0	0	90	270	270
90	0	0	90	0	270
180	0	0	90	90	270
270	0	0	90	180	270
0	0	5	90	270	275
0	0	30	90	270	300
0	0	307	90	270	217
0	90	0	90	270	180
0	90	30	90	270	210
45	335	0	107.39	312.19	288.25
45	335	342	107.39	312.18	270.25

The plan was initially created in Pinnacle^3 TPS using a single beam with the angle settings listed in Table 5.4. The phantom was the patient phantom with the density overwritten to a unit density (water) value. The dose distribution was calculated using the CCC algorithm with a 2 mm dose grid. The plan information was exported to the DICOM standard format, including the RT plan, RT dose, and CT images. This information was then exported to the Computation Environment for Radiotherapy Research (CERR) system for further analysis.

The CT images of the patient phantom with the water density override were used to create an associated EGSPHANT for the DOSXYZnrc simulation. All voxel densities inside the skin contour were changed to be water equivalent. The phantom had a voxel size of 0.2 cm in all directions. The BEAMnrc simulation of a single beam was performed to generate the phase space file that was scored at a 55 cm distance from the source. The phase space file was then used as input in the DOSXYZnrc simulation using a different beam orientation setting, as listed in Table 5.4. The obtained 3ddose file was then normalised using the absolute dose calibration factor obtained in Section 5.2.5 to convert the MC dose to Gy/MU unit. The MC dose distribution was then exported to the CERR system. The analysis was performed by comparing both TPS dose distribution and MC dose distribution in the CERR using a gamma criteria of 3% dose difference and 3 mm distance-to-agreement [142]. Visual evaluation was also performed to verify the accuracy of the beam geometry setting.

Further verification was performed by using a combination of several beams in the same phantom. Four different settings were used, as per the beam arrangement parameters presented in Table 5.5.

Table 5.5: *DICOM Beam Arrangement Parameters of the Lung SBRT Plan used for Verification of DOSXYZnrc Beam Orientation Setting*

Beams	DICOM angle settings		
	Gantry (°)	Couch (°)	Collimator (°)
1	120	0	0
2	90	0	0
3	325	0	55
4	30	0	290
5	18	0	18
6	331	0	296
7	45	0	347
8	64	0	15
9	248	0	20
10	133	0	325

The first simulation was performed by using a combination of two coplanar beams (beam 1 and 2). The second simulation was performed by using a combination of three beams with non-zero collimator angle (beam 3 to 5). The combination of beam 1 to 5 was also investigated. The last verification setting was performed by simulating 10 beams used in the lung SBRT plans. The experiment and analysis procedures were the same as those described for the single beam experiment.

5.2.8 Recalculation of lung SBRT plans using MC simulation

Once the beam orientation was validated, the simulation was then performed to calculate the dose distribution of the clinical lung SBRT plans in the patient geometry to be compared with the TPS dose distribution. All plan parameters were the same as those used in the TPS calculation. The BEAMnrc input files were created based on the MLC position information extracted from the DICOM RT Plan file described in Section 5.2.3.1. As each plan consisted of 10 beams, a total of 200 phase space files were generated using a full MC simulation. The simulation parameters described in Section 5.2.4 were used.

The phase space file was then used as an input in the DOSXYZnrc simulation using an EGSPHANT file to represent the patient geometry, developed based on the patient CT images data set. The beam orientation parameters (theta, phi, and phicol) were converted from the extracted gantry, couch, and collimator angles from DICOM RT Plan as described in Section 5.2.3 and verified as in Section 5.2.7. The DBS variance reduction technique was selected and the radius was calculated using Equation 5.1. The voxel size used in the DOSXYZnrc simulation was 2 mm in all directions.

A 3ddose file was produced for each beam of the lung SBRT plans. These individual beam files were then combined into one 3ddose file by taking into account the weighting of each beam, which was extracted from the DICOM RTPlan file. The summed 3ddose was then calibrated to Gy/MU unit using the calibration factor described in Section 5.2.5.

5.2.9 Analysis of TPS and MC dose distributions

Analysis of the dose distributions was performed using the CERR software version 4.6 written in Matlab language [112]. The TPS dose distribution was imported to the CERR. This required that all of the plan information be in the DICOM format (CT Images, RT Structure, RT Plan, and RT Dose) to be imported to the CERR. The MC dose distribution was also imported to the CERR allowing for comparison of the dose distribution between the TPS and MC simulation.

A three-dimensional gamma analysis was performed to compare the simulated and TPS dose distributions with a pass criteria of 3% dose difference and 3 mm distance-to-agreement by including dose points larger than 10% of the maximum dose [142]. The CERR software provides an option to perform gamma evaluation for each structure outlined in the lung SBRT plans.

Both cumulative and differential dose-volume histograms (DVHs) of the PTV and OARs were generated for both TPS and MC dose distributions. The dose to the PTV, conformity index, intermediate dose spillage, and dose to OARs were derived from the cumulative DVHs. The dosimetric evaluation was performed using the criteria adopted from the RTOG 1021 trial protocol due to the similarity of the fractionation schedule used in this study and the trial, as well as the requirement for the use of heterogeneity correction in the dose calculation. Although the TROG 0902 CHISEL trial also used the same fractionation schedule (i.e., 54 Gy in three fractions), the dosimetric criteria used in this trial protocol was based on RTOG 0618, in which the dose calculation was performed without heterogeneity correction. Therefore, the criteria from the RTOG 1021 trial protocol was used in this study, instead of the TROG 0902 CHISEL trial protocol.

The important planning criteria is the coverage of the prescription isodose surface, which is specified as the volume of the PTV that received the prescribed dose (PTV_{54Gy}), as well as the PTV volume that received 90% of the prescribed dose ($PTV_{48.6Gy}$). The predefined criteria for the PTV coverage were PTV_{54Gy} >95%, and $PTV_{48.6Gy}$ >99%. The PTV volume, minimum dose, mean dose, and maximum dose to the PTV were also recorded. The conformity index (CI) was determined using Equation 5.10.

$$CI = \frac{(TV_{PTV})^2}{TV \times PIV} \tag{5.10}$$

Where TV_{PTV} was the total volume of the PTV covered by the covering isodose (54 Gy), TV was the total volume of the PTV, and PIV was the total volume of the covering isodose in the patient. The predefined criterion for the CI was ≥0.75, the value ≥0.65 was considered to be an acceptable deviation and CI ≤0.65 was unacceptable [167].

Intermediate dose spillage criteria were determined using $R_{50\%}$ and D_{2cm} parameters and applying the criteria adopted in the RTOG 1021 protocol. These parameters were used to represent the dose fall-off outside the PTV. $R_{50\%}$ was defined as the ratio of the volume of 50% of the prescription dose (i.e., 27 Gy) isodose to the PTV volume. D_{2cm} dose constraint was defined as the maximum dose received at 2 cm away from the PTV in any direction. In the RTOG 1021 protocol, D_{2cm} was specified as a percentage (%) of the prescribed dose. The guidelines for the acceptable deviation of $R_{50\%}$ and D_{2cm} criteria are presented in Table 5.6. As these parameters were relative to the PTV size, linear interpolation was performed for the PTV volume of the lung SBRT plans evaluated in this research. The absolute difference between the TPS and MC D_{2cm} value to the no deviation criteria was recorded for each plan.

Table 5.6: *Dose Spillage Guidelines from RTOG 1021*

PTV volume (cm^3)	Ratio PIV to PTV		$R_{50\%}$		D_{2cm} (% of D_{pres})		V_{20} (%)	
	Deviation		Deviation		Deviation		Deviation	
	None	Acceptable	None	Acceptable	None	Acceptable	None	Acceptable
1.8	<1.2	<1.5	<5.9	<7.5	<50.0	<57.0	<10	<15
3.8	<1.2	<1.5	<5.5	<6.5	<50.0	<57.0	<10	<15
7.4	<1.2	<1.5	<5.1	<6.0	<50.0	<58.0	<10	<15
13.2	<1.2	<1.5	<4.7	<5.8	<50.0	<58.0	<10	<15
22.0	<1.2	<1.5	<4.5	<5.5	<54.0	<63.0	<10	<15
34.0	<1.2	<1.5	<4.3	<5.3	<58.0	<68.0	<10	<15
50.0	<1.2	<1.5	<4.0	<5.0	<62.0	<77.0	<10	<15
70.0	<1.2	<1.5	<3.5	<4.8	<66.0	<86.0	<10	<15
95.0	<1.2	<1.5	<3.3	<4.4	<70.0	<89.0	<10	<15
126.0	<1.2	<1.5	<3.1	<4.0	<73.0	<91.0	<10	<15
163.0	<1.2	<1.5	<2.9	<3.7	<77.0	<94.0	<10	<15

The dose constraint to normal tissues and critical organs were also adopted from the RTOG 1021 protocol, as that trial used the same dose prescription as used in this research (i.e., 54 Gy in three fractions). These normal tissue dose constraints were also recommended by Kong et al. [3]. An exception was the dose constraints for the ribs and the chest wall. The constraints for these OARs were adopted from those used by Fitzgerald et al. [167], which was slightly higher than the constraint defined in the RTOG 1021. The reason was that the PTV volume overlapped with the chest wall structure in 10 out of 20 evaluated lung SBRT plans. Table 5.7 presents the dose constraints for the OARs.

Table 5.7: *Dose Constraints of the OARs*

Critical organs (OARs)	Constraint(s)	Endpoint (≥ Grade 3)
Combined Lungs – ITV	11.4 Gy < 1000 cm^3 10.5 Gy < 1500 cm^3	Pneumonitis Basic lung function
Oesophagus	17.7 Gy < 5 cm^3 MPD < 25.2 Gy	Stenosis/fistula
Pericardium	24 Gy < 15 cm^3 MPD < 30 Gy	pericarditis
Spinal Cord	18 Gy < 0.35 cm^3 12.3 Gy < 1.2 cm^3 MPD < 21.9 Gy	Myelitis
Brachial Plexus	20.4 Gy < 3 cm^3 MPD < 24 Gy	Neuropathy
Trachea	15 Gy < 4 cm^3 MPD < 30Gy	Stenosis/fistula
Inferior vena cava (IVC)	39 Gy < 10 cm^3 MPD < 45 Gy	Aneurysm
Superior vena cava (SVC)	39 Gy < 10 cm^3 MPD < 45Gy	Aneurysm
Aorta	39 Gy < 10 cm^3 MPD < 45 Gy	Aneurysm
Chest wall (CW)	30 Gy < 30 cm^3 (< 70 cm^3 for tumours on the CW)	
Rib	40 Gy < 5 cm^3 MPD < 50 Gy	Pain or fracture
Skin	30 Gy < 10 cm^3 MPD < 33 Gy	Ulceration

*MPD = maximum point dose (a point is defined as a volume of 0.035 cc or less)

With the exception of lung tissue, all of the OARs listed in Table 5.7 are categorised as serial tissue, as recommended by the AAPM Report TG 101 [89]. The volume-dose constraints for the serial tissues were defined as the maximum critical volume receiving the dose above the threshold dose, while for parallel tissue they were defined as the minimum critical volume receiving the dose below the threshold dose. The maximum point dose (MPD) was determined for a point with a volume of 0.035 cm^3 or less.

To determine the difference between the CCC calculation and MC simulation for each dose parameter, the relative difference *(%Diff)* was calculated using Equation 5.11, with the MC as the reference. D_{CCC} represents the dose parameter calculated by the CCC and D_{MC} represents the dose parameter calculated by the MC. An average relative difference was calculated from 20 plans.

$$\%Diff = \frac{(D_{CCC} - D_{MC})}{D_{MC}} \times 100\% \tag{5.11}$$

5.2.10 Statistical Analysis

Statistical analysis was performed to evaluate whether the dose calculation by the CCC algorithm differed significantly from the dose calculation by the MC simulation. A normality test was first performed to evaluate the distribution of dosimetric parameters for the CCC and MC dose distributions. A paired student t-test was performed for normally distributed data using a 95% confidence interval. The data that was not satisfied the requirement for t-test was then performed for normally distributed data using a 95% confidence interval. The data that did not satisfy the requirement for t-test was evaluated using a related sample Wilcoxon test. The Bland-Altman test was performed to calculate the lower and upper levels of agreement between the CCC and MC calculations. The difference was considered to be significant for a P-value of <0.05. The statistical analysis was performed using SPSS software version 23.

5.3 RESULTS

5.3.1 Verification of MLCQ aperture setting

Comparison of the planar dose maps in water between the MC simulation and the TPS allowed for the verification of the leaf position setting used in the MC model. Table 5.8 shows the average field width difference of the square fields between the TPS and MC simulation. Overall, the difference was less than 1 mm, which is within the accepted tolerance (2 mm).

Table 5.8: *The Average Field Width Difference for all Simulated Plans*

Treatment field	Number of beams	Average X-axis field width difference (mm)	Average Y-axis field width difference (mm)
Square Fields	6	0.46 ± 0.28	0.31 ± 0.24
Lung RT Plan 1	10	0.08 ± 0.04	0.28 ± 0.14
Lung RT Plan 2	10	0.34 ± 0.15	0.40 ± 0.13
Lung RT Plan 3	10	0.23 ± 0.19	0.15 ± 0.11
Lung RT Plan 4	10	0.23 ± 0.12	0.21 ± 0.18
Lung RT Plan 5	10	0.30 ± 0.15	0.13 ± 0.11
Lung RT Plan 6	10	0.44 ± 0.25	0.26 ± 0.16

The dose map comparison for the simple square fields shows that the MC simulation agreed well with the TPS (Figure 5.4), as indicated by the difference of the field width (the width of 50% of the relative dose of lateral dose profile) of less than 1 mm both in the X and Y axes. It was found that the field width difference increased with an increase in the field size.

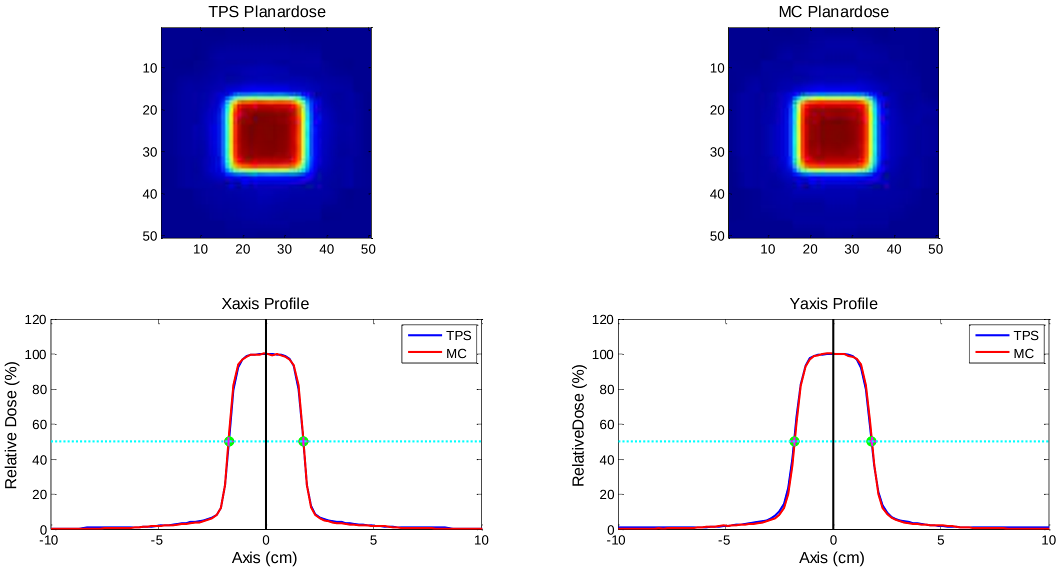

Figure 5.4. The planar dose maps of the TPS and MC of 3.2 cm x 3.2 cm.

However, further comparison of the MC and TPS profiles away from the central axis of lung SBRT treatment fields revealed some differences due to MLCQ positioning errors. This mainly occurred for cases where the leaves travelled across the beam axis toward the opposing leaf bank. In the Beam Modulator, leaves are located in a paired leaf bank, right and left leaf banks. Each leaf bank consists of 40 leaves, which are able to interdigitate, crossing the beam axis. A difference was observed in the leaf positions between the TPS, DICOM, and BEAMnrc systems. In the TPS, if leaves move away from the beam axis in their own leaf bank, the leaf will have a positive sign independent of the leaf bank in which the leaves are located. The leaves will have a negative sign if they are required to travel towards the opposing leaf bank, crossing the beam axis. DICOM defines the leaf bank as a negative leaf bank (X1) and positive leaf bank (X2). Therefore, the leaves in the negative leaf bank will have a negative sign if they move in their own leaf bank and will be positive if moving toward the positive leaf bank and vice versa. Ignoring this difference in convention causes an error during the leaf position conversion from the DICOM to the BEAMnrc input files.

For the clinical lung RT plans, the water planar dose map comparison also revealed two further types of errors. The first error was associated with an error in extracting the MLC information from the DICOM file (RT Plan.dcm). This caused an MLC positioning error in all leaf settings. The correction was performed in the Matlab scripts used for extracting the MLC position information. A manual check was performed by direct comparison of the leaf position between the Pinnacle^3 user interface screen and the extracted leaf position from the DICOM files. Figure 5.5 shows an example of this error type and the results of the correction.

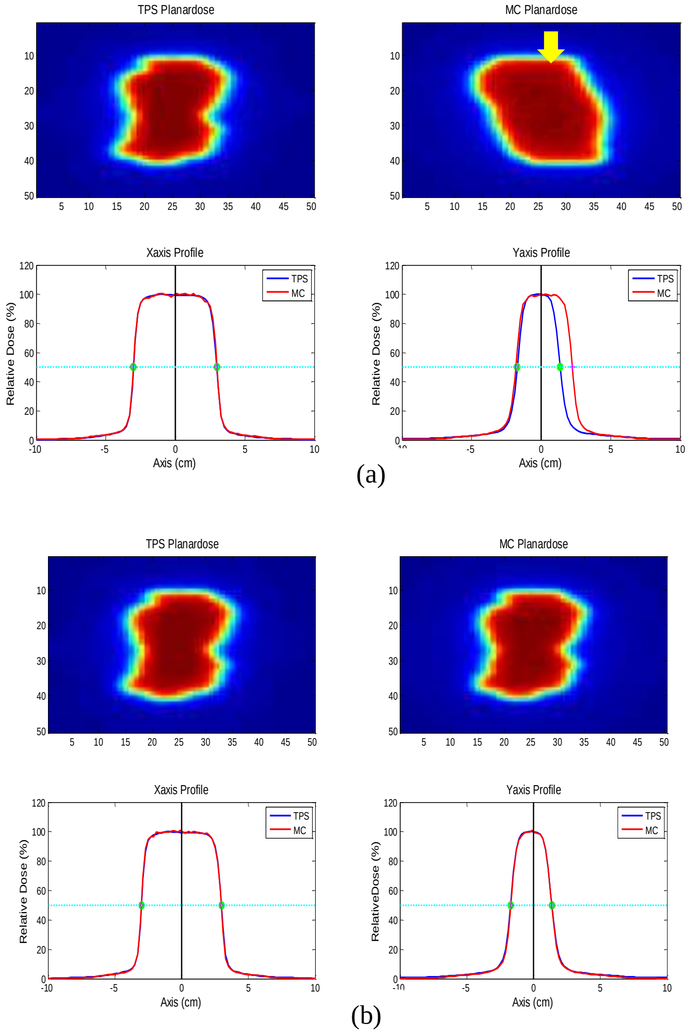

Figure 5.5. Planar dose map comparison of the lung RT plan 3 showing an error during MLC position extraction from the DICOM file (a). The correct dose map (b) was obtained after correcting the scripts used for the extraction.

The second type of error was associated with an error in converting the extracted MLC position to the BEAMnrc MLCQ leaf settings used to generate the phase space file. The errors occurred for the leaves that travelled toward the opposing leaf bank, crossing the beam axis (Figure 5.6a). This is because, in Equation 4.4 (Section 4.2.9) the radius of nominal field size (W) was taken to be an absolute value, ignoring the sign convention as described previously. By taking into account the positive or negative sign, depending on which leaf bank the leaves were located, the conversion gave the correct MLC position (Figure 5.6b). A manual check for this was performed by checking the BEAMnrc input file using a GUI, previewing the MLC setting and visually comparing it with the TPS planar dose map. Once the MLCQ preview in the

BEAMnrc GUI was matched with the TPS planar dose map, the DOSXYZnrc simulation was performed to obtain the MC planar dose map.

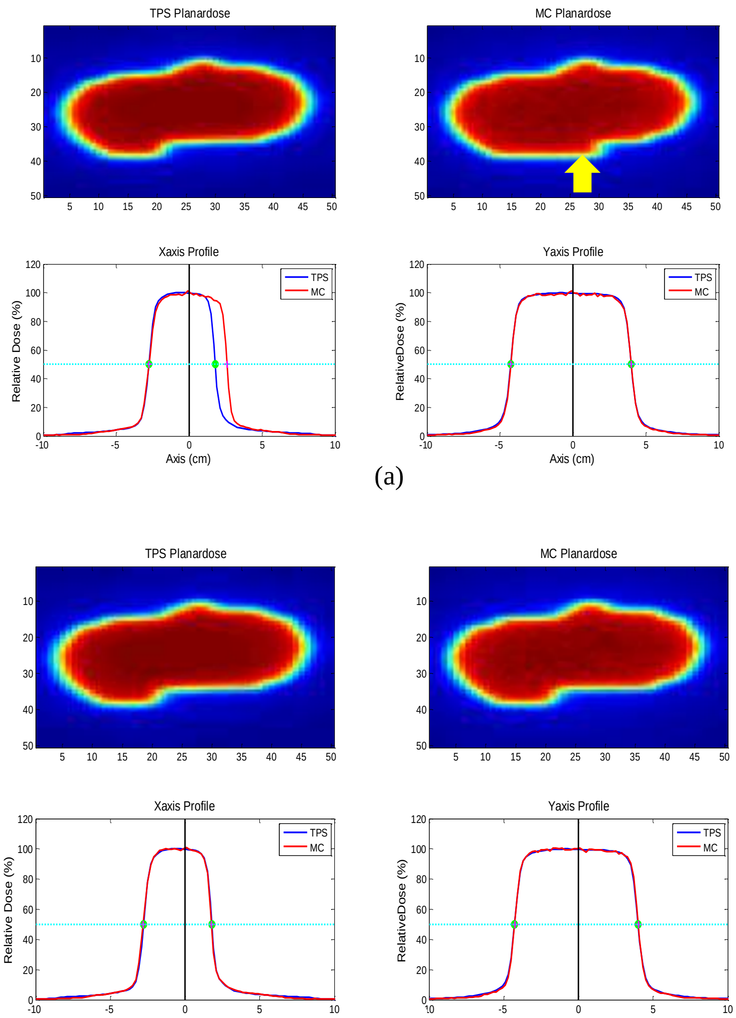

(a)

(b)

Figure 5.6. Comparison of the TPS and MC planar dose maps of the lung RT plan 5 showing an MLC positioning error in the simulated dose map (a) and after correction (b).

This work shows that the water planar dose map check is useful for quick visual detection of an MLC positioning error and to quantify the error that might occur during the extraction of the MLC information from the DICOM file and their conversion to the MLCQ opening setting used for the BEAMnrc simulation.

5.3.2 Verification of Beam Arrangement Setting

Although the previous section demonstrated the validity of the leaf position setting in the planar dose-to-water map comparison, the comparison of the simulated and TPS dose distributions showed a mismatch when the DOSXYZnrc beam arrangements were calculated using the formula described by Zhan *et al.* [171]. This difference is shown in Figure 5.7, and is possibly due to an incorrect beam orientation setting. It is shown that the beam orientation of the simulated dose distribution for the coplanar beam (Figure 5.7b) was flipped by 180° from the planned dose distribution (Figure 5.7a). Red and yellow arrows indicate the difference of the beam orientation of the coplanar beams used in the plans.

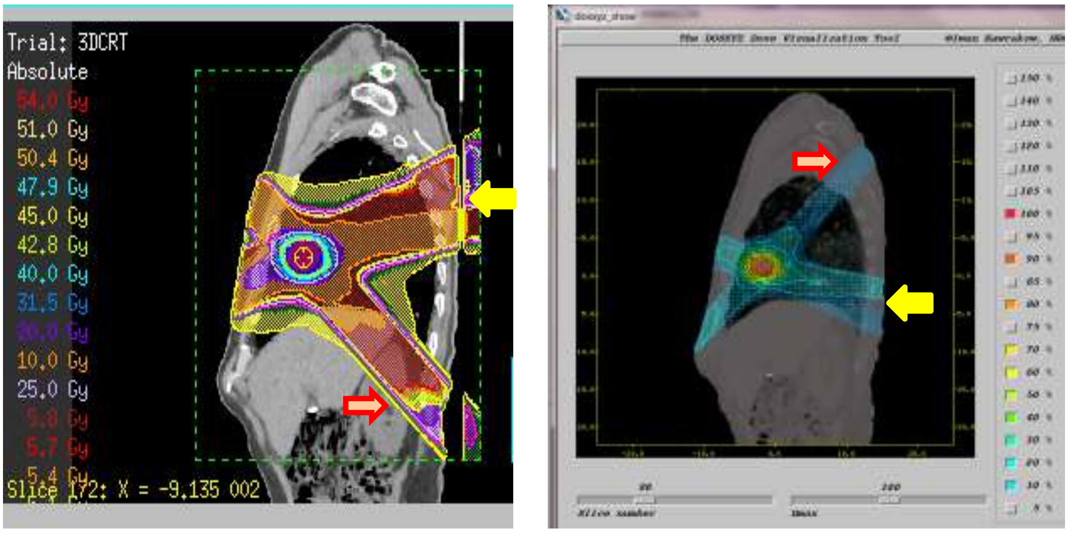

(a) (b)

Figure 5.7. The sagittal view of the TPS dose distribution displayed in the Pinnacle^3 RTPS (a) and the MC dose distribution displayed in DOSXYZ show (b) for one lung SBRT plan. Red and yellow arrows indicated a mismatch of the beam orientation used in the MC simulation.

The modification of the DOSXYZnrc beam orientations was performed by recalculating the polar and azimuth angles using Equations 5.6 and 5.7, as described by Thebaut and Zavgorodni [169], and the DOSXYZ collimator angle using Equation 5.9, as described by Crowe [157]. The result of recalculating the beam arrangement parameters for one of the SABR plans is shown in Figure 5.8. It seems that the polar and azimuth angles were correct, but the collimator angle was incorrect. The simulated coplanar beams are shown to be wider than the planned beams. This resulted in a difference in the shape of the high dose region indicated as a pink colour wash in Figure 5.8, which associated with the dose received by PTV.

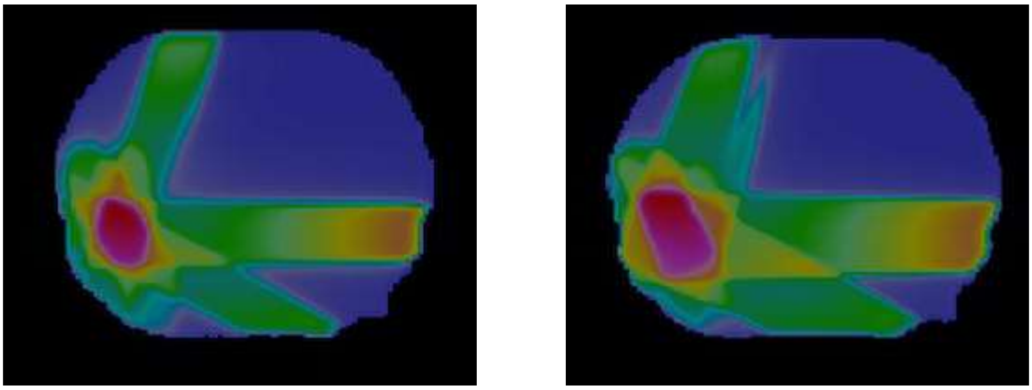

(a) TPS (b) Monte Carlo

Figure 5.8. The comparison of TPS dose distribution (a) and simulated dose distribution (b) in the transversal plane. The plan consisted of five beams (a combination of coplanar and non-coplanar beams). The two dose distributions show different shapes, indicating the incorrect setting of the beam orientation.

As each of the SABR plans consisted of a 10 beam configuration, it was difficult to identify whether the error originated from a single beam or from all beams. It should be noted that each plan had a combination of coplanar and non-coplanar beams. Therefore, an investigation was performed for a single beam using various beam orientation settings described in Section 5.2.7 to investigate whether the error came from incorrect calculations of the polar angle, azimuth angle, or phicol angle.

Figure 5.9 shows the coronal view of the TPS and simulated dose distribution of a single beam using three different beam orientation settings. Figure 5.9a and b show the dose distribution of zeroed setting, in which no rotation was made for the gantry, the couch, and the collimator. The difference in orientation was observed in the simulated dose distribution. Similar differences in orientations were also observed for two other beam orientations: the gantry angle of 0°, the couch angle of 90°, and the collimator angle of 30° (Figure 5.9c and d); and the gantry angle of 45°, the couch angle of 335°, the collimator angle of 342° (Figure 5.9e and f).

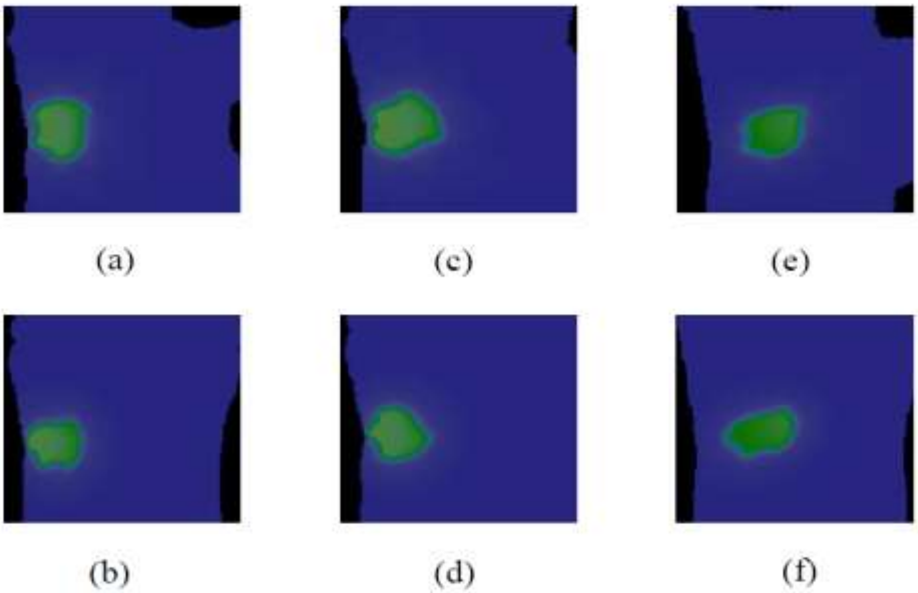
(a) (c) (e)

(b) (d) (f)

Figure 5.9. The TPS (top) and MC (bottom) dose distributions using different beam arrangement settings: (a) and (b) beam settings are G0T0C0, (c) and (d) beam settings are G0T90C30, (e) and (f) beam settings are G45T335C342. G is for gantry angle, T is for couch (patient table) angle, and C is for collimator angle.

When two coplanar beams were combined, this incorrect calculation was represented as a wider field in the MC dose distribution, as shown in Figure 5.10b. It seems that the polar and azimuth angles calculations were correct, but the collimator angle calculation was incorrect.

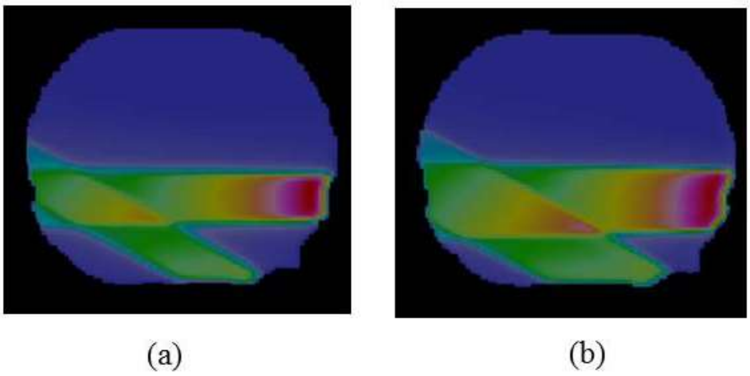
(a) (b)

Figure 5.10. Comparison of TPS (a) and MC (b) dose distribution from a combination of two coplanar beams in water phantom (no couch table and collimator rotations).

Further rotation of the DOSXYZnrc collimator angle by 90° clockwise resulted in a correct orientation of the top and bottom leaf settings; however, the orientation of the left and right leaf setting remained incorrect (Figure 5.11c). Inverting the leaf pair position from the left to the right and vice versa was required to obtain the correct dose distribution (Figure 5.11d).

(a) TPS (b) MCDTK

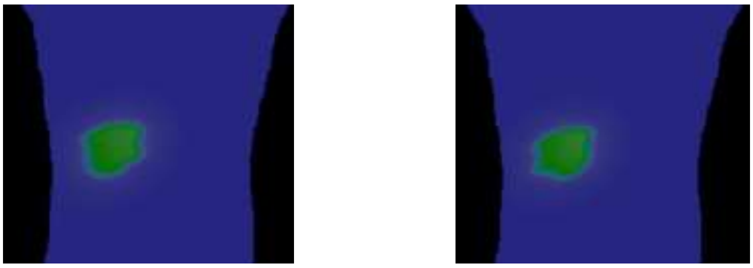

(c) MCDTK + 90 (d) MCDTK+90+inverted leaf bank

Figure 5.11. TPS dose distribution (a) and MC dose distribution calculated using equation 5.9 (b). Correction of the DOSXYZnrc collimator setting was achieved by adding 90° to Equation 5.9 (c) and changing the leaf pair position between the left and right leaf banks (d).

Another approach that can be used to correct the calculation of the DOSXYZnrc collimator setting is by changing the leaf orientation used in the BEAMnrc model from parallel to the Y-axis, to parallel to the X-axis. However, as the previously commissioned linear accelerator model had a leaf orientation parallel to the Y-axis, the previous approach was adopted in this work. As a consequence, it was necessary to modify the BEAMnrc input files of the lung SBRT plans to take into account the correct beam orientation and leaf bank settings.

A further test was performed on the water phantom for several beam combinations. The phantom was derived from the patient phantom but the density within the skin contour was set to the density of water. Four different settings were evaluated: a combination of two coplanar beams (beams 1 and 2), a combination of three non-coplanar beams (beams 3 to 5), a combination of coplanar and non-coplanar beams (beams 1 to 5), and a combination of 10 beams, as used in the actual lung SBRT plans, as described in Section 5.2.7. The conversion of the DICOM beam orientation settings to DOSXYZnrc beam orientation settings after applying the correction is given in Table 5.9.

Table 5.9: *Beam Arrangement Parameters of the Evaluated Plans in Water Phantom*

Beam	Gantry (°)	Collimator (°)	Couch (°)	Theta (°)	Phi (°)	Phicol (°)
1	120	0	0	90.00	30.00	0.00
2	90	0	0	90.00	360.00	0.00
3	325	0	55	118.02	248.12	310.52
4	30	0	290	118.02	281.17	67.20
5	18	0	18	84.52	287.17	342.83
6	331	0	296	64.17	256.34	60.85
7	45	0	347	99.15	314.26	9.27
8	64	0	15	76.55	333.21	353.30
9	248	0	20	108.49	156.73	7.76
10	133	0	325	114.80	48.70	334.47

The results of the combination of coplanar beams and the combination of 10 beams are presented in Figure 5.12. The visual evaluation of dose distribution shows that the beam orientations used in the DOSXYZnrc simulation were in agreement with the TPS dose distribution.

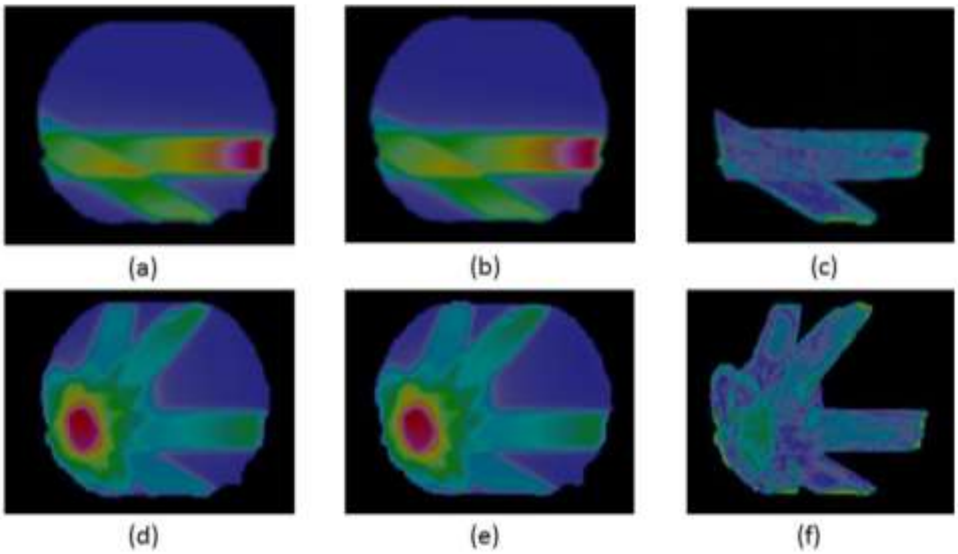

Figure 5.12. The TPS dose distribution (left), the MC dose distribution (middle), and gamma dose distribution 3% 3 mm (right) for coplanar beams (top) and for ten beams of lung SBRT plan (bottom). Good agreement was obtained after correction of the DOSXYZnrc beam orientation setting.

The dose profile comparison between the MC and TPS dose distributions shows good agreement, with a dose difference within 2% when all tissue densities within the skin contour were changed to water density, as shown in Figure 5.13. The agreement is also observed in the high dose gradient region, indicating that both algorithms accurately predicted the dose in a homogenous media with a unity density.

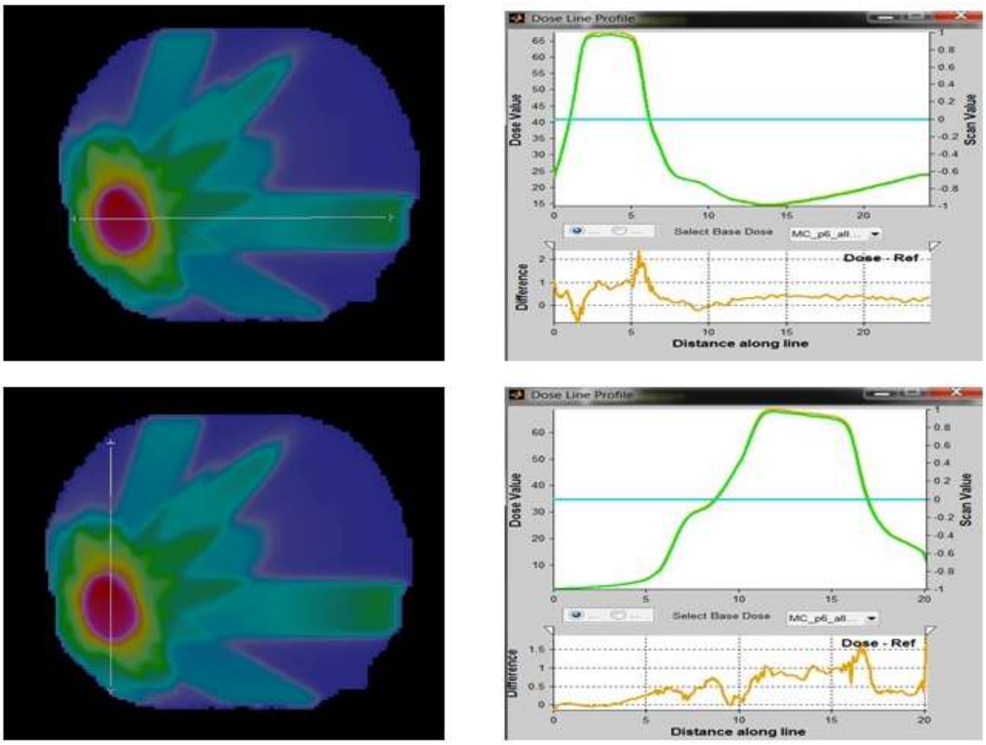

*Figure 5.13.*The dose profiles in the X axis (top) and Y axis (bottom) of the indicated white lines in the axial view of the TPS and MC dose distributions. The green and brown lines in the dose profile window show the dose profiles of the Monte Carlo simulation and TPS calculation, respectively. Good agreement was obtained in both low and high dose gradients.

5.3.3 Recalculation of lung SBRT plans using MC simulation

Previous sections demonstrated the validity of the MLC position setting and beam orientation setting used in the MC input files. The calculation of the CCC algorithm and the MC were also shown to agree to within ±2% in a homogenous media by changing the patient tissue density to water density. The next section presents the results of the dosimetric comparison between the CCC and MC calculation of the lung patient SBRT plans.

PTV characteristics

The PTV characteristics of the lung SBRT plans evaluated in this research are presented in Table 5.10.

Table 5.10: *The PTV Characteristics of the Lung Patient SBRT Plans*

Parameters	Value
Range	18.48 – 83.80 cm^3
Median value	29.42 cm^3
Mean value	36.58 cm^3
PTV volume < 50 cm^3	80%
Range	18.48 – 36.05 cm^3
Median	25.94 cm^3
Mean	26.66 cm^3
PTV volume > 50 cm^3	20%
Range	67.14 – 83.80 cm^3
Median	76.98 cm^3
Mean	76.22 cm^3
Parameters	Value
Right/Left location	14/6
Upper/Lower	14/6
Anterior/Posterior	4/16
PTV overlapped chest wall	10

The median PTV volume was 29.42 cm^3 (range 18.48 to 83.80 cm^3). The results indicate that 80% (16 out of 20) of the studied plans had a PTV volume less than 50 cm^3, and the remaining 20% had a PTV volume larger than 50 cm^3. The proportion of the tumours located on the right and left lungs was 70% and 30%, respectively. The majority of the tumours were located at the upper lobar (70%) and at the posterior side (80%). The PTV structure overlapped the chest wall in ten plans.

Comparison of the CCC and MC 3D dose distributions and cumulative dose-volume histograms (DVHs)

The evaluation of the CCC dose distribution relative to the MC dose distribution shows three general trends for the cumulative DVH of the PTV. The first trend was the similarity of the cumulative DVH shape of the PTV between the CCC and the MC dose distribution observed in nine out of 20 plans. Figure 5.14 shows this similarity in one plan (plan 20). The PTV volume for this plan was 32.22 cm^3 and located at the upper lobar of left. The quantitative analysis of the PTV coverage of the prescribed isodose (i.e., 54 Gy) shows that the coverage calculated by the CCC was slightly higher than that calculated by the MC, 95.08% and 94.40%, for the CCC and MC respectively.

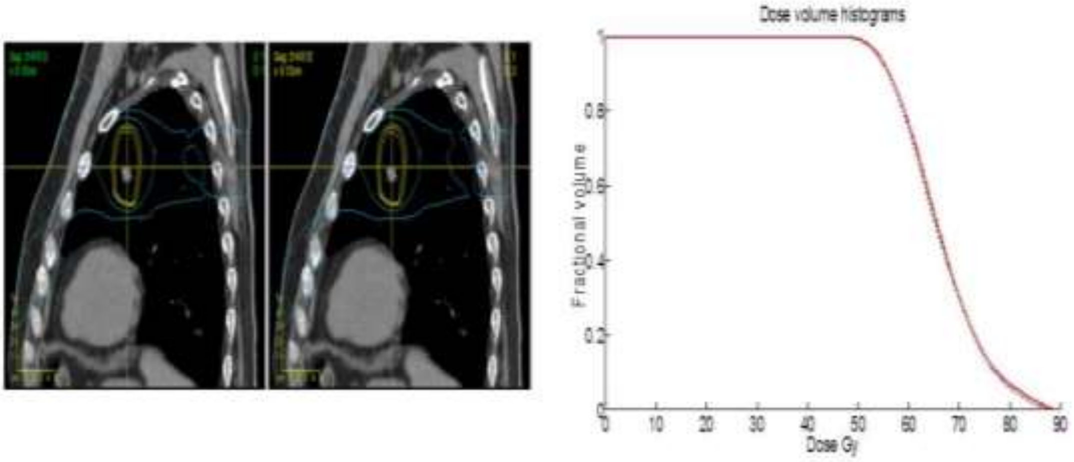

Figure 5.14. The dose distribution of one lung SBRT plan in the sagittal plane of the CCC calculation (left) and the MC simulation (right). The cumulative DVH to the PTV of the CCC (solid line) and MC (dashed line) is very similar. The isodose lines from the outer to inner lines represent the dose of 13.5 Gy (25%), 27 Gy (50%), 48.6 Gy (90%), 54 Gy (100%), and 59.6 Gy (110%).

The second trend was the overestimation of the PTV dose by the CCC algorithms observed in six plans (plans 6, 7, 8, 12, 13 and 14). Two of these plans (plan 6 and plan 12) had a PTV size of >50 cm^3. Figures 5.15 and 5.16 show the overestimation of the PTV dose in plan 12. This plan had a PTV volume of 67.14 cm^3 and the tumour was located at left lower lobar. The PTV_{54Gy} coverage calculated by the CCC was 93.38% for this plan, while the MC calculation only resulted in the PTV_{54Gy} coverage of 88.23%. There was a difference of 5.84% relative to the MC calculation. As shown in Figure 5.16, the dose-volume parameters to the rib structures calculated by the CCC were higher than those calculated by the MC. While the cumulative DVHs for the left lung and combined lungs were similar between the CCC and MC calculations.

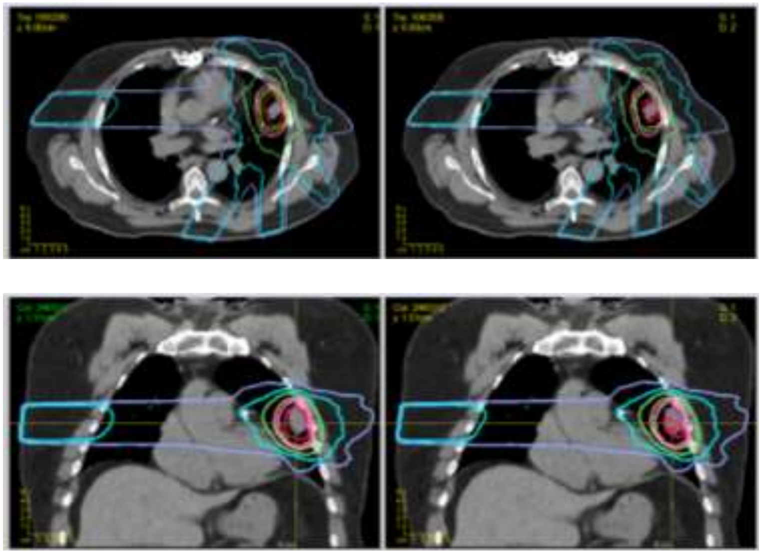

Figure 5.15. The dose distribution of the CCC (left figures) and MC calculations (right figures) in the plan with a large PTV volume. The isodose lines represented 110% (red), 100% (pink), 90% (orange), 50% (green), 25% (blue), and 10% (violet).

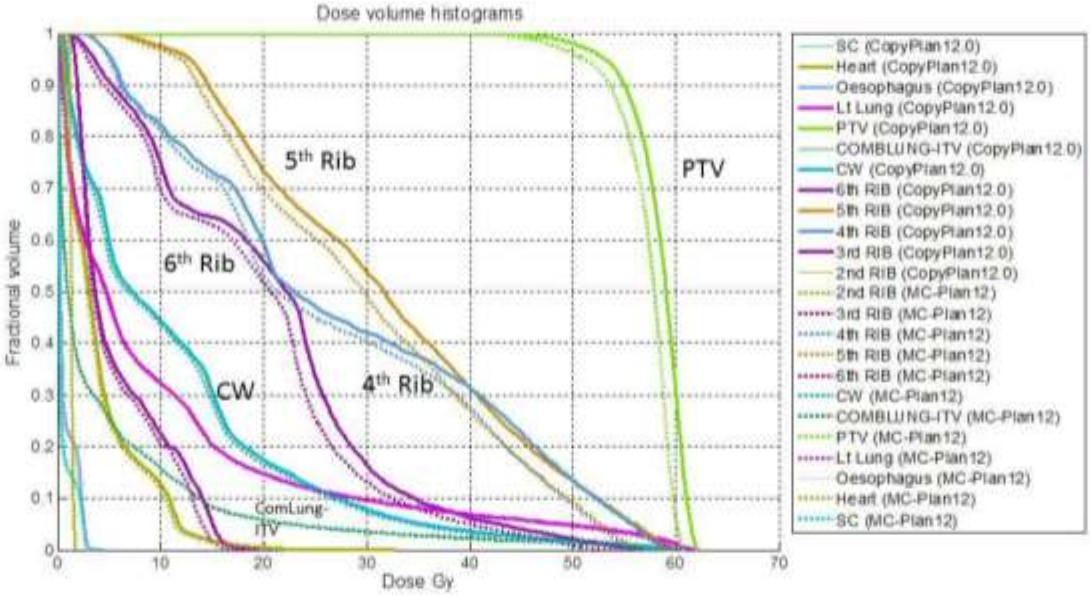

Figure 5.16. Cumulative DVH of the SBRT plan 12 which had a large PTV volume. The CCC (solid line) overestimated the dose to the PTV and organ at risk. Interestingly, the DVHs for the left lung (violet line) and the combined lungs (green line) were very similar between the CCC and the MC calculations.

The third trend was the underestimation of the PTV dose by the CCC algorithms observed in five plans (plans 1, 2, 3, 10 and 11), which had a PTV size between 20-40 cm^3. Figure 5.17 shows this underestimation observed in plan 1. This plan had a PTV volume of 27.00 cm^3. The PTV_{54Gy} coverage calculated by the CCC (92.49%) differed by 5.23% relative to the PTV_{54Gy} coverage calculated by the MC (97.60%).

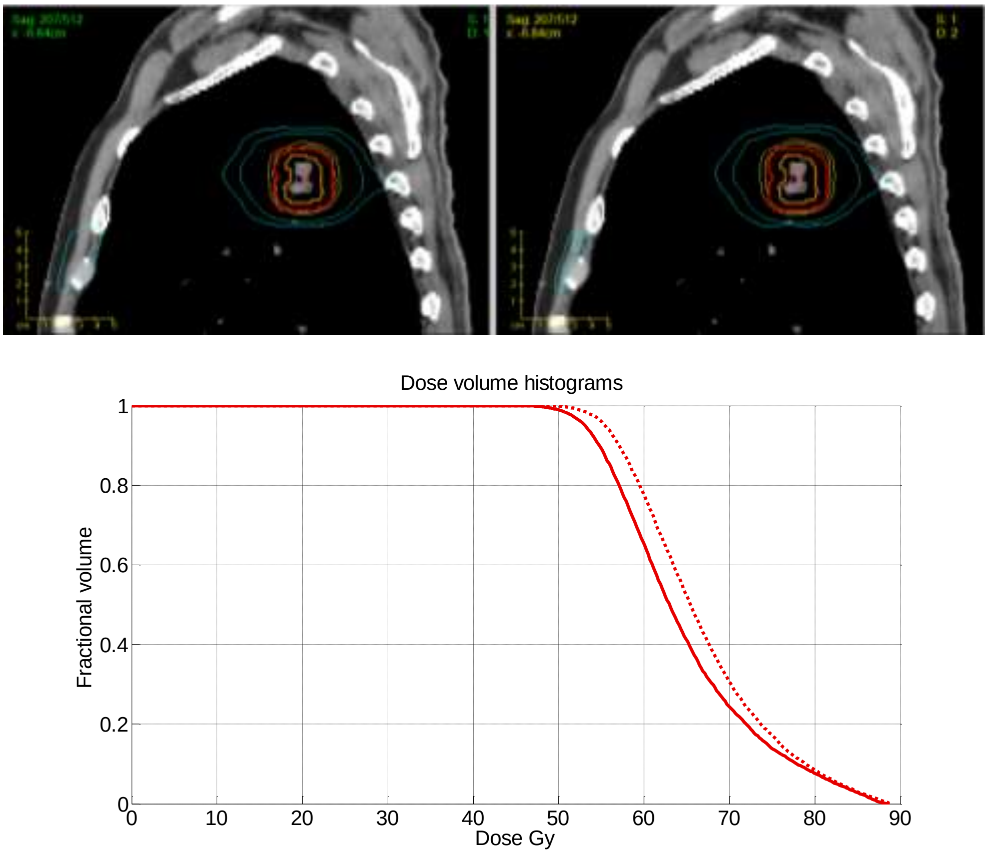

Figure 5.17. The top figure is the isodose distribution calculated by the CCC (top left) and by the MC (top right) for plan 1. The bright red colour indicates the PTV contour, while the yellow colour indicates the ITV contour. The cumulative DVH to the PTV (bottom figure) shows an underestimation of the dose to the PTV by the CCC algorithm of 5.23% relative to the MC calculation.

The quantitative analysis of the dose distribution and dose-volume parameters to the PTV and OARs are presented in the following subsections.

Gamma Analysis

To obtain a quantitative comparison between the CCC and MC dose distributions, a 3D gamma analysis was performed using a 3% dose difference and 3 mm DTA criteria. The use of tighter criteria was also investigated using a 2% dose difference and 2 mm DTA.

The results show that the average passing rate of the PTV using the selection criteria of 3%, 3 mm was 99.08% (93.70-100%) and decreased to 91.86% (59.86-99.53%) when tighter criteria of 2%, 2 mm were used (Figure 5.18). The significant decrease in the passing rate was observed for plan 1 (by 33.84%), which resulted in only about 60% of the dose points passing the selection.

The passing rate for the combined lung (minus ITV) and chest wall was >99% for both selection criteria, although the passing rate decreased slightly when calculated using the 2%, 2 mm criteria; however, the difference was relatively small (less than 1%). The passing rates for other OARs (spinal cord, heart/pericardium, great vessels, trachea, oesophagus, and aorta) were >99% for both defined selection criteria, in which almost all points passed the selection when the 3%, 3 mm criteria were used.

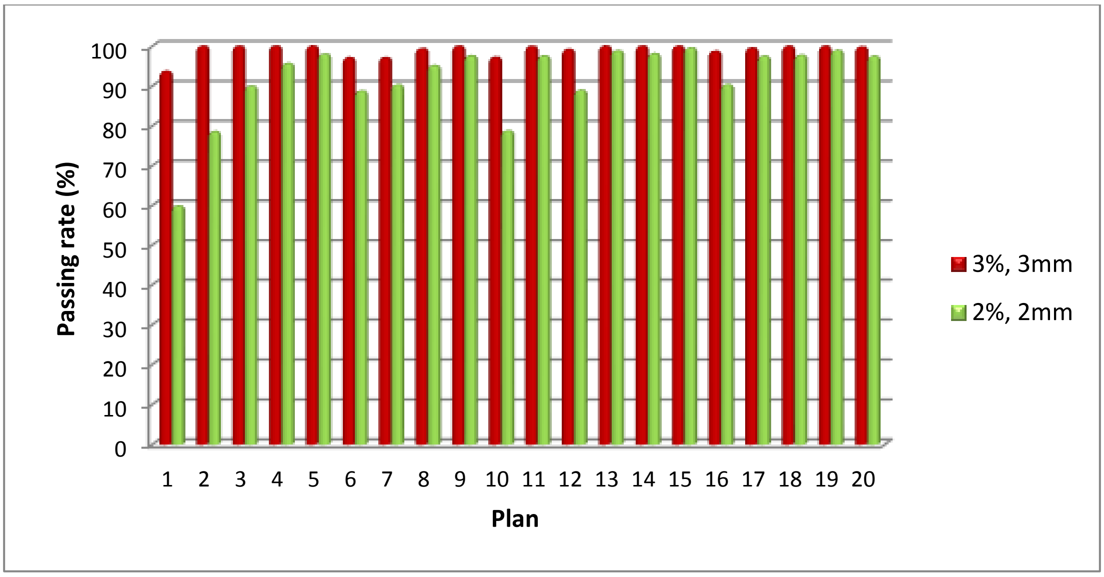

Figure 5.18. The passing rate of 3D gamma analysis for the PTV structure using selection criteria of 3%, 3 mm (red) and 2%, 2 mm (green). Reduction in the passing rate was observed after tightening the criteria to 2%, 2 mm.

5.3.4 Dosimetric parameters to the PTV

Table 5.11 presents the mean values of the PTV coverage, maximum, mean, and minimum dose to the PTV and conformity index of the evaluated lung SBRT plan and the P-value obtained from a paired student t-test. The results show that there was no significant difference of the dosimetric parameters to the PTV between the CCC and MC calculations for all twenty lung SBRT plans, with the exception of the maximum dose received by the PTV (D_{max} PTV) and the conformity index (CI).

Table 5.11: *Mean Values of the Dosimetric Parameters to the PTV and Conformity Index of All Lung SBRT Plans*

Parameters	CCC	MC	Relative difference (%)*	P-value
	Mean ± sd	Mean ± sd		
PTV_{54Gy} (%)	95.13±1.62	95.14±2.67	0.04 (-5.23 - 5.84)	0.97
$PTV_{48.6Gy}$ (%)	99.50±0.44	99.26±0.87	0.25 (-0.89 - 1.60)	0.07
D_{min} PTV (Gy)	44.51±3.44	43.85±4.46	1.81 (-4.79 -8.55)	0.12
D_{mean} PTV (Gy)	64.72±3.88	64.69±4.25	0.09 (-3.12 - 2.28)	0.89
D_{max} PTV (Gy)	79.41±10.43	78.89±10.73	0.73 (-0.91 - 2.08)	0.005
CI	0.814±0.035	0.807±0.038	0.97 (-1.98 - 3.73)	0.02

* The value is given as mean relative difference and range value (within the bracket)

PTV coverage of prescribed surface isodoses

CCC vs MC

There was no significant difference in the PTV_{54Gy} coverage between the CCC and MC calculations (p=0.97). However, the CCC overestimated the PTV_{54Gy} coverage in 11 plans, with an average overestimation of 1.52% (0.13-5.15%). The average underestimation of the PTV_{54Gy} coverage in nine plans was -1.95% (-0.42% to -5.23%). Overall, the agreement of the PTV_{54Gy} was within ±6%. However, it should be noted that the difference >5% was only observed in two plans (i.e., plan 1 and plan 12), while the remaining 18 plans had an agreement to within ±5%. The lower and upper levels of agreement calculated using Bland-Altman test were 4.82% and 4.89%, respectively.

Similarly, there was no significant difference in the $PTV_{48.6Gy}$ coverage between the CCC and MC calculations (p=0.07). However, better agreement of <2% was achieved for the $PTV_{48.6Gy}$ coverage compared to the PTV_{54Gy} coverage. The Bland-Altman test resulted in a narrower range of a lower and upper limit of agreement of -0.90% and 1.40%, indicating good agreement between the CCC and MC calculations. It was found that the CCC overestimated the $PTV_{48.6Gy}$ coverage in 14 plans, with an average overestimation of 0.52% (0–1.60%) and underestimated in the remaining six plans, with an average value of -0.29% (-0.07% to -0.89%). This indicates that 90% of the prescribed dose could be delivered to the target.

Deviation from the RTOG 1021 criteria

Figure 5.19 shows the PTV_{54Gy} coverage for the twenty evaluated lung SBRT plans from the CCC and MC calculations. The CCC calculation shows that eight plans met the requirement of more than 95% of the PTV volume receiving 100% of the prescribed dose (i.e. PTV_{54Gy} >95%), nine plans had PTV_{54Gy} coverage of >94% and only three plans had PTV_{54Gy} coverage <94%. The recalculation of the plans using the Monte Carlo simulation shows that 11 plans met the requirement of the PTV_{54Gy} coverage. For the rest of the plans, only one plan had a deviation of >5% from the RTOG 1021 criteria, which was observed in plan 12. The requirement was slightly harder to fulfil for this plan, in which only 88.23% of the PTV volume received the prescribed dose.

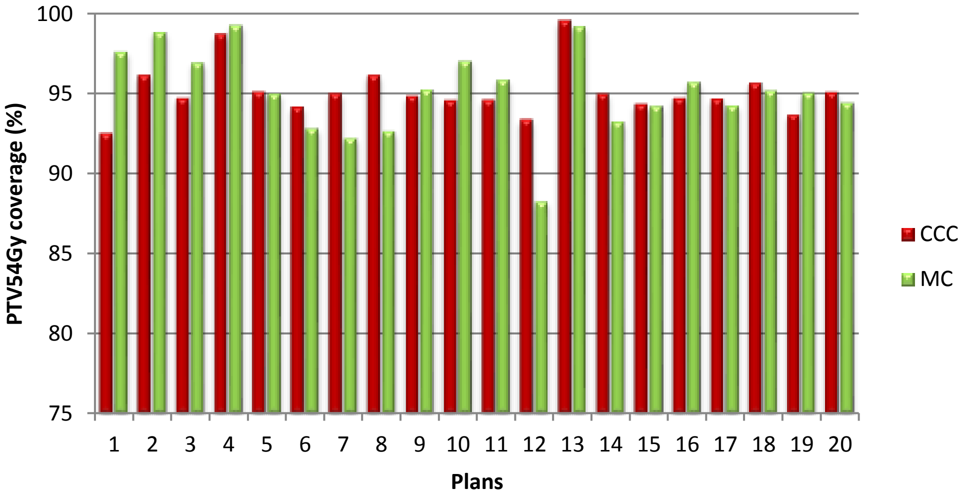

Figure 5.19. The PTV coverage of prescribed dose (PTV_{54Gy}) of the CCC (red bar) and MC (green bar). The lowest PTV_{54Gy} coverage was observed in plan 12 when recalculated using the MC simulation. Less than 90% of the PTV volume received the prescribed isodose for this plan.

The evaluation of $PTV_{48.6Gy}$ coverage shows that 15 plans calculated using the CCC algorithms met the objective of more than 99% of the PTV volume receiving 90% of the prescribed dose. The other five plans had $PTV_{48.6Gy}$ coverage of >98.5%, which was still close to the required coverage. However, the recalculation using the MC simulation shows that the $PTV_{48.6Gy}$ coverage in six plans was slightly lower, about 97%. The lowest $PTV_{48.6Gy}$ coverage was found in plan 12, which had a relatively large

PTV volume (67.14 cm^3) and the PTV structure overlapped the chest wall. This plan also had the lowest PTV$_{54y}$ coverage. Table 5.12 presents the number of the CCC and MC plans that deviated from the RTOG 1021 PTV coverage criteria. This indicates that the majority of the plans fulfilled the PTV$_{48.6Gy}$ criteria; however, it was more difficult to fulfil the PTV$_{54Gy}$ criteria, especially for the CCC plans.

Table 5.12: *The deviations of the CCC and MC plans from the PTV coverage criteria outlined in the RTOG 1021 protocol*

Deviation from protocol	PTV$_{54Gy}$		PTV$_{48.6Gy}$	
	CCC	MC	TPS	MC
None	8 plans	11 plans	15 plans	14 plans
< 2%	11 plans	5 plans	5 plans	6 plans
2 – 5%	1 plan	3 plans	-	-
>5%	-	1 plan	-	-
Average deviation (%)	0.13 (-2.64 – 4.77)	0.15 (-7.13 – 4.5)	0.51 (-0.24 – 1.01)	0.26 (-1.65 – 1.01)

PTV volume vs PTV coverage

The plot of the PTV volume against PTV$_{54Gy}$ coverage shows that the coverage for the larger tumour was slightly below the prescribed, while most of the smaller tumours met the required coverage, as shown in Figure 5.20.

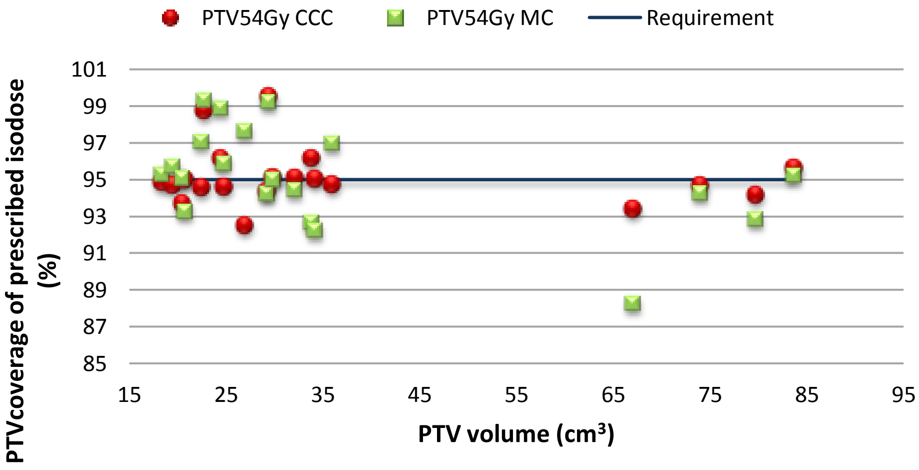

Figure 5.20. The relationship between the PTV volume and PTV$_{54Gy}$ coverage. The large PTV volume tended to have a PTV$_{54Gy}$ coverage less than the requirement of 95%, while plans with a lower PTV volume tended to fulfil the requirement of PTV$_{54Gy}$ coverage.

PTV D_{min}, D_{mean}, and D_{max}

Although there was no significant difference in the minimum dose (D_{min}) received by the PTV (p=0.12), the CCC overestimated the D_{min} of the PTV in 13 plans. The difference in the D_{min} between the CCC and MC calculations ranged from -4.79% to 8.55%. The largest difference was found in plan 17, which had a PTV volume of 74.10 cm^3 and was located close to the chest wall. The overestimation of the CCC calculation relative to the MC calculation was also found in the mean dose to the PTV (D_{mean}) in 11 plans and the maximum dose to the PTV (D_{max}) in 15 plans. The average differences of the D_{mean} and the D_{max} calculations were ±3.12% and ±2.08%, respectively. Table 5.13 presents the mean relative difference and lower and upper levels of agreement (95% confidence interval) between the CCC and MC calculations.

Table 5.13: *Mean Relative Difference and Lower and Upper Levels of Agreement of the Dosimetric Parameters to the PTV Between the CCC and MC Calculations*

Parameters	Mean Relative Difference (%)	SD of relative difference (%)	Lower LOA (%)	Upper LOA (%)
PTV_{54Gy}	0.04	2.48	-4.82	4.89
$PTV_{48.6Gy}$	0.25	0.59	-0.90	1.40
PTV D_{min}	1.81	4.17	-6.37	9.98
PTV D_{mean}	0.09	1.42	-2.69	2.86
PTV D_{max}	0.73	0.95	-1.13	2.58
CI	0.97	1.58	-2.12	4.06

SD = standard deviation, LOA = level of agreement

Conformity Index (CI)

There was a significant difference in the CI calculated by the CCC (mean = 0.814, sd = 0.035) and the MC (mean = 0.807, sd = 0.038), p = 0.019. Although the difference was statistically significant, it was not clinically significant, as most of the plans fulfilled the CI index criteria of >0.75. An exception was plan 10, in which the CI index was lower than the desired criteria for both the CCC (0.72) and the MC calculations (0.69). However, these values were considered to be within an acceptable deviation (>0.65). The agreement in the CI between the CCC and MC calculation was between ±2% in 17 plans, with only three plans having a difference of >3%. In most of the plans, the CI calculated by the CCC was higher than that calculated by the MC simulation, with a maximum difference of 3.73%. The lower and upper levels of agreement for the CI between the CCC and MC were -2.12% to 4.06%, respectively. As the desired CI criterion was fulfilled in most plans, this indicates that the beam arrangements used in the lung SBRT plans satisfied the plan conformity requirement.

Intermediate dose spillage

The results presented in Table 5.14 show that there was no significant difference in the intermediate dose spillage constraints ($R_{50\%}$ and D_{2cm}) between the CCC and MC calculations, with p-values of 0.45 and 0.57, respectively. The mean deviation of the $R_{50\%}$ value was within the acceptable tolerance defined in the RTOG 1021 protocol (<1.3). This indicates that the dose distribution surrounding the PTV had a rapid dose fall-off. A slightly larger $R_{50\%}$ deviation was observed for two plans (plan 1 and plan 3) calculated using the Monte Carlo simulation, with the absolute deviation of 1.03 and 1.13 relative to the acceptable $R_{50\%}$ value from the RTOG 1021 protocol. On average, the deviation of $R_{50\%}$ from the CCC calculation was slightly lower than the MC calculation. The maximum deviation of the $R_{50\%}$ was 0.93 for the CCC calculation and 1.13 for the MC simulation.

Table 5.14: *The Intermediate Dose Spillage Values from the CCC and MC Plans*

Parameters		Absolute Deviation from RTOG 1021 criteria	Difference between CCC and MC
$R_{50\%}$	CCC	0.22 (-0.60 – 0.93)	-0.03 (-0.41 – 0.15) P-value = 0.45
	MC	0.24 (-0.54 – 1.13)	
D_{2cm} (% of D_p)	CCC	-0.47 (-5.77 – 8.76)	-0.22 (-4.07 – 2.96) P-value = 0.57
	MC	-0.25 (-4.84 – 9.87)	

*The value is presented as mean absolute difference and the range

This study also found that the D_{2cm} values of all plans calculated from the CCC and MC were within the acceptable deviation defined by the RTOG 1021 protocol. Although the average deviation calculated by the CCC was slightly higher than the MC calculation, the difference was not statistically significant. Both algorithms show the largest deviation of the D_{2cm} value in plan 18 of 8.76 (or 13.52%) for the CCC and 9.87 (or 15.24%) for MC calculation. This plan had the largest PTV volume of 83.80 cm^3 and the PTV overlapped with the chest wall.

5.3.5 Dosimetric parameters to OARs

Table 5.15 presents the dose received by the OARs from 20 lung SBRT plans following the dose constraints guidelines adopted from the RTOG 1021 protocol.

Table 5.15: *Dose Received by OARs of Lung SBRT Plans from CCC and MC Calculations*

Parameters, (units)	TPS (Mean ± sd)	MC (Mean ± sd)	Mean Relative Difference (%)	P-value
Normal lungs				
$V_{11.4Gy} < 1000\ cm^3$, (cm^3)	429.06±126.93	431.77±133.76	-0.04	0.45
$V_{10.5Gy} < 1500\ cm^3$, (cm^3)	469.44±134.04	471.41±141.82	0.17	0.55
MLD (Gy)	4.11±0.18	4.01±0.19	2.81	<0.001
$V_{20Gy} < 15\%$, (%)	4.30±1.53	4.37±1.53	-1.64	0.002
Oesophagus				
MPD < 25.5 Gy, (Gy)	13.81±6.05	13.40±6.10	4.06	<0.001
$V_{17.7Gy} < 5\ cm^3$, (cm^3)	0.18±0.46	0.14±0.41	8.41	0.03
Pericardium				
MPD < 30 Gy, (Gy)	22.96±7.36	22.56±7.03	1.63	0.03
$V_{24Gy} < 15\ cm^3$, (cm^3)	0.97±2.68	0.74±2.15	8.67	0.04
Spinal canal				
MPD < 21.9 Gy, (Gy)	10.02±3.73	9.71±3.88	7.45	0.002
$V_{12.3Gy} < 1.2\ cm^3$, (cm^3)	0.18±0.36	0.18±0.37	2.44	0.34
Brachial plexus				
MPD < 24 Gy, (Gy)	3.93±0.90	3.82±0.50	74.47***	0.13
$V_{20.4Gy} < 3\ cm^3$, (cm^3)	0.01±0.02	0.01±0.03	-19.15	0.32
Trachea				
MPD < 30 Gy, (Gy)	9.79±7.56	9.44±7.67	15.43	0.001
$V_{15Gy} < 4\ cm^3$, (cm^3)	0.78±1.61	0.66±1.37	4.01	0.07
IVC MPD < 45 Gy, (Gy)	2.71±5.12	2.45±5.00	77.08***	0.001
SVC MPD < 45 Gy, (Gy)	12.65±6.67	11.79±7.18	15.22	0.18
Aorta MPD < 45 Gy, (Gy)	16.80±4.16	16.34±4.36	3.38	<0.001
Chest wall				
*$V_{30Gy} < 30\ cm^3$, (cm^3)	0.92±2.05	0.80±1.85	50.01	0.03
**$V_{30Gy} < 70\ cm^3$, (cm^3)	37.87±20.00	35.44±18.61	6.28	0.001
Ribs				
$V_{40Gy} < 5\ cm^3$, (cm^3)	1.12±0.52	0.94	4.42	0.04
MPD < 50 Gy, (Gy)	45.79±15.97	45.57±19.95	0.52	0.38

*The PTV did not overlap the chest wall, ** The PTV overlapped the chest wall

*** The percentage of relative difference was very large, as the absolute dose value was relatively small, less than 1 Gy (0.1 – 0.5 Gy), sd= standard deviation, MPD = Maximum Point Dose, MLD = Mean Lung Dose, V_{xGy} = volume of structure receiving the dose larger than x Gy

The dose constraints to OARs are important in evaluating the lung SBRT plans, because the large dose delivered to the target might result in a higher complication to normal structures. The dose constraints are different than those used in conventionally fractionated treatment (2 Gy per fraction). The results presented in Table 5.15 show that the CCC calculation tended to overestimate the dose to the OARs in most plans. An exception was the dose to the normal lung tissue volume (i.e., total lung volume excluding the ITV), where the CCC underestimated the dose. However, the difference was not statistically significant. The mean values for the maximum dose to the pericardium, $V_{12.3Gy}$ of the spinal canal, and $V_{20.4Gy}$ brachial plexus were the same between the CCC and MC calculations; thus, no significant difference was observed for these parameters. Further discussion of the dose parameters to each organ is presented in the following subsections.

Dose to Normal Lung Tissue

The results show that the dose received by the normal lung tissue was less than the threshold dose (i.e., 10.5 Gy and 11.4 Gy) for both the CCC and MC calculations. This is a good indicator that the lung SBRT treatments evaluated showed a small probability of the basic lung function disorder and radiation pneumonitis complication. There was no significant difference observed for the dose-volume parameters to the normal lung tissue between the CCC and MC calculations ($p = 0.045$ and 0.55). Similar underestimation of the dose to normal lung tissue by the CCC algorithm was observed in the lung V_{20} parameter. Although the lung V_{20} parameter dose is not outlined in the RTOG 1021 protocol, lung V_{20} is often used to predict the probability of radiation pneumonitis complication and is outlined in the TROG 0902 CHISEL trial protocol.

The evaluation of the mean lung dose (MLD) shows that the CCC overestimated the MLD compared to the MC calculation ($p<0.001$), with an average difference of 2.81%. The largest difference of 7.23% was observed in plan 13, with the PTV volume of 29.52 cm^3. However, the MLD for this plan was below 4 Gy for both the CCC and MC calculations. The highest MLD was observed in plan 5, which was 5.44 Gy for the CCC and 5.26 Gy for the MC. Although no threshold value for the MLD is outlined in the RTOG 1021 protocol, a MLD value of larger than 4 Gy could indicate a higher probability of radiation pneumonitis [174].

Dose to Oesophagus

The results show that the dose received by the oesophagus in all plans was within the allowable limits for both maximum dose and $V_{17.7Gy}$ dose constraints. The volume of the oesophagus receiving a dose larger than 17.7 Gy was zero in 16 plans, and below 5 cm^3 in the remaining four plans. The average relative difference between the CCC and MC dose distribution was 8.41%, which associated with an absolute difference of 0.03 Gy. Larger relative dose differences observed for this dose parameter were due to the small value of the dose-volume parameter. For example, in plan 1, the relative dose difference was 84.62%, which associated with the TPS value of 0.09 Gy and the MC value of 0.05 Gy. Although the paired t-test showed a significant difference for this dose parameter ($p=0.03$), it was not clinically significant, as the value was below the constraint defined in the trial protocol.

The CCC calculation overestimated the maximum dose to the oesophagus with the average difference of 4.06%. The difference was statistically significant ($p<0.001$), with the largest difference of 8.16% observed in plan 7. However, this difference between the CCC and MC calculations does not necessarily reflect a high value of maximum dose to the oesophagus in this plan, as the value is actually low, approximately 5 Gy. A high value of maximum dose to the oesophagus (>20 Gy) was observed in three plans (plans 11, 13 and 14), where the tumour was located in the right lobar. Among these plans, plan 14 had the largest maximum dose to the oesophagus of 23.5 Gy, but was still below the constraints. As the dose constraints were not exceeded, it was expected that there would be no stenosis/fistula incidence of grade >3 from the evaluated plans.

Dose to Pericardium

There was a significant difference in the V_{24Gy} calculated by the CCC and MC ($p=0.04$), with an average difference of 8.67%. However, this difference was not clinically significant, as the volume of the pericardium that received 24 Gy (V_{24Gy}) was zero in 12 plans, while V_{24Gy} in the remaining 8 plans was below 15 cm^3, as shown in Figure 5.21.

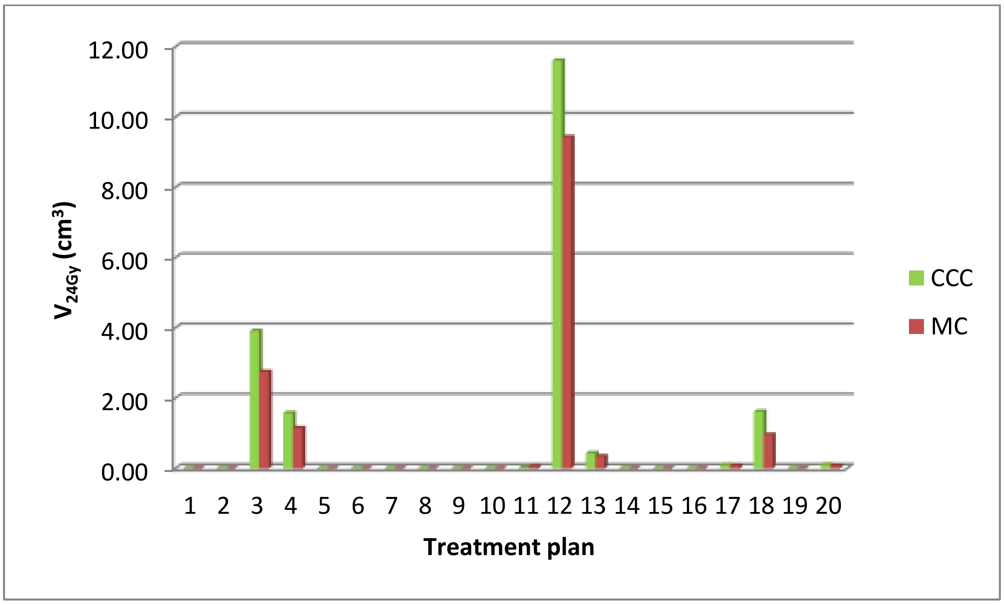

Figure 5.21. The volume of pericardium receiving a dose larger than 24 Gy (V_{24Gy}) in evaluated plans.

The different of the maximum point dose (MPD) calculated by the CCC and by the MC was statistically significant (p=0.03). It is important to note that the MPD in three plans exceeded the constraint of 30 Gy. The highest MPD was found in plan 12 (42.1 Gy for the CCC and 39.1 Gy for MC calculations), where the tumour was located in the lower lobar of the left lung, causing the pericardium to receive a higher dose. The volume of the pericardium receiving a dose of >24 Gy was also the highest in this plan (>9 cm^3).

Dose to Spinal Canal

No volume received a dose of larger than 18 Gy in all plans and only five plans received a dose larger than 12.3 Gy to the spinal canal structure. The dose-volume constraint of plan 10 was shown to be on the limit ($V_{12.3Gy}$ = 1.2 cm^3). No statistically significant difference was observed for this parameter (p=0.34).

The CCC overestimated the maximum point dose to the spinal canal in 18 plans. However, the value was still below the defined constraint. The difference was statistically significant (p=0.002), with an average difference of 7.45% for all 20 plans.

Dose to Brachial Plexus

There was no significant difference in the brachial plexus volume that received a dose of larger than 20.4 Gy ($V_{20.4Gy}$) between the CCC and MC calculations (p=0.32). The only plan that received a dose larger than 20.4 Gy was plan 18, while the remaining plans had zero $V_{20.4Gy}$. The maximum point dose received by the brachial plexus was shown to be slightly higher in the CCC calculation, but did not differ significantly from the MC calculation ($p=0.13$). In addition, the MPD in the majority of plans was relatively low (≤2 Gy), with the exception of plan 14 (16.3 Gy for the CCC and 17.3 Gy for the MC calculation) and plan 18 (>25 Gy). The MPD received by the brachial plexus in plan 18 exceeded the limits by 1.1-1.3 Gy. Although the average relative difference for the MPD to brachial plexus was very high (74.47%), this associated with a small average absolute dose difference of 0.11 Gy.

Dose to Trachea

Only four plans received a dose larger than 15 Gy (V_{15Gy}) to the trachea. The remaining 16 plans had a zero V_{15Gy} value. The constraint was slightly exceeded in plan 14, where more than 4 cm^3 of trachea received the dose of >15 Gy (4.44 cm^3 for the CCC and 4.08 cm^3 for the MC calculations). Although the maximum point dose calculated by the CCC was higher than the MC, no plans exceeded the maximum point dose constraint to the trachea. The difference of the MPD calculation was statistically significant ($p=0.001$), with an average difference of 15.3%. This difference seems relatively high, but this value is actually relatively similar to the MC value. As some plans had a lower value (less than 1 Gy), a small absolute difference resulted in a higher relative difference.

Dose to Great Vessels (Aorta, Inferior Vena Cava, and Superior Vena Cava)

The results show that the maximum point dose received by the major vessels, including the aorta, the inferior vena cava (IVC), and the superior vena cava (SVC), were all within the tolerance (<45 Gy). None of the plans were shown to have a major vessel volume receiving a dose larger than 39 Gy. In general, the CCC overestimated the MPD to the aorta, IVC, and SVC. Although the difference was statistically significant, with the exception of the MPD to the SVC, this may not be clinically significant, as the values were still below the constraints. The average relative difference was very high for the MPD to IVC, 77.08%. However, this high percentage was actually due to the small value of the dose. For example, the MPD in plan 1 for the CCC and MC calculations were 0.3 Gy and 0.1 Gy, respectively. The percentage relative difference for this plan was 200%. Figure 5.22 shows the MPD to the IVC in the twenty treatment plans.

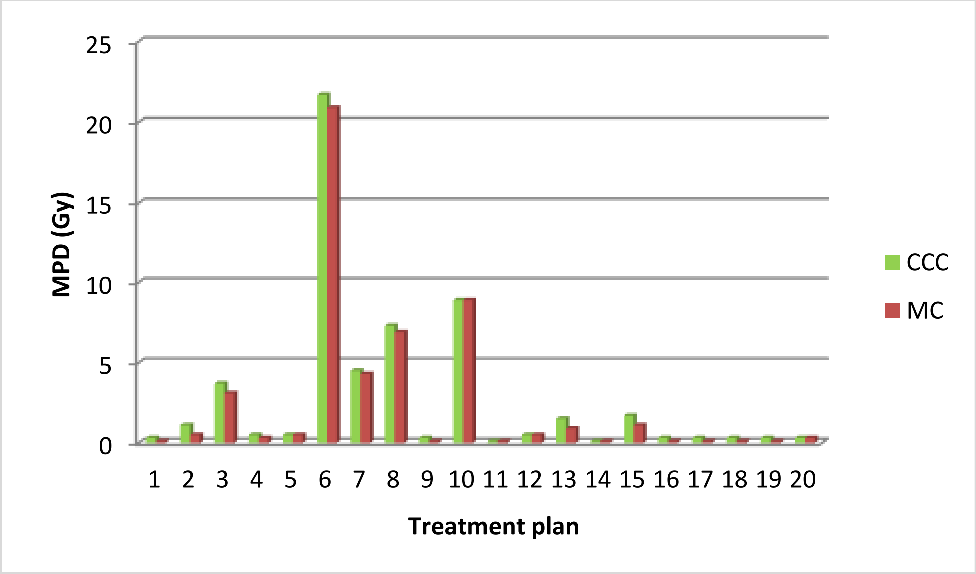

Figure 5.22. The maximum point dose to the inferior vena cava (IVC) structure in the twenty treatment plans.

Dose to Chest Wall

Dose constraints to the chest wall were classified into two groups. The first group was for PTV that had no intersection with the chest wall and the second group was for PTV that overlapped the chest wall. The dose constraints for the first and second groups were $V_{30Gy} < 30$ cm^3 and $V_{30Gy} < 70$ cm^3, respectively. Each group consisted of 10 plans. The results show that there was a significant difference between the V_{30Gy} calculated by the CCC and MC for both groups (p=0.03 and p=0.001, respectively).

The CCC overestimated the dose to the chest wall in most of the plans, with an average difference of 50.07% in the first group (ranges from 0% to 298.52%) and 6.28% in the second group (ranges from -4.98 % to 13.19%) relative to the MC calculation. The large relative dose difference observed in the first group was due to the small values of the V_{30Gy} observed in plans 3, 5 and 16, which were below 1 cm^3. One plan in the second group, plan 12, violated the dose constraint with more than 70 cm^3 of the chest wall volume receiving a dose of larger than 30 Gy (75.38 cm^3) when calculated using the CCC algorithm. Figure 5.23 shows the V_{30Gy} values in all plans disregarding the location of the PTV.

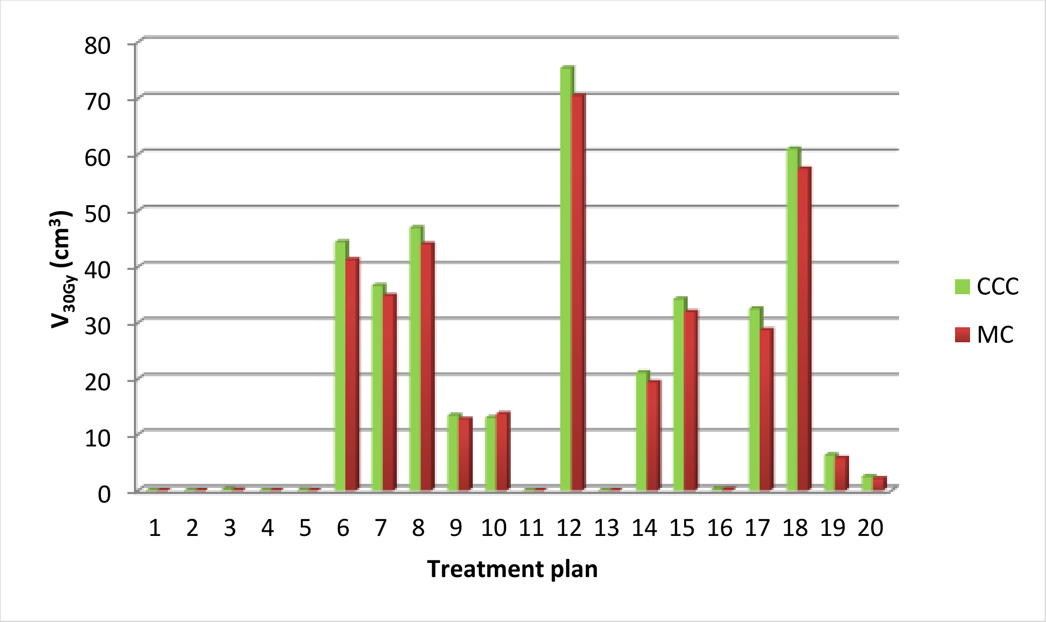

Figure 5.23. The V_{30Gy} values of the chest wall structure in all plans.

Dose to Ribs

The mean value of the dose received by the ribs over 20 lung SBRT plans was within the tolerance, as shown in Table 5.15. However, evaluation of the individual patient plans shows dose constraint violations in some plans, especially for those plans where the PTV overlapped the chest wall. Table 5.16 presents the dose received by the rib bones for the PTV on the chest wall or close to the chest wall. The maximum point dose to ribs is shown to have exceeded the limit of 50 Gy in 11 plans. With the exception of plan 19, where the PTV was located very close to the chest wall, the remaining 10 plans had a PTV structure that overlapped the chest wall. The maximum rib volume receiving a dose of larger than the 40 Gy (V_{40Gy}) limit was also exceeded in three plans (plan 8, 12 and 18). This might indicate a higher complication probability to the rib bones for a tumour located close to the rib bones or chest wall.

Although the paired student t-test indicates a significant difference for the maximum volume receiving a dose of 40 Gy ($p=0.04$), the maximum point dose calculated by two algorithms did not differ significantly ($p=0.38$). The CCC overestimated the dose to the ribs in 13 plans, with an average difference of 0.52% relative to the MC calculation. The largest difference of 9.08% was observed in plan 10.

Table 5.16: *Dose Received by Rib Bones for the Plan with the PTV on the Chest Wall*

Plan	Structure	Volume (cm^3)	$V_{40\ Gy}$ (in cm^3)		MPD (in Gy)		
			TPS	MC	TPS	MC	Diff (%)
Plan 6	8th rib	14.2477	3.56	2.59	61.7	62.9	-1.91
	9th rib	16.5616	2.95	2.25	57.9	58.5	-1.03
Plan 7	7th rib	16.1455	3.21	2.77	58.1	55.9	3.94
Plan 8	7th rib	16.4117	3.47	3.75	59.7	59.1	1.02
	8th rib	15.7772	3.93	5.42	58.5	58.7	-0.34
Plan 9	2nd rib	7.6891	0.30	0.26	60.7	61.7	-1.62
	3rd rib	7.3592	1.17	0.96	59.1	57.7	2.43
Plan 10	8th rib	12.2522	1.61	1.70	56.1	61.7	-9.08
	9th rib	13.295	1.21	1.09	57.7	59.5	-3.03
Plan 12	4th rib	17.3115	5.43	4.77	59.5	57.5	3.48
	5th rib	20.1071	6.32	5.43	60.3	59.7	1.01
	6th rib	20.7088	1.28	1.05	57.1	55.5	2.88
Plan 14	3rd rib	13.6489	2.52	2.13	58.5	57.7	1.39
Plan 15	7th rib	18.6906	2.20	1.66	59.1	58.7	0.68
	8th rib	16.1941	2.72	2.19	57.9	57.3	1.05
Plan 17	3rd rib	17.8443	2.52	1.76	56.5	53.5	5.61
	4th rib	17.9412	2.46	1.40	55.7	53.3	4.50
Plan 18	3rd rib	17.0438	1.46	1.13	58.1	58.9	-1.36
	4th rib	18.5917	5.33	4.16	58.7	57.7	1.73
	5th rib	19.443	4.55	3.61	58.7	56.7	3.53
Plan 19	4th rib	21.2732	1.61	1.25	58.9	57.7	2.08

MPD for the rib: the tolerance was MPD < 50 Gy, V40 Gy < 5 cm^3

5.4 DISCUSSION

The requirement for accurate TPS dose calculations has increased following the rapid adoption of SBRT or SABR techniques for medically inoperable early-stage NSCLC and other tumours in large heterogeneous tissues. The use of doses >10 Gy per fraction promises higher potential in killing tumour cells, but may also increase the probability of normal tissue complications. This could be true, especially when the

PTV structure contains a certain amount of the normal tissue to compensate for the uncertainty in the tumour position due to the respiratory motion.

The inappropriateness of using the pencil beam algorithm (algorithm type A) in the treatment of lung cancer has been widely explored by experimental studies in heterogeneous phantoms [14, 30, 33, 34] and in clinical treatment plans [18, 19, 28, 37]. As the results indicate, more advanced convolution/superposition algorithms (type B algorithms), such as CCC algorithms, are recommended for dose calculation in lung SBRT planning. Benchmarking of the convolution/superposition algorithms is often performed by comparing the dosimetric performance with the calculation from the Monte Carlo simulation as the gold standard algorithm, and/or with the standard measurement using ion chamber, TLD [20], or film [23, 39].

This study demonstrates the verification of the CCC dose calculation algorithm employed in the Pinnacle^3 RTPS using the EGSnrc/BEAMnrc Monte Carlo code. The verification was performed for medically inoperable early-stage NSCLC with the PTV size <85 cm^3. The modelling of a 6 MV photon beam produced from the Elekta Axesse linear accelerator equipped with high-resolution MLC Beam Modulator was described in Chapter 4. The commissioning of the developed model down to 1.6 x 1.6 cm^2 field size shows a suitability of the model to be used for studying the dosimetric parameters of lung SBRT plans.

The retrospectively studied lung SBRT plans were designed using the combination of 10 coplanar and non-coplanar beams with different orientations. The main reason for this arrangement was to meet the objective of high dose constraint and intermediate dose spillage. The high-resolution MLC with a leaf width of 4 mm was used to create a more conformal treatment field to the target. Therefore, it is critical to correctly model the MLC opening as well as the beam orientations.

This work shows that a comparison of water planar dose maps from the TPS and MC simulation can be used to verify the MLC opening used in the BEAMnrc Monte Carlo input files. This simple method aids in identifying the error that occurred during the file transfer and conversion of the plan information from the DICOM system to the BEAMnrc input parameters. In addition, this method also provides quantitative information regarding the agreement of the MLC setting between the TPS and MC, which was found to be within ±1 mm.

As the complication also exists in the conversion of the TPS beam orientation to the DOSXYZnrc beam orientation, this work has shown that verification is critical to ensure the correct conversion of these parameters. The fact that there are differences in the coordinate systems and/or axes conventions used in the TPS, DICOM, and Monte Carlo systems demonstrates that the conversion process is not a trivial matter. Adding to this complexity is the post-analysis of the TPS and MC dose distributions that had to be performed in external software, CERR, which also has its own axes convention.

The verification using a single beam in a homogenous phantom was shown to be useful in identifying an error in the conversion of the beam orientation. This simple procedure also aided in correcting the error that occurred through the modification of the formula. This work found that the conversion formula of the beam orientations proposed by Zhan *et al.* [171] was not appropriate for the plans studied in this work. Although the author reported that the formula was tested for the Pinnacle^3 RTPS, it was found that the correct beam arrangement conversion could be achieved using the polar and azimuth angles proposed by Thebaut and Zavgorodni [169] and a further modification of the phicol angle formula used in the MCDTK software [157]. The reason for this modification is that there is a difference in defining the MLC travel orientation between the TPS and the BEAMnrc linear accelerator. It was found that the MLC travels parallel to the X-axis in the Pinnacle^3 RTPS, while in the BEAMnrc model the MLC travels parallel to the Y-axis. It should be noted that the accelerator model developed in the BEAMnrc was constructed based on the manufacturer's specification that defined the MLC movements parallel to the Y-axis. As a consequence, the additional rotation of the MCDTK phicol formula and a modification of the position of the leaf bank pairs were required to obtain the correct beam configuration in the DOSXYZnrc input files.

Further verification of this modified formula in the clinical beam situation from the simple two coplanar beams configuration to the complex 10 coplanar and non-coplanar beams configuration confirmed that the formula is correct. The verification was performed in a homogenous media to exclude the effect of tissue heterogeneity to the dose distribution. Instead of using simple water phantom, the patient geometry phantom was used; however, the density of the tissues within the external skin contour was set to be unity (i.e., 1 g/cm^3) or water equivalent. This method was also adopted by Vanderstraeten *et al.* [28].

This work has shown that the calculation of the lung SBRT plan in a homogenous media results in good agreement between the CCC and MC calculations, to within 2% in both low and high dose gradients. This finding is similar to other studies where different algorithms performed very well for the unity density, even using the pencil beam algorithm, with a difference of within 2% [14, 28]. In a previous study by Aarup *et al.* [14], instead of using the patient phantom with density override, a cubic phantom with a spherical tumour model at the centre of the cubic phantom surrounded by lung tissue was used. They found that when the lung density was set to 1.0 g/cm^3 (i.e., water density), the different algorithms (pencil beam, AAA, and CCC) agreed very well with the BEAMnrc calculation to within 2%. A significant reduction of the dose calculated by the CCC and the BEAMnrc was observed when the lung density decreased to 0.1 g/cm^3.

The comparison between the CCC and MC dose distributions using the 3D gamma analysis with the passing criteria of 3%, 3 mm shows that the average passing rate of more than 99% for the PTV structure and the OARs could be achieved. This indicates that the dose calculated by the CCC algorithms is generally in agreement with the MC to within 3% and 3 mm. Tightening the criteria to 2%, 2 mm showed a reduction in the average passing rate of the PTV structure to 91.86%. This reduction is attributed to a significant decrease of the plan 1 passing rate, in which only 59.86% of the dose points passed the selection of 2%, 2 mm criteria. The evaluation of the plan 1 dose distribution shows that the CCC underestimated the dose to the PTV by 5.23%. This caused the passing rate of the 3D gamma analysis using the tighter criteria to be much lower than that of the standard criteria. The tumour in plan 1 was relatively small in size (27.00 cm^3) and completely surrounded by the lung tissue.

The comparison of the lung SBRT plans between the CCC and the MC simulation in the real phantom geometry shows that there was no significant difference of the dose-volume parameters to the PTV, with the exception of the maximum dose to the PTV and the conformity index. The PTV coverage of the prescription isodose (PTV_{54Gy}) was not significantly different between the CCC and MC calculation, although the CCC overestimated the PTV_{54Gy} in 11 out of 20 plans. The agreement of PTV_{54Gy} of all plans was within ±6%. The better agreement of ±2% was achieved for the PTV coverage of 90% of the prescribed dose ($PTV_{48.6Gy}$). The larger difference was observed for the minimum dose to the PTV, with the maximum difference of 8.55%. The difference of the mean dose and maximum dose to the PTV was much lower and within ±3.5%. It was also noted that although not occurring in all plans, the CCC tended to overestimate the dose to the PTV. In addition, the work found that the cumulative DVH of the PTV structure obtained from the CCC calculation was very similar to that from the MC calculation in nine plans. Overall, the agreement between the CCC and MC calculation for the PTV dose-volume parameters was within ±9%. This finding is consistent with findings from other studies, which reported a difference between the CCC and Monte Carlo to within 2-10% [18, 28, 32, 38, 39].

However, it should be noted that most of these studies were performed for conventionally fractionated lung treatments employing a smaller fraction size and smaller number of treatment fields (3-7 fields) than the plans evaluated in this study. Only the studies by Fotina et al. [38] and Calvo et al. [39] were performed for lung SBRT treatment and specifically compared the CCC algorithms with Monte Carlo algorithms. Fotina et al. [38] investigated the performance of enhanced CCC algorithms employed in Oncentra Masterplan TPS with a commercial MC-based TPS algorithm, XVMC, implemented in Monaco TPS, while in this study the comparison was performed for the CCC Pinnacle TPS with a general-purpose EGSnrc MC code. In addition, they only evaluated two lung SBRT plans, which may not adequately represent variations in tumour size, location, and patient anatomy among different patients. The inclusion of a larger number of patient plans (i.e., 11 lung SBRT plans) was investigated in a study by Calvo *et al.* [39], comparing the performance of the CCC algorithms employed in the $Pinnacle^3$ TPS with a general-purpose EGSnrc MC code. They found that the agreement of PTV mean dose calculated by the CCC and Monte Carlo was to within 5.6% for lung SBRT plans with fractionation schedule of 45 Gy in three fractions. However, instead of using the 3DCRT technique for the SBRT delivery, they used an IMRT technique consisting of five coplanar beams. Their study focused on investigating the dose calculation accuracy for different segment sizes used in the IMRT delivery. While this study focused on verification of lung SBRT plans delivered using 10-fields 3DCRT technique, as commonly implemented in the local radiotherapy centres.

Regarding the conformity index, it was found that the majority of plans satisfied CI requirement, with a value of >0.75. Although the CCC calculated a higher CI index in 11 plans, the average difference of all 20 plans was less than 1%. Fotina *et al.* [38] reported that the CI calculated by the enhanced CCC algorithm (Oncentra TPS) was slightly lower than the MC in their lung SBRT plans. However, as they only investigated two SBRT plans, the result might not be so different if more plans were included in the evaluation.

Evaluation of the mean value of dose parameters to the OARs showed that in general the CCC overestimated the dose to the OARs, an exception was the normal lung tissue and $V_{20.4Gy}$ constraint to the brachial plexus. The maximum point dose to the pericardium was also an exception, as there was no difference between the CCC and MC calculation. This finding is similar to that reported by Calvo *et al.* [39], where the dose to lung calculated by the CCC Pinnacle^3 was lower than the MC calculation. However, Fotina *et al.* [38] found that the enhanced CCC algorithm overestimated the dose to the lung. Evaluation of individual patient plans showed that overestimation of the lung dose (i.e., $V_{10.5Gy}$ and $V_{11.4Gy}$) occurred in 12 plans, while for the remaining eight plans the CCC underestimated the dose. The overestimation of the CCC Pinnacle^3 algorithm to the spinal cord and oesophagus structure was also reported by Calvo *et al.* [39]. A recent study by Stathakis *et al.* [175] also reported that OARs received a higher dose in the plans calculated using Pinnacle algorithms than the plans calculated using Monte Carlo. In some OARs, such as the spinal cord, the brachial plexus, the pericardium, and the inferior vena cava, a large percentage of relative dose difference was observed. This was mainly caused by the small absolute dose value of those OARs. As a result, a small absolute dose difference led to a high percentage difference. For example, a relative dose difference of 66.67% in maximum dose to the inferior vena cava was associated with the absolute difference of 0.2 Gy where the CCC dose was 0.5 Gy and the MC dose was 0.3 Gy. This is similar to that reported by Calvo *et al.* [39]. Although the dose difference between the CCC and MC were statistically significant in some OARs, such as the oesophagus, trachea, aorta, and great vessels, the values were still below the normal tissue dose constraints defined in the RTOG 1021 trial protocol. This indicates that the difference between the CCC and MC calculations might not be clinically significant.

The important result is the dose received by the chest wall and rib bones. Although the chest wall constraints were fulfilled in the majority plans, there was one plan that violated the dose constraint. It was observed that plan 12 had a $V_{30Gy} > 70$ cm^3, which seems to have a higher risk of chest wall toxicity. It has been reported that the constraint $V_{30Gy} < 30$ cm^3 is associated with a lower risk of the chest wall toxicity [176]. The larger V_{30Gy} value was attributed to grade 3 chest wall pain and rib fractures [176]. In term of the dose constraint to the ribs, Andolino *et al.* [177] reported that a dose of larger than 50 Gy to the ribs causes a significant increase in chest wall toxicity. The evaluation of the maximum dose to the ribs in 11 plans, where the PTV was located at or close to the chest wall structure, demonstrates that the rib cut-off dose of 50 Gy was exceeded. This indicates that the probability of the rib fracture and/or chest wall pain is higher for tumours located at the chest wall.

Overall, the dosimetric parameters of 10-field-3DCRT lung SBRT plans calculated by the CCC algorithms were in agreement with the MC calculation to within 6% for the doses to the target (except for PTV D_{min}), normal lung tissue and rib. A larger difference of >10% was observed in some OARs, mostly due to their small dose values. Although some dose criteria were more difficult to achieve in several plans, for example, PTV_{54Gy} coverage and maximum dose to the ribs, the majority of the plans calculated using the CCC algorithms satisfied the dosimetric requirement outlined in the RTOG 1021 protocol. This indicates that the CCC algorithms implemented in the Pinnacle^3 TPS are still accurate enough for lung SBRT planning. The superiority of the CCC algorithms relative to other type B algorithms have been reported in the literature, for example, when compared with AAA in both slab phantom studies and clinical cases [14, 30-32, 85]. The superiority of the CCC algorithm, especially that employed in the Pinnacle^3 RTPS, was demonstrated in the study by Vanderstraeten *et al.* [28] involving lung IMRT treatments. They found that the CCC-Pinnacle^3 performed better in calculating the dose to the tumour compared to the CCC algorithm employed in Helax TMS. However, in regard to the OARs dose calculation, the CCC-Helax had a better performance than the CCC-Pinnacle^3.

There are some limitations of this study which come from the use of small number of materials in the patient tissue composition in the Monte Carlo simulation and from the impact of Monte Carlo dose conversion from dose-to-tissue to dose-to-water. In this study, the patient geometry was only defined using 4 materials, i.e. air, lung, soft tissue and bone. The adipose/fat and muscle tissues were not defined, which might have an impact to the calculation of the dose to the lung and other organs that might be composed by the adipose tissues. The inclusion of more material could be performed in a future study to obtain more accurate dose calculation from the Monte Carlo simulation. Another limitation is the uncertainty resulted from the dose conversion of the Monte Carlo plan from dose-to-tissue to dose-to-water, which has been reported by Andreo (2015) [178] to be significant for bone tissue and adipose tissue for a lesser extent. In this study, we observed the mean relative difference of the mean dose to the lung between the CCC and MC plans of 2.81% while Andreo reported that the the conversion from dose-to-tissue to dose-to-water in lung results in a dose change of about 1%. Therefore, there is possibility that 1% of dose difference in the mean lung dose is contributed by the changes in Monte Carlo dose conversion. For the dose to the rib bone, the mean difference of maximum dose between the CCC and MC plan is less than 1%. This value is much smaller than the changes resulted from dose-to-tissue to dose-to-water conversion reported by Andreo, which is about 3-6%. The effect of dose reporting to the dosimetric evaluation between different treatment plans, especially when comparison is made with the Monte Carlo-based algorithms could be explored more in a future study.

5.5 CONCLUSION

Twenty lung SBRT treatment plans delivered using a 10-field 3DCRT technique were retrospectively studied in this research to verify the dose calculation accuracy of the CCC algorithm employed in the Pinnacle^3 RTPS. The verification was performed by recalculating the dose distribution of the plans using the EGSnrc/BEAMnrc Monte Carlo codes. Verification of the Monte Carlo input files was performed to ensure that the treatment plan parameters were correctly modelled. The results show that the CCC showed agreement with the MC simulation to within ±6% for the PTV coverage, PTV D_{mean}, PTV D_{max}, and conformity index. The difference in overall plans was not statistically significant for the PTV dose parameters. The evaluation of intermediate dose spillage shows that all plans show an acceptable intermediate dose spillage, although the difference between the CCC and the MC was slightly higher than the difference observed in the PTV dose parameters. For the OARs, the CCC overestimated the dose to the OARs, with the exception of the normal lung tissue, maximum dose to the pericardium, and $V_{20.4Gy}$ constraint to the brachial plexus. A significant deviation from the RTOG 1021 normal tissue dose constraints was observed for the maximum dose to the ribs in the plans where the PTV overlapped the chest wall.

As the performance of the CCC Pinnacle^3 is relatively closer to the MC calculation, it would appear that the CCC algorithm is adequately accurate for dose calculation in the treatment planning of lung SBRT plans. However, with regards to the dose difference in the PTV and OARs, it is important to investigate how this difference will impact on the TCP and NTCP as the estimate of the treatment outcome, which is discussed in Chapter 6.

Chapter 6: The Impact of the Dose Calculation Uncertainties on the TCP and NTCP of Lung SBRT Plans

6.1 OVERVIEW

The previous chapter discussed the dose distribution comparison between the CCC algorithm (TPS) and the Monte Carlo simulation for twenty lung SBRT plans. Although the difference of the PTV coverage of the prescribed dose between the TPS and MC was not statistically significant, a maximum difference of 5.84% was observed. For the dose to the OARs, the maximum dose to the ribs was found to exceed the dose limits in 11 plans, with the largest difference being 9.08%. This chapter evaluates whether this dose difference (dose calculation uncertainties) of the PTV and OARs might have any clinical significance through a radiobiological model analysis. The radiobiological parameters that were calculated included the tumour control probability (TCP) and normal tissue complication probability (NTCP). To estimate the probability of these parameters, the calculations were performed using existing radiobiological models: the Linear Quadratic (LQ) Poisson "Marsden" model for the TCP calculation and Lyman-Kutcher-Burman (LKB) model for the NTCP calculation.

The use of TCP and NTCP parameters in treatment plan evaluation has been recommended as the complement of dose-volume based analysis [107, 179]. This enables the comparison of different plans from the TPS algorithm, or different radiation delivery techniques, or different fraction sizes, in order to select the optimum plan that would give the highest therapeutic ratio (i.e., highest TCP at a specified NTCP) [107]. Many previous works comparing the performance between different TPS algorithms for NSCLC treatments have focused only on the physical dose evaluation of the plans. Few studies have attempted to relate the calculated dose distributions to the TCP [22, 94, 166, 180] and NTCP [166, 180-183]. The studies by Chetty *et al.* [22] and Liu *et al.* [94] evaluated the TCP of the lung SBRT plans initially created using path length (EPL) pencil beam algorithms showing an overestimation of the TCP using this correction-based algorithm type. The TCP evaluation of lung SBRT treatment plans designed using AAA, a model-based algorithm, were evaluated in studies by Huang *et al.* [180] and Liang *et al.* [166]. Although these recent studies involved the NTCP evaluation of radiation pneumonitis in normal lung structure, none of studies evaluated the NTCP for rib fracture. This chapter presents a study of the evaluation of the TCP and NTCP of the lung SBRT plans evaluated by CCC algorithms, another type of model-based algorithms apart from AAA. The inclusion of the NTCP evaluation for rib fracture endpoints provides benefit in estimating the potential toxicity of the lung SBRT dose distributions calculated using the CCC algorithms. This aids in the optimisation of treatment plans, as well as the evaluation of the plans to select the best plan to be delivered in the actual treatment.

6.2 MATERIALS AND METHODS

6.2.1 Software and input data

The radiobiological analysis was performed using the BioSuite software developed by Uzan and Nahum [113]. The input data was the differential dose-volume histograms (DVHs) of the twenty lung SBRT plans from the TPS and MC dose distributions. These DVHs were extracted using the CERR software with a bin width of 0.2 Gy. In order to match the DVH format of the Biosuite software, the dose from the CERR DVH was converted from Gy to cGy and the irradiated volume was maintained in cm^3 (or cc).

For the remainder of the chapter, the plans calculated using the TPS algorithm are referred to as the CCC plans, while the plans calculated using the MC simulation are referred to as the MC plans.

6.2.2 Parameters of TCP calculation

The TCP was calculated using the LQ Poisson “Marsden” model [184] using the two sets of parameters presented in Table 6.1. The parameters were adopted from those used in a study by Valdes *et al.* [185], including the lower and upper bound values. The reason for the selection of these parameters was the similarity of the dose prescription used in the study, which was 54 Gy in three fractions.

The calculation was performed for each set parameter using two different clonogenic cell densities of 10^7 cells/cm^3 and 10^8 cells/cm^3 to include the lower and upper bound values found in the literature. The clonogenic density of 10^7 cells/cm^3 was the default value used in the Biosuite software [113], which was also adopted in the radiobiological modelling study by Chetty *et al.* [22], while the clonogenic density of 10^8 cells/cm^3 used in the study involved SBRT treatment for NSCLC [180, 185, 186].

Table 6.1: *Parameters of the LQ-Poisson "Marsden" TCP model* [185]

Parameters	Biosuite default value	Set 1 (lower bound of α/β)	Set 2 (upper bound of α/β)
α (Gy^{-1})	0.307	0.19	0.3
α spread	0.037	0.02	0.02
α/β (Gy)	10	9.5	15
Repopulation constant	3.7	3.7	3.7
Day before repopulation (days)	21	21	21

6.2.3 Parameters of NTCP calculation

The NTCP calculation was performed to estimate the probability of radiation pneumonitis, pericarditis, oesophagitis, and rib fracture. The estimation was performed using the LKB model, in which three equations were used to describe the NTCP:

$$NTCP = \frac{1}{\sqrt{2\pi}} \int_{-\infty}^{t} e^{-\frac{x^2}{2}} dx \tag{6.1}$$

$$t = \frac{D_{eff} - TD_{50}}{mTD_{50}} \tag{6.2}$$

$$D_{eff} = \left(\sum_i v_i D_i^{1/n}\right)^n \tag{6.3}$$

where D_{eff} is the dose that gives the same NTCP for a non-uniform dose distribution as if the volume was irradiated uniformly, TD_{50} is the uniform dose that results in 50% of complication probability, m is a slope of the sigmoidal dose response curve represented by the integral of the normal distribution, n is a volume effect parameter, and (D_i, v_i) are the bins of a differential DVH.

The Biosuite software provides an option to calculate the NTCP using the LKB models, in which users are only required to define the values of four parameters: m (slope), TD_{50}, n (volume effect), and α/β. The following section describes the details of the estimation endpoints: radiation pneumonitis, pericarditis, acute oesophagitis and rib fracture from the twenty lung SBRT plans.

Radiation pneumonitis (RP)

Radiation pneumonitis is the most significant normal tissue complication experienced by lung cancer patients receiving radiation treatment. Estimation of its probability is often performed using the LKB model [187-189]. However, there is a large variation in the value of LKB model parameters used in previous studies. This study used the two different LKB model parameters adopted from Wennberg *et al.* [190] and Hedin and Bäck [183]. The LKB parameters used in Wennberg et al.'s study were corrected for the hypo-fractionation SBRT treatments, while the parameters used in Hedin and Bäck's study were refitted for the dose distribution calculated using the CCC algorithm. Table 6.2 presents the LKB model parameters used for estimate the NTCP of radiation pneumonitis.

Table 6.2: *Parameters of the LKB Model for Radiation-pneumonitis End Point*

Parameters	Slope (m)	TD_{50} (cGy)	n	α/β (Gy)
Biosuite default value	0.45	2920	1	3
Wennberg et al. [190]	0.4	3000	0.9	3
Hedin and Bäck [183]	0.374	2840	0.99	3

As lung tissue is categorised as a late-responding normal tissue, the alpha/beta ratio of 3 Gy was selected. This value was also used in most of the previous studies [183, 187-190]. Although pneumonitis can also be an acute effect, this study focused on the pneumonitis as a late effect. The m represents the slope of the dose-response curve. A steeper slope means a small change in the dose will result in a large change in the complication probability. For radiation pneumonitis, the value of m in the literature ranges from 0.18 to 0.41 [189]. TD_{50Gy} represents the dose required to produce a 50% complication. The value of TD_{50Gy} from the existing study ranges from 16.4 Gy (the lower bound) to 30.8 Gy (the upper bound) [189]. The volume effect parameter (n) represents the tissue architecture of the organs of interest, which in the case of radiation pneumonitis, is the lung. As the lung is categorised as a parallel tissue arrangement, the value of n is close to 1 (0.86-1.02) [189].

Pericarditis

Pericarditis is the endpoint for the normal tissue complication modelling to the heart. The LKB model parameters for estimation of the pericarditis were adopted from Gagliardi *et al.* [191], as shown in Table 6.3.

Table 6.3: *LKB Model Parameters to Calculate NTCP for Pericarditis Endpoint*

Parameters	Slope (m)	TD_{50} (cGy)	n	α/β (Gy)
Gagliardi et al. [181]	0.13	5060	0.64	3

Oesophagus complication

The oesophagus is categorised as a serial tissue arrangement. For this serial organ arrangement, the dose-volume constraint is the maximum critical volume that should receive a dose equal or greater than the indicated threshold dose [89]. The endpoints relevant to the oesophagus are acute oesophagitis and late oesophagitis. Two LKB model parameter sets were used in this study to evaluate the probability of acute oesophagitis, which were adopted from Belderbos et al. and Chapet et al. [192, 193]. For late oesophagitis, the LKB model parameters were adopted from Burman et al. [187]. Table 6.4 lists the LKB models parameters for the estimation of the acute and late oesophagitis risks.

Table 6.4: *Parameters of the LKB model for NTCP Calculation of Oesophagitis Endpoint*

Reference	m	TD_{50} (Gy)	n	α/β (Gy)	End points
Belderbos *et al.* [192]	0.36 (0.25 - 0.55)	47 (41 - 60)	0.69 (0.18 - 6.3)	10	Acute oesophagitis
Chapet *et al.* [193]	0.32 (0.25 – 0.43)	51 (40 - 63)	0.44 (0.25 - 0.79)	10	Acute oesophagitis
Burman *et al.* [187]	0.11	68	0.06	3	Late oesophagitis

Rib fractures

Rib fracture and associated chest-wall pain are often reported after lung radiotherapy treatments. It is important to estimate the probability of rib fracture, as the previous chapter showed that the dose-volume constraints to the rib were exceeded in the plans where the tumour was located close to the chest wall. This might indicate a higher probability of rib complications. The parameters used for the LKB models were adopted from Burman et al. [187], representing the conventionally standard fractionation treatment, and from Scheenstra [194], representing the SBRT treatment (three fractions of 18 Gy/fraction).

Table 6.5: *Parameters of the LKB model for NTCP Calculation of Rib Fracture Endpoint*

Reference	m	TD_{50} (cGy)	n	α/β (Gy)	End points
Burman *et al.* [187]	0.21	6800	0.1	3	Pathological fracture
Scheenstra [194]	0.348 (0.311 – 0.384)	39550 (24430 – 5510)	0.03	3	Rib fractures

6.3 ANALYSIS

A paired student t-test was performed to evaluate the significant difference of the TCP and NTCP values between the CCC plans and MC plans for normally distributed data. While for non-normally distributed data, a Wilcoxon related sample test was performed. The difference was considered to be significant if the p-value was <0.05.

Bivariate analysis was performed to investigate the correlation between the PTV dose (D_{min}, D_{max}, D_{mean}, and PTV_{54Gy} coverage) to the TCP, as well as the correlation between the PTV volume and the TCP. For radiation pneumonitis (RP), the bivariate analysis was performed to investigate the correlation between the mean lung dose (MLD), V_{20Gy}, and $V_{11.4Gy}$ to the NTCP of radiation pneumonitis, as well as the correlation of the PTV volume and the NTCP of RP. For the oesophagus and ribs, the correlation between the maximum dose to the oesophagus and ribs and the NTCP was investigated. The bivariate correlation analysis was performed using a Pearson test for normally distributed data and a Spearman's rho test for non-normally distributed data. All statistical analysis was performed in SPSS Version 23.

6.4 RESULTS

6.4.1 TCP estimation

The mean TCP value of the CCC plans and MC plans from the twenty lung SBRT plans is presented in Table 6.6. The calculation of the TCP using the LQ Poisson parameter set 1 (i.e., lower bound) shows that average TCP value of >90% was achieved in all plans. Evaluation of individual plans shows that a TCP of 100% was achieved in eight CCC plans and nine MC plans (out of 20 plans) when the clonogenic cell density was assumed to be 10^7 cells/cm^3. The lowest TCP was 96.5% and 87% for the CCC and MC plans, respectively, which was found in plan 17. This plan had a PTV volume of 74.10 cm^3 and the tumour was located close to the chest wall. The difference in the TCP value between the CCC plans and MC plans was statistically significant (p=0.010), with the maximum difference of 9.50% observed in plan 17.

Table 6.6: T*he Mean TCP Value of Twenty Lung SBRT Plans from the CCC and MC Dose Distributions*

Parameters	ρ (cells/cm^3)	TCP value		Mean difference (%)	P-value
		CCC (%)	MC (%)		
TCP Set 1	10^7	99.53±0.16	98.42±3.21	1.12 (-0.10 – 9.50)	0.010
	10^8	96.71±5.65	92.16±13.17	4.55 (-0.70 – 27.80)	0.038
TCP Set 2	10^7	100±0.00	99.99±0.05	0.02 (0.00 – 0.20)	0.180
	10^8	99.98±0.07	99.86±0.41	0.12 (0.00 – 1.50)	0.042
TCP Biosuite	10^7	100±0.00	100±0.00	0.00	NA

When a higher clonogenic density of 10^8 cells/cm^3 was used, the mean TCP value decreased in both the CCC plans (96.71 ± 5.65%) and MC plans (92.16 ± 13.17%). It was found that only two CCC plans and four MC plans had 100% TCP. The greater decrease was observed in the MC plans, resulting in a lower mean TCP value compared to the CCC plans. The difference was statistically significant (p=0.038), with the maximum difference of up to 27.80%. This largest difference was observed in plan 17, which associated with a TCP reduction from 79.30% when the plan was calculated using CCC to 51.50% when the Monte Carlo simulation was used. The TCP reduction was also observed for plans 6, 12, and 18, which all had a relatively large PTV volume (>50 cm^3), as shown in Figure 6.1. Interestingly, plan 7, which had a medium PTV volume (i.e., 34.29 cm^3), also demonstrated a significant difference (13.80%) between the CCC and MC plans.

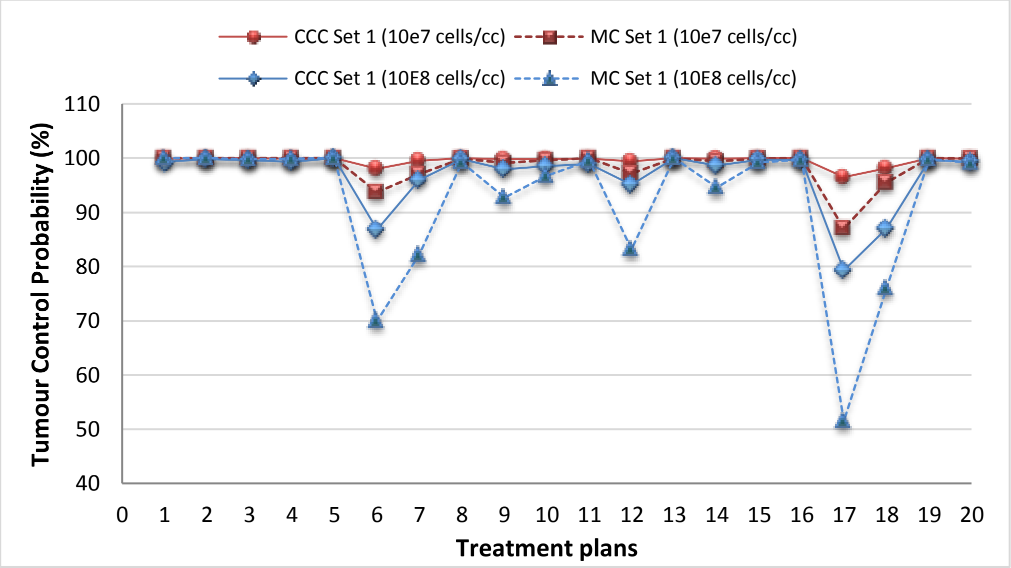

Figure 6.1. TCP value of the lung SBRT plans calculated using the first parameter set of the Poisson LQ model with the clonogenic cell density of 10^7 cell/cc (red markers) and 10^8 cells/cc (blue markers). A significant reduction on the TCP value was observed in the plans with a large PTV volume when the plans were calculated using the MC algorithm.

The TCP calculation using the second set of the LQ Poisson model parameters shows that the TCP of >99% was achieved almost in all plans for both the clonogenic cell densities, as shown in Figure 6.2. An exception was again the MC plan of patient 17, in which the TCP value was 98.2%. There was no significant difference in the TCP value between the CCC (mean value of 100%) and MC (mean value of 99.99% ± 0.05%) plans for the 10^7 cells/cc clonogenic density (p=0.18), while the difference in the TCP value calculated using the clonogenic density of 10^8 cells/cc was statistically significant (p=0.042). The TCP calculation using the default model parameters in the Biosuite software resulted in all plans having a TCP of 100%. This may be attributed to the dose received by the tumour being in the flat part of the dose-response curve, resulting in a constant value of the TCP.

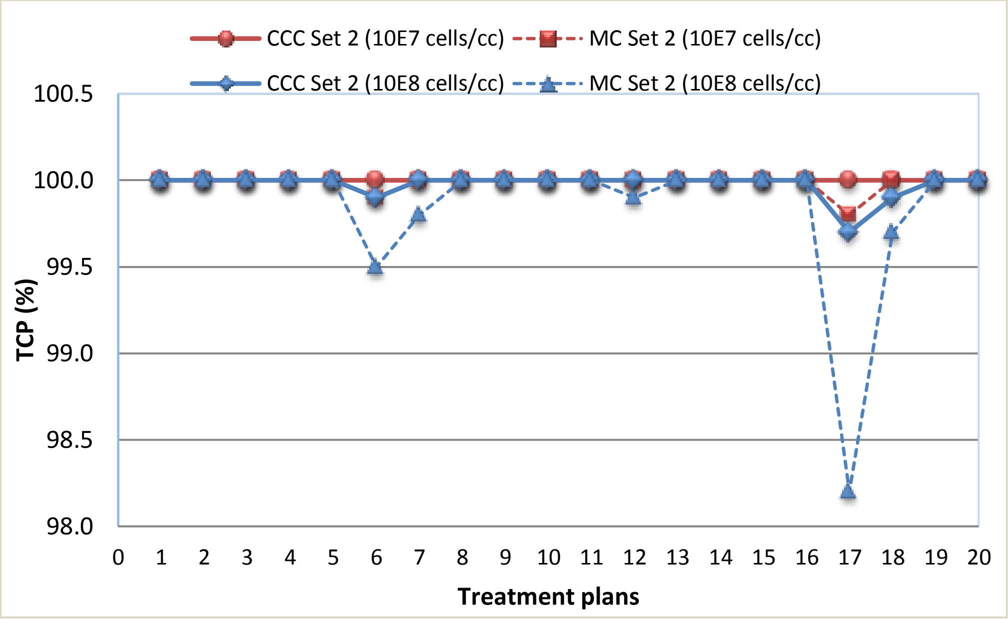

Figure 6.2. The TCP of lung SBRT plans calculated using the second parameter set of Poisson model with the clonogenic density of 10^7 (red markers) and 10^8 cells/cc (blue markers).

Plotting the PTV volume against the TCP from both the CCC and MC plans shows that the TCP difference tended to be larger for a PTV volume larger than 50 cm^3 (Figure 6.3). This explains why plans 6, 12, 17, and 18 showed larger differences, as these plans had a relatively larger PTV volume.

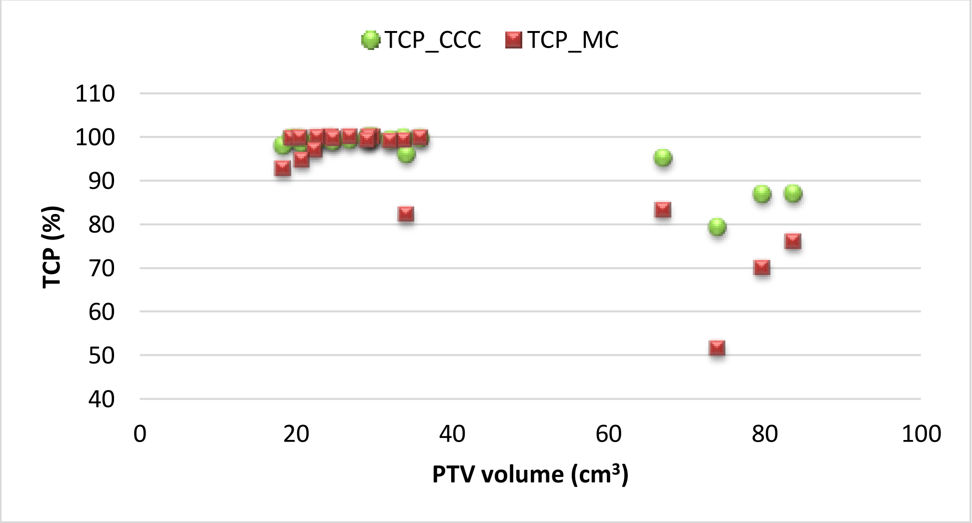

Figure 6.3. The relationship between the PTV volume and TCP calculated using the first set of the LQ Poisson model parameters with the clonogenic cell density of 10^8 cells/cc.

It was initially thought that the difference in the calculated TCP between the CCC and MC plans was caused by the difference in the PTV coverage of the prescribed isodose (PTV_{54Gy}). However, as shown in Figure 6.4, there was no linear relationship between the difference in the PTV_{54Gy} coverage and the difference in the TCP from the CCC and MC plans.

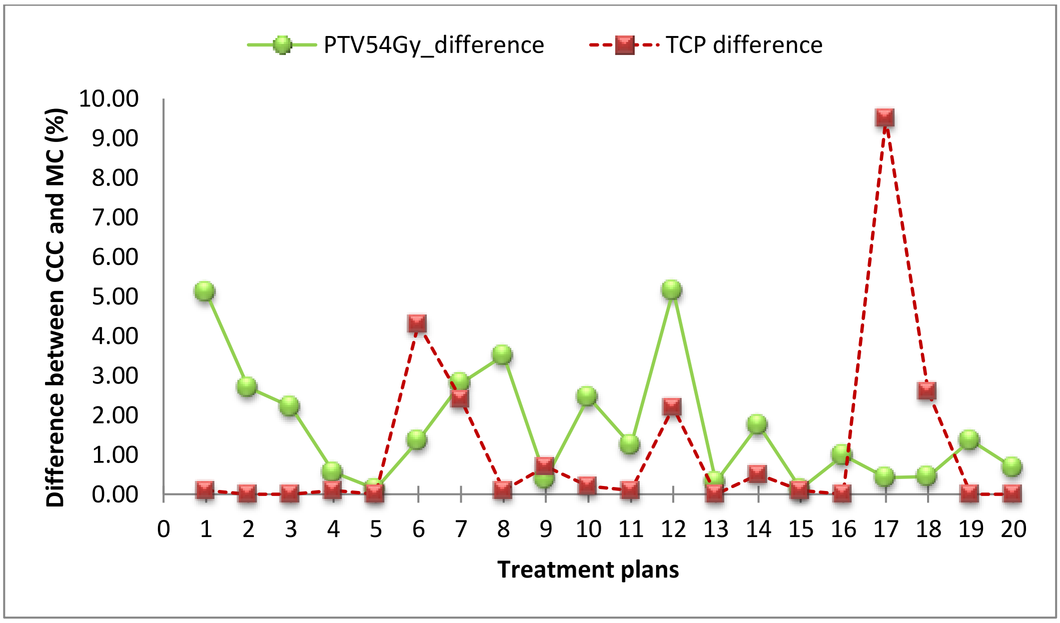

Figure 6.4. The relationship between the difference in the PTV_{54Gy} coverage and the difference in the TCP from the CCC and MC plans. No linear relationship could be drawn between the PTV_{54Gy} coverage and the TCP.

Figure 6.5 shows that the minimum dose to the PTV (D_{min}) seems to have better correlation with the TCP value. There is a tendency that as the PTV D_{min} increases the TCP will increase and reach a maximum value after the PTV D_{min} of about 45 Gy. Plan 7, which was previously shown to have a relatively lower TCP compared to the other plans with a medium PTV volume size, was found to have the PTV D_{min} of 40.1 Gy when the plans were recalculated using the MC simulation. This D_{min} value was close to the D_{min} value of the plans with a larger PTV volume. The relationship between the PTV D_{min} and the TCP values from the lower bound of model parameters was described with a correlation coefficient from Spearman's rho test of 0.84 and 0.90 for the CCC and MC plans, indicating a strong correlation for both lower and upper clonogenic density values.

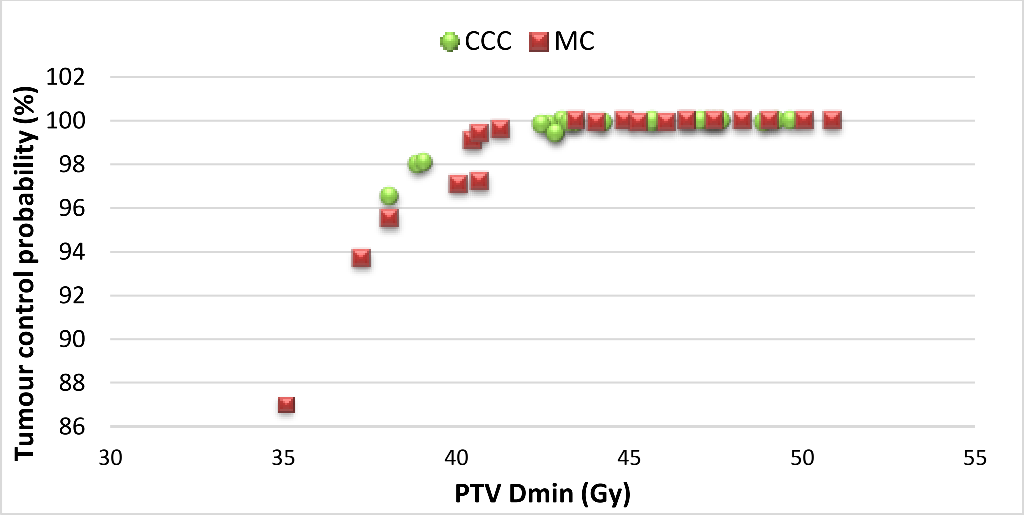

Figure 6.5. The relationship between the PTV D_{min} to the TCP calculated using the first set of the LQ Poisson parameters with the clonogenic cell density of 10^7 cells/cm^3.

6.4.2 NTCP estimation

Table 6.7 presents the NTCP values of the total normal lung tissue (minus ITV), oesophagus, heart, and rib complications.

Table 6.7: *The NTCP Values of Radiation Pneumonitis, Acute and Late Oesophagitis, Pericarditis, and Rib Fracture*

Endpoints	LKB model parameters	Mean NTCP value		Mean difference (%)	P-value
		CCC (%)	MC (%)		
Radiation pneumonitis	Wennberg's	5.60±2.82	5.60±2.77	0.00 (-0.40 – 0.30)	1.00
	Hedin's	3.15±1.59	3.11±1.55	0.03 (-0.20 – 0.30)	0.25
Acute oesophagitis	Chapet's	0.41±0.31	0.38±0.27	0.03 (0.00 – 0.10)	0.01
	Belderbos'	0.67±0.31	0.62±0.29	0.06 (0.00 – 0.20)	0.001
Late oesophagitis	Burman's	0	0	0	NA
Pericarditis	Glagiardi's	0	0	0	NA
Rib Fracture	Burman's	59.54±46.97	58.31±47.90	1.24 (0.00 – 11.30)	0.07
	Scheenstra's	10.70±9.13	10.58±9.56	0.12 (-5.40 – 2.90)	0.77

With the exception of the NTCP for the rib fracture, the mean NTCP values for the selected organs at risk were relatively low. The paired t-test analysis also shows that there was no significant difference in the NTCP from the CCC and MC plans, with the exception of the acute oesophagitis complication probability. The NTCP for late oesophagitis and pericarditis was zero in all plans.

Radiation pneumonitis (RP)

The probability of the RP from the twenty lung SBRT plans is presented in Figure 6.6. There was no significant difference between the RP of the CCC plans and the RP of the MC plans calculated using Wennberg (p=1.00) and Hedin LKB model parameters (p=0.25). The NTCP values calculated using these two parameters show a similar trend. However, the NTCP value of the RP calculated using the Wennberg parameter was higher than those calculated using the Hedin parameter. The probability of radiation pneumonitis is likely to be higher for cases with a large PTV volume. Figure 6.6 shows that plans 6, 12, 17, and 18, which had the largest PTV volume (>50 cm^3), showed higher RP probabilities. The highest RP probability of 13.4% was observed in plan 18, which had the largest PTV volume among all plans.

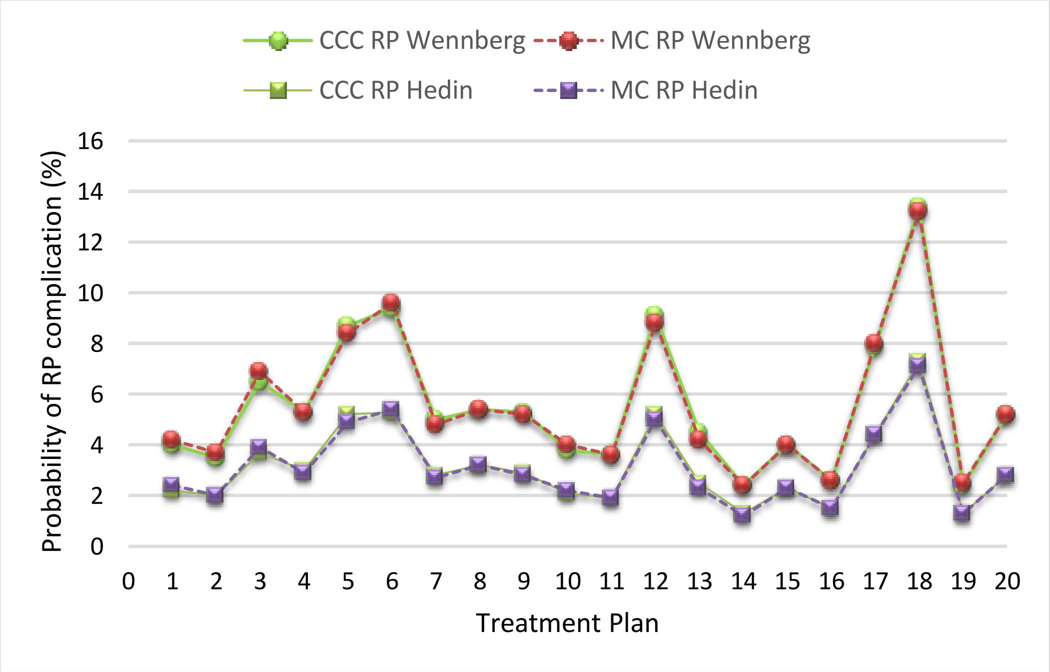

Figure 6.6. The probability of radiation pneumonitis complication calculated using two different sets of LKB parameters. No significant difference was observed between the RP of the CCC plans and the RP of MC plans for two LKB parameter sets (p=1.00 and p = 0.25, for the Wennberg and the Hedin parameters, respectively).

A bivariate correlation analysis was performed to evaluate the relationships between the lung dose-parameters and the NTCP of RP endpoint. The Pearson correlation test was used, as the RP data was distributed normally, assuming a linear relationship. The relationship between the RP probability calculated using the Wennberg parameter and the PTV volume is shown in Figure 6.7. It is shown that four plans with a PTV volume of >50 cm^3 had a higher probability of RP complication (>8%) compared to other plans. An exception is plan 5, which also shows a higher RP probability, although the PTV volume for this plan was <50 cm^3. The Pearson correlation coefficient was 0.86 for the CCC plans and 0.87 for the MC plans, indicating a strong correlation between the PTV volume and the RP probability.

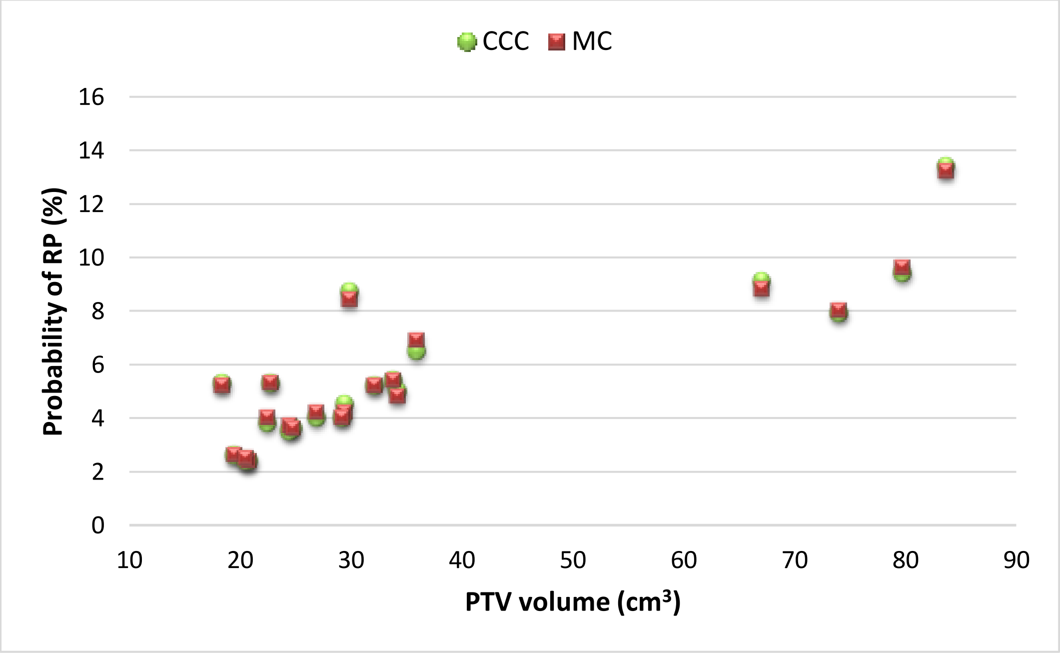

Figure 6.7. The relationship between the probability of RP complication calculated using Wennberg parameters and the PTV volume. The plans with a PTV volume >50 cm^3 show a higher probability of RP.

The investigation of the relationship between the mean lung dose (MLD) and the probability of RP showed a strong correlation between these parameters, as depicted in Figure 6.8. The Pearson correlation coefficient for these parameters was 0.84 for both the CCC plans and the MC plans. There is a tendency that the probability of RP is higher (>6%) when the MLD is above 4.5 Gy.

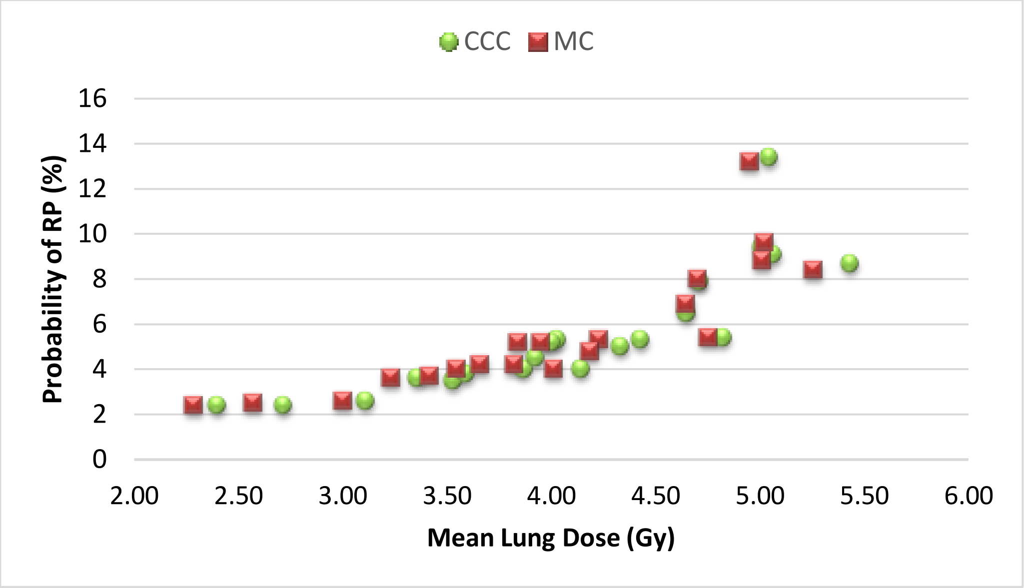

Figure 6.8. The correlation between the mean lung dose and probability of radiation pneumonitis complication. The probability of the radiation pneumonitis is likely to be higher if the mean dose to the normal lung tissue increases.

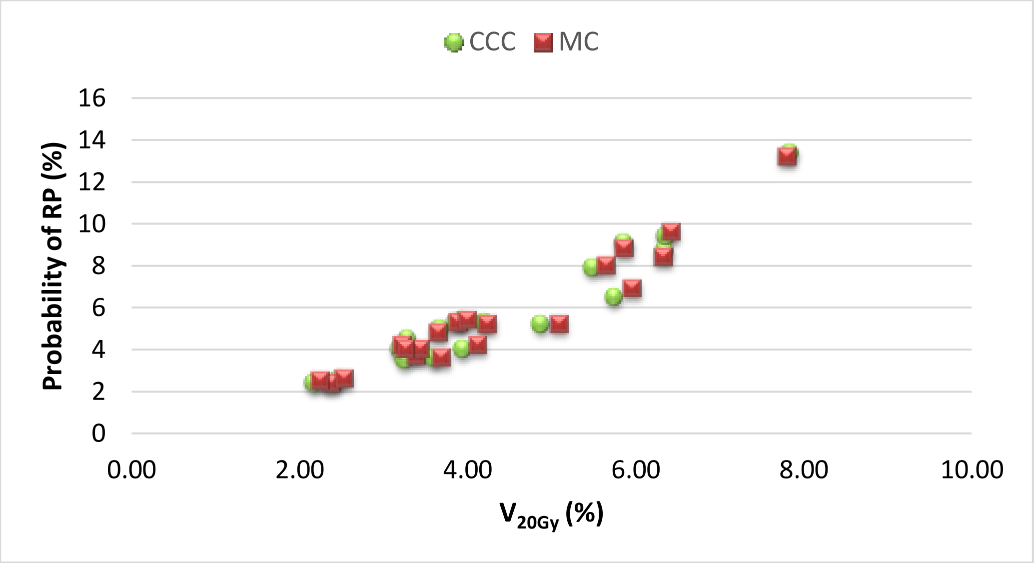

Figure 6.9. A positive correlation between the V_{20Gy} and the probability of the radiation pneumonitis for the CCC and MC plans.

In addition to the MLD, the volume of the normal lung tissue receiving a dose of larger than 20 Gy (V_{20Gy}) is commonly used as the predictor of RP [174]. Figure 6.9 shows the correlation between the V_{20Gy} and the NTCP for RP for the twenty lung SBRT plans. Similar to the MLD, a positive correlation was also observed between V_{20Gy} and the probability of RP as expected. This confirms why V_{20Gy} is used as a constraint for normal lung tissue as recommended in the TROG 0902 CHISEL trial. The Pearson correlation test resulted in a correlation coefficient of 0.96 between these parameters for both the CCC and MC plans. This indicates a strong relationship between V_{20Gy} and the RP probability.

The use of MLD and V_{20Gy} as predictors of radiation pneumonitis risk was outlined in the RTOG 0236 and 0618 trial protocols. A similar relationship was also observed for the $V_{11.4Gy}$ parameter, as outlined in the RTOG 1021 protocol. Table 6.8 lists the correlation coefficient of the lung dose-volume parameters to the estimation of RP probability. The V_{20Gy} is shown to have the highest correlation coefficient compared to the other dose-volume parameters, indicating that the V_{20Gy} could be used as a predictive factor of RP probability.

Table 6.8: *The Pearson Correlation Coefficient of the Lung Dose-volume Parameters and the Probability of Radiation Pneumonitis*

Parameters	Pearson correlation coefficient		Strength of relationship
	CCC	MC	
MLD	0.84	0.84	Strong
V_{20Gy}	0.96	0.96	Strong
$V_{11.4Gy}$	0.77	0.76	Strong
$V_{10.5Gy}$	0.78	0.77	Strong
PTV volume	0.86	0.87	Strong

Figure 6.10 shows the plot of the V_{20Gy} and the probability of RP for the twenty lung SBRT plans. Plan 5, which had a PTV volume of <50 cm^3, showed a higher probability of having RP due to the high value of its lung V_{20Gy}. The V_{20Gy} of this plan was almost as high as the V_{20Gy} of plan 6 that had a PTV volume of >50 cm^3. Further investigation showed that the volume of normal lung tissue receiving a dose larger than 11.4 Gy in plan 5 ($V_{11.4Gy}$) was the same as the value in plan 6, that is, 0.16% of the total normal lung tissue of these plans. However, it should be noted that the total volume of normal lung tissue in plan 6 was higher than plan 5. The $V_{11.4Gy}$ values of these two plans were the highest compared to other plans. This indicates that volume is an important parameter for maintaining a lower toxicity to the normal lung tissue. There was significant difference in the mean V_{20Gy} calculated by the CCC plans, 4.30%

(2.18%-7.85%) and the MC plans, 4.37% (2.25%-7.81%) with the p-value of 0.002. The relative difference of the V_{20Gy} calculated using the CCC and MC plans was -1.64% on average, ranging from -4.51% to 1.87%.

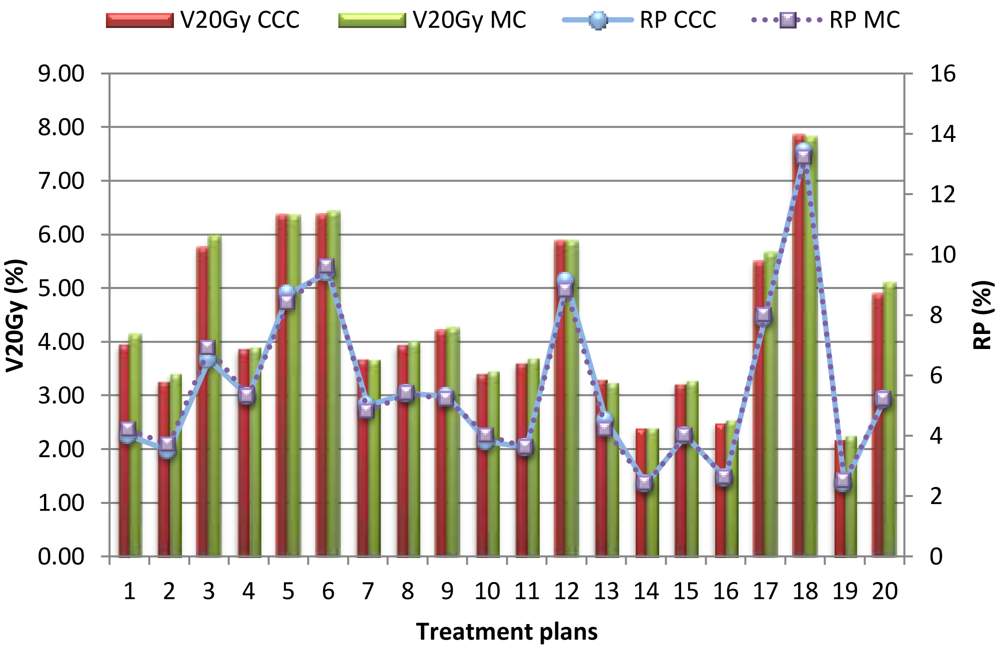

Figure 6.10. The relationship between the V_{20Gy} and the RP probability of the twenty SBRT plans.

Pericarditis

The NTCP modelling of pericarditis showed zero value in all plans. This indicates that the probability of pericarditis from the SBRT treatment evaluated in this study was negligible. However, it should be noted that the maximum dose to the pericardium exceeded the constraint in three plans (plans 3, 12, and 18). The largest maximum dose to the pericardium was observed in plan 12, i.e., 39.1 Gy for both the CCC and MC plans, exceeding the maximum dose cut-off of 30 Gy. In this plan, the tumour was located in the middle lobar of the left lung, which caused the pericardium to receive a higher dose. For the rest of the plans, the dose to the pericardium was below the threshold dose, as most of the tumours were located in the right lung (14 out of 20 plans).

Stenosis/fistula of oesophagus

The oesophagus is considered to function as a serial organ arrangement. The NTCP modelling of late oesophagitis shows a zero value, indicating that the complication would be very small. As shown in Chapter 4, the dose-volume parameters of the oesophagus were below the constraints in all plans. Therefore, the expected complication would also be minimal.

The NTCP modelling of acute oesophagitis had a mean value of 0.67% (CCC plans) and 0.62% (MC plans) for the Belderbos LKB parameters and 0.41% and 0.38% for the Chapet LKB parameters. The highest NTCP for acute oesophagitis was observed in plan 8, where the likelihood of complications was 1.5% for the CCC plan and 1.3% of the MC plans (Figure 6.11). These values were associated with no toxicity of grade 2-3 oesophagitis, as these were lower than the threshold value of 9.8%, as reported by Chapet *et al.* [193].

There was a significant difference for acute oesophagitis between the CCC and MC plans, in which the CCC showed a higher probability of acute oesophagitis compared to the MC plans. This appears to be due to the oesophagus structure receiving a higher maximum dose when the plan was calculated using the CCC. The Pearson correlation test shows a correlation coefficient of 0.67 (CCC) and 0.69 (MC) between the maximum dose to the oesophagus and the acute oesophagus probability.

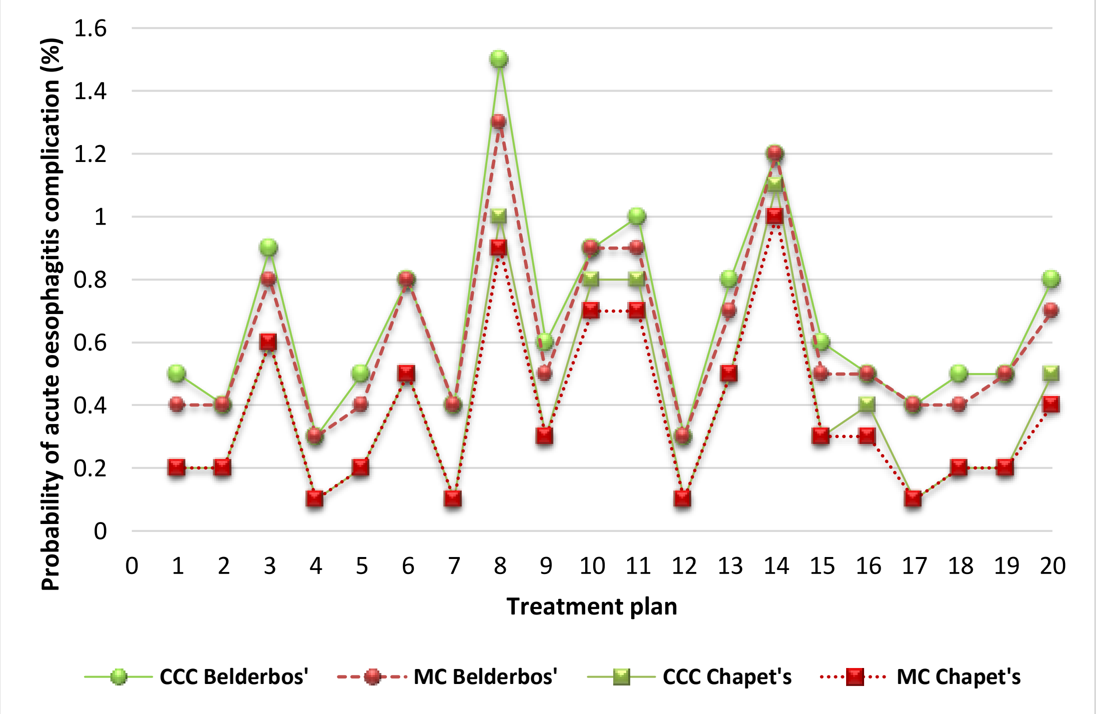

Figure 6.11. The probability of the acute oesophagitis from the CCC and MC plans calculated using the LKB parameters adopted from Belderbos and Chapet.

Rib fractures

Rib fracture and associated chest wall pain have been reported after SBRT treatments. The NTCP modelling of rib fracture using the LKB model parameters adopted from Burman *et al.* [187] showed a 100% complication probability in plans with a PTV close to or overlapping the chest wall PTV (11 out of 20 plans). The rest of the plans showed a probability of rib fracture of less than 50%. This high complication probability is possibly due to the high maximum point dose received by the rib structure. As shown in the previous chapter, the maximum point dose in these 11 plans exceeded the defined dose threshold (i.e., 50 Gy).

However, the NTCP modelling that used the LKB parameters fitted for the SBRT treatment [194] showed a lower rib fracture probability compared to the Burman LKB parameters results. The mean value of NTCP was 10.70% (0.50%-25.10%) and 10.58% (0.50%-30.50%) for the CCC plans and MC plans, respectively. There was no significant difference in the rib fracture probability between the CCC and MC plans (p=0.77). The plans a PTV structure at the chest wall had a probability of rib fracture of larger than 10%. The highest probability of rib fracture was observed in plan 10, which had an estimated 25.10% and 30.50% complication risk for the CCC and MC plans. This was attributed to the maximum dose to the ribs of this plan, which was the highest of all plans, 63.1 Gy and 65.5 Gy for the CCC and MC plans, respectively.

The Pearson correlation coefficient for the maximum dose to the ribs (MPD) and the rib fracture probability was 0.97 for the CCC plans and 0.95 for the MC plans. This indicates that maximum dose to the ribs had a better correlation to the probability of rib fracture risk. Figure 6.12 shows this relationship, in which the risk of rib fracture increased significantly after the maximum point dose exceeded 50 Gy value, while when below 50 Gy, the risk of rib fracture increased more slowly.

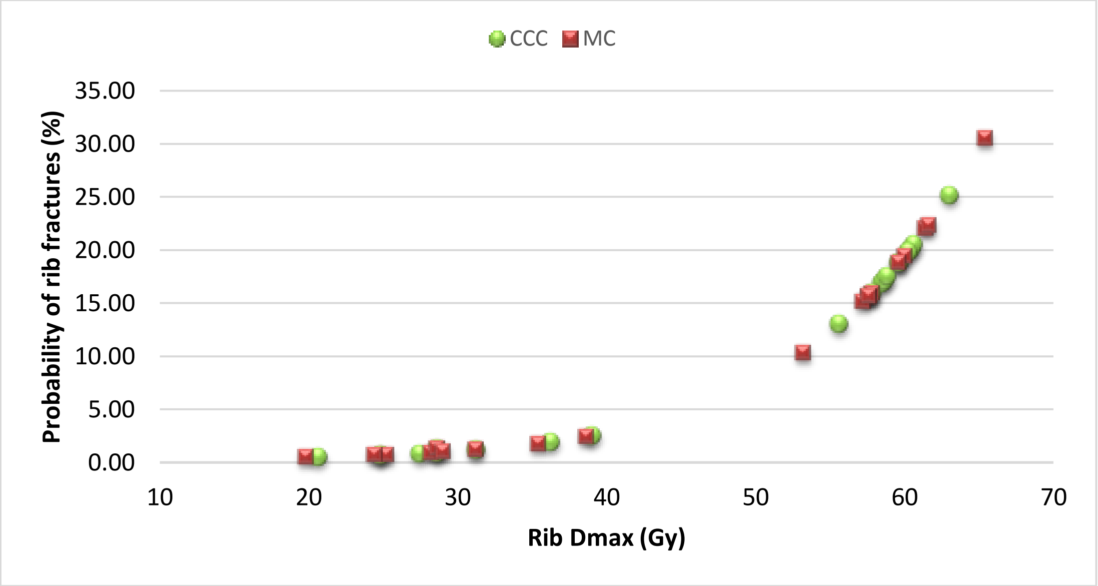

Figure 6.12. The relationship between the maximum point dose to the ribs and the probability of rib fracture complication.

6.5 DISCUSSION

Radiobiological modelling provides an estimation of the probability of tumour control and normal tissue complication for given dose distributions. This aids in optimisation of treatment plan dosimetry, and complements the physical dose parameters, such as isodose lines and dose-volume histogram, which are commonly used. Biological evaluation has now been integrated into commercial TPS in order to achieve an optimal radio therapeutic ratio.

The results of this study show that there was a significant difference in the TCP estimation between the CCC and the MC plans calculated using the lower bound of the LQ Poisson model parameters with the clonogenic density of 10^7 cells/cm^3 and 10^8 cells/cm^3. The mean value of the estimated TCP of the CCC plans was higher than that of the MC plans, which might indicate an overestimation of the dose to the PTV by the CCC plans. However, the TCP estimation using the upper bound of the LQ Poisson model parameters showed a significant difference only when the clonogenic cell density of 10^8 cells/cm^3 was used. In addition, the estimated TCP using the upper bound had a value of >99% in almost all plans, except in one plan, which had a TCP value of 98.02%.

The difference in the TCP value estimated using the lower and upper bound of the LQ Poisson parameters might be attributed to the value of the alpha parameter. As shown in Table 6.1, other than the alpha and the alpha/beta ratio, all variables in set 1 (lower bound) and set 2 (upper bound) contained the same values. The alpha value used in set 2 was closer to the default value used in the Biosuite software, which was derived from Webb and Nahum [184]. The calculation using the Biosuite LQ Poisson model parameters resulted in a TCP of 100% in all plans, in both the CCC and MC plans. Although the higher alpha/beta ratio was used in set 2, the estimated TCP value from all plans was >98%, indicating that the prescribed dose results in excellent local tumour control. In addition, it is most likely the case that the biologically effective dose received by the target (PTV) is in the high dose flat region of the dose-response curve; therefore, a change in the dose only resulted in a small change in the TCP [185].

However, when lowering the alpha value to 0.19 Gy^{-1} in set 1 with an alpha/beta ratio of 9.5 Gy^{-1}, a TCP reduction up to 9.5% was observed in the MC plans. Increasing the density of clonogenic cells to 10^8 cells/cm^3 caused a further TCP reduction of up to 27.80% in the MC plans. It would appear that the alpha value that represents the probability of irreparable damage has a significant influence on the TCP estimation. If the alpha value is lower, the portion of irreparable damage of the tumour clonogens is lower [98]. If this situation is also accompanied by a constant value of beta, the portion of the tumour clonogens that undergo repair after the irradiation damage will be higher. As a consequence, this reduces the probability of tumour control; as the repairable damage to tumour cells is much higher than the irreparably damaged tumours cells. The effect is more significant if the density of the tumour clonogens is higher (e.g., increases from 10^7 to 10^8 cells/cm^3). This has consequences for inter-patient variability in dose response, that is, the same dose delivered to different patients will result in different responses due to clonogenic density. Moreover, for intra-patient variability, variability in tumour clonogenic cell density across a tumour will result in a variable response. In addition, the sensitivity of a patient to dose uncertainties is also dependent on clonogenic cell density. This highlights the importance of quality assurance of radiotherapy treatment to ensure that the delivered dose is as per the planned dose, and the importance of accurate dose calculation. The reduction of the probability of local control is more significant for larger tumour volumes, which contain more tumour clonogens compared to the smaller tumours. This explains why a greater reduction in

TCP was observed in the plan with a large PTV volume (>50 cm^3), as shown in Figure 6.3.

This study has also shown that the minimum dose (D_{min}) to the PTV strongly correlated with the estimated TCP value compared to other PTV dosimetric parameters. This explains why plan 7, with a PTV volume <50 cm^3, also experienced a greater TCP reduction when calculated using the Monte Carlo simulation. In this plan, the PTV D_{min} was 40.1 Gy, slightly lower than the PTV D_{min} of plan 12 (i.e., 40.7 Gy), which had a larger PTV volume. Above a D_{min} of approximately 45 Gy, the TCP will reach its maximum value and remain constant. As the CCC overestimated the D_{min} in 13 plans, this translates to a higher TCP value estimated from the CCC plans.

A similar finding for the strong relationship between the PTV D_{min} and the TCP was reported by Chetty *et al.* [22]. They investigated the TCP from the plans calculated using a pencil beam (PB) algorithm with a 1-D equivalent path length and recalculated the plans using more advanced model based algorithms. They found that recalculating the PB-plans using the superposition convolution algorithms (AAA, CCC, and Acuros XB) showed a PTV D_{95} reduction of up to 20%. However, it was not the D_{95} that had a strong impact on the TCP, but the PTV D_{min}.

The overestimation of the dose to the target by the CCC that would cause an under-dosage to the tumour is likely due to the limitation of the CCC in modelling the lateral electron scattering at the tissue interface. The additional lower dose of the laterally scattered electron energy might then be deposited into the normal lung tissue. The situation is worse in smaller tumour volumes that are completely surrounded by normal lung tissue, due to the combination effect of a loss of charged particle equilibrium and an increase of lateral electron scattering. However, the effect might not be obvious in the lung SBRT plans compared to the slab phantom experiment, which only used a single beam. In the SBRT plans, a small amount of normal lung tissue was included in the PTV volume to take into account tumour motion due to the breathing. As the dose is prescribed at the PTV periphery, it could be assumed that the tumour (not the PTV) received an adequate dose. Therefore, the effect of an under-dosage ring surrounding the tumour could be minimised. Valdes *et al.* [185] found a TCP of >99% from the lung SBRT plans with the dose prescription of 3 x 18 Gy/fractions and argued that as long as an adequate dose was applied along with the use of image guidance, local control of >90% could be achieved.

The second important finding of this study is the low NTCP value of radiation pneumonitis with a mean value of 5.60 ± 2.82% and 5.60 ± 2.77%, for the CCC and MC plans, respectively. There was no significant difference in the RP probability from the CCC and MC plans. The majority of the plans had an NTCP of RP probability of below 10%, with only one plan with a large PTV volume with an NTCP of 13.4%. This might indicate that the risk of RP is relatively low for the lung SBRT plans evaluated in this study.

This study shows that the lung V_{20} had strong correlation with the NTCP for RP, followed by the mean lung dose (MLD). These two dose parameters might be useful as the predicting factor of RP. The V_{20} was 4.30% (2.18%-7.85%) for the CCC plans and 4.37% (2.25%-7.81%) for the MC plans. This correlates with an NTCP of 5.6% (2.4%-13.4%) and 5.6% (2.4%-13.2%) for the CCC and MC plans, respectively. The V_{20} parameter was recommended in the RTOG 0236 and 0618 trials with the limit value of 10% and should be kept below 5% whenever achievable. As this study shows that majority of plans had the V_{20} of ≤5% (14 of plans) and the maximum V_{20} was still below 10%, this may correlate with the <10% risk of grade 2-4 pneumonitis as reported by Barriger *et al.* [174].

Barriger *et al.* [174] recommended the use of MLD as the predicting factor of the RP as a complement to the $V_{20.}$ In this study, the MLD value ranged from 2.29 to 5.40 Gy, with a corresponding NTCP of less than 10%. An exception in one plan with an MLD of 5.05 Gy (CCC) and 4.95 Gy (MC) gave a NTCP of 13.4% and 13.2%, respectively. Although the MLD of this plan was not the highest among all plans, it's V_{20} was the highest. The QUANTEC paper recommended to use MLD to predict the RP complication, in which MLD of 7 Gy was associated with complication rate of 5% [195]. Although in this study V_{20} has a stronger correlation with the RP than MLD, both V_{20} and MLD could be used for the RP risk prediction. It is important to note that the higher value of V_{20} observed in this study was associated with a lower volume of total lung (minus ITV). Therefore, it might be useful to consider using a lower dose prescription for patients with a smaller lung volume, as the risk of the RP will be higher for those patients if the same dose is prescribed as for those with a larger lung volume.

In addition, this study found that as the PTV volume increased, the probability of RP also increased, as predicted by Barriger *et al.* [174]. The plans with a PTV volume >50 cm^3 had a higher risk of RP, which is indicated by the NTCP values of >

8%. Barriger *et al.* [174] reported a cut-off PTV volume of ≤48 cm^3 associated with 6.4% risk of grade 2-4 pneumonitis. Above this volume, a risk of grade 2-4 pneumonitis of up to 13% was observed. This is possibly due to the amount of normal lung tissue that received the prescribed dose being higher for the large PTV volume. The MC simulation showed a larger volume of normal lung tissue receiving the prescribed dose (i.e., 54 Gy) in 12 plans, which was underestimated by the CCC algorithm. This possibly explains the additional dose to the normal lung at the margins of the tumour due to the effect of an increase in lateral electron scattering and different tissue density values of the tumour and lung. The process might be more complex when the tumour is located close to bony tissues, such as ribs, as the degree of heterogeneity increases.

These findings support the recommendation for restricting the use of SBRT treatment for “small” volume lung tumours to limit the volume of normal lung tissue exposed to the ablative dose (>10Gy/fraction). This is because a larger PTV results in a larger amount of normal lung tissue being irradiated, which potentially poses a higher risk for radiation pneumonitis. For larger tumours, modified dose fractionated schedules need to be used, that is, more fractions or larger dose/fraction.

Another critical volume parameter $V_{11.4Gy}$, which was recommended by the RTOG 1021 and commonly used in the SBRT plan evaluation, is also useful as the predicting factor of the RP. The risk of RP increases as $V_{11.4Gy}$ increases. However, this study shows that the predictive factor of these volume parameters was lower than V_{20Gy} and MLD. In addition, the use of lung V20, MLD and $V_{11.4Gy}$ dose parameters as the predictive factors of RP risk needs to be validated in the actual treatment by evaluating the reported RP toxicities during follow up of the treatments.

No risk of pericarditis and no late oesophagitis were observed from the NTCP estimation in this study. This is possibly due to the dose constraint of these organs being below the defined constraint. An exception was the maximum point dose to the pericardium in plan 12 which had a value of 39.1 Gy, exceeding the dose constraint of 30 Gy. For this case, the tumour was located closer to the pericardium, causing the higher dose to the pericardium.

The estimation of acute oesophagitis shows that the maximum NTCP of 1.5% for the CCC and 1.3% for the MC plans was observed. These values are much lower than reported by Chapet *et al.* [193] to produce the acute oesophageal toxicity. Chapet *et al.* [193] found that most grade 2-3 acute oesophagitis had an NTCP of >11% and no toxicity was observed for the NTCP <9.8%. This indicates that the risk of acute oesophagitis in the plans evaluated in this study was very low. The NTCP calculated using the LKB parameters from [192] was even lower than those calculated using Chapet's LKB parameter. In addition, this study found a positive correlation between the maximum point dose and NTCP of acute oesophagitis. This implies the maximum point dose could be used as a predictive factor of the probability of acute oesophagitis risk.

The NTCP calculation to estimate the risk of rib fracture resulted in a mean value of 10.70% for the CCC and 10.58% for the MC plans. There was no significant difference in the rib fracture NTCP between the CCC and MC plans. It is important to note that the plans with the tumour at the chest wall showed a higher risk of rib fracture, with the NTCP value of >10%. There was a strong correlation of the maximum dose to the rib and the NTCP of the rib fracture. The probability of rib fracture increased rapidly after the maximum dose exceeded 50 Gy. A similar finding was reported by Andolino *et al.* [177], in which the dose maximum cut-off for the rib toxicities was 50 Gy. As observed in this study, the risk of rib toxicities also increased significantly with the probability of chest wall pain. Most of the previous studies related the dose-volume parameters to the chest wall as the predictive factor of the rib fracture and chest wall pain. For instance, Dunlap *et al.* [196] reported that a V_{30} of 35 cc to the chest wall was correlated with a 30% risk of severe chest wall pain. While Stephans *et al.* [197] found that the V_{30} cut-off of 30 cc might result in a 10-15% risk of chest wall toxicity. This study found that the V_{30} to the chest wall exceeded 30 cc in 7 plans. These plans also had the maximum dose to the ribs, >50 Gy, which resulted in a higher NTCP value for the rib fracture probability estimation. Here, the role of radiobiological modelling is critical; thus, the plan is optimised not only based on the physical dosimetric parameters, but also the probability of tumour control and normal tissue complication. There could be a trade-off between the PTV coverage and the level of normal tissue toxicity.

Different levels of biological optimisation proposed by Nahum and Uzan [57] could be adopted. The first level is varying the dose prescription while maintaining a constant NTCP of the critical organs, maintaining a fixed isotoxicity. The second level is optimising the dose prescription and the fractionation for a fixed isotoxicity. The third level involves an inverse planning approach in which the TCP is maximized for a given NTCP. And the last level includes patient specific functional imaging information, such as clonogen location. Considering these biological optimisation levels, it might be possible to move from population-based dose prescription to individual-patient based dose prescription, offering a higher chance of optimising the radio therapeutic ratio.

The limitation of this study comes from difficulty in finding the appropriate biology modelling parameters to calculate the TCP and NTCP. The parameters were adopted from literature, which may be fitted from treatment plans with different dose fractionation and/or different algorithms. In addition, the use of LQ model for a large fraction treatment (>10Gy), which occur on the linear portion of survival curve, are still a matter of debate regarding its validity. There is some issue of overestimation of cell kill by the LQ model for the dose >6 Gy. Some models have been proposed to model the dose response curve for SABR treatment, such as multitarget model, or lethal-potentially model [74].

However, it should be noted that the use of radiobiological models in the TPS is aimed only at a comparative evaluation tool in the treatment plan optimisation process. It provides metrics (i.e., TCP and NTCP) that are more relevant to a clinical outcome than an evaluation based on physical dose only, such as DVHs. Therefore, the radiobiological models are not suitable for absolute assessment of TCP and NTCP in individual patients. Comprehensive discussion on the use of radiobiological models in the treatment planning was presented in the AAPM TG-166 report, which can be used as a guideline for radiobiological optimisation of radiotherapy plans [107].

6.6 CONCLUSION

This study found that there was a significant difference in the estimated TCP values from the CCC plans and MC plans; however, no significance was observed in the NTCP of the radiation pneumonitis and rib fracture. The study also found that the probability for pericarditis and oesophagitis from the evaluated plans was relatively low. A greater risk of rib fracture was observed, especially for the plans with a wall-seated tumour. The study found that the PTV D_{min} had a strong correlation with the TCP, as well as the selection of an alpha value of the LQ Poisson model. Lung V_{20} and MLD had a strong correlation with the risk of radiation pneumonitis, while maximum dose to the oesophagus and ribs showed a better correlation for acute oesophagitis and rib fracture probabilities.

Chapter 7: Conclusions

This chapter outlines the general discussion of the key research findings (Section 7.1), the recommendation for future works (Section 7.2), and the conclusions drawn from the research (Section 7.3).

7.1 GENERAL DISCUSSION

The main aim of this research was to investigate the dose calculation accuracy of the TPS algorithm used in the planning of SBRT treatment for early stage NSCLC (T1-T2aN0M0) using Monte Carlo simulation. The problems addressed in this research were the accuracy of the CCC algorithm employed in the Pinnacle^3 Radiotherapy TPS in calculating the dose to the PTV and OARs of lung patient SBRT plans and the impact of any dose uncertainties on the estimation of treatment outcomes represented by tumour control probability (TCP) and normal tissue complication probability (NTCP). In order to achieve the research aim, the research was undertaken in three phases:

- Phase 1: Development and commissioning of a Monte Carlo model of an Elekta Axesse linear accelerator used for radiation delivery of lung SBRT treatments.
- Phase 2: Dosimetric verification of the lung SBRT plans previously optimised using CCC algorithm in the Pinnacle^3 TPS by recalculating the plans using Monte Carlo simulation.
- Phase 3: Evaluation of TCP and NTCP of the lung patient SBRT plans through the use of radiobiological models.

The following section provides a summary of the key findings and outcomes for each of the research objectives.

7.1.1 Research Objective 1: Development and validation of a Monte Carlo model of an Elekta Axesse linear accelerator used for delivery of the lung SBRT treatment plans

In Phase 1, a Monte Carlo model of the Elekta Axesse linear accelerator equipped with Beam Modulator micro-MLC producing a 6 MV photon beam was developed and commissioned against the measured dosimetry data. This linear accelerator was specifically designed for stereotactic treatments by the inclusion of a 4 mm MLC leaf width, enabling the creation of a highly conformal treatment field shape. The linear accelerator modelling was the first step in order to use the Monte Carlo technique as an independent verification tool of the TPS algorithm performance. Commissioning of the model was essential to ensure the validity of the model, which included a comparison of the depth dose curves, lateral dose profiles, and output factors.

The optimisation of the electron beam parameters, as described in Chapter 4, showed an optimum incident electron beam energy of 6.2 MeV, with an elliptical FWHM of 0.2 cm in the leaf-side direction and 0.3 cm in the leaf-end direction. The validation of the model to the field size down to 1.6 cm x 1.6 cm showed excellent agreement with the measured dosimetry data to within 1.5% in the flat dose region and 1 mm in the penumbra region. Good agreement was also achieved for the output factors to within 1% between the simulation and the measurement. The study also found that a leaf offset of 0.45 mm was required to define the MLCQ position setting for a field size of less than 5 cm in order to obtain a match between the simulated and measured profiles. This field size (<5 cm) is commonly used in lung SBRT treatments for early stage NSCLC. A small offset was also required in the direction perpendicular to the leaf travel, as the MLCQ CM does not include the air gap in the model. The statistical uncertainty of the Monte Carlo simulation in this work was better than 1%.

This research was the first study that developed an EGSnrc-BEAMnrc Monte Carlo model for specific combination of Elekta Axesse linear accelerator equipped with the Beam Modulator micro-MLC used for lung SBRT plans. The model and its source parameters optimised in this study complements previous studies that have modelled other Elekta machines used for stereotactic radiosurgery or SBRT treatments. Another platform released by Elekta for stereotactic treatments is the Elekta Synergy S, which has been modelled in previous works [67, 150]. Although the Elekta Axesse has a similar design to the Elekta Synergy S, the optimum electron beam energy found in this study was slightly lower (i.e., 6.2 MeV) than that reported for the Elekta Synergy S model (i.e., 6.5 MeV). A difference was also observed for the shape of the electron beam. This study showed that the radial dimension of the electron beam is best modelled using an elliptical shape, rather than a circular shape. This elliptical radiation source shape is similar to that reported by other groups that modelled Elekta

Synergy linear accelerators [148, 149]. Although the Elekta Synergy linear accelerator is not specifically designed for stereotactic treatments, attachment of the Beam Modulator MLC system or Elekta Agility MLC system is possible for the implementation of the stereotactic treatment.

The outcome of this part of the study demonstrated the suitability of the developed model for use in the verification of the lung SBRT treatment plans that involve the use of a small radiation field of <5 cm. The model could also be implemented to verify the SBRT plans for other tumour sites, such as the kidneys or heart. This model was then used in the next phase of the study, to verify the accuracy of the CCC algorithm for dose calculation in the planning of lung SBRT treatments.

7.1.2 Research Objective 2: Re-calculation of the dose distribution of lung SBRT treatment plans using the EGSnrc/BEAMnrc Monte Carlo codes in comparison to the TPS calculation

Phase 2 evaluated the accuracy of dose calculation by the CCC algorithm in lung SBRT plans. Twenty early stage NSCLC lung SBRT plans that had previously been optimised using the CCC algorithm employed in the Pinnacle^3 TPS were recalculated using the Monte Carlo simulation. The simulation employed the EGSnrc/BEAMnrc Elekta Axesse/Beam Modulator micro-MLC model which was developed in Research Phase 1 (described in Chapter 4).

Prior to the simulation of lung SBRT plans in CT-based patient anatomy, the BEAMnrc and DOSXYZnrc input files were generated based on the treatment plan information retrieved from the DICOM files. Verification of MLC position setting and beam orientation settings were performed to ensure that the plan information had been exported and correctly converted in the simulation input files. The verification of the MLC position setting was performed by comparing the TPS and Monte Carlo dose maps obtained in a simple homogenous water phantom. Two types of error were revealed through this simple verification method. The first error related to the error in extracting the MLC position information from the DICOM files, which affected all leaf settings. The second error related to the error in converting the DICOM-defined MLC position to the BEAMnrc-defined MLC position, which affected the individual leaf setting, especially the interdigitated leaf. The verification also found that the simulated fields reproduced the planned fields to a distance of agreement within 1 mm. The verification of the beam arrangement setting was performed to evaluate that the

DICOM-defined beam orientations (gantry, couch, and collimator rotation angles) were correctly converted to the DOSXYZnrc-defined beam orientations (theta, phi, and phicol angles). It was found that modification of the formula used to convert the DICOM-defined beam orientations to the DOSXYZnrc-defined beam orientations was required.

To investigate the agreement between the CCC algorithm and the Monte Carlo simulation in the homogenous medium, one plan was calculated using a unity density by overriding the density of all tissues within the skin contour to that of the density of water. The agreement was found to be within 2% between the CCC and Monte Carlo calculations for both low and high dose gradient regions. This result is consistent with the findings reported by other groups, in which most of the TPS algorithms, including the pencil beam algorithm, performed well in homogenous media with unity density [14, 21, 85].

As the CCC showed a good performance in the homogenous media relative to the Monte Carlo simulation, its performance in the heterogeneous patient anatomy was evaluated by comparing the dose distributions of twenty lung SBRT plans from the CCC and MC calculations in CT-based patient anatomy. The 3D gamma evaluation of the PTV structure using selection criteria of a 3% dose difference and 3 mm distance-to-agreement showed that all plans had a >99% passing rate. The average passing rate of all plans decreased to 91.86% when tighter selection criteria of 2%, 2 mm were used. The passing rate for the normal lungs (total left and right lungs minus ITV) and the chest wall was >99% for both selection criteria, although a slight reduction was observed for tighter criteria. For other OARs, the passing rate of >99% was achieved for both selection criteria. This indicates that the CCC dose distributions had good agreement with the MC dose distributions.

Further evaluation of the dosimetric parameters for the PTV and OARs were performed based on criteria outlined in the RTOG 1021 protocol due to the similarity of the dose prescription used in the trial and this study. The paired student t-test analysis showed no significant difference in the dosimetric parameters of the PTV observed between the CCC and the Monte Carlo plans. This includes the PTV coverage of the prescribed isodose (PTV_{54Gy}) and the 90% of the prescribed dose ($PTV_{48.6Gy}$), the PTV D_{min}, the PTV D_{mean}, and dose spillage parameters (i.e., $R_{50\%}$ and D_{2cm}). The exception was for the PTV D_{max} and the conformity index, which showed a statistically significant difference (p-value <0.05). The PTV_{54Gy} coverage calculated by the CCC for overall plans agreed to within ±6% with the Monte Carlo simulation. However, only two out of twenty plans that had a difference >5%. Better agreement was observed for the $PTV_{48.6Gy}$ coverage to within 2%. A larger difference was observed for the PTV D_{min}, with the maximum difference of 8.55% occurring in the plan with large PTV volume. These findings are consistent with findings from other groups which reported the difference between the CCC and Monte Carlo calculations to be within 2-10% in clinical lung treatments [18, 28, 32, 38, 39].

For the dosimetric parameters to the OARs, the CCC tended to overestimate the dose to OARs in most plans. The exception was for $V_{11.4Gy}$ and $V_{10.5Gy}$ of normal lung tissue and $V_{20.4Gy}$ of brachial plexus, where the CCC underestimated the dose-volume parameters to these structures, and the maximum point dose to the pericardium, where the values calculated by the CCC and Monte Carlo were equal. However, the paired t-test showed a variation in terms of statistical significance. A significant difference (p <0.05) was mostly observed for the maximum point dose parameter, with the exception of the brachial plexus, superior vena cava, and rib. This indicates that the OARs were more sensitive to the selection of the dose calculation algorithm compared to the PTV. However, it is important to note that the dose-volume parameters observed in most of the plans were still below the dose constraints outlined in the RTOG 1021 protocol. Although outliers were found in some dose-volume parameters to OARs, the most significant dose constraint violation was for the maximum point dose to the ribs. In this case, the maximum point dose limit was exceeded in 11 plans. This violation mostly occurred in plans with tumours adjacent to the chest wall.

This study demonstrates that the CCC algorithm of the Pinnacle^3 shows better agreement with the Monte Carlo simulation in predicting the dose-volume parameters to the PTV, rather than those to the OARs. This is similar to the finding reported by Vanderstraeten *et al.* [28]. They reported that the agreement of the Pinnacle-CCC and Monte Carlo dose engine was below 5% for the target structure, but above 5% for the OARs. They further noted that the CCC algorithms implemented in Helax-TMS performed much better for OARs dose calculation than the CCC Pinnacle^3.

The findings from this study suggest that the CCC algorithm was still sufficiently accurate for dose calculation in treatment planning of lung SBRT, as the difference of the CCC algorithm was <5% for the dose parameters to target in most plans. However, further consideration should be taken for plans with a tumour adjacent to the chest wall, as the current dose prescription results in a violation of the maximum dose to the rib structure. This suggests that reducing the prescribed dose for plans with a tumour close to the chest wall could be worthwhile in reducing the probability of the rib toxicity.

As the evaluation of the physical dose parameters does not reflect the biology aspect of the treatment, the differential DVHs derived in this phase were used to calculate the TCP and NTCP in the next phase to estimate the effect of dose calculation uncertainties on the treatment outcomes.

7.1.3 Research Objective 3: Estimating the effect of dose calculation uncertainties on the prediction of tumour control probability (TCP) and normal tissue complication probability (NTCP) through the use of radiobiological models.

Phase 3 investigated the impact of the difference in dosimetric parameters calculated by the CCC and MC to the treatment outcomes prediction through the use of radiobiological models. The treatment outcome prediction was represented as the TCP and NTCP for the tumour target and normal tissues, respectively. For this purpose, the Marsden LQ Poisson model was used to calculate the TCP and the Lyman-Kutcher-Burman model was used to calculate the NTCP using parameters from the literature. It was found that the selection of model parameters affected the estimated TCP and NTCP.

The paired student t-test showed a significant difference of the mean TCP value calculated from the CCC plans and the MC plans. The TCP calculation using lower alpha value and higher clonogenic density shows the greater difference of the TCP from the CCC plans and the MC plans, especially for the large PTV volume. For instance, the use of lower bound of LQ Poisson parameters ($\alpha = 0.19\ \text{Gy}^{-1}$, $\sigma_\alpha = 0.02$, $\alpha/\beta = 9.5$ Gy, repopulation constant = 3.7, days before repopulation = 21 days) with the clonogenic density of 10^8 per cm^3 resulted in a TCP (absolute) difference of 27.80%. This was associated with a TCP overestimation of 53.98% in the CCC plans relative to the Monte Carlo plans observed in plan 17, which had a PTV volume of 74.10 cm^3. Although the mean difference from overall plans is 4.55% (-0.70%-27.80%), a difference of >10% was observed for plans with a large PTV volume. This might indicate that the SBRT treatment would be more suitable for a PTV volume of <50 cm^3, as the TCP estimated for the plans with a small PTV volume is >90%. This occurred when the high clonogenic density was used in the TCP calculation. Selecting a lower clonogenic density of 10^7 per cm^3, which was used as the default value in Biosuite software, showed a TCP of >99% in the plans with a small PTV volume (<50 cm^3) and even reach a maximum value. The TCP tended to decrease as the PTV volume increased although the linear relationship was not evident. An explanation for this could be that a larger tumour contains more tumour clonogenic cells; thus, requiring a higher dose to kill all of the tumour cells. This finding confirms the recommendation that SBRT treatment is more beneficial and should be restricted for the treatment of early stage NSCLC with small tumour size.

This study showed that the PTV_{54Gy} coverage had a weak correlation with the TCP. For example, for plan 17, which showed the largest TCP difference (27.80%), the PTV_{54Gy} difference was only 0.42% between the CCC and MC plans. This value was lower than the PTV_{54Gy} difference in plan 1 (-5.11%), which was associated with the TCP difference of only -0.70%. A strong correlation was observed between the PTV D_{min} and the TCP. This is similar to the finding reported by Chetty et al. [22] in which PTV D_{min} showed a strong influence on the TCP, rather than PTV D_{95}. This finding suggests that the PTV D_{min} should be kept ≥45 Gy in order to achieve maximum TCP.

The evaluation of the NTCP calculation showed no significant difference between the CCC and MC plans for the mean NTCP value of radiation pneumonitis and rib fractures end points. There was a tendency for the probability of RP to be higher in a larger tumour and smaller lung volume. However, the value observed in this study was less than 10% in most plans, indicating a relatively low toxicity to the normal lung tissue. The dose-volume parameters for the normal lung tissue volume, such as $V_{20,}$ MLD, and $V_{11.4}$ were important parameters in estimating the risk of radiation pneumonitis, as those parameters showed a strong correlation with the NTCP of radiation pneumonitis. Possible toxicity might occur to the ribs, especially for plans with a PTV overlapping the chest wall, which have NTCP values of 10-30.50%. This effect could possibly be reduced by lowering the prescribed dose for plans with a tumour at the chest wall location. Further investigation is required to confirm this finding in a larger patient cohort. Although the NTCP for acute oesophagitis showed a statistically significant difference between the CCC and MC dose distributions, it may not be clinically significant, as the NTCP value was <1%. The risk of acute oesophagitis will be significant if the NTCP is larger than 9.8% as reported by Chapet et al. [193]. No toxicity was found for the pericardium, as the NTCP calculation resulted in a zero value for both the CCC and MC plans. This could be due to the fact that most of the tumours were located in the right lung.

This finding suggests that the TCP is more sensitive to dose calculation uncertainties than the NTCP. However, at the same time this sensitivity is greatly influenced by the selection of radiobiological model parameters. The findings from this study complement the results from recent studies on radiobiological modelling of lung SBRT plans calculated using AAA dose calculation algorithms [166, 180]. The added value from this research is the inclusion of the modelling of rib fracture complication, which was not investigated in previous studies.

7.1.4 Limitations of the Study

This study has some limitations as follow:

- Although a good agreement has been obtained between the Monte Carlo and measurement, there is some limitations in the Monte Carlo model arises from the limitations of the measured data used for commissioning of the model. This is because the measured data which includes lateral dose profiles, depth dose profiles, and output factor used to commission the Monte Carlo model were measured using a finite size ionisation chamber (i.e. CC04 with a cavity radius of 2.0 mm and a cavity volume of 0.04 cm^3 for the field size ≥ 4 cm x 4 cm). It has been known that the use of finite size detector causes volume averaging effect which lead to penumbra broadening.
- The use of small number of materials in the patient tissue composition in the Monte Carlo simulation potentially affect the accuracy of dose calculation in the patient geometry. In this study, the patient geometry was only defined using 4 materials, i.e. air, lung, soft tissue and bone. The adipose/fat and muscle tissues were not defined, which might have an impact to the calculation of the dose to the lung and other organs that might be composed by the adipose tissues. Additional uncertainty comes from the conversion of the Monte Carlo dose from dose-to-tissue to dose-to-water.

- The use of radiobiological parameters from literature and the issue with validity of the LQ model for the dose fraction > 10Gy/fraction might affect the estimation of TCP and NTCP of the SBRT plans (i.e. over or underestimation of the TCP and NTCP values).

7.2 FUTURE WORKS

The outcome of this research has the potential to be further developed in the following areas:

1. The investigation of the optimisation of the prescribed dose for wall-seated tumours to keep the rib MPD below the dose constraint, as well as the optimisation of the number of fractions, possibly through the implementation of radiobiological optimisation level I and level II recommended by Nahum and Uzan [57].
2. The investigation of the dose calculation accuracy of the TPS algorithms for different radiation delivery techniques of SBRT treatment, namely 3DCRT, IMRT, and VMAT.
3. The evaluation of TCP and NTCP using different radiobiological models.
4. The determination of the best-fitted Poisson LQ TCP model parameters based on the clinical outcome of the lung SBRT treatments, as well as the determination of the best-fitted LKB NTCP model parameters for the chest wall and rib toxicity endpoint.
5. The evaluation of the impact of the tumour location to the TCP and NTCP, especially for tumours adjacent to the chest wall

7.3 CONCLUSION

Overall, this research has demonstrated that the CCC algorithm used in the Pinnacle^3 TPS is sufficiently accurate for treatment planning of lung SBRT plans. This is supported by the evidence that there was no significant difference in the PTV dose-volume parameters calculated by the CCC algorithm and the Monte Carlo calculation. However, there was a tendency of dose overestimation to the OARs calculated by the CCC algorithm, with exceptions for normal lung tissue, the pericardium, and the brachial plexus. The uncertainties in dose calculation have a more significant impact to the TCP, rather than the NTCP. However, the sensitivity of TCP and NTCP to dose uncertainties was dependent on the selection of parameters used in the radiobiological models. The radiobiological modelling evaluation suggests that the prescribed dose of 54 Gy may need to be reduced for tumours located at the chest wall, due to the high probability of rib fracture complication.

Therefore, this study suggests that radiotherapy centres that currently employ CCC algorithms in their TPS could treat lung cancer patients using SBRT treatment. This would benefit the patient in terms of having a higher chance to be cured of the disease, while minimising the time away from home, and saving on the costs of transport and the hospital stay. This also offers advantages to the radiotherapy centres in reducing the daily workload, enabling the treatment of more patients using existing resources.

As this study only evaluated twenty treatment plans, evaluation of more patient plans will provide more confidence in the planning of lung SBRT plans using the CCC algorithms. Certainly, the CCC algorithm is superior to correction-based algorithms. The CCC algorithm is the potential alternative to the Monte Carlo-based TPS algorithm, as it has been widely implemented in many radiotherapy centres. However, it is not impossible that MC-based TPS algorithms will quickly gain popularity and become widely adopted in many centres within the next few years.

Bibliography

1. WHO, *Cancer Fact Sheet*. 2012, World Health Organization.
2. AIHW, *Cancer incidence projections Australia, 2011 to 2020*, in *Cancer Series Number 66*. 2012, Australian Institute of Health and Welfare: Canberra.
3. Kong, F.-M., et al., *Cancers of Thorax*, in *Treatment Planning in Radiation Oncology*, F.M. Khan and B.J. Gerbi, Editors. 2012, Wolters Kluwer Lippincott Williams & Wilkins: Philadelpia. p. 677-732.
4. Joiner, M. and A.v.d. Kogel, *Basic clinical radiobiology*. 2009, London: Hodder Education.
5. Vicini, F.A., et al., *Optimizing breast cancer treatment efficacy with intensity-modulated radiotherapy.* International Journal of Radiation Oncology, Biology, Physics, 2002. **54**(5): p. 1336-1344.
6. Mendenhall, W.M., et al., *Radiotherapy for cutaneous squamous and basal cell carcinomas of the head and neck.* Laryngoscope, 2009. **119**(10): p. 1994-1999.
7. Hoffman, P.C., A.M. Mauer, and E.E. Vokes, *Lung cancer.* Lancet, 2000. **355**(9202): p. 479-485.
8. Gomez, D., et al., *Radiation Time, Dose, and Fractionation in the Treatment of Lung Cancer*, in *Advances in Radiation Oncology in Lung Cancer*, B. Jeremic, Editor. 2011. p. 122.
9. Martel, M.K., *3D Radiation Treatment Planning and Execution*, in *Advances in Radiation Oncology in Lung Cancer,* , B. Jeremic, Editor. 2011, Springer-Verlag Berlin Heidelberg. p. 143-156.
10. Li, J. and C.M.C. Ma, *Monte Carlo as a QA Tool for Advanced Radiation Therapy*, J. Seco, Editor. 2013. p. 145-154.
11. Reynaert, N., et al., *Monte Carlo treatment planning for photon and electron beams.* Radiation Physics and Chemistry, 2007. **76**(4): p. 643-686.
12. Haedinger, U., et al., *Influence of calculation model on dose distribution in stereotactic radiotherapy for pulmonary targets.* International Journal of Radiation Oncology Biology Physics, 2005. **61**(1): p. 239-249.
13. Ding, G.X., et al., *Impact of inhomogeneity corrections on dose coverage in the treatment of lung cancer using stereotactic body radiation therapy.* Medical Physics, 2007. **34**(7): p. 2985-2994.
14. Aarup, L.R., et al., *The effect of different lung densities on the accuracy of various radiotherapy dose calculation methods: Implications for tumour coverage.* Radiotherapy and Oncology, 2009. **91**(3): p. 405-414.
15. Zhuang, T., et al., *Dose calculation differences between Monte Carlo and pencil beam depend on the tumor locations and volumes for lung stereotactic body radiation therapy.* Journal of applied clinical medical physics / American College of Medical Physics, 2013. **14**(2): p. 4011.
16. Ojala, J.J., et al., *Performance of dose calculation algorithms from three generations in lung SBRT: Comparison with full Monte Carlo-based dose distributions.* Journal of Applied Clinical Medical Physics, 2014. **15**(2): p. 4-18.
17. Miura, H., et al., *Clinical introduction of Monte Carlo treatment planning for lung stereotactic body radiotherapy.* Journal of Applied Clinical Medical Physics, 2014. **15**(1): p. 38-46.

18. Zhao, Y., et al., *A clinical study of lung cancer dose calculation accuracy with Monte Carlo simulation.* Radiation Oncology, 2014. **9**(1).
19. Troeller, A., et al., *Stereotactic radiotherapy of intrapulmonary lesions: Comparison of different dose calculation algorithms for Oncentra MasterPlan®.* Radiation Oncology, 2015. **10**(1).
20. Davidson, S.E., et al., *Accuracy of two heterogeneity dose calculation algorithms for IMRT in treatment plans designed using an anthropomorphic thorax phantom.* Medical Physics, 2007. **34**(5): p. 1850-1857.
21. Carrasco, P., et al., *Comparison of dose calculation algorithms in phantoms with lung equivalent heterogeneities under conditions of lateral electronic disequilibrium.* Medical Physics, 2004. **31**(10): p. 2899-2911.
22. Chetty, I.J., et al., *Correlation of dose computed using different algorithms with local control following stereotactic ablative radiotherapy (SABR)-based treatment of non-small-cell lung cancer.* Radiotherapy and Oncology, 2013. **109**(3): p. 498-504.
23. Dobler, B., et al., *Optimization of extracranial stereotactic radiation therapy of small lung lesions using accurate dose calculation algorithms.* Radiation Oncology, 2006. **1**(1).
24. TROG, *A Randomised Phase III Trial of Highly Conformal Hypofractionated Image Guided ("Stereotactic") Radiotherapy (HypoRT) versus Conventionally Fractionated Radiotherapy (ConRT) for Inoperable Early Stage 1 Non-small Cell Lung Cancer (CHISEL). ,* in *Trans Tasman Radiation Oncology Group*. 2009.
25. Xiao, Y., et al., *Dosimetric Evaluation of Heterogeneity Corrections for RTOG 0236: Stereotactic Body Radiotherapy of Inoperable Stage I-II Non-Small-Cell Lung Cancer.* International Journal of Radiation Oncology Biology Physics, 2009. **73**(4): p. 1235-1242.
26. Rogers, D.W.O., et al., *BEAM: A Monte Carlo code to simulate radiotherapy treatment units.* Medical Physics, 1995. **22**(5): p. 503-524.
27. Verhaegen, F. and J. Seuntjens, *Monte Carlo modelling of external radiotherapy photon beams.* Physics in medicine and biology, 2003. **48**(21): p. R107-R164.
28. Vanderstraeten, B., et al., *Accuracy of patient dose calculation for lung IMRT: A comparison of Monte Carlo, convolution/superposition, and pencil beam computations.* Medical Physics, 2006. **33**(9): p. 3149-3158.
29. Latifi, K., et al., *Study of 201 non-small cell lung cancer patients given stereotactic ablative radiation therapy shows local control dependence on dose calculation algorithm.* International Journal of Radiation Oncology Biology Physics, 2014. **88**(5): p. 1108-1113.
30. Panettieri, V., et al., *SBRT of lung tumours: Monte Carlo simulation with PENELOPE of dose distributions including respiratory motion and comparison with different treatment planning systems.* Physics in Medicine and Biology, 2007. **52**(14): p. 4265-4281.
31. Fotina, I., et al., *Advanced kernel methods vs. Monte Carlo-based dose calculation for high energy photon beams.* Radiotherapy and Oncology, 2009. **93**(3): p. 645-653.
32. Hasenbalg, F., et al., *Collapsed cone convolution and analytical anisotropic algorithm dose calculations compared to VMC++ Monte Carlo simulations in clinical cases.* Physics in Medicine and Biology, 2007. **52**(13): p. 3679-3691.

33. Krieger, T. and O.A. Sauer, *Monte Carlo- versus pencil-beam-/collapsed-cone-dose calculation in a heterogeneous multi-layer phantom.* Physics in Medicine and Biology, 2005. **50**(5): p. 859-868.
34. Aspradakis, M.M., H.M. McCallum, and N. Wilson, *Dosimetric and treatment planning considerations for radiotherapy of the chest wall.* British Journal of Radiology, 2006. **79**(946): p. 828-836.
35. Han, T., et al., *Dosimetric impact of Acuros XB deterministic radiation transport algorithm for heterogeneous dose calculation in lung cancer.* Medical Physics, 2013. **40**(5).
36. Nisbet, A., et al., *Dosimetric verification of a commercial collapsed cone algorithm in simulated clinical situations.* Radiotherapy and Oncology, 2004. **73**(1): p. 79-88.
37. Pearson, M., et al., *The Implementation of an Advanced Treatment Planning Algorithm in the Treatment of Lung Cancer with Conventional Radiotherapy.* Clinical Oncology, 2009. **21**(3): p. 168-174.
38. Fotina, I., et al., *Clinical comparison of dose calculation using the enhanced collapsed cone algorithm vs. a new Monte Carlo algorithm.* Strahlentherapie und Onkologie, 2011. **187**(7): p. 433-441.
39. Calvo, O.I., et al., *On the quantification of the dosimetric accuracy of collapsed cone convolution superposition (CCCS) algorithm for small lung volumes using IMRT.* Journal of applied clinical medical physics / American College of Medical Physics, 2012. **13**(3): p. 3751.
40. Fraass, B.A., J. Smathers, and J. Deye, *Summary and recommendations of a National Cancer Institute workshop on issues limiting the clinical use of Monte Carlo dose calculation algorithms for megavoltage external beam radiation therapy.* Medical Physics, 2003. **30**(12): p. 3206-3216.
41. Chetty, I.J., et al., *Report of the AAPM Task Group No. 105: Issues associated with clinical implementation of Monte Carlo-based photon and electron external beam treatment planning.* Medical Physics, 2007. **34**(12): p. 4818.
42. Ruddon, R.W., *Cancer biology*. Vol. 4th. 2007, Oxford;New York;: Oxford University Press.
43. Tortora, G.J., et al., *Principles of anatomy & physiology*. Vol. First Asia-Pacific. 2016, Milton, Qld: John Wiley & Sons.
44. (NCI), N.C.I., *What You Need To Know About Lung Cancer*, N.I.o.H. U.S. Department of Health and Human Services, Editor.
45. Parkin, D.M., et al., *Global cancer statistics, 2002.* Ca : a Cancer Journal for Clinicians, 2005. **55**(2): p. 74-108.
46. Ferlay, J., et al., *Estimates of worldwide burden of cancer in 2008: GLOBOCAN 2008.* International Journal of Cancer, 2010. **127**(12): p. 2893-2917.
47. International Agency for Research on Cancer, W.H.O., *Globocan 2012: Estimated Cancer Incidence, Mortality and Prevalence Worldwide in 2012.* 2012.
48. Australian Institute of Health Welfare, A., *Cancer in Australia: Actual incidence data from 1991 to 2009 and mortality data from 1991 to 2010 with projections to 2012.* Asia‐Pacific Journal of Clinical Oncology, 2013. **9**(3): p. 199-213.
49. Goldstraw, P., et al., *Non-small-cell lung cancer.* The Lancet, 2011. **378**(9804): p. 1727-1740.

50. Mirsadraee, S., et al., *The 7th lung cancer TNM classification and staging system: Review of the changes and implications.* World journal of radiology, 2012. **4**(4): p. 128-134.
51. Scott, W.J., *Lung Cancer: A Guide to Diagnosis and Treatment*. 2012, Chicago: Addicus Books.
52. Chao, K.S.C., C.A. Perez, and L.W. Brady, *Radiation oncology: management decisions*. 2011, Philadelphia: Wolters Kluwer Health/Lippincott Williams & Wilkins.
53. Fix, M.K., *Photons: Clinical Considerations and Applications*, in *Monte Carlo Techniques in Radiation Therapy*, J. Seco and F. Verhaegen, Editors. 2013, CRC Press p. 167-184.
54. Brock, J., et al., *Review of hypofractionated small volume radiotherapy for early-stage non-small cell lung cancer.* Clinical Oncology (Royal College Of Radiologists (Great Britain)), 2008. **20**(9): p. 666-676.
55. Withers, H.R., J.M. Taylor, and B. Maciejewski, *The hazard of accelerated tumor clonogen repopulation during radiotherapy.* Acta oncologica (Stockholm, Sweden), 1988. **27**(2): p. 131-146.
56. Teoh, M., et al., *Volumetric modulated arc therapy: a review of current literature and clinical use in practice.* The British journal of radiology, 2011. **84**(1007): p. 967-996.
57. Nahum, A.E. and J. Uzan, *(Radio)Biological Optimization of External-Beam Radiotherapy.* Computational and Mathematical Methods in Medicine, 2012. **2012**: p. 13.
58. Baumann, M., et al., *Dose and fractionation concepts in the primary radiotherapy of non-small cell lung cancer.* Lung Cancer, 2001. **33**(Journal Article): p. S35-S45.
59. Hoffmann, A.L., et al., *Individualized dose prescription for hypofractionation in advanced non-small-cell lung cancer radiotherapy: an in silico trial.* International Journal Of Radiation Oncology, Biology, Physics, 2012. **83**(5): p. 1596-1602.
60. Muriel, V.P., *Hypofractionation in radiotherapy.* Clinical & translational oncology : official publication of the Federation of Spanish Oncology Societies and of the National Cancer Institute of Mexico, 2007. **9**(1): p. 21-27.
61. Haasbeek, C.J.A., B.J. Slotman, and S. Senan, *Radiotherapy for lung cancer: clinical impact of recent technical advances.* Lung cancer (Amsterdam, Netherlands), 2009. **64**(1): p. 1-8.
62. Hartmann Siantar, C.L., et al., *Description and dosimetric verification of the PEREGRINE Monte Carlo dose calculation system for photon beams incident on a water phantom.* Medical Physics, 2001. **28**(7): p. 1322-1337.
63. Boyer, A.L., *Intensity-modulated radiation therapy*, in *Treatment planning in radiation oncology*, F.M. Khan, Editor. 2010, Lippincot Williams&Wilkins: Philadelpia.
64. Otto, K., *Volumetric modulated arc therapy: IMRT in a single gantry arc.* Medical Physics, 2008. **35**(1): p. 310-317.
65. Webb, S., *VMAT: Its Role in Radiotherapy.* Medical Physics Web review, 2009. **Winter 2009**.
66. Tipton, K.N., et al., *Stereotactic Body Radiation Therapy*, in *Technical Brief No. 6. AHRQ Publication No. 10 (11)-EHC058-EF*. 2011, Agency for Healthcare Research and Quality: Rockville, MD.

67. Asnaashari, K., J.C.L. Chow, and M. Heydarian, *Dosimetric comparison between two MLC systems commonly used for stereotactic radiosurgery and radiotherapy: a Monte Carlo and experimental study.* Physica Medica, 2013. **29**(4): p. 350-356.
68. Yang, J., et al., *Cyberknife System*, in *Stereotactic Body Radiation Therapy*, S.S. Lo, et al., Editors. 2012, Springer-Verlag: Berlin Heidelberg. p. 37-50.
69. Vogelius, I.S., et al., *Hypofractionation does not increase radiation pneumonitis risk with modern conformal radiation delivery techniques.* Acta oncologica (Stockholm, Sweden), 2010. **49**(7): p. 1052-1057.
70. Patel, I., A.G. Glendinning, and M.C. Kirby, *Dosimetric characteristics of the Elekta Beam Modulator.* Physics in Medicine and Biology, 2005. **50**(23): p. 5479-5492.
71. Cranmer-Sargison, G., et al., *Small field dosimetric characterization of a new 160-leaf MLC.* Physics in Medicine and Biology, 2013. **58**(20): p. 7343-7354.
72. Martin, A. and A. Gaya, *Stereotactic Body Radiotherapy: A Review.* Clinical Oncology, 2010. **22**(3): p. 157-172.
73. Goldsmith, C. and A. Gaya, *Stereotactic ablative body radiotherapy (SABR) for primary and secondary lung tumours.* Cancer imaging : the official publication of the International Cancer Imaging Society, 2012. **12**(2): p. 351-360.
74. Heinzerling, J.H. and R.D. Timmerman, *Stereotactic Ablative Radiotherapy for Early Stage Lung Cancer*, in *Advances in Radiation Oncology in Lung Cancer*, B. Jeremic, Editor. 2011, Springer-Verlag: Berlin Heidelberg. p. 343-361.
75. Rule, W.G., S. Jain, and T.P. Boike, *Stereotactic Body Radiation Therapy*, in *Treatment Planning in Radiation Oncology*, F.M. Khan and B.J. Gerbi, Editors. 2012, Wolters Kluwer Lippincott Williams&Kluwer: Philadelpia. p. 278-297.
76. Chi, A., et al., *Stereotactic Body Radiation Therapy in Non–Small-Cell Lung Cancer: Linking Radiobiological Modeling and Clinical Outcome.* American Journal of Clinical Oncology, 2011. **34**(4): p. 432-441 10.1097/COC.0b013e3181df4b3f.
77. Onishi, H., et al., *Hypofractionated stereotactic radiotherapy (HypoFXSRT) for stage I non-small cell lung cancer: updated results of 257 patients in a Japanese multi-institutional study.* Journal Of Thoracic Oncology: Official Publication Of The International Association For The Study Of Lung Cancer, 2007. **2**(7 Suppl 3): p. S94-S100.
78. Solberg, T.D., B. Kavanagh, and P.M. Medin, *Image-guided Stereotactic Radiosurgery and Stereotactic Body Radiation therapy*, in *Iamge-Guided and Adaptive Radiation Therapy*, R. Timmerman and L. Xing, Editors. 2010, Lippincott Williams & Welkins: Philadelpia. p. 85-98.
79. Taylor, M.L., T. Kron, and R.D. Franich, *A contemporary review of stereotactic radiotherapy: inherent dosimetric complexities and the potential for detriment.* Acta oncologica (Stockholm, Sweden), 2011. **50**(4): p. 483-508.
80. Fogliata, A., et al., *On the dosimetric behaviour of photon dose calculation algorithms in the presence of simple geometric heterogeneities: Comparison with Monte Carlo calculations.* Physics in Medicine and Biology, 2007. **52**(5): p. 1363-1385.

81. Papanikolaou, N. and S. Stathakis, *Dose-calculation algorithms in the context of inhomogeneity corrections for high energy photon beams.* Medical Physics, 2009. **36**(10): p. 4765-4775.
82. Metcalfe, P., et al., *The physics of radiotherapy x-rays and electrons*. 2007, Madison, Wis: Medical Physics Pub.
83. Gete, E., T. Teke, and W. Kwa, *Evaluation of the AAA treatment planning algorithm for SBRT lung treatment: Comparison with monte carlo and homogeneous pencil beam dose calculations.* Journal of Medical Imaging and Radiation Sciences, 2012. **43**(1): p. 26-33.
84. Bragg, C.M. and J. Conway, *Dosimetric verification of the anisotropic analytical algorithm for radiotherapy treatment planning.* Radiotherapy and Oncology, 2006. **81**(3): p. 315-323.
85. Han, T., et al., *Dosimetric comparison of Acuros XB deterministic radiation transport method with Monte Carlo and model-based convolution methods in heterogeneous media.* Medical Physics, 2011. **38**(5): p. 2651-2664.
86. Fogliata, A., et al., *Critical appraisal of acuros XB and anisotropic analytic algorithm dose calculation in advanced non-small-cell lung cancer treatments.* International Journal of Radiation Oncology Biology Physics, 2012. **83**(5): p. 1587-1595.
87. Rassiah-Szegedi, P., et al., *Dosimetric evaluation of a Monte Carlo IMRT treatment planning system incorporating the MIMiC.* Physics in Medicine and Biology, 2007. **52**(23): p. 6931-6941.
88. Fragoso, M., et al., *Dosimetric verification and clinical evaluation of a new commercially available Monte Carlo-based dose algorithm for application in stereotactic body radiation therapy (SBRT) treatment planning.* Physics in Medicine and Biology, 2010. **55**(16): p. 4445-4464.
89. Benedict, S.H., et al., *Stereotactic body radiation therapy: The report of AAPM Task Group 101.* Medical Physics, 2010. **37**(8): p. 4078-4101.
90. Ahnesjö, A. and M.M. Aspradakis, *Dose calculations for external photon beams in radiotherapy*. Physics in Medicine and Biology, 1999. **44**(11): p. R99-R155.
91. Paelinck, L., et al., *Experimental verification of lung dose with radiochromic film: Comparison with Monte Carlo simulations and commercially available treatment planning systems.* Physics in Medicine and Biology, 2005. **50**(9): p. 2055-2069.
92. Takahashi, W., et al., *Evaluation of heterogeneity dose distributions for Stereotactic Radiotherapy (SRT): Comparison of commercially available Monte Carlo dose calculation with other algorithms.* Radiation Oncology, 2012. **7**(1).
93. Luo, W., et al., *Monte Carlo dose verification for lung SBRT with CMS/Xio superposition algorithm.* Biomedical Physics & Engineering Express, 2016. **2**(1): p. 015020.
94. Liu, M.B., et al., *Clinical impact of dose overestimation by effective path length calculation in stereotactic ablative radiation therapy of lung tumors.* Practical Radiation Oncology, 2013. **3**(4): p. 294-300.
95. McDermott, L. and A. Perkins, *Comparison of measured and calculated radiotherapy doses in the chest region of an inhomogeneous humanoid phantom.* Australasian Physical and Engineering Sciences in Medicine, 2004. **27**(1): p. 16-21.

96. Hall, E.J. and A.J. Giaccia, *Radiobiology for the Radiobiologist* Seventh Edition ed. 2012: Wolter Kluwer Lippincot Williams and Wilkins.
97. Bushong, S.C., *Radiologic science for technologists: physics, biology, and protection*. Vol. Tenth. 2013, St. Louis: Elsevier Mosby.
98. Orton, C.G., *Fractionation: Radiobiological Principles and Clinical Practice*, in *Treatment Planning in Radiation Oncology*, F.M. Khan and B.J. Gerbi, Editors. 2012, Lippincott Williams & Wilkins: Philadelphia. p. 405 -419.
99. Hall, E.J. and A.J. Giaccia, *Radiobiology for the radiologist*. 2006, Philadelphia: Lippincott Williams & Wilkins.
100. Fowler, J.F., *Development of radiobiology for oncology—a personal view*. Physics in medicine and biology, 2006. **51**(13): p. R263-R286.
101. Chao, K.S.C., et al. *Radiation Oncology Management Decisions*. [1 online resource (879 p.)] 2011; 3.:[Available from: http://qut.eblib.com.au/patron/FullRecord.aspx?p=2031876.
102. Scheenstra, A., et al., *101 oral VALIDATION OF THE LQL MODEL FOR NTCP PREDICTION IN LUNG CANCER PATIENTS TREATED WITH SBRT.* Radiotherapy and Oncology, 2011. **99**: p. S37-S37.
103. Song, C.W., et al., *Radiobiology of stereotactic body radiation therapy/stereotactic radiosurgery and the linear-quadratic model.* International Journal of Radiation Oncology Biology Physics, 2013. **87**(1): p. 18-19.
104. Brown, J.M., D.J. Carlson, and D.J. Brenner, *The Tumor Radiobiology of SRS and SBRT: Are More Than the 5 Rs Involved?* International Journal of Radiation OncologyBiologyPhysics, 2014. **88**(2): p. 254-262.
105. Holloway, L., *Of what use is radiobiological modelling?* Australasian physical & engineering sciences in medicine / supported by the Australasian College of Physical Scientists in Medicine and the Australasian Association of Physical Sciences in Medicine, 2009. **32**(2): p. xi-xiv.
106. Fraass, B., et al., *American Association of Physicists in Medicine Radiation Therapy Committee Task Group 53: quality assurance for clinical radiotherapy treatment planning.* Medical Physics, 1998. **25**(10): p. 1773.
107. Allen Li, X., et al., *The use and QA of biologically related models for treatment planning: Short report of the TG-166 of the therapy physics committee of the AAPM a.* Medical Physics, 2012. **39**(3): p. 1386-1409.
108. Panettieri, V., et al., *Influence of dose calculation algorithms on isotoxic dose-escalation of non-small cell lung cancer radiotherapy.* RADIOTHERAPY AND ONCOLOGY, 2010. **97**: p. 418 - 424.
109. Warkentin, B., et al., *A TCP-NTCP estimation module using DVHs and known radiobiological models and parameter sets.* Journal of Applied Clinical Medical Physics, 2004. **5**(1): p. 50-63.
110. Hardcastle, N., et al., *Comparison of prostate IMRT and VMAT biologically optimised treatment plans.* Medical dosimetry : official journal of the American Association of Medical Dosimetrists, 2011. **36**(3): p. 292-298.
111. Sanchez-Nieto, B. and A.E. Nahum, *BIOPLAN: software for the biological evaluation of. Radiotherapy treatment plans.* Medical dosimetry : official journal of the American Association of Medical Dosimetrists, 2000. **25**(2): p. 71-76.
112. Deasy, J.O., A.I. Blanco, and V.H. Clark, *CERR: a computational environment for radiotherapy research.* Medical Physics, 2003. **30**(5): p. 979-985.

113. Uzan, J. and A.E. Nahum, *Radiobiologically guided optimisation of the prescription dose and fractionation scheme in radiotherapy using BioSuite.* British Journal of Radiology, 2012. **85**(1017): p. 1279-1286.
114. Bielajew, A.F., *History of Monte Carlo*, in *Monte Carlo Techniques in Radiation Therapy*, J. Seco and F. Verhaegen, Editors. 2013, CRC Press: Boca Raton. p. 3-16.
115. Kalos, M.H. and P.A. Whitlock, *Monte Carlo methods*. Vol. 2nd rev. and enl.;2. Aufl.;2;. 2008, Weinheim: Wiley-Blackwell.
116. Haghighat, A., *Monte Carlo Methods for Particle Transport*. 2014, Hoboken: CRC Press.
117. Bielajew, A.F., *Fundamentals of the Monte Carlo method for neutral and charged particle transport*. 2001, The University of Michigan: Michigan USA.
118. Dunn, W.L. and J.K. Shultis, *Exploring Monte Carlo Methods*. 2012, NL: Elsevier Science.
119. Chow, J.C.L., M.K.K. Leung, and J. Van Dyk, *Variations of lung density and geometry on inhomogeneity correction algorithms: A Monte Carlo dosimetric evaluation.* Medical Physics, 2009. **36**(8): p. 3619-3630.
120. Chen, H., et al., *Stereotactic, single-dose irradiation of lung tumors: A comparison of absolute dose and dose distribution between pencil beam and monte carlo algorithms based on actual patient ct scans.* International Journal of Radiation Oncology Biology Physics, 2010. **78**(3): p. 955-963.
121. van der Voort van Zyp, N.C., et al., *Clinical introduction of Monte Carlo treatment planning: A different prescription dose for non-small cell lung cancer according to tumor location and size.* Radiotherapy and Oncology, 2010. **96**(1): p. 55-60.
122. Bush, K., et al., *Dosimetric validation of Acuros® XB with Monte Carlo methods for photon dose calculations.* Medical Physics, 2011. **38**(4): p. 2208-2221.
123. Wilcox, E.E., G.M. Daskalov, and H. Lincoln, *Stereotactic radiosurgery-radiotherapy: Should Monte Carlo treatment planning be used for all sites?* Practical Radiation Oncology, 2011. **1**(4): p. 251-260.
124. Keall, P.J., et al., *The effect of dose calculation uncertainty on the evaluation of radiotherapy plans.* Medical Physics, 2000. **27**(3): p. 478-484.
125. Fippel, M., *Variance Reduction Techniques*, J. Seco, Editor. 2013. p. 29-39.
126. Kawrakow, I., D.W.O. Rogers, and B.R.B. Walters, *Large efficiency improvements in BEAMnrc using directional bremsstrahlung splitting.* Medical Physics, 2004. **31**(10): p. 2883-2898.
127. Fippel, M., *Basics of Monte Carlo Simulations*, J. Seco, Editor. 2013. p. 17-28.
128. Khan, F.M., *The Physics of Radiation Therapy*. Fourth Edition ed. 2010, Philadelphia: Lippincott Williams & Wilkins.
129. Kawrakow, I., *Accurate condensed history Monte Carlo simulation of electron transport. I. EGSnrc, the new EGS4 version.* Medical Physics, 2000. **27**(3): p. 485-498.
130. Lewis, G. and E. Spezi, *An overview of Monte Carlo treatment planning for radiotherapy.* Radiation Protection Dosimetry, 2008. **131**(1): p. 123-129.
131. Lewis, D.G., E. Spezi, and P.W. Chin, *Monte Carlo simulation of portal dosimetry on a rectilinear voxel geometry: a variable gantry angle solution.* Physics in medicine and biology, 2003. **48**(16): p. N231-N238.
132. Rogers, D.W.O., B. Walter, and I. Kawrakow, *BEAMnrc Users Manual*. 2013, Ottawa: Ionizing Radiation Standards National Research Council of Canada.

133. Walters, B., I. Kawrakow, and D.W.O. Rogers, *DOSXYZnrc Users Manual*. 2013, Ottawa: Ionising Radiation Standards National Research Council of Canada.
134. Kawrakow, I. and B.R.B. Walters, *Efficient photon beam dose calculations using DOSXYZnrc with BEAMnrc.* Medical Physics, 2006. **33**(8): p. 3046-3056.
135. Verhaegen, F., *Monte Carlo Modeling of External Photon Beams in Radiotherapy*, J. Seco, Editor. 2013. p. 63-86.
136. Vlamynck, K.D., et al., *Dose measurements compared with Monte Carlo simulations of narrow 6 MV multileaf collimator shaped photon beams.* Medical Physics, 1999. **26**(9): p. 1874-1882.
137. Walle, J.V.d., et al., *Monte Carlo model of the Elekta SLiplus accelerator: validation of a new MLC component module in BEAM for a 6 MV beam.* Physics in Medicine and Biology, 2003. **48**(3): p. 371-385.
138. Reynaert, N., et al., *Monte Carlo treatment planning for photon and electron beams.* RADIATION PHYSICS AND CHEMISTRY, 2006. **76**(4): p. 643-686.
139. Sheikh-Bagheri, D. and D.W.O. Rogers, *Monte Carlo calculation of nine megavoltage photon beam spectra using the BEAM code.* Medical Physics, 2002. **29**(3): p. 391.
140. Pena, J., et al., *Automatic determination of primary electron beam parameters in Monte Carlo simulation.* Medical Physics, 2007. **34**(3): p. 1076-1084.
141. Low, D.A., et al., *A technique for the quantitative evaluation of dose distributions.* Medical Physics, 1998. **25**(5): p. 656-661.
142. Low, D.A., *Gamma Dose Distribution Evaluation Tool.* Journal of Physics: Conference Series, 2010. **250**: p. 012071-359.
143. Spezi, E. and D.G. Lewis, *Gamma histograms for radiotherapy plan evaluation.* Radiotherapy and Oncology, 2006. **79**(2): p. 224-230.
144. Keall, P.J., et al., *Determining the incident electron fluence for Monte Carlo-based photon treatment planning using a standard measured data set.* Medical Physics, 2003. **30**(4): p. 574.
145. Dermott, P.N. and C.G. Orton, *The Physics & Technology of Radiation Therapy*. 2010, Madison, Wiconsin: Medical Physics Publishing.
146. Ma, C.M., et al., *BEAM: a Monte Carlo code to simulate radiotherapy treatment units.* Medical physics, 1995. **22**(5): p. 503.
147. Kairn, T., et al., *Radiotherapy treatment verification using radiological thickness measured with an amorphous silicon electronic portal imaging device: Monte Carlo simulation and experiment.* Physics in Medicine and Biology, 2008. **53**(14): p. 3903-3919.
148. Francescon, P., N. Satariano, and S. Cora, *Calculation of k Q clin , Q msr f clin , f msr for several small detectors and for two linear accelerators using Monte Carlo simulations.* Medical Physics, 2011. **38**(12): p. 6513-6527.
149. Almberg, S.S., et al., *Monte Carlo linear accelerator simulation of megavoltage photon beams: Independent determination of initial beam parameters.* Medical Physics, 2012. **39**(1): p. 40-47.
150. Heydarian, M., et al., *Dosimetric evaluation of a dedicated stereotactic linear accelerator using measurement and Monte Carlo simulation.* Medical Physics, 2008. **35**(9): p. 3943-3954.
151. Perks, J.R., et al., *Elekta System*, in *Stereotactic Body Radiation Therapy*, S.S. Lo, et al., Editors. 2012, Springer-Verlag: Heidelberd. p. 78-89.

152. Vikraman, S., et al., *Study of Interleaf Leakage and Leaf Transmission in Elekta Synergy S Beam Modulator.* International Journal of Radiation Oncology, Biology, Physics, 2010. **78**(3): p. S756-S757.
153. Sheikh-Bagheri, D. and D.W.O. Rogers, *Sensitivity of megavoltage photon beam Monte Carlo simulations to electron beam and other parameters.* Medical Physics, 2002. **29**(3): p. 379-390.
154. Keall, P.J., et al., *Determining the incident electron fluence for Monte Carlo-based photon treatment planning using a standard measured data set.* Medical Physics, 2003. **30**(4): p. 574-582.
155. Pena, J., et al., *Commissioning of a medical accelerator photon beam Monte Carlo simulation using wide-field profiles.* Physics in Medicine and Biology, 2004. **49**(21): p. 4929-4942.
156. Wang, L.L.W. and K. Leszczynski, *Estimation of the focal spot size and shape for a medical linear accelerator by Monte Carlo simulation.* Medical Physics, 2007. **34**(2): p. 485-488.
157. Crowe, S.B., *The development of Monte Carlo techniques for the verification of radiotherapy treatments*. 2011, Queensland University of Technology. p. xviii, 190.
158. Elekta, *Information for Monte Carlo modelling of the elekta linear accelerator-machine 5463 onwards*. 2005, Elekta.
159. Podder, T.K., et al., *Physical characterization and comparison of two commercially available micro-MLCs.* Physica Medica, 2011. **27**(1): p. 52-57.
160. Tonkopi, E., et al., *Influence of ion chamber response on in-air profile measurements in megavoltage photon beams.* Medical Physics, 2005. **32**(9): p. 2918-2927.
161. Tsuruta, Y., et al., *Dosimetric comparison of Acuros XB, AAA, and XVMC in stereotactic body radiotherapy for lung cancer.* Medical Physics, 2014. **41**(8).
162. Wang, L. and G.X. Ding, *The accuracy of the out-of-field dose calculations using a model based algorithm in a commercial treatment planning system.* Physics in Medicine and Biology, 2014. **59**(13): p. N113-N128.
163. Huang, B., et al., *Dose calculation of Acuros XB and Anisotropic Analytical Algorithm in lung stereotactic body radiotherapy treatment with flattening filter free beams and the potential role of calculation grid size.* Radiation Oncology, 2015. **10**(1).
164. Ohtakara, K. and H. Hoshi, *Comparison of pencil beam-based homogeneous vs inhomogeneous target dose planning for stereotactic body radiotherapy of peripheral lung tumors through Monte Carlo-based recalculation.* Medical Dosimetry, 2015. **40**(3): p. 248-255.
165. Pokhrel, D., et al., *Technical note: Dosimetric evaluation of Monte Carlo algorithm in iPlan for stereotactic ablative body radiotherapy (SABR) for lung cancer patients using RTOG 0813 parameters.* Journal of Applied Clinical Medical Physics, 2015. **16**(1): p. 349-359.
166. Liang, X., et al., *Radiobiological impact of dose calculation algorithms on biologically optimized IMRT lung stereotactic body radiation therapy plans.* Radiation Oncology, 2016. **11**(1).
167. Fitzgerald, R., et al., *The effect of beam arrangements and the impact of non‐coplanar beams on the treatment planning of stereotactic ablative radiation therapy for early stage lung cancer.* Journal of Medical Radiation Sciences, 2016. **63**(1): p. 31-40.

168. Crowe, S., et al. *Experimental evaluation of MCDTK, the Monte Carlo DICOM Tool-Kit*. in *World Congress on Medical Physics and Biomedical Engineering*. 2012. Beijing, China: Springer.

169. Thebaut, J. and S. Zavgorodni, *Coordinate transformations for BEAM/EGSnrc Monte Carlo dose calculations of non-coplanar fields received from a DICOM-compliant treatment planning system.* Physics in Medicine and Biology, 2006. **51**(23): p. N441-N449.

170. Bush, K.K. and S.F. Zavgorodni, *IEC accelerator beam coordinate transformations for clinical Monte Carlo simulation from a phase space or full BEAMnrc particle source.* Australasian Physical and Engineering Sciences in Medicine, 2010. **33**(4): p. 351-355.

171. Zhan, L., R. Jiang, and E.K. Osei, *Beam coordinate transformations from DICOM to DOSXYZnrc.* Physics in Medicine and Biology, 2012. **57**(24): p. N513.

172. Schlect, D., et al., *Technical Note: Modeling a complex micro-multileaf collimator using the standard BEAMnrc distribution.* Medical Physics, 2010. **37**(4): p. 1761-1767.

173. Boyer, A.L. and S. Li, *Geometric analysis of light-field position of a multileaf collimator with curved ends.* Medical Physics, 1997. **24**(5): p. 757-762.

174. Barriger, R.B., et al., *A dose-volume analysis of radiation pneumonitis in non-small cell lung cancer patients treated with stereotactic body radiation therapy.* International Journal Of Radiation Oncology, Biology, Physics, 2012. **82**(1): p. 457-462.

175. Stathakis, S., et al., *SU-F-T-623: Dosimetric and Radiobiological Comparison of Conventional and Monte Carlo Treatment Plans of Lung Tumors Using SBRT.* Medical Physics, 2016. **43**(6): p. 3607-3607.

176. Lo, S.S., et al., *Stereotactic Body Radiation Therapy*. 2012, Dordrecht: Springer.

177. Andolino, D.L., et al., *Chest Wall Toxicity After Stereotactic Body Radiotherapy for Malignant Lesions of the Lung and Liver.* International Journal of Radiation Oncology, Biology, Physics, 2011. **80**(3): p. 692-697.

178. Andreo, P., *Dose to 'water-like' media or dose to tissue in MV photons radiotherapy treatment planning: still a matter of debate.* PHYSICS IN MEDICINE AND BIOLOGY, 2015. **60**(1): p. 309-337.

179. Jackson, A. and G.J. Kutcher, *Treatment Plan Evaluation*, in *Treatment Planning in Radiation oncology*, F.M. Khan and B.J. Gerbi, Editors. 2012, Wolters Kluwer Lippincott Williams &Wilkins: Philadelpia. p. 443-445.

180. Huang, B.T., et al., *Radiobiological modeling analysis of the optimal fraction scheme in patients with peripheral non-small cell lung cancer undergoing stereotactic body radiotherapy.* Scientific Reports, 2015. **5**.

181. Nielsen, T.B., et al., *Influence of dose calculation algorithms on the predicted dose distributions and NTCP values for NSCLC patients.* Medical Physics, 2011. **38**(5): p. 2412-2418.

182. Bufacchi, A., et al., *Clinical implications in the use of the PBC algorithm versus the AAA by comparison of different NTCP models/parameters.* Radiation Oncology, 2013. **8**(1).

183. Hedin, E. and A. Bäck, *Influence of different dose calculation algorithms on the estimate of NTCP for lung complications.* Journal of Applied Clinical Medical Physics, 2013. **14**(5): p. 127-139.

184. Webb, S. and A.E. Nahum, *A model for calculating tumour control probability in radiotherapy including the effects of inhomogeneous distributions of dose and clonogenic cell density.* Physics in Medicine and Biology, 1993. **38**(6): p. 653.
185. Valdes, G., et al., *Tumor control probability and the utility of 4D vs 3D dose calculations for stereotactic body radiotherapy for lung cancer.* Medical Dosimetry, 2015. **40**(1): p. 64-69.
186. Qi, X., et al., *Analysis of Outcomes in Early-Stage Non-small Cell Lung Cancer Irradiation: Fractionation Scheme Implications for Stage I Versus Stage II Disease.* International Journal of Radiation Oncology*Biology*Physics, 2012. **84**(3, Supplement): p. S566.
187. Burman, C., et al., *Fitting of normal tissue tolerance data to an analytic function.* International Journal of Radiation Oncology, Biology, Physics, 1991. **21**(1): p. 123-135.
188. Seppenwoolde, Y., et al., *Comparing different NTCP models that predict the incidence of radiation pneumonitis.* International Journal of Radiation Oncology, Biology, Physics, 2003. **55**(3): p. 724-735.
189. Semenenko, V.A. and X.A. Li, *Lyman–Kutcher–Burman NTCP model parameters for radiation pneumonitis and xerostomia based on combined analysis of published clinical data.* Physics in Medicine and Biology, 2008. **53**(3): p. 737.
190. Wennberg, B.M., et al., *NTCP modelling of lung toxicity after SBRT comparing the universal survival curve and the linear quadratic model for fractionation correction.* Acta Oncologica, 2011. **50**(4): p. 518-527.
191. Gagliardi, G., et al., *Radiation Dose–Volume Effects in the Heart.* International Journal of Radiation Oncology, Biology, Physics, 2010. **76**(3): p. S77-S85.
192. Belderbos, J., et al., *Acute esophageal toxicity in non-small cell lung cancer patients after high dose conformal radiotherapy.* Radiotherapy and Oncology, 2005. **75**(2): p. 157-164.
193. Chapet, O., et al., *Normal tissue complication probability modeling for acute esophagitis in patients treated with conformal radiation therapy for non-small cell lung cancer.* Radiotherapy and Oncology, 2005. **77**(2): p. 176-181.
194. Scheenstra, A. *O10.07 - Dose-response analysis of radiation induced rib fractures after SBRT for NSCLC*. in *15th World Conference on Lung Cancer*. 2013. Sydney, Australia: IASLC (International Association for the Study of Lung Cancer).
195. Marks, L.B., et al., *Use of Normal Tissue Complication Probability Models in the Clinic.* International Journal of Radiation Oncology, Biology, Physics, 2010. **76**(3): p. S10-S19.
196. Dunlap, N.E., et al., *Chest wall volume receiving >30 Gy predicts risk of severe pain and/or rib fracture after lung stereotactic body radiotherapy.* Int J Radiat Oncol Biol Phys, 2010. **76**(3): p. 796-801.
197. Stephans, K.L., et al., *Prediction of chest wall toxicity from lung stereotactic body radiotherapy (SBRT).* Int J Radiat Oncol Biol Phys, 2012. **82**(2): p. 974-80.

Appendices

Appendix A
Dissemination of Work

A.1 Online Proceedings

Herwiningsih, S. and A. Fielding, *Focal spot estimation of an Elekta dedicated stereotactic linear accelerator Monte Carlo model.* Journal of Physics: Conference Series, 2016. **694**(1): p. 012013

A.2 Conference presentations

S. Herwiningsih and A. Fielding 2014 Monte Carlo modelling of Elekta Axesse linear accelerator, ACOMP/SEACOMP conference (Ho Chi Minh City, Vietnam)

S. Herwiningsih and A. Fielding 2015 Validation of an Elekta Beam Modulator Monte Carlo model, EPSM Conference (Wellington, New Zealand)

S. Herwiningsih and A. Fielding 2015 Monte Carlo modelling and commissioning of an Elekta Axesse beam modulator linear accelerator, IHBI Inspires Postgraduate Student Conference (Brisbane, Australia)

S. Herwiningsih and A. Fielding 2015 Focal Spot estimation of an elekta dedicated stereotactic linear accelerator model, SEACOMP conference (Yogyakarta, Indonesia)

S. Herwiningsih and A. Fielding 2016 MLC positioning error detection using water planar dose maps, the 6th Annual BSIC conference (Malang, Indonesia)